Regional Scale Wind Farm Aerodynamics

The Role of Atmospheric Gravity Waves

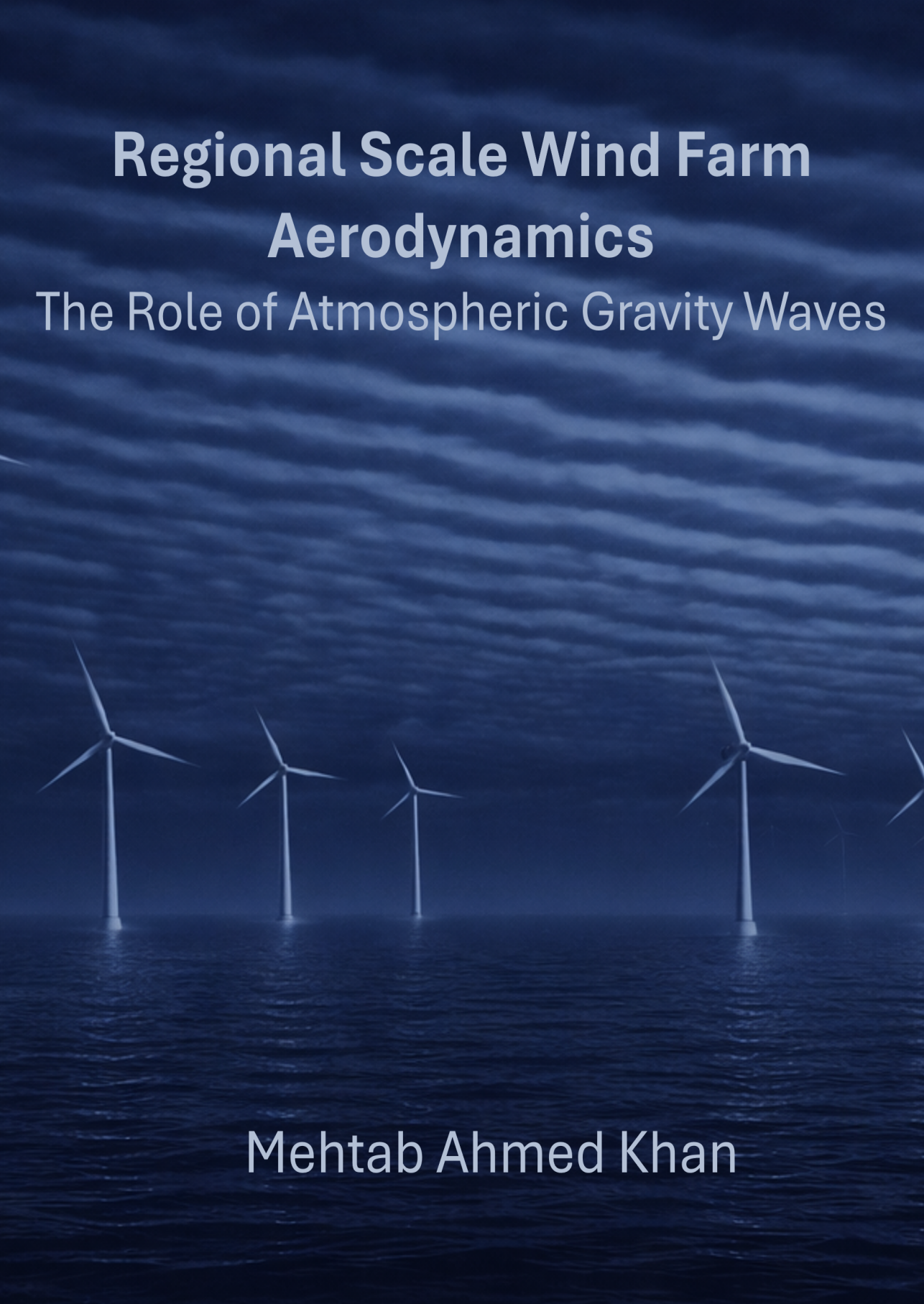

Mehtab Ahmed Khan

REGIONAL SCALE WIND FARM AERODYNAMICS

THE ROLE OF ATMOSPHERIC GRAVITY WAVES

REGIONAL SCALE WIND FARM AERODYNAMICS

THE ROLE OF ATMOSPHERIC GRAVITY WAVES

Dissertation

for the purpose of obtaining the degree of doctor
at Delft University of Technology,
by authority of the Rector Magnificus Prof.dr.ir. H. Bijl, chair of the Board for Doctorates,
to be defended publicly on
Wednesday, 8 April, 2026 at 10:00 o'clock

by

Mehtab Ahmed KHAN

This dissertation has been approved by the promotors and the external adviser

Composition of the doctoral committee:

Rector Magnificus,	chairperson
Prof. dr. S.J. Watson	Delft University of Technology, promotor
Prof. dr. D.A. Von Terzi	Delft University of Technology, promotor
Dr. M.J. Churchfield	National Renewable Energy Laboratory, external adviser

Independent Members:

Prof. dr. ir. J.W. Van Wingerden	Delft University of Technology
Prof. dr. S. Ivanell	Uppsala University, Sweden
Dr. ir. R.J.A.M. Stevens	University of Twente, Netherlands
Dr. ir. S.P. Porchetta	Delft University of Technology
Prof. dr. ir. A.C. Vire	Delft University of Technology, reserve member

Dr. ir. D.J.N. Allaerts has contributed significantly to the realization of this dissertation.

Keywords: Wind Farm Aerodynamics, Atmospheric Gravity Waves, Large Eddy Simulations, Stratification Effects.

Printed by: Ipskamp Printing | https://www.ipskampprinting.nl

Cover By: Likhitha Ramesh Reddy.

ISBN/EAN: 978-94-6518-289-6

An electronic version of this dissertation is available at:
http://repository.tudelft.nl/.

My heartfelt thanks to Dries Allaerts.

CONTENTS

SUMMARY

Large offshore wind farms and wind-farm clusters, referred to as regional-scale wind farms in this study, interact with the atmosphere beyond their boundaries. Besides their wakes extending to tens of kilometers horizontally, regional-scale wind farms induce atmospheric gravity waves (AGWs) interacting with shallow capping inversions and the free atmosphere aloft. As the size and number of regional-scale wind farms are growing, predicting their performance is becoming vital, as it directly links with wind farm planning and operations, and therefore the associated economics. Understanding the physical processes is essential for an accurate prediction of wind farm performance. There is significant knowledge concerning wind farm wakes and internal boundary layers, but the study of wind-farm-induced atmospheric gravity waves is relatively new to the wind energy community. Given the large size and relatively low amplitudes of these waves, field experiments are difficult. Engineering models often rely on analytical solutions to provide sufficient physical insight, but at this point, there is no analytical solution available for wind-farm-induced atmospheric gravity waves. Thus, high-fidelity numerical modeling, mostly large eddy simulations (LES), is the most viable method to investigate wind-farm-induced atmospheric gravity waves.

Only a few researchers have employed LES to investigate the impact of AGWs on hypothetical wind farms under canonical atmospheric conditions based on real weather data. These researchers show that AGWs can create unfavorable pressure gradients that decelerate the flow ahead of the wind farm, contributing to the wind farm blockage effect, and they also can form favorable pressure gradients at the back of the farm that assists in wake recovery. However, LES of wind farm flows, including AGWs, requires damping layers to mitigate spurious reflections of AGWs off of domain boundaries, a process that requires case-specific tuning. This case-specific tuning of the simulation domain setup is time-consuming and computationally expensive. Moreover, a unified description of the AGW phenomena, their types, and a thorough understanding of their impacts on both isolated and clustered wind farms is still an open topic. Therefore, the aim of this research is to provide systematic guidance on the setting up LES codes in simulating wind farms and to give insight into the role of AGWs in wind farm aerodynamics.

A systematic approach to simulating wind-farm and atmospheric interactions is presented using non-dimensional analysis to address the complexity arising from numerous interdependent and variable parameters. These parameters relate to atmospheric conditions, wind farm characteristics, and LES configurations for wind farm modeling. Because varying one parameter at a time is tedious and hard to comprehend, key parameters are identified and dimensional reasoning applied to define nine non-dimensional parameters. Among the non-dimensional parameters, four—the Froude numbers for the free atmosphere and capping inversion (Fr and Fr_i), and the vertical aspect ratios of the atmospheric boundary layer (ABL) and wind farm ($\tilde{H}_i$ and $\tilde{S}_h$)–serve as physical parameters that define the governing flow physics. The remaining five—$\tilde{X}$, $\tilde{L}_z$, $\tilde{L}_d$,

$\tilde{L}_a$, and ξ—are simulation parameters that determine whether the domain captures the AGW wavelengths and the damping layers are configured to avoid spurious AGWs. The work is focused on conventionally neutral boundary layers (CNBL), which consist of a neutral ABL capped by a strong temperature inversion and an overlying weakly stratified free atmosphere.

The physical non-dimensional parameters determine AGW characteristics, and the simulation parameters link the AGW wavelengths to the LES domain size and damping layer configuration. Therefore, the setup of the wind farm LES becomes a simple systematic procedure that starts with calculating the physical non-dimensional parameters and estimating expected AGW wavelengths. Then, the domain size and damping layer thickness should be set to capture at least a wavelength, while the normalized damping frequency should be set in the range of 1 to 10 when scaled with the Brunt-Väisälä frequency, which is a function of the free-atmospheric lapse rate. It is emphasized that wind farms trigger a spectrum of AGWs, and the domain and damping layer sizing should be related to the effective wavelengths, which are representative of the whole spectrum. These wavelengths can be assumed from this thesis or estimated with linear wave theory or a reduced-order atmospheric perturbation model such as the Multi-Scale Coupled model.

AGW phenomena, their types, and characteristics for practical wind farm flow conditions were investigated to provide a unified and baseline understanding for the wind energy community. Wind-farm-induced atmospheric gravity waves are driven by buoyancy, which attempts to restore the displacing capping inversion caused by wind farm perturbations. The two main perturbations are upward flow deflection at the start of the wind farm and downward flow deflection at the end of it, which trigger two out of phase wave fields. A couple of concepts are critical to understand AGW phenomena: firstly, only wave modes supported by the buoyancy (i.e. frequencies $< N$) of the free atmosphere can propagate; unsupported wave modes are evanescent, decaying exponentially. Secondly, the wave speed relative to the advection speed of the flow determines three regimes, which are distinguished based on the value of Fr_i. If both the flow and wave propagation speed are the same ($Fr_i = 1.0$), we call this "critical" and the waves are choked from propagating against the flow. If the wave propagation speed is faster than the flow speed ($Fr_i < 1.0$), we call this "subcritical," and waves propagate in all directions. If the wave propagation speed is slower than the flow speed ($Fr_i > 1.0$), we call this "supercritical," and the flow advects the waves downstream creating a wave pattern tilted toward downstream. Three main types of AGW are identified, namely the propagating internal waves in the free atmosphere, interfacial waves along the capping inversion, and transient trapped waves confined inside the capping inversion, as their frequencies are higher than N. The internal waves have an intrinsic feature whereby they bend—like an arc of a circle—downstream of the obstacle (i.e. wind farm or a hill), thus always leaving an imprint on the capping inversion. For $Fr_i \leq 1.0$, the evanescent waves propagate atop the capping inversion and do not smoothly blend with the internal waves. Therefore, downstream of the obstacle, they appear distinct and are called the trapped lee waves, which significantly modulate the imprints of the internal waves.

It is obvious from the above insights how AGW characteristics are critical to both configuring accurate and realistic wind farm simulations and understanding wind-farm-

atmosphere interactions. Thus, LES configurations fully resolving AGWs (i.e. capturing at least a wavelength) are compared with those partially or not resolving them (i.e. truly neutral boundary layers and rigid-lid approximation). We observe that LES power predictions are dependent on the simulation configuration, and fully resolving AGWs is the most realistic representation of the interactions. Therefore, the AGW characteristics are investigated with CNBL configurations fully resolving the AGWs. Since interfacial and internal waves are most critical to wind farms, the dependence of their wavelengths, amplitudes, and directions on the physical non-dimensional parameters is studied. Interfacial wave characteristics depend mainly on Fr_i, as their wavelengths become shorter than half the wind farm length for subcritical conditions and about the wind farm length for supercritical conditions. These waves are blunt (i.e. perpendicular to inflow) for $Fr_i \leq 1.0$ and increasingly bend in a V-shape downstream for $Fr_i > 1.0$. Their amplitudes are the highest at critical conditions and for a given Fr_i vary the most as a function of $\tilde{H}_i$, with an approximately linearly decreasing trend with increasing $\tilde{H}_i$, as ABL depth directly affects the amplitude of the perturbed capping inversion. The properties of internal waves depend mainly on Fr, except for their amplitudes, which are most sensitive to ABL-depth. The inclination angles decrease with increasing Fr but more gradually for $Fr > 0.15$. The horizontal wavelengths increase linearly for increasing values of Fr, where the internal waves are larger than the wind farm length for $Fr > 0.15$. Thus, the wave train at the start of the wind farm is dilated across the wind farm. The amplitudes of the internal waves have similar trends as a function of the non-dimensional parameters as those of the interfacial waves, but their values are much smaller.

The performance of a wind farm operating in a CNBL is compared with that of operating in a Truly Neutral Boundary Layer (TNBL). A TNBL completely neglects buoyancy effects so it cannot support AGWs. The AGWs simulated in the CNBL are seen to decrease power produced compared to the TNBL case, mainly because there is always an increase in wind farm blockage, and any gains due to a positive pressure gradient through the wind farm are outweighed by wake losses. The variations in spatial power output due to stratification are related with the capping inversion shape at steady state, which is wavy with corresponding converging and diverging flow zones in the ABL. The sizes of these zones resemble the interfacial wavelengths, thus, mainly dependent on Fr_i. The strength of pressure gradients in these zones is also sensitive to $\tilde{H}_i$, such that shallow ABLs have stronger gradients than deeper ones.

In investigating farm-farm interactions, the inter-farm distance between the two wind farms simulated was fixed such that the interfacial waves for supercritical conditions would constructively interfere. Therefore, in comparison to the wave field around an isolated wind farm of the same characteristics, the wave fields are always distorted around the second one. Most distorted wave fields occur for subcritical conditions and around both wind farms, as waves propagate in all directions. The simulated wind farms produce less power under CNBL conditions than their counterparts in a TNBL, with the second wind farm incurring higher losses. The first wind farm performs slightly better than an isolated wind farm for the same CNBL conditions, but the second one always underperforms, particularly in shallow boundary layers and for subcritical conditions. The cluster wake is horizontally skewed in the shallowest boundary layer (i.e. $H_i = 250$ m), which indicates how a low capping inversion reduces vertical flow mixing and the wake

recovery relies more on lateral mixing.

In conclusion to this research, we established a systematic method to simulate wind farms using CFD, focusing on LES, that overcomes tedious and computationally expensive processes in fine-tuning the simulation setups. This method relies on four physical non-dimensional parameters, which govern the physics of the flow and AGW characteristics. The step-by-step procedure to set up accurate and realistic simulations requires determining these non-dimensional parameters and then estimating wavelengths of internal and interfacial waves to ensure fully resolving them in the physical domain and effectively damping them in the damping layers to prevent reflections. The same systematic method is extended to investigate AGW phenomena, their types and characteristics, and the stratification effects on regional-scale wind farm performance. We observe that the ABL-aspect ratio is the most critical non-dimensional parameter to both the characteristics of the AGWs and wind farm performance. This implies that the capping inversion is a flexible lid to the turbulent ABL and couples the flow variations in the free atmosphere with the flow in the ABL. In comparison to non-stratified atmospheric conditions (i.e. TNBL), a stratified atmosphere beyond the ABL has a negative impact on the performance of regional-scale wind farms. This is because stratification effects always increase wind farm blockage, and the gains through the wind farms are less than the losses incurred by wakes.

This study establishes how numerical modeling of wind farm aerodynamics is more realistic with fully resolved AGWs. It further highlights the need to incorporate AGWs in wind farm planning, such that losses due to stratification effects are minimized. Note that this investigation is limited to canonical CNBL conditions; thus, simulating more realistic atmospheric conditions is strongly recommended. This also indicates the need for a measurement campaign to observe wind farm-induced atmospheric gravity waves. We emphasize that the presented wind farm performance is aimed at understanding trends and should be interpreted in the context of comparing performance for varying CNBL and TBNL conditions.

SAMENVATTING

Grote windparken en clusters van windparken op zee, hier aangeduid als windparken op regionaal schaalniveau, hebben interactie met de atmosfeer voorbij hun grenzen. Naast hun zoggen die zich horizontaal tientallen kilometers verspreiden, veroorzaken windparken op regionaal schaalniveau zwaartekrachtsgolven die invloed hebben op de inversie boven de atmosferische grenslaag (hierna, de dekselinversie) en de vrije atmosfeer daarboven. Naarmate het formaat van de windparken op regionaal schaalniveau en hun aantal toeneemt neemt ook het belang van het voorspellen van hun energieproductie toe, gezien dit direct verband houdt met hun planning en bedrijfsvoering en daarmee de bijbehorende economie. Begrip van de fysische processen is essentieel voor het nauwkeurig voorspellen van de energieproductie van windparken. Waar er voldoende kennis is van de zog en interne grenslagen van windparken, zijn atmosferische zwaartekrachtsgolven een relatief nieuw concept voor de windenergie gemeenschap. De grote golflengtes en lage amplitudes van zwaartekrachtsgolven maakt metingen in het veld lastig. Technische modellen zijn vaak afhankelijk van analytische oplossingen om voldoende fysisch inzicht te kunnen bieden, maar op het moment zijn er geen analytische oplossingen beschikbaar voor zwaartekrachtsgolven afkomstig van windparken. Dus, het gebruik van numerieke modellen met een hoge werkelijkheidsweergave, met name grote wervel simulaties (LES), is het meest geschikt voor onderzoek van zwaartekrachtsgolven afkomstig van windparken.

Atmosferische zwaartekrachtsgolven (AGW) zijn nieuw voor de windenergie gemeenschap; slechts enkele onderzoekers hebben LES ingezet om hun invloed op hypothetische windparken in kanonieke atmosferische omstandigheden, gebaseerd op data van echt weer, te onderzoeken. Deze onderzoekers laten zien dat AGW's ongunstige drukgradiënten kunnen veroorzaken die de stroming voor het windpark afremmen en hierdoor bijdragen aan het blokkade effect, en ook dat ze gunstige drukgradiënten achter het windpark kunnen vormen die bijdragen aan zogherstel. Echter, LES van windparkstromingen, inclusief AGW's, vereisen dempinglagen om onrealistische reflecties van AGW's tegen de randen van het domein tegen te gaan. Het afstemmen van het simulatiedomein, inclusief dempinglagen, kost veel tijd en computerkracht. Verder is een eenduidige beschrijving van het AGW fenomeen, hun types, en een grondig begrip van hun invloed op zowel geïsoleerde als geclusterde windparken onderwerp van discussie. Het doel van dit onderzoek is daarom om systematische begeleiding te bieden bij het opzetten van LES voor het modelleren van windparken en inzicht te bieden in de rol van AGW's op de aerodynamica van windparken.

We presenteren een systematische aanpak voor het modelleren van windparken en atmosferische interacties door het gebruik van dimensieloze analyse waarmee we ons richten op de complexiteit die ontstaat door de veelvuldigheid van parameters die van elkaar afhangen en evolueren. Deze parameters hebben temaken met atmosferische condities, karakteristieken van het windpark en met de LES configuratie die wordt ge-

bruikt om de windparken te modelleren. In plaats van het variëren van enkele parameters per keer, wat intensief en lastig te begrijpen is, identificeren we dimensieloze parameters op basis van enkele sleutelparameters. Onder deze dimensieloze parameters dienen vier hiervan – het Froudegetal voor de vrije atmosfeer en dekselinversie (Fr and Fr_i) en de verticale aspect ratio's van de atmosferische grenslaag (ABL) en windpark ($\tilde{H}_i$ en $\tilde{S}_h$) – als parameters om de heersende vloeistoffysica te definiëren. De resterende vijf – $\tilde{X}$, $\tilde{L}_z$, $\tilde{L}_d$, $\tilde{L}_a$ en ξ – zijn parameters afkomstig van de simulatie die bepalen of het domein de AGW golflengtes bevat en of de dempinglaag zodanig is afgesteld om onrealistische AGW's te voorkomen. We richten ons op de conventioneel neutrale grenslaag (CNBL), die uit een neutrale ABL bestaat, vanboven besloten met een krachtige temperatuurinversie, met daarboven een zwak gestratificeerde vrije atmosfeer.

De fysische dimensieloze parameters bepalen de karakteristieken van de AGW. De simulatieparameters beschrijven de verbinding tussen enerzijds de AGW golflengtes en anderzijds de grootte van het LES domein en de configuratie van de dempinglaag. Zo wordt het opzetten van een windpark LES een simpele systematische procedure die begint met het berekenen van de fysische dimensieloze parameters en het schatten van de verwachte AGW golflengtes. Hierna moet de grootte van het domein en de dikte van de dempinglaag zodanig worden gekozen dat deze tenminste een golflengte bevat, terwijl de dempingfrequentie tussen de 1 en 10 maal de Brunt-Väisälä wordt gekozen, welke een functie is van het temperatuurverval in de vrije atmosfeer. Hier benadrukken we dat het windpark een heel spectrum aan AGW's tot stand brengt, waarbij de domeingrootte en dempinglaagdikte bepaald worden aan de hand van de effectieve golflengte, representatief voor het gehele spectrum. Aannames over deze golflengtes kunnen worden gemaakt op basis van dit proefschrift of worden geschat met behulp van lineaire golftheorie of een atmosferisch verstoringsmodel van lagere orde, zoals bijvoorbeeld het "Multi-Scale Coupled model".

We onderzoeken AGW fenomenen, hun types en karakteristieken geldig voor een praktische set condities die voor kunnen komen in een windpark, om tot een eenduidig basisbegrip voor de windenergie gemeenschap te komen. Zwaartekrachtsgolven afkomstig van windparken worden gedreven door het drijfvermogen van de lucht die verstoringen van de dekselinversie door het windpark probeert te herstellen. De twee belangrijkste verstoringen zijn de opwaartse afbuigen van de stroming aan de voorkant van het windpark en neerwaartse afbuiging van de stroming aan de achterkant. Deze verstoringen veroorzaken twee golfvelden die uit fase zijn. Een aantal concepten zijn cruciaal voor het begrip van AGW fenomenen: Ten eerste kunnen alleen golfmodi die ondersteund worden door het drijfvermogen van de vrije atmosfeer (die met frequenties kleiner dan N) voortplanten; golfmodi die niet worden ondersteund zijn vergankelijk, onderhevig aan exponentieel verval. Ten tweede bepaalt de golfsnelheid relatief tot de advectiesnelheid drie regimes, die worden onderscheiden aan de hand van de waarde van Fr_i. Waar deze snelheden gelijk zijn in kritische condities ($Fr_i = 1.0$), is de golfsnelheid sneller dan de advectiesnelheid in subkritische condities ($Fr_i < 1.0$) waardoor golven in alle richtingen kunnen voortplanten. In superkritische condities ($Fr_i > 1.0$) verdrijft de advectiesnelheid de golven in de benedenwindse richting en wordt het golfveld benedenwinds afgebogen. Drie hoofdtypes van AGW zijn de voortplantende interne golven in de vrije atmosfeer, golven langs het grensvlak van de dekselinversie (hierna,

grensvlakgolven) en vergankelijke golven gevangen in de dekselinversie zelf, waarvan de frequenties hoger zijn dan N. De interne golven hebben de intrinsieke eigenschap om benedenwinds van het obstakel (bijvoorbeeld het windpark of een heuvel) af te buigen — als een cirkelboog — waarbij ze altijd een afdruk op de dekselinversie achterlaten. Wanneer $Fr_i \leq 1.0$ planten de vergankelijke golven langs de bovenkant van de dekselinversie voort en vermengen niet met de interne golven. Hierdoor kunnen deze golven apart worden waargenomen benedenwinds van het obstakel. Deze golven, ook bekend als gevangen loefgolven, zorgen voor significante modulatie van de afdruk van de interne golven.

De bovengenoemde inzichten maken duidelijk hoe karakteristieken van de AGW cruciaal zijn voor het afstellen van nauwkeurige en realistische windpark simulaties en voor het begrip van de interactie tussen windpark en atmosfeer. Daarom hebben we LES configuraties vergeleken waarin AGW's volledig beschreven worden (die tenminste een golflengte bevatten) en deze waarin dat niet of in mindere mate het geval is (bij volwaardig neutrale grenslagen en de starre deksel benadering). We nemen waar dat voorspellingen van energieproductie met LES afhankelijk zijn van de configuratie van de simulatie, waarbij het volledig beschrijven van AGW de meest realistische representatie van de interacties geeft. Om deze reden worden AGW karakteristieken onderzocht met CNBL configuraties die de AGW's volledig beschrijven. Gezien interne- en grensvlakgolven het meest kritisch zijn voor windparken, wordt bestudeerd hoe hun golflengtes, amplitudes en richtingen afhankelijk zijn van de fysische dimensieloze parameters. Karakteristieken van grensvlakgolven hangen met name van Fr_i af, gezien hun golflengtes korter worden dan de helft van de lengte van het windpark in subkritische condities en ongeveer dezelfde lengte hebben in superkritische condities. Deze golven zijn stomp (het golffront loodrecht op de stroming) wanneer $Fr_i \leq 1.0$ en buigen in toenemende mate benedenwinds af, waarbij het front een V-vorm aanneemt, wanneer $Fr_i > 1.0$. Hun amplitudes zijn het grootst in kritische condities en voor een gegeven Fr_i variëren deze het meest als functie van $\tilde{H}_i$, wat bij benadering een lineair afnemende trend beschrijft voor toenemende $\tilde{H}_i$, gezien de diepte van de ABL de amplitude van de verstoorde dekselinversie direkt beïnvloedt. De eigenschappen van de interne golven hangen vooral af van Fr, met uitzondering van hun amplitudes die het meest gevoelig zijn voor de diepte van de ABL. De hellingshoek neemt af bij toenemende Fr en geleidelijker bij $Fr > 0.15$. De horizontale golflengtes nemen lineair toe bij toenemende Fr, waarbij de interne golven groter zijn dan de lengte van het windpark bij $Fr > 0.15$. De golftrein aan het begin van het windpark verwijdt over het windpark. De amplitudes van de interne golven laten een soortgelijke trend zien als functie van de dimensieloze parameters als die van de grensvlakgolven, alhoewel hun waardes veel kleiner zijn.

De energieproductie van een windpark in een CNBL wordt vergeleken met dat van een windpark in een Werkelijk Neutrale Grenslaag (TNBL). Een TNBL verwaarloost volledig de effecten van drijfvermogen en ondersteunen dus geen AGW's. De AGW's gesimuleerd in de CNBL leiden tot een afname in energieproductie, hoofdzakelijk omdat dit altijd tot een toename van het blokkade effect leidt, en de voordelen worden gecompenseerd door verlies ten gevolge van zogeffecten. De variatie in energieproductie van het windpark ten gevolge van stratificatie is gecorreleerd met de vorm van de dekselinversie; een golf bestaande uit opeenvolgende convergente en divergente stromingszones in de

ABL. De groottes van deze zones belichamen de golflengte van de grensvlakgolf en zijn dus met name afhankelijk van Fr_i. De sterkte van drukgradiënten in deze zones is tevens gevoelig voor $\tilde{H}_i$, zodat ondiepe ABL's gepaard gaan met sterkere gradiënten dan diepere grenslagen.

In de studie naar park-park interacties was voor een constante afstand tussen de parken gekozen zodanig dat de grensvlakgolven voor superkritische omstandigheden constructief interfereren. Het golfveld bevat hierdoor, in vergelijking met een geïsoleerd windpark, de meest uitgesproken verstoring rond het tweede park. De meeste golfvelden met uitgesproken verstoringen komen voor bij subkritische condities en rond beide windparken, gezien de golven in alle richtingen propageren. De simulaties tonen lagere energieproductie bij CNBL- dan bij TNBL condities, waarbij het tweede windpark grotere verliezen ziet. In CNBL condities produceert het eerste windpark enigszins meer dan een soortgelijk geïsoleerd windpark, waarbij het tweede altijd minder produceert dan de geïsoleerde variant, vooral wanneer de grenslaag ondiep is en bij subkritische condities. De zog van het cluster is scheef, in horizontale richting, bij de ondiepste grenslaag ($H_i = 250$ m), wat aangeeft hoe een lage dekselinversie verticale menging vermindert en meer op laterale menging leunt.

Tot slot; we hebben een systematische methode bewerkstelligd om windparken te simuleren in het kader van CFD methodes, ons hierbij met name gericht op LES, waarmee het moeizame en (in termen van computerkracht) kostbare proces van het afstellen van de opzet van de simulatie wordt overkomen. Deze methode maakt gebruik van vier fysische dimensieloze parameters die de fysica van de stroming en AGW karakteristieken beheren. De stap-voor-stap procedure voor het opzetten van nauwkeurige en realistische simulaties vergt dus dat deze dimensieloze parameters worden bepaald, waarna de golflengtes van interne- en grensvlakgolven geschat dienen te worden, om vast te stellen dat deze golven volledige beschreven worden alsmede dat deze effectief gedempt worden in de dempinglagen om reflecties te voorkomen. Dezelfde methode is uitgebreid om AGW fenomenen, hun types en karakteristieken, en stratificatie effecten op de energieproductie van windparken van regionaal schaalniveau, te bestuderen. We zien dat voor zowel de AGW karakteristieken als energieproductie van windparken de aspectverhouding van de ABL de belangrijkste dimensieloze parameter is. Dit impliceert dat de dekselinversie dient als een flexibele deksel op de turbulente ABL en voor koppeling zorgt tussen stroming in de ABL en stromingsvariaties in de vrije atmosfeer. In vergelijking met de ongestratificeerde situatie (de TNBL) heeft de gestratificeerde atmosfeer een negatieve invloed op de energieproductie van windparken op regionaal schaalniveau. Dit komt doordat stratificatie altijd het blokkade effect versterkt, en dat het voordeel voor de rest van het windpark minder is dan de verliezen van de zoggen.

Deze studie stelt vast hoe het numeriek modelleren van de aerodynamica van windparken realistischer is wanneer AGW's volledig beschrijven zijn. Het benadrukt verder de noodzaak om met AGW's rekening te houden in de planning van het windpark om verliezen door stratificatie effecten te minimaliseren. Let op dat dit werk zich beperkt tot de kanonieke CNBL situatie; het is dus sterk aangeraden om realistischere atmosferische condities te simuleren. Dit geeft ook de noodzaak van een meetcampagne weer om de zwaartekrachtsgolven afkomstig van windparken waar te nemen. We benadrukken dat de getoonde energieopbrengsten bedoeld zijn om trends te begrijpen en dienen

te worden geïnterpreteerd in de context van de vergelijking in energieproductie onder variërende CNBL- danwel TNBL condities.

Dutch Translation by Evert Wiegant

PREFACE

This computational fluid dynamic (CFD) study is at the intersection of atmospheric sciences and wind energy science, which is challenging to comprehend and articulate precisely. On the one hand, it requires an extensive understanding of the atmosphere's structure and various atmospheric phenomena, and on the other, it demands a deeper comprehension of the wind farm-atmosphere interaction on various scales. The complete range of scales, e.g. Micro to Meso, are extremely challenging to cover in a single CFD study. Thus, this thesis focuses on the wind farm scale flow interactions with the atmosphere, while following recent approaches that incorporate other scales relevant to wind farms. One of the primary interactions of this type is the induction of atmospheric gravity waves (AGWs) by wind farms, which are relatively new to the wind energy community. AGWs are buoyancy-driven waves triggered in the layers above the turbulent atmospheric boundary layer, and they can affect wind farm performance under certain atmospheric conditions.

Although this study is mainly focused on AGWs, I have endeavored to provide an overview of wind farm aerodynamics in the first two chapters. The second chapter, in particular, is written for a beginner's introduction to wind farm aerodynamics. As a whole, however, it is limited in detail and should be considered an overview to the subject. This chapter also elaborates on the investigation of wind farm aerodynamics with Large Eddy Simulations (LES). The later part of the thesis focuses on three main aspects related to AGWs. Firstly, a systematic method is proposed to accurately model wind farm flows including AGWs, as ad hoc tuning of the simulation setup was required to avoid their spurious interaction with the simulation boundaries. Secondly, the characteristics of AGWs are investigated to advance the understanding of this phenomenon and to account for the relationship between the simulation setup and AGW properties. Finally, the impact of AGWs on an isolated and two neighboring wind farms was investigated.

I hope this contribution will be useful to students and researchers in understanding atmospheric gravity waves, and to the wind energy industry in advancing the use of wind farm aerodynamics for building more efficient wind farms.

Mehtab Ahmed Khan
Delft, November 2025

Photo by Dries J.N. Allaerts,
Wezemaal, Belgium

1

INTRODUCTION

This chapter introduces the societal relevance, key research problems, the aim, and the overarching method of this study.

Parts of this chapter are published in Wind Energy Science, **Investigating the relationship between simulation parameters and flow variables in simulating atmospheric gravity waves for wind energy applications**, M. A. Khan, D. Allaerts, S. J. Watson, and M. J. Churchfield (2025) [1].

1

1.1. WHY WIND ENERGY?

Wind energy is one of the main and rapidly growing renewable energy resources that is critical to meeting net-zero emission targets by 2050. The fossil fuel-based global energy sector has been one of the main contributors to climate change, and a transition to cleaner and renewable energy resources is underway to mitigate this contribution. Wind energy, is seen as a main contributor to the clean energy mix, with its contribution so far and forecast growth. For instance, the installed global wind energy capacity reached 1020 *GW* at the beginning of 2024, which is providing 7.6 % of the global energy consumption [2]. Moreover, wind energy is expected to contribute a quarter of the new renewable energy if the global pledge to triple renewable power capacity by 2030 is achieved [3]. Altogether, the potential of wind energy to contribute to the energy transition is promising rooted in maturing technology, improved operations, and reduced price of electricity it delivers.

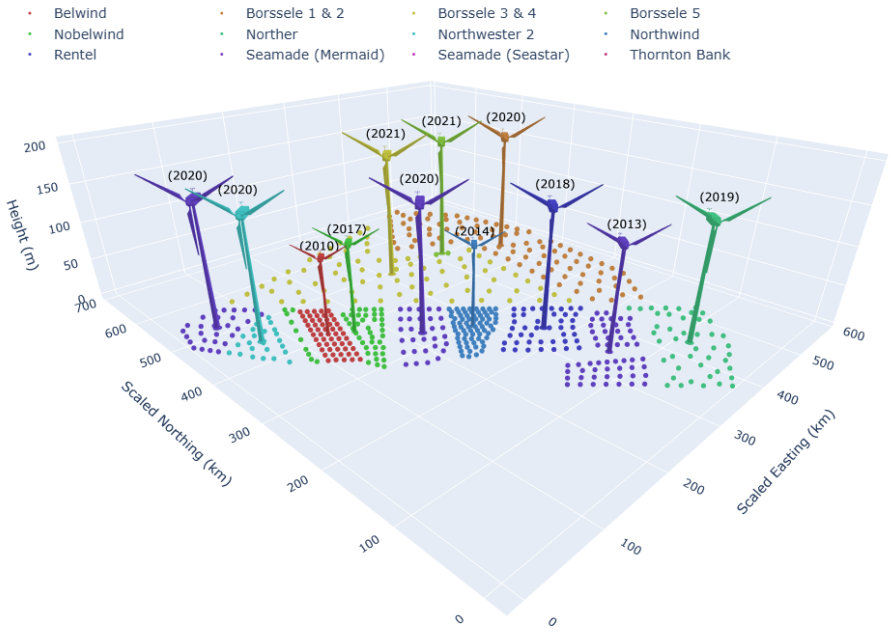

Figure 1.1: The layout of the Belgian-Dutch cluster in the North Sea with a turbine model showing the increase in size of turbines over a decade; the years show dates of commissioning of each wind farm. The horizontal distances are scaled by a factor of 20 for clear illustration.

The main contributors to wind energy growth include the increase in number of installed wind projects, size of wind turbines, and size of wind farms. The installed global wind energy capacity doubled over the last decade, increasing from 432.9 GW in 2015 [4] to 1136 GW in 2025 [5]. The wind turbine size has also been increasing. For example, the current largest installed wind turbine with a capacity of 15 MW has a rotor diameter of 236 m. In contrast, the largest installed wind turbine a decade ago had a capacity and

size of 8 MW and 164 m rotor diameter, respectively. Likewise, the wind farm size has been increasing; for instance, Seagreen became fully operational in 2023, spanning an area of 2850 km^2 and installed capacity of 1075 MW in comparison to the London array, commissioned in 2013, which covers 245 km^2 with installed capacity of 630 MW. Since wind speed is more uniform and higher on average offshore than onshore, this has encouraged an increasing number of offshore wind farms to be built. However, offshore wind farms are clustered in wind corridors (i.e. sites with consistently high winds) for ease of installation, dispatching power, maintenance, and maximizing suitable seabed utility. The whole concept around larger turbines and wind farms, and clustering is to maximize the extraction of wind energy by exposing the wind turbines, as much as possible, to smoother and consistently higher winds in a wind corridor. This is evident from the growth of the Belgian-Dutch cluster in the North Sea over a decade, as shown in Fig. 1.1. Clearly, deploying large wind farms of large wind turbines, likely in clusters, is the way wind energy is expected to grow.

1.2. WIND FARM AERODYNAMICS

Maximizing energy extraction from wind farms depends on understanding the atmospheric processes that lead to prevailing flow conditions but also the flow dynamics within and between wind farms [6–8]. The atmosphere is inherently chaotic and a complex amalgam of various phenomena, which makes wind energy intermittent and difficult to predict. However, wind energy forecasting has been a critical aspect of wind farm yield, planning, operation, and maintenance. For instance, numerical weather forecasting is widely used to predict the wind speed and direction that directly relate to the wind farm output. Such forecasting relies on a thorough understanding of the physical phenomena involved in driving atmospheric conditions. The meteorology community provides a comprehensive understanding of atmospheric phenomena critical to wind energy, enabling its reliable forecast. Thus, it is fair to assume that atmospheric processes vital to wind conditions are reasonably well understood. However, the phenomena related to the flow dynamics within a wind farm have been the focus of ongoing research in the wind energy community.

The energy extraction by wind farms, almost exclusively formed by horizontal-axis wind turbines, is a coupled process, where the wind affects the farm and its turbines and vice versa. In principle, the coupled interactions for an isolated turbine and a wind farm are similar but differ in intensity and size. In the case of a wind turbine, its aerodynamic design is such that the wind exerts torque on the rotor and converts mechanical wind energy into electrical energy through a generator. The energy extraction results in a slower but more turbulent wind behind the turbine, which is termed the wake. Since the wind turbine is a solid object, it also blocks the incoming flow, which is felt upstream of the wind turbine and is called the induction zone. Thus, the rotation of the wind turbine rotor is on one hand an effect of the wind on the turbine and, on the other hand, the wake and flow blockage are the effects of the turbine on the wind. For a wind farm, the individual turbine wakes combine into the wind farm wake. In addition, the upstream wind feels a cumulative blockage, that is, the sum of the blockage of individual turbines. Moreover, an array of wind turbines is similar to a transition in the roughness of the surface causing a developing internal boundary layer (IBL) as a function of the downstream

distance. The internal boundary layer is a significant phenomenon for wind farm flows. It determines how the flow, perturbed by the wind farm, mixes vertically with the inflow. In the end, a wind farm has a stronger, longer and wider flow blockage and wakes than those of an isolated wind turbine. The interaction through the wind farm is so strong that it develops a boundary layer of its own, where the wind speed, direction, and turbulence are affected by the wind farm.

The wider and stronger blockage, wakes, and a growing internal boundary layer of a wind farm lead to wind-farm–atmosphere interaction beyond the wind farm boundaries. This regional-scale spread of wind farm effects on the flow can invoke other wind-farm–atmosphere interactions that can be significant to the wind farm itself and others in its vicinity. One such interaction is the wind-farm-induced atmospheric gravity wave (AGW), which has a feedback effect on the wind farm's performance. When the atmospheric boundary layer (ABL), that is, the turbulent layer adjacent to the ground, is shallow, the flow deflected by the wind farm blockage and entrained by the farm wake can perturb the capping inversion above it. Since both the capping inversion and the free atmosphere aloft are always stratified, the buoyancy of each layer can restore the perturbations leading to an AGW. In other words, the AGW is a buoyancy-driven wave in the stratified layers of the atmosphere, such as the capping inversion and the free atmosphere. The wavelengths of such an AGW is of the order of the wind farm size, thus affecting the flow around the wind farms in all directions. This can result in altered wind farm power outputs. Hence, the main phenomena in the coupled regional-scale wind-farm–atmosphere interaction include the wind farm blockage effect and wakes, internal boundary layers, and the wind farm-induced atmospheric gravity waves.

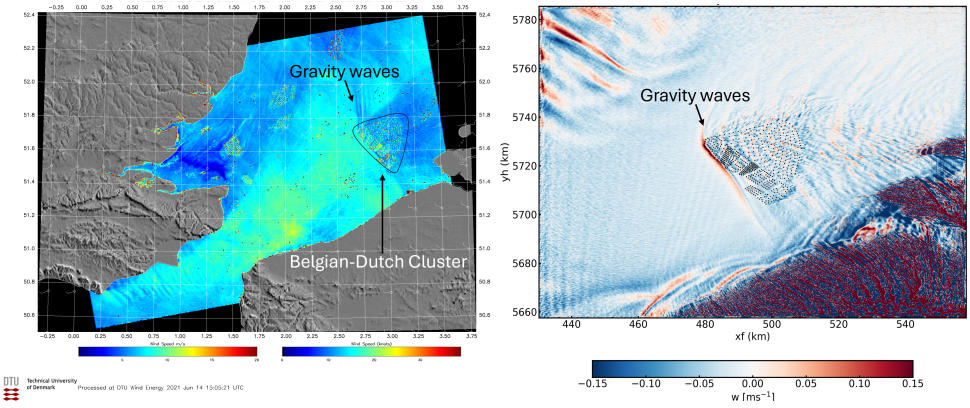

Figure 1.2: (Left) processed satellite scan of the North Sea showing wind-farm-induced atmospheric gravity waves as surface wind speed projected to the hub-height of the Belgian-Dutch cluster in the North Sea, and (right) vertical velocity contour showing the same from a meso-microscale LES simulation of flow around the cluster.Reanalyzed ERA5 weather data for 14th June 2021 was used as boundary conditions in Aspire, which is the LES model of Whiffle wind. The processed synthetic aperture radar image is provided by the Technical University of Denmark, Department of Wind Energy (DTU Wind Energy).

A clear understanding of the phenomena involved in wind-farm–atmosphere interactions is critical to wind farm performance. As discussed in more detail below, some

understanding and sufficient evidence, both experimental and modeled, of the cumulative blockage effect and wind-farm wakes are available in the literature. This is not the case for the existence and impact of an AGW. Only satellite scans, as shown in fig. 1.2 (left), and Large Eddy Simulations (LES) of wind farms, shown in fig. 1.2 (right), have shown indications of AGWs. The wind energy community has focused on the interaction of wind turbines and wind farms with the ABL. Therefore, inter- and intra-farm wakes, internal boundary layer growth, and the local blockage effect are better understood than AGWs. Porté-Agel *et al.* [8] summarizes numerous recent contributions made by experimental, computational, and theoretical research advancing the understanding of wind farm-ABL interactions. Likewise, Mehta *et al.* [9] reviewed wind farm aerodynamic studies based on LES, providing evidence of abundant studies related to the understanding of these phenomena. Since AGWs are new to the wind energy community, only a few recent numerical investigations have shown both positive and negative impacts of the AGWs on wind farm performance. AGWs are found to contribute to wind farm blockage and cause favorable pressure distributions through and downstream of the wind farm, both on spatial scales related to their large wavelengths [10–12]. The blockage caused by AGWs is termed the global blockage effect, in contrast to the local blockage effect confined to the induction zone and associated with the cumulative wind turbine blockage. Allaerts and Meyers [10], Stipa *et al.* [11], Lanzilao and Meyers [12] have focused on the impacts of AGWs on wind farms and highlight how modeling AGWs with LES is extremely challenging and relies on ad hoc processes. However, systematic modeling of wind-farm-induced AGWs and a clear understanding of this phenomenon and its characteristics are yet to be explored.

1.3. RESEARCH AIM

A wind-farm-induced AGW can affect wind farm performance by creating a streamwise pressure gradient that accelerates or decelerates the flow into and through the farm. This contributes to the phenomenon of 'wind farm blockage' and affects the way the consolidated wind farm wake recovers. Some researchers believe that AGWs are the main driver behind the wind farm blockage effect at the entrance of a wind farm [13–15]. On the other hand, Wu and Porté-Agel [16] suggest that the wind farm blockage effect is the combined effect of AGWs and cumulative turbine induction. The term 'regional efficiency' of wind farms was introduced by Allaerts and Meyers [17] to characterize the impact of atmospheric gravity waves on wind farm performance. They claim that regional efficiency is of the same order as wake-induced wind farm efficiency losses. Allaerts *et al.* [14] estimated a 4 to 6% decrease in the annual energy production of an offshore wind farm caused by the blockage effect created by AGWs. On the other hand, Lanzilao and Meyers [18] and Stipa *et al.* [19] argue that AGWs can also assist wind farm wake recovery because they can create a locally favorable pressure gradient at the downstream end and behind the wind farm. However, the extent of the favorable pressure gradient region and whether it always improves wind farm wake recovery is still unknown. One of the main reasons for this is that few, if any, experimental data are available to quantify AGW effects on wind farms. Not surprisingly, most investigations of wind-farm-induced AGWs have been numerical to date.

The simulation of wind-farm-induced atmospheric gravity waves in a finite domain

requires special treatment at all domain boundaries other than the ground to stop the gravity waves from spuriously reflecting off these boundaries that do not exist in reality. An AGW can propagate in all directions, so it can spuriously interact with artificial inflow, outflow, and top boundaries. Unfortunately, current approaches applied to the study of AGWs in wind farms to avoid wave reflection at artificial domain boundaries are ad-hoc and require extensive fine-tuning [18, 20]. Thus, setting up reflection-free simulations is currently tedious, computationally expensive, and time-consuming, and there is a lack of clear guidance. Damping layers, particularly Rayleigh and advection damping, are commonly used in wind farm LES, but a systematic approach to set up the simulations is still missing. Therefore, the overarching question of this thesis is:

How should wind-farm-induced atmospheric gravity waves be systematically investigated using Large Eddy Simulations in order to gain a clear understanding of regional-scale wind farm aerodynamics?

The main research question is split into four key questions. The first two questions, given below, focus on proposing and validating a computational setup of a wind farm LES that resolves AGWs.

- How can a wind farm LES be systematically set up using common damping techniques to eliminate the impact of spurious AGWs?
- How can the proposed systematic procedure to set up accurate simulations be validated for practical wind farm flow conditions?

This systematic approach can be used to investigate the wind-farm–atmosphere interactions by focusing on the AGWs and their significance in wind farm performance predictions. The literature focuses on the impacts of AGWs on wind farm performance, with limited insight into the AGW phenomenon itself [11, 12, 14]. For instance, the literature consistently shows that AGWs cause a feedback effect on the flow in the ABL. Stipa *et al.* [11], Lanzilao and Meyers [12], Smith [13], Stipa *et al.* [19], Allaerts and Meyers [21] argue that AGWs are responsible for the adverse pressure gradients upstream of the wind farm that create a blockage effect and favorable pressure gradients over and downstream of it. Smith [13] describes the capping inversion displacement caused by the deceleration of the flow within the wind farm as the trigger of the AGWs. Stipa *et al.* [11] describes how the capping inversion displacement couples AGW flow perturbations in the free atmosphere to perturbations within the ABL.

A good description of how AGWs then affect the capping inversion displacement, which triggers those waves in the first place, is lacking. Moreover, different types of wind-farm-induced AGW are mentioned in the literature without clearly distinguishing them. For example, the work of Khan *et al.* [1, 22] is related to “internal” AGWs, whereas Stipa *et al.* [11], Lanzilao and Meyers [12], Smith [13], Allaerts and Meyers [21] speak of “interfacial” AGWs as most critical for wind farm performance. “Trapped” AGWs in the capping inversion and even AGWs within the ABL are mentioned [10, 12, 22]. There is a need to describe the AGW phenomena clearly, distinguish all the kinds of AGWs, and

identify how each kind influences wind farm performance and simulation set-up. Thus, the third key question addressed in this thesis is the following:

- How can the proposed systematic approach be extended to investigate the characteristics and types of AGWs induced by an isolated wind farm to relate them to its performance?

The wakes and AGWs induced by a wind farm can affect neighboring wind farms and are becoming more relevant with the increasing trend of wind farm clustering. The inter-farm wakes effects under various ABL stability conditions and for different wind farm layouts have been the subject of recent investigation. For instance, Stieren and Stevens [23] simulated two neighboring wind farms of aligned and staggered layouts but without resolving the AGWs and found that the infer-farm wake can affect the power output of all turbines in the downstream wind farm. Likewise, Abraham *et al.* [24] analyzed the wake effects of three onshore wind farms using dual-doppler radar measurement data. The observed data show the wakes extending to about 30 km downstream of one of the wind farms for stable ABL conditions. Moreover, the spanwise momentum transfer is found to be a key mechanism in wind farm wake development and recovery. A recent review of widely used numerical frameworks for wind farm flow studies indicates thermal stability in ABL and the Coriolis force being critical for farm-to-farm interactions, and that gravity waves may induce secondary effects that are yet to be explored [25]. Given their large size, it is probable that the AGWs induced by a wind farm could affect other wind farms on a scale comparable to their wavelengths. Moreover, each wind farm in a cluster would trigger its own AGWs, as the flow conditions for the clustered wind farms might be similar. Thus, the AGWs induced by each wind farm can superimpose, and the resultant waves would be critical for the feedback effect, which would be different from that of the wind farms operating in isolation. Thus, an investigation of AGWs, their characteristics, and impacts on individual wind farms within a cluster is essential in understanding regional-scale wind farm flow dynamics. Therefore, the last key question to be answered in this thesis is

- How can the proposed systematic approach be extended to investigate the characteristics of AGWs induced by two neighboring wind farms to examine the impact of AGWs on their performance?

1.4. RESEARCH METHOD

At the moment, numerical modelling, particularly LES, is the most promising method to investigate AGWs. Given the increasing computing power and accessibility to high-performance computers, LES of wind farm flows is the norm in investigating wind farm aerodynamics. More importantly, the suitable spatial and temporal resolution and controllability of the simulation configuration make LES the ideal method to study AGWs and their impacts on wind farm performance. Field campaigns and engineering models based on analytical linear models can be other approaches to investigate AGWs, but the former seems unfeasible, and the latter is inaccurate in predicting wind farm performance. Measurement techniques are confined by the fact that AGWs are bigger than a wind farm in size, and a number of instruments would be required to measure them. Moreover, the instruments used in wind farm flow measurements are not yet capable

of detecting AGW effects in an isolated manner. However, scanning radars of horizontal spatial resolution similar to wind farm LES have detected gravity waves propagating into wind farm sites that are induced either by upstream terrain or by some kind of special atmospheric phenomena like bores [24]. On the other hand, engineering models based on linear wave theory are quick and reliable in investigating AGWs alone. However, the impacts of AGWs on wind farm performance are not or only crudely captured by engineering models. Thus, given the available resources, instruments, techniques, and models, LES seems to be the most viable approach to investigate AGWs and their impacts on wind-farm performance in a systematic and scientific manner.

wind-farm–atmosphere interactions are governed by numerous interdependent and constantly evolving flow parameters and wind farm characteristics, making systematic investigation inherently challenging. For offshore sites, the most critical atmospheric parameters include wind speed and direction, surface roughness, surface heat flux, inflow turbulence intensity, the temperature inversion strength, free atmospheric lapse rate, Coriolis force, and mesoscale pressure gradients. On the wind farm side, key factors influencing aerodynamic interactions include the layout, turbine spacing (which defines the farm's length and width), rotor tip height (i.e., hub height plus rotor radius), and turbine type. Numerical modeling introduces additional configuration parameters that, while not directly defining the flow, can significantly impact simulation accuracy if improperly set. Therefore, careful alignment between simulation setup, flow conditions, and wind farm specifications is essential. However, studying the interaction by varying one parameter at a time is both time-consuming and often limited to simplified, less realistic scenarios. A more systematic and streamlined approach is desirable for effectively exploring wind-farm–atmosphere interactions.

Table 1.1: The principal variables involved in simulating wind farms, including atmospheric gravity waves under conventionally neutral boundary layer conditions.

Variable	Variable Type	Definition
Geostrophic wind (U)	Flow	Uniform wind speed in the free atmosphere
Brunt-Väisälä frequency (N)	Flow	A measure of lapse rate in the free atmosphere
Capping inversion strength ($\Delta\theta$)	Flow	Temperature jump across the capping inversion
ABL height (H_i)	Flow	Depth of the turbulent ABL
Effective length (L)	Wind Farm	Wind farm length or Half-length of hill
Effective height (H)	Wind Farm	Rotor tip or maximum Hill height
Domain length (X)	Simulation	Length of the simulation domain
Domain height (L_z)	Simulation	Height of the simulation domain
Damping thickness (L_d)	Simulation	Depth of the Rayleigh damping layer
Buffer length (L_a)	Simulation	Buffer length of the advection damping layer
Damping coefficient ($1/\tau$)	Simulation	Strength of the Rayleigh damping layer

One way to devise a systematic approach to investigate the wind-farm–atmosphere interaction by flow modeling is to determine non-dimensional parameters critical to this interaction. To this end, we identify the most important flow, wind farm, and simulation

parameters in LES of wind farms, including AGWs, and apply dimensional reasoning in defining a few non-dimensional parameters. It is important to note that we focus on conventionally neutral boundary layers (CNBL) that occur reasonably frequently at offshore sites [26]. A CNBL is characterized by a potential temperature profile, where a neutral ABL is capped by a capping inversion of strong temperature stratification and a free atmosphere of weaker stratification aloft. The definitions of the variables and non-dimensional numbers determined as key to model wind-farm-induced AGWs are given in Tab. 1.1 and Tab. 1.2, respectively. Note that in this study only capping inversion strength ($\Delta\theta$) is considered important, which is used to compute reduced gravity (i.e. $g\prime = \sqrt{g\Delta\theta/\theta_0}$). The first four non-dimensional parameters, the Froude numbers for the free atmosphere and capping inversion (Fr and Fr_i), and the vertical aspect ratios of the ABL and the wind farm ($\tilde{H}_i$ and $\tilde{S}_h$) are distinguished as physical parameters, as they determine the relevant physics. The remaining five, $\tilde{X}$, $\tilde{L}_z$, $\tilde{L}_d$, $\tilde{L}_a$, ξ, are simulation parameters that link the AGW characteristics to the domain size and damping characteristics in systematically modeling wind farms, including AGWs. In other words, the simulation parameters can affect the solution, but do not determine the flow conditions and AGW characteristics. Thus, taking this non-dimensional approach reduces the complexity of a large dimensional parameter space by relating wind farm features, AGW characteristics, and critical simulation parameters.

Table 1.2: Non-dimensional parameters critical in LES of wind farms for CNBL conditions.

NDPs	Definition	Description
Fr	U/NL	Ratio of wind speed to wave speed in the free atmosphere
Fr_i	$U/\sqrt{g'H_i}$	Ratio of wind speed to wave speed atop the capping inversion
$\tilde{H}_i$	H_i/L	ABL-aspect ratio w.r.t. effective length
S_h	H/L	Wind farm-aspect ratio w.r.t. effective length
$\tilde{X}$	X/λ_{hor}	Ratio of domain length to effective horizontal wavelength
$\tilde{L}_z$	L_z/λ_{ver}	Ratio of domain height to effective vertical wavelength
$\tilde{L}_d$	L_d/λ_{ver}	Ratio of damping layer thickness to effective vertical wavelength
$\tilde{L}_a$	$L_a/\lambda_{hor-tgw}$	Ratio of Buffer length to horizontal wavelength of tapped waves
ξ	$1/(\tau N)$	Damping layer coefficient normalized with Brunt-Väisälä frequency

In conducting this research, we use the above-introduced non-dimensional parameters to first propose a systematic approach to model the wind farms, including AGWs. The proposed modeling approach links the flow, wind farm, and simulation parameters to characteristics of AGWs, particularly wavelengths. Thus, most of the phenomena critical to wind farm flow modeling are captured as the typical spatial and temporal resolution of wind farm LES captures turbulence, and the much larger wavelengths and longer time periods of AGWs encapsulate any phenomena in the range of resolved turbulence and gravity waves. In linking the simulation parameters with flow and wind farm parameters, the analytical solution of a flow over a bell-shaped two-dimensional hill is also utilized. This helped in validating our initial simulations and estimating AGW wavelengths apriori, ensuring correct sizing of simulation domains. After validating the approach, it is applied to investigate the AGW characteristics and wind farm performance in both isolated and clustered configurations. The investigation is limited to convention-

ally neutral boundary conditions; extending this approach to stable and unstable ABLs is future work. We also note that this study uses standard turbine, wall stress, and subgrid scale models in LES of wind farms. Therefore, the parameters related to these aspects are taken from the literature, assuming they are well-established from previous wind farm LES studies. Moreover, including non-dimensional parameters for thermal stability in ABL and turbulence is highly recommended as an extension to this approach.

1.5. THESIS OUTLINE

This dissertation is presented in four parts that are briefly described below. A schematic layout of the thesis is shown in Fig. 1.3.

PART I: PROLOGUE

The dissertation starts with a top-level introduction of the research and a comprehensive background supporting the overall study. This part is written with a beginner to wind farm aerodynamics in mind.

- **Chapter 1** motivates the relevance of this study to society at large and the wind energy research community in particular. The chapter establishes why this study is needed, but also explains the research objective and the overarching method applicable to the whole dissertation.
- **Chapter 2** gives an overall background to the study by explaining important concepts and principles relevant to wind-farm–atmosphere interactions. Moreover, it gives an overview of wind farm aerodynamics and the computational ingredients needed for LES.

PART II: Establishing and Validating a Systematic Approach to Simulate AGWs

In the second part of the dissertation, a systematic approach to simulate AGWs is established and validated. This part is more relevant for researchers using high-fidelity CFD for wind farm aerodynamics.

- **Chapter 3** investigates the relationship of flow parameters with simulation parameters in proposing a systematic approach to simulate AGWs in linearly stratified conditions only.
- **Chapter 4** extends the systematic approach to modeling of wind farms for conventionally neutral boundary layer conditions. This chapter also includes the validation of the systematic approach and the Boussinesq approximation commonly used in wind farm LES.

PART III: Stratification effects—AGW Impacts—on Wind Farm Performance

The third part of the dissertation presents the application of the systematic approach to investigate AGW characteristics and wind farm performance in both isolated and clustered configurations while fully resolving AGWs. This part is relevant for the entire wind energy community.

- **Chapter 5** investigates the dependency of AGW characteristics and wind farm performance on key physical non-dimensional numbers for an isolated wind farm.

- **Chapter 6** extends the approach from Chapter 5 to clustered wind farms by applying it to flow through two aligned wind farms.

PART IV: EPILOGUE

The last part of the dissertation summarizes the main findings of the research and proposes future studies.

- **Chapter 7** concludes the thesis by providing recommendations on how to systematically investigate wind-farm–atmosphere interactions with LES. Ideas on extending this research are also proposed.

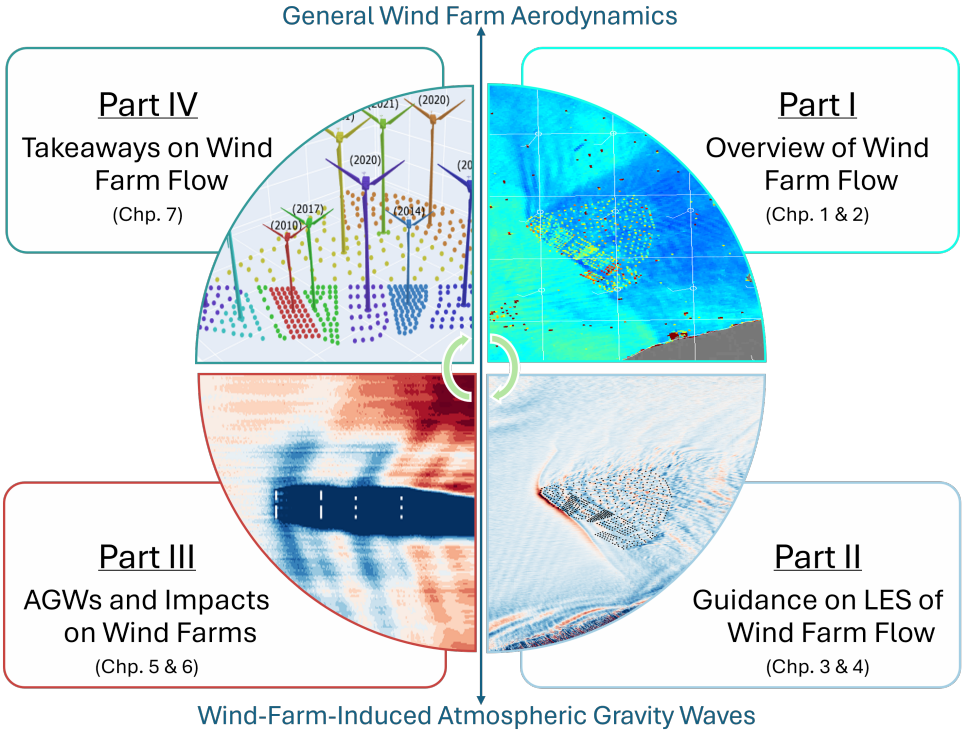

Figure 1.3: An illustration of the thesis outline, which is split into four parts. The vertical arrow distinguishes the parts related to general wind farm aerodynamics from those more focused on gravity waves. The curved arrows guide a reader of the proposed sequence of following this dissertation.

REFERENCES

[1] M. A. Khan, D. Allaerts, S. J. Watson, and M. J. Churchfield, *Investigating the relationship between simulation parameters and flow variables in simulating atmospheric gravity waves for wind energy applications,* Wind Energy Science **10**, 1167 (2025).

[2] G. (2024), *Global wind report*, Tech. Rep. (GWEC, 2024).

[3] I. (2024), *Integrating Solar and Wind*, Tech. Rep. (IEA, Paris, 2024).

[4] G. (2016), *Global Wind Report: Annual Market Update 2015*, Tech. Rep. (GWEC, 2016).

[5] G. (2025), *Global wind report*, Tech. Rep. (GWEC, 2025).

[6] S. E. Haupt, B. E. Kosovie, J. A. Lee, and P. A. Jiménez, *Mesoscale modeling of the atmosphere,* in *Wind Energy Modeling and Simulation - Volume 1: Atmosphere and Plant*, Chap. Chapter 3, pp. 65–115, https://digital-library.theiet.org/doi/pdf/10.1049/PBPO125F$_c$h3 .

[7] R. J. Stevens and C. Meneveau, *Flow structure and turbulence in wind farms,* Annual Review of Fluid Mechanics **49**, 311 (2017).

[8] F. Porté-Agel, M. Bastankhah, and S. Shamsoddin, *Wind-turbine and wind-farm flows: A review,* Boundary-Layer Meteorology **174**, 1 (2020).

[9] D. Mehta, A. H. van Zuijlen, B. Koren, J. G. Holierhoek, and H. Bijl, *Large eddy simulation of wind farm aerodynamics: A review,* Journal of Wind Engineering and Industrial Aerodynamics **133**, 1 (2014).

[10] D. Allaerts and J. Meyers, *Boundary-layer development and gravity waves in conventionally neutral wind farms,* Journal of Fluid Mechanics **814**, 95 (2017).

[11] S. Stipa, M. Ahmed Khan, D. Allaerts, and J. Brinkerhoff, *A large-eddy simulation (LES) model for wind-farm-induced atmospheric gravity wave effects inside conventionally neutral boundary layers,* Wind Energy Science **9**, 1647 (2024).

[12] L. Lanzilao and J. Meyers, *A parametric large-eddy simulation study of wind-farm blockage and gravity waves in conventionally neutral boundary layers,* Journal of Fluid Mechanics **979**, A54 (2024).

[13] R. B. Smith, *Gravity wave effects on wind farm efficiency,* Wind Energy **13**, 449 (2010).

[14] D. Allaerts, S. V. Broucke, N. Van Lipzig, and J. Meyers, *Annual impact of wind-farm gravity waves on the Belgian-Dutch offshore wind-farm cluster,* Journal of Physics: Conference Series **1037** (2018), 10.1088/1742-6596/1037/7/072006.

[15] L. Lanzilao and J. Meyers, *Set-point optimization in wind farms to mitigate effects of flow blockage induced by atmospheric gravity waves,* Wind Energy Science **6**, 247 (2021).

[16] K. L. Wu and F. Porté-Agel, *Flow adjustment inside and around large finite-size wind farms,* Energies **10**, 4 (2017).

[17] D. Allaerts and J. Meyers, *Gravity waves and wind-farm efficiency in neutral and stable conditions,* Boundary-Layer Meteorology **166**, 269 (2018).

[18] L. Lanzilao and J. Meyers, *An improved fringe-region technique for the representation of gravity waves in large-eddy simulation with application to wind farms,* Boundary-Layer Meteorology **186**, 567 (2023).

[19] S. Stipa, A. Ajay, D. Allaerts, and J. Brinkerhoff, *TOSCA – an open-source, finite-volume, large-eddy simulation (LES) environment for wind farm flows,* Wind Energy Science **9**, 297 (2024).

[20] D. Allaerts, *Large-eddy Simulation of Wind Farms in Conventionally Neutral and Stable Atmospheric Boundary Layers*, Ph.D. thesis (2016).

[21] D. Allaerts and J. Meyers, *Large eddy simulation of a large wind-turbine array in a conventionally neutral atmospheric boundary layer,* Physics of Fluids **27**, 065108 (2015).

[22] M. A. Khan, S. J. Watson, D. J. N. Allaerts, and M. Churchfield, *Recommendations on setup in simulating atmospheric gravity waves under conventionally neutral boundary layer conditions,* Journal of Physics: Conference Series **2767**, 092042 (2024).

[23] A. Stieren and R. J. A. M. Stevens, *Impact of wind farm wakes on flow structures in and around downstream wind farms,* Flow **2**, E21 (2022).

[24] A. Abraham, N. Hamilton, N. Bodini, B. Hirth, J. Schroeder, S. Letizia, R. Krishnamurthy, R. Newsom, and P. Moriarty, *Land-based wind plant wake characterization using dual-doppler radar measurements at AWAKEN,* Journal of Physics: Conference Series **2767**, 092037 (2024).

[25] P. Ouro, M. Ghobrial, K. Ali, and T. Stallard, *Numerical modelling of offshore wind-farm cluster wakes,* Renewable and Sustainable Energy Reviews **215**, 115526 (2025).

[26] G. P. N. Diaz, M. L. Mayol, M. Rowen, B. Schliffke, S. Freitas, and S. Erbsloeh, *Impact of coastal gradients on wind farm energy yield assessment: model comparison,* Journal of Physics: Conference Series **3016**, 012039 (2025), article number: 012039.

Photo by Simon J. Watson,
Rotterdam, Netherlands

2

WIND-FARM–ATMOSPHERE INTERACTIONS

This chapter introduces critical aspects of wind-farm–atmosphere interactions. An overview of atmospheric flow features, particularly the thermal state, is given. The atmosphere's thermal state is related to wind-farm-induced atmospheric gravity waves. Moreover, we give an overview of wind farm aerodynamics by suggesting a couple of changes to its existing understanding, particularly for a finite wind farm operating in shallow boundary layers. Finally, we introduce the main components of an LES framework for investigating wind-farm flows with atmospheric gravity waves present.

Parts of this chapter are under review for a publication in Wind Energy Science, **Dependence of Wind Farm-Induced Gravity Waves and Wind-Farm Performance on Non-Dimensional Atmospheric Parameters and Simulation Configuration**, M. A. Khan, M. J. Churchfield, and S. J. Watson (2025) [1].

2.1. ATMOSPHERIC FLOW FEATURES

The Earth's atmosphere consists of interwoven phenomena spanning scales from planetary circulation down to microscopic turbulence, yet its behavior can be described by focusing on a few key features. Uneven solar heating creates temperature and pressure gradients, caused by differences in surface properties and atmospheric composition, that drive air from high-pressure to low-pressure regions as wind. Meanwhile, Earth's rotation deflects these wind flows: to the right in the Northern Hemisphere and to the left in the Southern Hemisphere—a phenomenon known as the Coriolis effect, which can shape the wind even locally. Thus, the atmosphere around a wind farm can be described in terms of wind and the effect of a wind farm site's thermal state and the Coriolis effect on wind. While wind, the Coriolis effect, and the thermal state of the atmosphere are all important for wind farm dynamics, this study focuses primarily on the thermal state due to its direct link to atmospheric gravity waves. A brief overview of wind and the Coriolis effect is provided below, followed by an overview of the atmospheric thermal structure in the context of wind-farm atmosphere interaction, particularly relating it to atmospheric gravity waves.

2.1.1. THE WIND

Wind, the natural movement of air near the Earth's surface, is categorized into mean wind, turbulence, and waves by Stull [2]. For a site like a wind farm, the mean wind is typically driven by a horizontal pressure gradient over a region much larger than the site. As a result, the mean wind flow dominates horizontal momentum and energy transport, which are linked to wind farm performance. A sheared mean wind profile is created due to the roughness of the Earth's surface, as it slows down the wind. The Earth's surface is also primarily responsible for generating turbulence, which is normally defined as the fluctuating component of the wind over a relatively short time period, typically seconds or minutes. The orography of a site and any positive surface heat flux induce random nonlinear perturbations to the surface mean wind, which spread in the vertical until an equilibrium with the laminar mean wind forced by the pressure gradient is reached. Thus, turbulence gives a basis to split the troposphere into two layers: the lowermost turbulent part directly affected by the surface roughness and heating is the atmospheric boundary layer. The laminar layer unaffected by surface forcing is the free atmosphere, where only the mean wind and waves can occur. Waves can be seen as periodic fluctuations over time periods longer than turbulence that are superimposed on the mean wind. Such waves can exist both in the ABL and the free atmosphere, but unlike mean wind and turbulence, they are not always present, as they are generally generated by flow over pronounced obstacles or by significant variations in the mean wind profile. While turbulence is responsible for wind farm wake recovery and internal boundary layer growth over a wind farm, waves have a secondary but significant impact on its performance.

2.1.2. THE CORIOLIS EFFECT

The Coriolis effect arises because Earth rotates, creating an apparent lateral force—the Coriolis force—on wind. This force acts perpendicular to the wind direction and the Earth's rotation axis.Its magnitude depends on wind speed and latitude, and it causes wind veer, which describes how wind direction changes with height through the atmo-

spheric boundary layer. Aloft, the mean wind (geostrophic wind) results from a balance between the horizontal pressure-gradient force and the Coriolis force, flowing parallel to isobars (i.e. lines of constant atmospheric pressure). Closer to the surface, friction reduces wind speed and introduces a cross-gradient component toward lower pressure, causing the wind to gradually veer. Wind veer significantly influences wind farm performance, underscoring the critical role of the Coriolis force. Additionally, large wind farms alter the effective surface roughness, which, together with pressure gradient, turbulence-induced drag, and the Coriolis effect, change the force balance locally. As a result, the interplay between these forces varies within and around the farm, which may cause both incoming and downstream wind to deflect. Consequently, the Coriolis effect becomes even more important for large and clustered wind farms.

2.1.3. THE THERMAL STATE

Although the thermal state of the atmosphere depends on solar irradiance, it is greatly affected by surface properties and atmospheric composition. The surface properties dominate the thermal forcing on the wind in the ABL, as little solar radiation is absorbed by the air in this layer. This thermal forcing is inherently unsteady and nonuniform as the surface composition is inconsistent and irregular. The impact of unsteady and nonuniform surface-thermal forcing reduces with height and does not affect the thermal conditions in the free atmosphere. Therefore, the thermal state of the atmosphere beyond the ABL top is steadier and more uniform than in the ABL and depends mainly on the amount of irradiance absorbed by the constituents of these upper layers and meso- to synoptic-scale phenomena such as weather patterns.

The thermal state of the atmosphere is often characterized by its potential temperature structure. Potential temperature is a theoretical quantity that excludes the compression and expansion effects of an air parcel as it moves up and down. It is a common variable used in meteorology that is defined as the temperature of an air parcel adiabatically brought to a reference pressure typically 1000 hPa. Thus, it excludes the impact of changes in pressure with altitude for vertical motions of dry air. The virtual potential temperature can be considered in case moisture is important for an atmospheric process like cloud formation. These features make potential temperature an ideal quantity to describe the thermal state of the atmosphere in terms of stability classes. The expression for potential temperature of dry air is,

$$\theta = T\left(\frac{P_0}{P}\right)^{\frac{R}{cp}} \tag{2.1}$$

Where T represents the actual temperature of an air parcel, while P denotes the ambient pressure at the parcel's current altitude. The constant P_0 is a reference pressure—commonly 1000 hPa (or 1×10^5 Pa)—used to standardize different conditions. The exponent κ is defined as R/c_p, where R is the specific gas constant for dry air (approximately 287 $\mathrm{Jkg^{-1}\ K^{-1}}$) and c_p is the specific heat capacity at constant pressure (around 1004 $\mathrm{Jkg^{-1}\ K^{-1}}$). This exponent accounts for adiabatic compression or expansion and yields a temperature value (θ) that remains constant for dry, reversible movements of the parcel, hence commonly used in studies of atmospheric stability and stratification.

Potential temperature can describe the thermal structure —different layers and at-

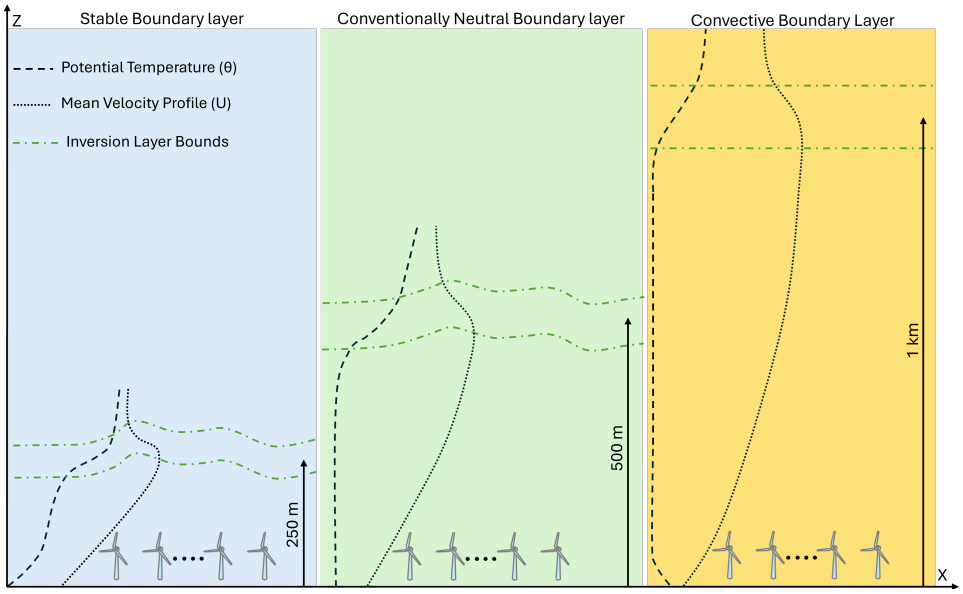

Figure 2.1: Examples of potential temperature and mean velocity profiles for stable, conventionally neutral, and convective boundary layers. The region between the horizontal dashed-green lines is the capping inversion.

mospheric stability in each layer—of the troposphere. The sign of the potential temperature gradient determines the stability of a layer, and its magnitude gives the strength of the stability state. A positive gradient indicates a stable layer, whereas a negative gradient shows an unstable one; neutral layers have zero gradients. Neutral layers do not thermally induce vertical perturbations to the wind flow, whereas an unstable layer would augment, while a stable layer would tend to diminish them. Generally, the free atmosphere is weakly stable, and the state inside the ABL is dependent on the thermal forcing at the surface, mainly the heat flux from the surface. Surface heat flux is primarily responsible for the thermal state of the ABL. Negative, zero, and positive heat flux cause stable, neutral, and unstable potential temperature profiles in the ABL, respectively. The stable free atmosphere requires a thermal balance with that of the ABL underneath. This thermal balance often creates a thin layer—the capping inversion—with a steep temperature jump across it. The capping inversion is also stable but much stronger than the free atmosphere aloft, acting as a '*movable lid*' to the ABL. While it stops turbulence from penetrating the free atmosphere, it can couple the fluctuations (i.e. waves) in the free atmosphere with the flow in the ABL. Altogether, the troposphere can be characterized by three layers based on the potential temperature profile. Unlike the normally stable capping inversion layer and the free atmosphere, the ABL's stability can vary between stable, neutral, and unstable (often called convective) over a day depending on the prevailing weather conditions. Fig. 2.1 shows potential temperature profiles of these stability states along with mean velocity profiles.

The thermal state of the atmospheric boundary layer is important for wind farm per-

formance as it directly influences turbulence, which is linked to wake recovery and associated power losses. Turbulence is enhanced by vertical convective currents when the surface has a positive heat flux. The rising currents can extend the ABL to a couple of kilometers, and such a thermal state is called a convective boundary layer (CBL). The convective currents assist the wake mixing, and the wake recovery is enhanced, which reduces power losses. On the contrary, a stable ABL (SBL) destroys turbulence as it tends to reduce any perturbations, which leads to slower wake recovery, thus longer wakes. In a conventionally,neutral boundary layer (CNBL), wakes are longer than in a CBL but shorter than in an SBL.

Besides impacting turbulence and, in turn, wake recovery, the thermal state of the atmosphere can affect the internal boundary layer development over the wind farm. Internal boundary layer is the region over the wind farm where wind-farm-induced turbulence is more dominant than the inflow turbulence. When the capping inversion is high, like in a CBL, the flow affected by wind farm roughness has sufficient space in the ABL to expand and reach an equilibrium with the inflow wind. However, for low inversion heights, expected for CNBLs and certainly SBLs, the vertical expansion of the IBL is confined if it reaches the capping inversion before achieving an equilibrium with the inflow wind. This would result in the capping inversion displacing in response to the IBL's tendency to expand vertically, as shown in Fig. 2.3. For very low capping inversion heights, an IBL may not even initiate as the perturbations from the turbines would reach the capping inversion before the inflow wind would balance the perturbations. IBL growth entails the vertical entrainment of energy from aloft into the wind farm, which is the most important source of wake mixing. Therefore, partially expanded IBLs determined by the thermal structure of the atmosphere (i.e. ABL depth) affect wind farm performance.

Another way the thermal state of the atmosphere can impact a wind farm is by supporting buoyancy-driven waves in the layers aloft the ABL. These buoyancy-driven waves—atmospheric gravity waves—are induced by a wind farm when the capping inversion is low (i.e. ABL shallower than a kilometer). Therefore, besides the stable nature of the capping inversion and the free atmosphere, the capping inversion height is important. The expanding IBL may not perturb the capping inversion in CBLs, as they are a few kilometers deep and dominated by convective currents. However, for CNBLs and SBLs, the capping inversion is low enough for the IBL or the upward-deflected flow by the wind farm to perturb it. Once perturbed, the buoyancy of the capping inversion restores it. Since the perturbations are periodic, waves will form above the wind farm. Some of these oscillations are supported by the buoyancy in the free atmosphere, allowing them to propagate through it. Because the capping inversion is wavy, continuity enforces converging and diverging zones beneath it in the ABL that influence the mean wind at those locations. These variations in mean wind affect the power output of wind turbines in the vicinity.

In this thesis, we confine ourselves to the study of wind-farm-induced atmospheric gravity waves in CNBLs. SBLs definitely support AGWs, but investigating SBLs with flow modeling is much harder. CBLs are unlikely to support AGWs, at least not those that would affect wind farms. Since AGW behavior will be similar in SBLs and CNBLs, we opt to study only the latter as they are simpler to simulate, and our aim is to understand AGWs in the context of wind-farm–atmosphere interaction. Wind farm wakes,

both intra- and inter-farm, and IBL growth are well-studied in the wind farm flow-related literature, which will be briefly revised in Section 2.2.

2.1.4. ATMOSPHERIC GRAVITY WAVES

Various kinds of AGWs are described in the literature, and it is sometimes challenging to synthesize all the information. Let us give some examples: "interfacial" and "internal" AGWs are described as occurring within the capping inversion and in the free atmosphere, respectively [3–6]. Allaerts and Meyers [5] and Lanzilao and Meyers [6] describe interfacial waves as two-dimensional waves somehow bound to the top of the capping inversion. They also discuss waves similar to interfacial waves inside the neutral boundary layer, reaching all the way down to the hub height. Khan *et al.* [7] identify "trapped" waves confined within the capping inversion, and Ollier and Watson [8] describes topographically-induced "trapped lee" waves affecting wind farms. Lee waves may also be induced by wind farms, which can affect the flow in a way similar to shallow topography. Because the literature is vast and spread out, we attempt to briefly weave the different kinds of AGWs and their effects into an essential story, giving the reader enough background to understand the results and discussion presented in this thesis.

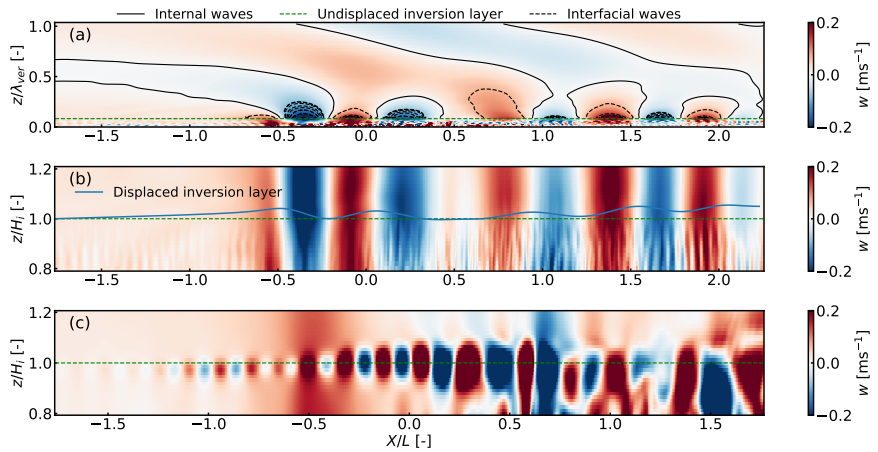

Figure 2.2: Contours of vertical velocity, w, on a vertical streamwise slice through the middle of the wind farm for Froude number of 0.15, inversion Froude number of 0.75, and wind farm shape factor of 0.025: (a) temporally averaged field showing the internal and interfacial waves; (b) temporally averaged field showing the capping inversion displacement, interfacial waves, and their signature in the ABL; and (c) instantaneous field from a non-precursor driven simulation that shows the trapped waves in the capping inversion triggered when the wind-farm-induced turbulence hits the capping inversion. The capping inversion mid-point height is at $z = 500$ m, and the wind farm start and end are at $x/L = -0.5$ and $+0.5$, respectively, where L is wind farm length.

The causes of wind-farm-induced atmospheric gravity waves involve mass conservation, buoyancy, and wave theory. A wind farm is a sink of horizontal momentum and appears similar to a porous blockage, causing the flow to decelerate through the farm. It then begins to accelerate behind the farm as the wind farm wake recovers. As a result of flow continuity, the flow in the ABL is deflected upward at the start of the wind farm and

downward at the end of it in response to the horizontal deceleration and acceleration [5]. The capping inversion, as its name implies, is the "cap" on top of the ABL. It is a relatively thin layer of air that is strongly stable in thermal stratification, so it acts as a flexible cap or lid atop the boundary layer. Vertical motions of turbulence within the boundary layer generally do not penetrate this layer—it strongly suppresses them with buoyancy forces. Therefore, it displaces upward over the wind farm and downwards at the end of it due to the flow deflected by the wind farm in that manner. To the flow aloft in the free atmosphere, this deflected capping inversion appears similar to a gentle hill above the wind farm. As does the vertical flow caused by real hills, the vertical flow over the displaced capping inversion activates buoyancy forces that tend to restore air displacements in the free atmosphere and the capping inversion itself, resulting in AGWs.

AGWs can be classified into a few different types based on their characteristics and whether they occur in the capping inversion, in the free atmosphere, or at the interface of the two. AGWs are composed of an entire spectrum of wavelengths; however, there is an apparent wavelength dictated by local thermal stratification strength and horizontal wind speed. AGWs propagating in the free atmosphere are referred to as "internal" gravity waves, which are steady if the conditions are steady, as shown in Fig. 2.2(a). Internal waves have a tendency to curve—like an arc of a circle—downstream of the obstacle causing them, and may mildly perturb the capping inversion, but only downstream of the obstacle. AGWs that may occur in the capping inversion, if its depth is great enough, are referred to as "trapped" waves because they are confined within that layer. The unsteady turbulence that is constantly pushing on the capping inversion from below contributes to the unsteadiness of these trapped waves. An example of trapped waves can be seen in the instantaneous vertical velocity field in Fig. 2.2(c). Because the free atmosphere and capping inversion have different stratification strengths and wind speeds, they support different apparent wavelengths of AGWs. As shown in Fig. 2.2(b), at the interface between the free atmosphere and the capping inversion, we see "interfacial" waves that smoothly blend the internal and trapped gravity waves, and they have their own apparent wavelength. The wavelengths of trapped waves not supported in the free atmosphere are called evanescent waves, and they decay with height. They are contained and advected along the interface [9]. For subcritical conditions—wave speed faster than background wind speed—a large part of the wave spectrum becomes evanescent and travels faster than the background wind speed along the interface, especially downstream. These evanescent waves downstream of the obstacle are the "trapped lee waves", which can relatively strongly perturb the capping inversion.

Although we summarize AGW formation as a succession of events, we stress that it is really a tightly coupled integrated set of phenomena that happen almost in lockstep. If one parameter in the system changes, the entire ABL-AGW system quickly responds, settling toward a new equilibrium.

2.2. WIND FARM AERODYNAMICS

Flow through a wind farm can be classified into a few regions depending on wind farm size and the thermal state of the atmosphere. The description of the wind farm flow discussed here is taken from the review of this subject by Porté-Agel *et al.* [10], and additional insight is provided based on our current study. Three regions, the induction,

developing, and wind farm wake region, always exist for a wind farm at a site with a homogeneous surface, e.g., offshore sites. The induction region is upstream of the first wind turbine row, where the cumulative blockage effect of the wind farm decelerates the free-stream velocity. This zone would also include the contribution of gravity waves to the wind farm blockage effect when CNBL or SBL conditions are considered. In the developing region, flow is dominated by individual turbine wakes as they still mix with the background flow and other wakes. The IBL above the rotor layer is still affected by the wind farm and becomes increasingly homogeneous. For large enough wind farms, the IBL expands vertically and reaches an equilibrium with the geostrophic wind just like the atmospheric turbulence does in the ABL. At this point, the ABL depth and IBL height above the surface are the same. The wind farm wake region is influenced by a sudden drop in the drag force downstream of the wind farm, which enhances flow entrainment at the wind farm exit. However, it is important to note that the existence of a wind farm wake region depends on wind farm layout and size. For instance, in a small wind farm or one with a coarse layout, the heterogeneous flow in the evolving region might prevail downstream, as the individual wakes may not merge into a homogeneous wind-farm wake.

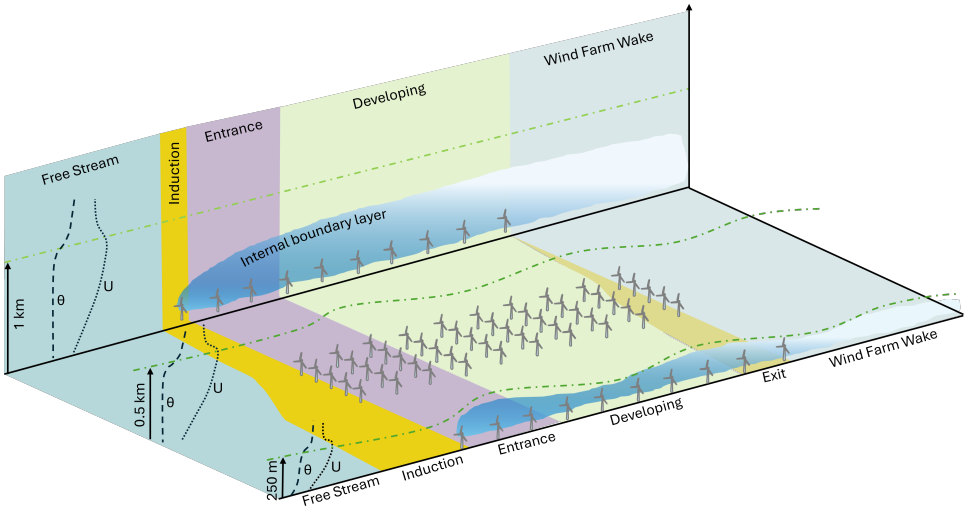

Figure 2.3: Schematic of flow-zones in a large wind-farm in shallow to deep boundary layers.

Large wind farms may have two further regions: the fully developed and exit regions. In the former, the individual turbine wakes merge into horizontally homogeneous flow at a certain location along the wind farm length. Beyond this point, the inflow conditions do not affect the downstream wind turbines. Moreover, flow entrainment from the layer above the rotors is the only source of kinetic energy to balance the energy extraction by the turbines. A wind farm with fully developed flow is often called an infinite wind farm; thus, others can be termed finite wind farms. The exit region is also related to infinite wind farms and strong free-atmospheric stability. According to Porté-Agel *et al.* [10], a standing atmospheric gravity wave is triggered at the wind farm exit, which prop-

agates upstream for subcritical conditions. (i.e. strong free-atmospheric stratification). The flow then accelerates in the exit zone of the wind farm, resulting in increased power output of turbines in that zone relative to those immediately upstream.

Based on our investigations, we suggest a modified description of the wind farm flow, which is mainly based on the boundary layer height. A schematic of flow zones through a finite wind farm for deep to shallow boundary layers is shown in Fig. 2.3. In a deep boundary layer (i.e. CBL), the description of Porté-Agel *et al.* [10]'s wind farm flow for an infinite wind farm holds, as the capping inversion is barely perturbed from below. However, in shallow boundary layers (i.e. SBLs and CNBLs), the capping inversion plays a vital role in the wind farm flow in the exit and wind-farm wake zones. As shown in Fig. 2.3(bottom), the capping inversion is perturbed by the flow deflected upwards at the start of the wind farm and entrained at the end of the wind farm. Thus, the flow in the ABL may have several converging and diverging zones, even downstream of the wind farm, owing to the capping inversion's deformed shape. For instance, the induction zone is extended further upstream as the air columns in the region are expanded, slowing down the inflow more than in a deep boundary layer. Likewise, the air columns in the exit zone are compressed, causing an acceleration, which is not necessarily linked to infinite wind farms and strong free-atmospheric stratification, but instead to shallow boundary layers. Moreover, a well-defined internal boundary layer might not form for very shallow boundary layers (i.e. $H_i < 500\ m$). These aspects will be discussed in Chapter 5 with a more in-depth analysis of flow through a finite wind farm in CNBLs.

2.3. METHODS OF CHOICE TO STUDY WIND FARM FLOWS

In the past, wind farm flow has been investigated using three different approaches: through experimental campaigns at scale and in the field, computational fluid dynamics (CFD) modeling, and analytical modeling or non-CFD modeling. It is important to note that existing wind farms might all be considered finite because they are smaller than the lengths required for the flow to develop fully. The wind farm length has to be a couple of orders of magnitude larger than the ABL depth for the flow to develop fully[11]. However, some studies have shown that fully-developed flows might appear at shorter lengths but for a certain wind farm layout and wind direction [12–15]. Hypothetical infinite wind farms are well studied with CFD and non-CFD modeling. For example, Calaf *et al.* [16] and Abkar and Porté-Agel [17] extended Frandsen [18]'s 1D analytical model by including wake eddy-viscosity and free-atmospheric stability, respectively. These models predict the effective surface roughness of an infinite wind farm and the vertical mean wind profiles. Whereas Calaf *et al.* [16, 19], Abkar and Porté-Agel [17], and Yang *et al.* [20] are examples of the LES investigation of infinite wind farm flows. As wind farms become larger and are clustered, fully developed flow will become more relevant. But the existing understanding of wind farm flows supported by all three approaches mentioned above is more representative of finite wind farms. A brief overview of studies using these methods to investigate different features of wind farm flows is given below.

Field campaigns are desirable but rather limited, as measurement tools and methods are either inadequate or expensive, such as a scanning radar. Moreover, the large size of a wind farm and varying atmospheric conditions make it difficult to design and control the measurements of various features (i.e. blockage effect, wakes, gravity waves, and IBL

height) in an isolated manner and simultaneously. Nonetheless, a few field campaigns have studied wind farm wakes and the blockage effect. For instance, Barthelmie *et al.* [12] and Gaumond *et al.* [21] analyzed measurements in the Horns Rev wind farm, focusing on the impact of wind direction change on power output and found that wind directions leading to increased turbine distancing improved intra-farm wake recovery and, in turn, power output of the wind farm. Bleeg *et al.* [22] investigated wind farm blockage based on met mast measurements of wind speed and direction upstream of three wind farms before and after their dates of commissioning. These measurements confirmed significant slowdowns in the freestream wind on the wind farm scale, which was attributed to the global blockage effect. A more recent field campaign dedicated to measuring global blockage (i.e. wind-farm-scale blockage) concluded that it exists, and boundary layer height is closely linked to this phenomenon [23]. The American WAKE experimeNt (AWAKEN) is another notable onshore field campaign that has been advancing the understanding of wind turbine and farm interactions with the atmosphere. The analysis of raw data measured with several kinds of state-of-the-art instruments, such as scanning radars and LiDARs, has given more insight into the intra- and inter-farm wake effects [24]. In addition, the impact of unique atmospheric events such as natural atmospheric gravity waves and low-level jets on wind farms at the AWAKEN site has been investigated [25].

Wind tunnel measurements and satellite scans of wind farm sites have been used to investigate wind farm flows. Notable wind tunnel wake measurements of turbine arrays include [13, 15, 26]. Satellite scans have confirmed wind farm wakes [27] and wind-farm-induced atmospheric gravity waves as shown in chapter 1. Measurements are often complemented by Supervisory Control and Data Acquisition (SCADA) data collected by individual operating wind turbines. Together with SCADA data, the measurements are useful in understanding wind farm flows and validating numerical and analytical models.

CFD modelling of wind farms, particularly large eddy simulation (LES), is by far the most powerful method to investigate wind farm flows. The controllability of simulation configurations and the coupled nature of the governing flow equations solved make CFD frameworks suitable for wind farm flow studies. Therefore, CFD frameworks are extensively used in studies that have focused on various features of wind farm flows. For example, Abkar and Porté-Agel [28], Xie and Archer [29], Wang *et al.* [30] looked into the intra-farm wake interactions for various stability conditions. A common finding of these studies is that wake recovery and the associated power losses are inversely proportional to thermal stability in the boundary layer. Which means that wakes recover faster in CBLs than in CNBLs and SBLs. Since thermal conditions of the atmosphere change over time, wind farm flows during diurnal cycles have also been investigated with various CFD models, ranging in scale from mesoscale weather forecasting models Fitch *et al.* [31] to micro-scale LES Sharma *et al.* [32]. Besides observing the same relation between wake recovery and ABL stability, these studies noticed low-level jets in the rotor layer and significant wind veer at night (i.e. in SBLs) that turn the wakes. Wind-farm wakes or inter-farm wakes have been a topic of recent CFD investigations, such as Stieren and Stevens [33] and Stipa *et al.* [34]'s studies of two neighboring wind farms in truly neutral conditions (i.e. without gravity waves). These studies and others find

inter-farm wake interactions important in designing the layout of clustered wind farms for optimal performance. Recent LES investigations have focused on the importance of wind-farm-induced atmospheric gravity waves [5, 6, 35, 36]. These studies have simulated CNBLs by varying the capping inversion characteristics and the lapse rate of the free atmosphere. Only Allaerts and Meyers [37] and Souaiby and Porte-Agel [38] have performed LES investigations of wind farms including AGWs in CNBLs, SBLs, and CBLs. A common finding of all of these studies is that AGWs contribute to the wind farm blockage effect, affecting the induction zone and enhancing the power output of the wind turbines in the exit region. Moreover, favorable pressure gradients appear downstream of the wind farm, which might be beneficial to a wind farm there.

Unlike CFD frameworks, reduce order and engineering models—collectively called non-CFD frameworks hereafter—couple together different independent models to model different aspects of the physical processes which affect wind farm flow. For instance, wind farm induction and wind turbine wakes are often modeled independently of each other and superimposed to estimate wind farm flow fields. Such an approach is simple but comes at the cost of higher inaccuracies and uncertainty. One of the most prominent non-CFD frameworks for wind farm flows is the Multi-Scale Coupled (MSC) model. It couples mesoscale phenomena with micro-scale processes by superimposing inflow, turbine and wind farm induction, individual wakes, wind farm wakes, and AGW effects on the ABL flow [39]. MSC is an extension of a three-layer model (3LM) [40], which includes both the adverse and favorable pressure gradients caused by AGWs. Other commonly used non-CFD frameworks are the Wind Atlas Analysis and Application Program (WAsP) [41] and FLOw Redirection and Steady State Systems Engineering (FLORIS) [42]. All of these frameworks primarily rely on wake models, wake superimposition models, and models for other processes, depending on the utility of the framework. Several models for wakes and their superimposition have been developed, and their improvement is ongoing. The biggest strength of non-CFD frameworks is their speed, which allows them to be used for site feasibility assessments, annual energy production forecasts, and wind farm layout optimization. However, non-CFD frameworks are limited in their ability fo give insight into unknown atmospheric processes and phenomena like atmospheric gravity waves, as they would always rely on higher fidelity models and measurement data for validation.

2.4. LARGE EDDY SIMULATION

The overview in Section 2.2 establishes how a CFD framework, particularly LES, is the most viable option to understand the physics of wind-farm–atmosphere interactions in terms of accuracy and computational affordability. The setup of a wind farm simulation in a CFD framework is highly dependent on the chosen form of the governing equations and the implementation of, for example, the wind turbines. While models for individual physical processes are essential, the CFD framework (i.e. usually a code) that puts together all the essential models is equally important. CFD frameworks can be classified based on whether the incompressibility assumption is applied, i.e. density is considered constant except where it appears with the gravitational acceleration. In compressible CFD frameworks, density is a variable quantity. Examples of codes used for wind farm CFD include WRF and ERF. Since wind farm flows have Mach numbers <

0.3, they are often considered incompressible flows. The common incompressible CFD frameworks used to simulate wind farms include the OpenFOAM-based SOWFA [43], TOSCA [44], Aspire [45], PALM [46], Ellipsys3D [47], SP-Wind [5], and AMR-Wind [48]. In this study, incompressible LES is adopted to investigate wind-farm–atmosphere interactions. The main components of an LES framework required to simulate wind farm flow are described in the following section.

2.4.1. GOVERNING EQUATIONS

In their fundamental form, the fluid-flow governing equations couple all physical processes that the spatio-temporal resolution and extent of the CFD model can resolve. These equations are compressible and impose the conservation of mass, momentum, and energy, and can be written as follows:

$$\frac{\partial \rho}{\partial t} + \frac{\partial}{\partial x_j}(\rho u_j) = 0, \tag{2.2}$$

$$\frac{\partial}{\partial t}(\rho u_i) + \frac{\partial}{\partial x_j}(\rho u_j u_i) = -\frac{\partial p}{\partial x_i} - \rho \varepsilon_{ijk}\Omega_j u_k + \frac{\partial \tau_{ij}}{\partial x_j} + \rho g_i + \rho f_i, \tag{2.3}$$

$$\frac{\partial}{\partial t}(\rho h) + \frac{\partial}{\partial x_j}\left(\rho u_j h\right) = \frac{\partial p}{\partial t} + u_j \frac{\partial p}{\partial x_j} - \frac{\partial q_j}{\partial x_j} + \tau_{ij}\frac{\partial u_i}{\partial x_j}, \tag{2.4}$$

$$p = \rho R T, \tag{2.5}$$

where ρ is the density, u_i is the velocity in the i-th direction, u_j is the velocity in the j-th direction, p is the pressure, h is the specific enthalpy, T is the temperature, t is time, x_i is the spatial coordinate in the i-th direction, x_j is the spatial coordinate in the j-th direction, τ_{ij} is the viscous stress tensor component, q_j is the heat flux in the j-th direction, g_i is the gravitational acceleration in the i-th direction, f_i is any additional body force per unit mass in the i-th direction, Ω_j is the component of the planetary rotation vector in the j-th direction, ε_{ijk} is the Levi-Civita symbol, and R is the specific gas constant.

The first term in the continuity equation 2.2 represents the local temporal rate of change of density. The second term is the divergence of mass flux, which quantifies how mass is moving in or out of a control volume due to fluid motion. Equation 2.3 are the Navier-Stokes equations that enforce conservation of momentum in a control volume. The first term on the left side represents the local rate of change of momentum in the i-th (i.e. x, y, z) direction. The second term is the convective transport of momentum due to the fluid's motion. On the right-hand side, the first term is the pressure gradient force driving the flow. The second term on the right side is the Coriolis force, accounting for the rotation of the reference frame (e.g. Earth's rotation). The third term is the divergence of the viscous stress tensor, representing internal friction due to velocity gradients. The fourth term accounts for the gravitational body force, and the last term includes any additional body forces, such as wind turbine drag or modeled turbulence effects. Equation 2.4 describes the conservation of total energy. The left-hand side includes terms for the temporal change in energy and the advective transport of energy, respectively. Here, h is specific enthalpy. On the right-hand side, the first two terms represent the

reversible work done by pressure (also associated with compression or expansion). The third term accounts for energy loss or gain due to heat conduction. Finally, the last term represents viscous dissipation—energy lost due to internal friction and deformation in the fluid. Equation 2.5 imposes the ideal gas law as the working fluid is air. This relation is required to close the set of equations.

Anelastic equations are another form of equations derived from the fully compressible ones under a set of assumptions appropriate for atmospheric or geophysical flows with low Mach number, where acoustic waves are not important. The key assumptions are as follows:

- The flow is characterized by small perturbations about a hydrostatically balanced, time-independent base state that varies only in the vertical direction (e.g. base density $\rho_b(z)$).
- Density variations are neglected in the time derivative and advection terms, except where they appear in the buoyancy term, preserving the role of stratification.
- The flow is subsonic (i.e. $M < 1$) and mostly incompressible, so acoustic waves are not accounted for. This allows replacing the full compressible continuity equation with the anelastic constraint: $\nabla \cdot (\bar{\rho}\mathbf{u}) = 0$.
- The equation of state is linearized around the base state to relate pressure, density, and temperature (or potential temperature) perturbations.
- Pressure perturbations do not drive sound waves but instead adjust to maintain mass conservation under the anelastic constraint.

These simplifications reduce computational stiffness and allow for efficient simulation of stratified, low-Mach-number (i.e. $M << 1$) atmospheric flows without resolving fast acoustic modes (i.e. sound waves).

$$\frac{\partial}{\partial x_j}\left(\rho_b(z)u_j\right) = 0 \tag{2.6}$$

$$\rho_b(z)\frac{\partial u_i}{\partial t} + \frac{\partial}{\partial x_j}\left(\rho_b(z)u_j u_i\right) = -\frac{\partial p}{\partial x_i} - \rho_b(z)\Omega_j u_k \varepsilon_{ijk} + \frac{\partial}{\partial x_j}\left(\mu\frac{\partial u_i}{\partial x_j}\right) + bg_i + \rho_b(z)f_i \tag{2.7}$$

$$\rho_b(z)\frac{\partial T}{\partial t} + \frac{\partial}{\partial x_j}\left(\rho_b(z)u_j T\right) = \frac{\partial}{\partial x_j}\left(\kappa_T\frac{\partial T}{\partial x_j}\right) \tag{2.8}$$

$$b = \rho_b(z) + \rho' \tag{2.9}$$

The anelastic approximation assumes a reference density profile $\rho_b(z)$ that varies with height but filters out sound waves by neglecting density variations in the continuity equation, except where they multiply velocity. The continuity equation 2.6 enforces mass conservation for a stratified fluid with incompressible motions. The momentum

equation 2.7 describes the evolution of the velocity field u_i and includes unsteady acceleration $\rho_b(z)\frac{\partial u_i}{\partial t}$, advection $\frac{\partial}{\partial x_j}(\rho_b(z)u_j u_i)$, the pressure gradient force $-\frac{\partial p}{\partial x_i}$, Coriolis acceleration $-\rho_b(z)\Omega_j u_k \varepsilon_{ijk}$ due to planetary rotation, viscous diffusion $\frac{\partial}{\partial x_j}(\mu\frac{\partial u_i}{\partial x_j})$ where μ is kinematic viscosity, gravitational acceleration $g_i b$ related to buoyancy $b = \rho_b(z)+\rho'$, and a body forcing term f_i. ρ' in b is the perturbed density about the base density, which for dry air is given by $\frac{RT(z)}{P_b(z)}$, where $T(z)$ and $P_b(z)$ are the reference temperature and pressure profiles in hydrostatic balance, respectively. The terms in the scalar transport equation 2.8 for temperature T account for local time change, advection, and diffusion, respectively, and $\kappa_T = \rho_b(z)k_T$ is the thermal diffusivity times the base density.

The Boussinesq approximation is a further simplification of the anelastic approximation, commonly used in geophysical fluid dynamics for flows where vertical scales are small compared to the density scale height. The main assumptions applied to the anelastic set of equations are:

- The base-state density ρ_0 is constant and representative of the entire domain.
- Density variations are neglected everywhere except in the buoyancy term of the vertical momentum equation.
- The flow is incompressible, leading to the constraint $\nabla\cdot\mathbf{u} = 0$.
- The thermodynamic variable (e.g. temperature or potential temperature) perturbation θ' is used to compute buoyancy.
- Acoustic waves are filtered out entirely.
- Vertical variations in the base state (e.g. $\bar{\theta}(z)$) can be retained in the buoyancy source term but are otherwise neglected in fluid properties.

In meteorology, these assumptions are valid for small-scale flows (e.g. convection, boundary-layer turbulence) with weak compressibility and small vertical density stratification. The governing equations in the Boussinesq form are similar to those of anelastic approximation, but are given here for clarity.

$$\frac{\partial u_j}{\partial x_j} = 0 \tag{2.10}$$

$$\frac{\partial u_i}{\partial t} + \frac{\partial}{\partial x_j}(u_j u_i) = -\frac{1}{\rho_0}\frac{\partial p}{\partial x_i} - \Omega_j u_k \varepsilon_{ijk} + \frac{\partial}{\partial x_j}\left(\nu\frac{\partial u_i}{\partial x_j}\right) + \frac{\rho_0+\rho'}{\rho_0}g_i + f_i \tag{2.11}$$

$$\frac{\partial T}{\partial t} + \frac{\partial}{\partial x_j}(u_j T) = \frac{\partial}{\partial x_j}\left(k_T\frac{\partial T}{\partial x_j}\right) \tag{2.12}$$

$$\frac{\rho_0+\rho'}{\rho_0} = 1-\beta(T-T_0) \tag{2.13}$$

The Boussinesq approximation is a simplification to describe fluid flow under the assumption that density variations are small and only significant in the buoyancy term

of the momentum equation. The mass continuity equation 2.10 represents the incompressibility condition of the flow. The momentum equation 2.11 describes the evolution of the velocity field u_i as described earlier. The scalar transport equation 2.12 is the same as that of the anelastic one, except that density drops out because it is constant. Finally, the linearized equation of state, Equation 2.13, relates the density perturbation ρ' to the temperature deviation $T - T_0$ through the thermal expansion coefficient β, where T_0 is the reference temperature and ρ_0 is the reference density.

Wind farm flows are often solved with incompressible Boussinesq equations as the vertical scales are much smaller than the density scale height. Indeed, mesoscale frameworks like WRF solve fully compressible equations. The use of the Boussinesq approximation has become a concern in simulating wind-farm-induced atmospheric gravity waves, as such models require resolving the atmosphere up to 30 km. Since density does not remain constant at such high altitudes, it is necessary to assess the impact of compressibility assumptions on wind farm performance. This topic will be covered in Chapter 4 by comparing the anelastic and Boussinesq approximations in wind farm modeling, including atmospheric gravity waves.

2.4.2. TURBULENCE MODEL

Turbulence covers a wide range of spatio-temporal sizes. For instance, the eddy size in wind farm flows ranges from Kolmogorov's (i.e. a millimeter) to integral length scales (i.e, a few hundred meters). The size of a wind farm, several kilometers wide in each spatial direction, makes CFD models extremely computationally expensive if attempting to fully resolve turbulence at all scales. One way to relate the physical scale of a flow model to computational affordability is through the Reynolds number (Re). Computational cost in core-hours—using a CPU for an hour— increases with roughly the cube of Re, with $Re \approx 10^7$ for a typical wind farm flow. The cost of Direct Numerical Simulations (DNS) resolving all scales of the flow around the wind farm simulated in this study would be 10^{25} core-hours, assuming a uniform grid with the size of 0.00025 m, to resolve the shallowest ABL simulated (i.e. only 300 m tall). This means the current largest available supercomputer—El Capitan of Lawrence Livermore National Lab, USA, with 11 million cores, both CPUs and GPUs combined— is 1.6×10^{17} cores short of that required to run this case with a code such as TOSCA. Such an allocation of computational resources, assuming other challenges are addressed, is impossible. Therefore, DNS of wind farm flows is unlikely even in the foreseeable future.

To make CFD computationally affordable, the governing equations are filtered either in space or time to resolve large flow processes and model smaller ones. Since space and time are linked in numerically solving the equations through the Courant-Friedrichs-Lewy number, spatial filtering would impose temporal filtering or vice versa. Filtering leads to the Large Eddy Simulation (LES) form of the governing equations, which resolves large-scale phenomena, and those smaller than the grid size (i.e. subgrid-scale turbulence) are modeled with subgrid-scale models. When mean flow is of interest, the governing equations are often averaged to get the Reynolds-Averaged Navier-Stokes (RANS) form. RANS simulations solve for the mean flow while modeling all the impacts of turbulence on the mean flow. The filtered LES equations applied in an incompressible Boussinesq form, which is widely used in wind farm flows and also in this study, are

given below.

$$\frac{\partial \overline{u}_j}{\partial x_j} = 0 \tag{2.14}$$

$$\frac{\partial \overline{u}_i}{\partial t} + \frac{\partial}{\partial x_j}\left(\overline{u}_j\,\overline{u}_i\right) + \Omega_j\,\overline{u}_k\,\epsilon_{ijk} = -\frac{1}{\bar{\rho}}\frac{\partial \overline{p}}{\partial x_i} + \frac{\partial}{\partial x_j}\left(\nu\frac{\partial \overline{u}_i}{\partial x_j}\right) + \frac{\partial R_{ij}}{\partial x_j} + g_i + f_i \tag{2.15}$$

$$\frac{\partial \overline{T}}{\partial t} + \frac{\partial}{\partial x_j}\left(\overline{u}_j\,\overline{T}\right) = -\frac{\partial}{\partial x_j}\left(k_T\frac{\partial \overline{T}}{\partial x_j}\right) + \frac{\partial Q_j}{\partial x_j} \tag{2.16}$$

$$R_{ij} = -\nu_{sgs}\left(\frac{\partial \overline{u}_i}{\partial x_j} + \frac{\partial \overline{u}_j}{\partial x_i}\right) + \frac{2}{3}k\,\delta_{ij} \tag{2.17}$$

$$Q_j = -\frac{\nu_{sgs}}{\mathrm{Pr}_t}\frac{\partial \overline{T}}{\partial x_j} \tag{2.18}$$

Where the overbar on the prognostic variables in these equations indicates spatial filtering, and R_{ij} and Q_{ij} are the subgrid-scale stress and thermal fluxes, respectively. Subgrid-scale viscosity (i.e. $\nu_{sgs} = C_k k^{1/2} l$), and C_k is a model constant, k is turbulent kinetic energy, $l = \left(0.76\,g\,\theta_0\,(\partial\bar{\theta}/\partial z)^{-1}\right)^{1/2}$ is a length scale, δ_{ij} is Kronecker delta, and Pr_t is the turbulent Prandtl number. R_{ij} and Q_{ij} appear as a result of filtering the tensor stress term and the advection of the temperature term in the momentum and temperature transport equations, respectively. These extra terms require additional information to attain a closed system of equations, and the turbulence models (i.e. SGS models for LES) serve this purpose. In LES, turbulence models approximate SGS stresses and heat fluxes as functions of resolved variables like filtered velocity and temperature, based on physical principles such as eddy viscosity or scalar diffusivity concepts. There are several SGS models used with different LES frameworks in modeling wind farm flows, such as the one-equation model in SOWFA, the dynamic Smagorinsky model with Lagrangian averaging in TOSCA, and the Rozema model in Aspire. The basic formulation of the SGS models is similar, and the one-equation model used in SOWFA is given below as an example.

$$\frac{\partial k_{\mathrm{sgs}}}{\partial t} + \frac{\partial}{\partial x_j}\left(\overline{u}_j\,k_{\mathrm{sgs}}\right) = -R_{ij}\frac{\partial \overline{u}_i}{\partial x_j} - C_\varepsilon\frac{k_{\mathrm{sgs}}^{3/2}}{\Delta} + \frac{\partial}{\partial x_j}\left[\left(\nu + \nu_{\mathrm{sgs}}\right)\frac{\partial k_{\mathrm{sgs}}}{\partial x_j}\right] \tag{2.19}$$

Equation 2.19 is the transport equation for subgrid-scale turbulent kinetic energy (k_{sgs}), where C_ϵ is a model constant parameterizing the dissipation rate of subgrid-scale turbulent kinetic energy. Once k_{sgs} is known, ν_{sgs} is calculated explicitly.

Most SGS models, including the one-equation model, are based on the linear turbulent stress-strain relationship that relates the SGS stress to resolved-scale strain rate, which is given as follows.

$$\tau_{ij}^D = -2\,\nu_{sgs}\,\overline{S}_{ij}, \tag{2.20}$$

where τ_{ij}^{D} is the deviatoric SGS stress tensor and

$$\overline{S}_{ij} = \frac{1}{2}\left(\frac{\partial \overline{U}_i}{\partial x_j} + \frac{\partial \overline{U}_j}{\partial x_i}\right) \tag{2.21}$$

is the resolved-scale strain rate tensor. The standard Smagorinsky model [49] computes ν_{sgs} as,

$$\nu_{sgs} = \left(C_s \overline{\Delta}\right)^2 \overline{S}, \tag{2.22}$$

in which C_s is a fixed constant and $\overline{\Delta}$ is usually related to the mesh as $\overline{\Delta} = (\Delta x \Delta y \Delta z)^{1/3}$,

where Δx, Δy, and Δz are the mesh cell lengths in the x-, y-, and z-directions, respectively, and $\overline{S} = \left(2\overline{S}_{ij}\overline{S}_{ij}\right)^{1/2}$.

Dynamic Smagorinsky models are mostly based on Germano *et al.* [50]'s formulation to compute C_s in space and time. Often, these dynamic models require some kind of averaging to ensure numerical stability. For flows over flat terrain, planar averaging is fine; however, for complex terrain, models use Lagrangian averaging, tracking flow along its paths back in time. Moreover, C_s can be considered dependent or independent of the filtering length scale. This, together with the flow averaging strategy, has led to several formulations, such as the Lagrangian-averaged scale-independent model used for the most part in this work in TOSCA simulations; see Meneveau *et al.* [51] for details. The Rozema model in Aspire [52] is also an eddy-viscosity model developed for anisotropic grids.

2.4.3. NUMERICAL METHOD

The filtered governing equations are solved numerically by discretizing the simulation domain into smaller units or cells. The choice of numerical methods and schemes is a standard procedure in CFD and well-tested. Wind farm flows have been investigated with a variety of numerical methods, including pseudo-spectral, Finite Volume, Finite Differences, and Lattice Boltzmann. Each method has its advantages and disadvantages, and choosing one for a wind farm simulation might depend on the complexity of the terrain, flow characteristics, and required resolution.

Pseudo-spectral methods offer high accuracy and fast error convergence for smooth, periodic domains, making them suitable for idealized simulations such as flat terrain and periodic wind farms. However, they are not well-suited for complex geometries or heterogeneous boundary conditions, limiting their applicability in realistic atmospheric flow over complex terrain. See Allaerts [53] for an example of a pseudo-spectral code used to investigate wind farm aerodynamics.

Finite volume methods might be suitable for wind farm simulations due to their strong conservation properties, ability to handle unstructured meshes, and suitability for complex topography, such as hills or coastal terrain. They also allow local mesh refinement around turbines and in regions of interest. However, they may exhibit higher numerical diffusion and slower convergence rates unless higher-order schemes are employed.

Finite element methods are weakly conservative and most suitable for complex geometries and boundaries of the solution domain, as they are usually applied to unstruc-

tured grids. Although, often used in structural analysis, they can be applied to wind farm flows, but their implementation is complex and can be computationally heavy.

Finite difference methods are computationally efficient and relatively simple to implement, particularly on structured grids. They are effective for flat domains or idealized layouts, but they struggle with irregular or unstructured meshes, making them less flexible for incorporating terrain features or highly localized refinement near turbines. See Ferziger and Perić [54] for more details on the finite volume, finite difference, and finite element methods.

Lattice Boltzmann methods (LBM) provide an alternative, mesoscopic approach that is naturally parallelizable and handles complex boundaries, such as turbine blades or forest canopies, with relative ease. However, LBM typically requires finer grids and handling variable boundary conditions such as atmospheric inflow profiles or geophysical terrain remains more challenging and less mature compared to traditional methods. Wang *et al.* [30] is a recent example of an LBM based LES study to investigate wind farm wakes.

In this study, we used finite-volume codes (SOWFA, TOSCA, and Aspire), which are suitable for wind farm LES. The first two are open source, which is desirable for research.

2.4.4. WALL BOUNDARY MODELS

The underlying terrain (land or sea) of a wind farm is often considered a wall from the point of view of flow modeling. Depending on its roughness, the surface retards the wind flow immediately above, imposing shear stresses on the flow in the wall-parallel directions. The sheared wind profile in the ABL is thus a consequence of these wall stresses. Like any boundary layer, the ABL has turbulent eddies as small as the Kolmogorov length scale in an inner layer, where viscosity effects are dominant. In an outer layer, larger eddies are present where molecular viscosity effects are negligible. As discussed in the previous section, resolving the inner-layer eddies in an ABL is beyond the current computational affordability, as resolving these structures requires extremely fine meshes and ideally DNS or at least LES. A simpler way is to model the wall stress and impose it as a boundary condition on the outer layer flow, usually applied to the first grid cell above the surface. This is the philosophy behind classic wall-stress modeling (i.e. law-of-the-wall or equilibrium laws), where a logarithmic velocity profile is often considered in the inner layer such that the shear stress between the wall and the first grid point is constant. In other words, the effect of the inner layer flow (i.e. mainly wall shear stress) on that of the outer flow is modeled, while resolving the outer layer flow.

In LES of wind farm flows, classical law-of-the-wall models are used to predict the wall shear stress. The outer layer flow is resolved with LES, whereas the inner layer is modeled in a similar fashion to that of a Reynolds-averaged code. This means that the grid is coarse enough to bypass several life cycles of a typical eddy in the inner layer, so that its temporally averaged behavior can be represented. Hence, the wall shear stress at the first grid point is computed, given that the velocity at the first point is known from the solution of the outer layer flow. Often, the Monin and Obukhov similarity theory [55] is used in ABL-wind farm flows to model the wall stresses and heat flux in an SBL or CBL. The expressions for the friction velocity (u^*), the inner-layer temperature scale (θ^*), and the wall shear stresses (τ_{xz}^w and τ_{yz}^w), including corrections for stratification, are

the following,

$$u^* = \frac{\kappa\sqrt{u_1^2 + v_1^2}}{ln(\frac{z_1}{z_o}) - \Psi_m(\frac{z_1}{L})} \tag{2.23}$$

$$\theta^* = \frac{\kappa(\theta_1 - \theta_s)}{ln(\frac{z_1}{z_o}) - \Psi_q(\frac{z_1}{L})} \tag{2.24}$$

$$\tau_{xz}^w = -\rho_0 u^{*2} \frac{u_1}{\sqrt{u_1^2 + v_1^2}} \tag{2.25}$$

$$\tau_{yz}^w = -\rho_0 u^{*2} \frac{v_1}{\sqrt{u_1^2 + v_1^2}} \tag{2.26}$$

Where κ is the von Kármán constant, z_1 is the height of the first grid point, and z_o is the surface roughness height. Whereas, u_1 and v_1 are the streamwise and spanwise velocity components, and θ_s is surface potential temperature. The correction terms (i.e. Ψ_m and Ψ_q) in Equation 2.23 and 2.24 account for stratification in the ABL, and are based on the Obukhov length (i.e. $L = -u^{*3}/\kappa\left(g/\theta\right)\overline{w'\theta'}$). Here, θ is the potential temperature of dry air, and $w'\theta'$ is the turbulent heat flux in kinematic form. Heat flux at the first point is required in modeling SBLs and CBLs only; thus, Equation 2.24 and the correction term Ψ_m are not required in modeling neutral ABLs.

Stipa *et al.* [34] gives a detailed analysis of wind farm LES with law-of-the-wall modeling for neutral ABLs. They conclude that typical grids used in wind farm LES depart from the law-of-the-wall criteria, resulting in inaccurate velocity and shear stress profiles and, in turn, inaccurate wind farm flow solutions. Thus, they suggest predicting u^* from a precursor simulation with a mesh finer than those typically used in wind farm simulations and correcting the u^* in the wind farm simulation accordingly.

Alternatives to the law-of-the-wall or equilibrium laws are zonal approaches that do not explicitly compute the wall shear stress; instead, they solve the governing equations to characterize the flow in the inner and outer layers. In these methods, the inner layer flow is treated using a Reynolds-averaged approach and a finer grid in the wall-normal direction, and the outer layer with a coarser grid where the flow is governed by LES equations, i.e. a hybrid RANS/LES method is used (see Fröhlich and von Terzi [56] for a review). Detached eddy simulation (DES) is one such approach, but uses a single grid where RANS is applied to the attached boundary layer flow and the method switches to LES for the detached part of the boundary layer flow (see Spalart [57] for a dedicated review on this method).

2.4.5. FARM AND TURBINE MODELS

A wind farm can be modeled in an LES framework in a number of ways: from a roughness entity (i.e. like a canopy) to an ensemble of blade-resolved wind turbines. In fact, the general aim is to capture the coupled flow interactions of each turbine and the wind farm with the atmosphere as in-depth as permitted by the filtered length. However, in some cases, parameterizing the wind farm as a roughness entity or momentum sink, imposing a thrust force on the flow, can be sufficient. The latter approach can allow

investigation of mesoscale interactions of the wind farm with the atmosphere, such as inducing gravity waves and affecting downstream local flow. Here, a brief description of the range of wind farm and wind turbine models used in LES investigations is given.

The wind farm canopy (WFC) is a simple formulation that applies the cumulative thrust force of a wind farm to the incoming flow. In concept, this is closer to the Fitch parametrization used in mesoscale weather forecasting models like WRF [58]. The WFC model acts as a momentum sink that can be applied to coarse grids (i.e. $\Delta x \approx 200\ m$) in microscale CFD models. It offers computational affordability to investigate wind farm scale phenomena like AGWs and cluster wakes. The WFC model mainly relies on the wind farm thrust coefficient, which is a function of either the free-stream or the local velocity, the turbine spacing, and the wind turbine thrust coefficient. The detailed formulation of the WFC model used in this study is given in chapter 3.

The actuator farm model (AFM) is a higher fidelity model of a wind farm that imposes the thrust force of each wind turbine over its rotor area around the rotor center [34]. For refined meshes (i.e. Δx and $\Delta y < 30\ m$), AFM resembles the uniform actuator disk model of a wind turbine that is described below. The AFM model is desirable when investigating cluster wind farm interactions and predicting their performance. It is also suitable for investigating AGWs induced by large wind farms.

The accuracy of wind farm performance predictions improves when wind turbines are modeled with their actual physical geometry. This level of detail is achieved using blade-resolved simulations, where the turbine structures, including blades, nacelle, and tower, are represented using body-conforming meshes. Although this approach captures the turbine aerodynamics accurately, it requires extensive meshing and results in a prohibitively high computational cost when applied to full wind farms. Consequently, blade-resolved methods are typically limited to simulations of (parts of) isolated turbines Lawson *et al.* [59], Vijayakumar and Brasseur [60].

For practical reasons, in order to balance accuracy with computational efficiency, actuator models are widely used to represent wind turbines. These models approximate the aerodynamic forces exerted by the turbines and apply them directly to the flow field, eliminating the need for body-conforming meshes. Actuator models are mesh-relaxed, meaning a uniform structured grid is sufficient to simulate turbine effects. The fidelity of actuator models varies based on the complexity of force representation. The most detailed is the actuator surface model, which distributes forces along both the chord and span of each blade using airfoil-specific data. The actuator line model simplifies this by applying forces only along a line representing each blade, without chord-wise distribution. The actuator disk model (ADM) is simpler still; it distributes the thrust force over the rotor area at discrete points arranged radially and azimuthally.

The simplest variant of the ADM is the uniform ADM, which neglects tangential forces and radial variations in thrust. In this model, the total thrust force is applied uniformly over the rotor disk. The thrust force "$\mathbf{T}$" imposed on the flow is given by:

$$\mathbf{T} = \frac{1}{2}\rho C_t U_\infty^2 A$$

where ρ is the air density, C_t is the thrust coefficient, U_∞ is the free stream velocity, A is the area of the actuator disk.

In this study, the uniform ADM is used due to its computational efficiency and the fact that modeling wind-farm-induced atmospheric gravity waves is less sensitive to details of turbine-scale flows.

2.4.6. TURBULENT INFLOW CONDITIONS

Wind farm LES is largely confined by computational resources, and simulating as small a region around the wind farm as possible is highly desirable. At the same time, including atmospheric flow features, like turbulence, from outside the simulation domain is essential. This is often done by prescribing boundary conditions that represent the flow at the boundaries that impose the prevailing atmospheric conditions at the wind farm site. These boundary conditions can be referred to as inflows to the simulation domain that are often applied at the streamwise and lateral boundaries. Usually, inflow data is prescribed at the inlet streamwise boundary of the simulation domain containing the wind farm, which is called the successor simulation. The concept of a successor simulation is rooted in the fact that inflow data is usually created with a precursor simulation. This wind-farm-less simulation captures a small fetch of flat surface that extends up to a few hundred meters of the free atmosphere. Initial mean wind and temperature profiles, surface roughness, heat flux at the bottom boundary–if stratification in the ABL is critical–and latitude to include the Coriolis effect are provided with random perturbations in the ABL to generate turbulence. Periodic boundary conditions are used in the streamwise and lateral directions to develop the turbulence until it reaches a statistically developed state. A constant pressure gradient or geostrophic wind vector is applied to drive the flow through the precursor domain. Inflow data, usually 2D planes, after the spin-up phase, are either mapped directly onto the inlet boundaries of the successor simulation or saved to be used as an offline inflow dataset. The former, concurrent-precursor method, requires running the precursor and successor simultaneously. Either way, the inflow data must satisfy the governing equations in the successor simulation, which is usually the case as the precursor solves the same equations.

Generally, the features of inflow data depend on whether turbulence is treated in the successor simulation. If resolved turbulence is irrelevant or unaffordable for an investigation, RANS models are suitable, which require profiles of mean flow and turbulent quantities depending on the turbulence model used. For instance, using the $k-\epsilon$ model requires either fixed values or coarse time series of turbulent kinetic energy and turbulent dissipation rates. The mean profiles of flow and turbulent quantities can be created with single-column precursor simulations, as RANS does not resolve any turbulence, and only vertical gradients may matter if heat flux or mesoscale flow varies on a time scale resolved by RANS. By contrast, LES requires inflow data that contain turbulence resolved on finer temporal scales (i.e. as small as a second). Thus, the precursor method is suitable as it can resolve turbulence in the same manner as the successor simulation. The precursor simulations incur a computational cost that is a fraction of the successor simulation.

Non-precursor approaches can eliminate the additional computational cost of a precursor, but at the cost of unresolved turbulence. Still, non-precursor approaches are useful for theoretical investigations as they can apply mean profiles of wind, temperature, and other scalars to a simulation. The simplest approach in this regard is to use

logarithmic or power law profiles for mean wind speed and an approximate potential temperature profile. More complicated mean profiles can be acquired from mesoscale simulations, like WRF and Aspire, and assimilated measurement data. Given the coarseness of the mesoscale and measured field data—hundreds of meters to kilometers spatially and tens of minutes to days temporally—turbulence is not captured and requires measures to include it. Synthetic turbulence generation for wind turbine LES [61] is a notable approach among many that superimposes turbulence on a deterministic mean inflow for neutral boundary layers. In this approach, turbulence is generated on a plane far upstream of a wind turbine by applying body forces varying in time and space. The perturbations created by the body forcing evolve over the distance between the plane and the wind turbine, satisfying the filtered equations driving the flow. The reader is referred to [62] for further non-precursor methods and their details.

REFERENCES

[1] M. A. Khan, M. J. Churchfield, and S. J. Watson, *Dependence of wind-farm-induced gravity waves and wind-farm performance on non-dimensional atmospheric parameters and simulation configuration,* Wind Energy Science Discussions **2025**, 1 (2025).

[2] R. B. Stull, *An Introduction to Boundary Layer Meteorology*, Atmospheric and Oceanographic Sciences Library, Vol. 13 (Springer Netherlands, Dordrecht, 1988).

[3] M. A. Khan, D. Allaerts, S. J. Watson, and M. J. Churchfield, *Investigating the relationship between simulation parameters and flow variables in simulating atmospheric gravity waves for wind energy applications,* Wind Energy Science **10**, 1167 (2025).

[4] R. B. Smith, *Gravity wave effects on wind farm efficiency,* Wind Energy **13**, 449 (2010).

[5] D. Allaerts and J. Meyers, *Boundary-layer development and gravity waves in conventionally neutral wind farms,* Journal of Fluid Mechanics **814**, 95 (2017).

[6] L. Lanzilao and J. Meyers, *A parametric large-eddy simulation study of wind-farm blockage and gravity waves in conventionally neutral boundary layers,* Journal of Fluid Mechanics **979**, A54 (2024).

[7] M. A. Khan, S. J. Watson, D. J. N. Allaerts, and M. Churchfield, *Recommendations on setup in simulating atmospheric gravity waves under conventionally neutral boundary layer conditions,* Journal of Physics: Conference Series **2767**, 092042 (2024).

[8] S. J. Ollier and S. J. Watson, *Modelling the impact of trapped lee waves on offshore wind farm power output,* Wind Energy Science **8**, 1179 (2023).

[9] J. Sachsperger, S. Serafin, and V. Grubišić, *Lee waves on the boundary-layer inversion and their dependence on free-atmospheric stability,* Frontiers in Earth Science **3** (2015), 10.3389/feart.2015.00070.

[10] F. Porté-Agel, M. Bastankhah, and S. Shamsoddin, *Wind-turbine and wind-farm flows: A review,* Boundary-Layer Meteorology **174**, 1 (2020).

[11] K. L. Wu and F. Porté-Agel, *Flow adjustment inside and around large finite-size wind farms,* Energies **10**, 4 (2017).

[12] R. J. Barthelmie, S. C. Pryor, S. T. Frandsen, K. S. Hansen, J. G. Schepers, K. Rados, W. Schlez, A. Neubert, L. E. Jensen, and S. Neckelmann, *Quantifying the impact of wind turbine wakes on power output at offshore wind farms,* Journal of Atmospheric and Oceanic Technology **27**, 1302 (2010).

[13] L. P. Chamorro and F. Porté-Agel, *Turbulent flow inside and above a wind farm: A wind-tunnel study,* Energies **4**, 1916 (2011).

[14] C. L. Archer, S. Mirzaeisefat, and S. Lee, *Quantifying the sensitivity of wind farm performance to array layout options using large-eddy simulation,* Geophysical Research Letters **40**, 4963 (2013), https://agupubs.onlinelibrary.wiley.com/doi/pdf/10.1002/grl.50911 .

[15] N. Hamilton, M. Melius, and R. B. Cal, *Wind turbine boundary layer arrays for cartesian and staggered configurations – part i: Flow field and power measurements,* Wind Energy **17**, 939 (2014).

[16] M. Calaf, C. Meneveau, and J. Meyers, *Large eddy simulation study of fully developed wind-turbine array boundary layers,* Physics of Fluids **22**, 015110 (2010).

[17] M. Abkar and F. Porté-Agel, *The effect of free-atmosphere stratification on boundary-layer flow and power output from very large wind farms,* Energies **6**, 2338 (2013).

[18] S. Frandsen, *On the wind speed reduction in the center of large clusters of wind turbines,* Journal of Wind Engineering and Industrial Aerodynamics **39**, 251 (1992).

[19] M. Calaf, M. B. Parlange, and C. Meneveau, *Large eddy simulation study of scalar transport in fully developed wind-turbine array boundary layers,* Physics of Fluids **23**, 126603 (2011), https://pubs.aip.org/aip/pof/article-pdf/doi/10.1063/1.3663376/13704482/126603_1_online.pdf .

[20] D. Yang, C. Meneveau, and L. Shen, *Large-eddy simulation of offshore wind farm,* Physics of Fluids **26** (2014), 10.1063/1.4863096.

[21] M. Gaumond, P.-E. Réthoré, S. Ott, A. Peña, A. Bechmann, and K. S. Hansen, *Evaluation of the wind direction uncertainty and its impact on wake modeling at the horns rev offshore wind farm,* Wind Energy **17**, 1169 (2014), https://onlinelibrary.wiley.com/doi/pdf/10.1002/we.1625 .

[22] J. Bleeg, M. Purcell, R. Ruisi, and E. Traiger, *Wind farm blockage and the consequences of neglecting its impact on energy production,* Energies **11** (2018), 10.3390/en11061609.

[23] C. Rodaway, K. Gunn, S. Williams, A. Sebastiani, E. Simon, M. Courtney, G. R. Thorsen, E. Clausen, M. Turrini, D. Wouters, Y. Liu, J. Gottschall, M. Dörenkämper, E. Patschke, L.-Y. Hun, and N. Adams, *Owa globe: Measuring and modelling the global blockage effect to achieve industry consensus,* in *WindEurope Technology Workshop 2024: Resource Assessment & Analysis of Operating Wind Farms* (Dublin, Ireland, 2024) poster.

[24] A. Abraham, N. Hamilton, N. Bodini, B. Hirth, J. Schroeder, S. Letizia, R. Krishnamurthy, R. Newsom, and P. Moriarty, *Land-based wind plant wake characterization using dual-doppler radar measurements at AWAKEN,* Journal of Physics: Conference Series **2767**, 092037 (2024).

[25] A. S. Wise, R. S. Arthur, A. Abraham, S. Wharton, R. Krishnamurthy, R. Newsom, B. Hirth, J. Schroeder, P. Moriarty, and F. K. Chow, *Large-eddy simulation of an atmospheric bore and associated gravity wave effects on wind farm performance in the southern great plains,* Wind Energy Science Discussions **2024**, 1 (2024).

[26] L. P. Chamorro and F. Porté-Agel, *Experimental study on the wake meandering within a scale model wind farm subject to a wind-tunnel flow simulating an atmospheric boundary layer,* Boundary-Layer Meteorology **166**, 449 (2017).

[27] M. B. Christiansen and C. B. Hasager, *Wake effects of large offshore wind farms identified from satellite SAR,* Remote Sensing of Environment **98**, 251 (2005).

[28] M. Abkar and F. Porté-Agel, *Influence of atmospheric stability on wind-turbine wakes: A large-eddy simulation study,* Physics of Fluids **27**, 035104 (2015).

[29] S. Xie and C. L. Archer, *A numerical study of wind-turbine wakes for three atmospheric stability conditions,* Boundary-Layer Meteorology **165**, 87 (2017).

[30] Z. Wang, J. Jacob, F. Marlow, and P. Sagaut, *Lattice boltzmann method-based large eddy simulation of the influence of atmospheric stability on wind farm wake,* Physics of Fluids **37**, 065131 (2025).

[31] A. C. Fitch, J. K. Lundquist, and J. B. Olson, *Mesoscale influences of wind farms throughout a diurnal cycle,* Monthly Weather Review **141**, 2173 (2013).

[32] V. Sharma, M. B. Parlange, and M. Calaf, *Perturbations to the spatial and temporal characteristics of the diurnally-varying atmospheric boundary layer due to an extensive wind farm,* Boundary-Layer Meteorology **162**, 255 (2017).

[33] A. Stieren and R. J. A. M. Stevens, *Impact of wind farm wakes on flow structures in and around downstream wind farms,* Flow **2**, E21 (2022).

[34] S. Stipa, A. Ajay, and J. Brinkerhoff, *The actuator farm model for large eddy simulation (LES) of wind-farm-induced atmospheric gravity waves and farm–farm interaction,* Wind Energy Science **9**, 2301 (2024).

[35] O. Maas, *From gigawatt to multi-gigawatt wind farms: wake effects, energy budgets and inertial gravity waves investigated by large-eddy simulations,* Wind Energy Science Discussions **2022**, 1 (2022).

[36] S. Stipa, M. Ahmed Khan, D. Allaerts, and J. Brinkerhoff, *A large-eddy simulation (LES) model for wind-farm-induced atmospheric gravity wave effects inside conventionally neutral boundary layers,* Wind Energy Science **9**, 1647 (2024).

[37] D. Allaerts and J. Meyers, *Gravity waves and wind-farm efficiency in neutral and stable conditions,* Boundary-Layer Meteorology **166**, 269 (2018).

[38] M. Souaiby and F. Porte-Agel, *Atmospheric stability effect on wind farm flow and performance,* Physics of Fluids **37**, 095152 (2025).

[39] S. Stipa, A. Ajay, D. Allaerts, and J. Brinkerhoff, *The multi-scale coupled model: a new framework capturing wind farm-atmosphere interaction and global blockage effects,* Wind Energy Science Discussions **2023**, 1 (2023).

[40] D. Allaerts, S. V. Broucke, N. Van Lipzig, and J. Meyers, *Annual impact of wind-farm gravity waves on the Belgian-Dutch offshore wind-farm cluster,* Journal of Physics: Conference Series **1037** (2018), 10.1088/1742-6596/1037/7/072006.

[41] N. G. Mortensen and E. L. Petersen, *WAsP – The Wind Atlas Analysis and Application Program: User's Guide,* Risø DTU, Technical University of Denmark, Roskilde, Denmark (2008).

[42] J. Annoni, P. Fleming, A. Scholbrock, J. Roadman, S. Dana, C. Adcock, F. Porte-Agel, S. Raach, F. Haizmann, and D. Schlipf, *Analysis of control-oriented wake modeling tools using lidar field results,* Wind Energy Science **3**, 819 (2018).

[43] M. J. Churchfield, S. Lee, J. Michalakes, and P. J. Moriarty, *A numerical study of the effects of atmospheric and wake turbulence on wind turbine dynamics,* Journal of Turbulence **13**, 1 (2012).

[44] S. Stipa, A. Ajay, D. Allaerts, and J. Brinkerhoff, *TOSCA – an open-source, finite-volume, large-eddy simulation (LES) environment for wind farm flows,* Wind Energy Science **9**, 297 (2024).

[45] J. Schalkwijk, H. J. J. Jonker, A. P. Siebesma, and E. van Meijgaard, *Weather forecasting using gpu-based large-eddy simulations,* Bulletin of the American Meteorological Society **96**, 715 (2015).

[46] B. Maronga, M. Gryschka, R. Heinze, F. Hoffmann, F. Kanani-Sühring, M. Keck, K. Ketelsen, M. O. Letzel, M. Sühring, and S. Raasch, *The parallelized large-eddy simulation model (palm) version 4.0 for atmospheric and oceanic flows: model formulation, recent developments, and future perspectives,* Geoscientific Model Development **8**, 1539 (2015).

[47] N. N. Sørensen, *General Purpose Flow Solver Applied to Flow Over Hills*, Doctoral thesis, Risø National Laboratory for Sustainable Energy, Wind Energy Division, Aeroelastic Design (1995).

[48] M. B. Kuhn, M. T. Henry de Frahan, P. Mohan, G. Deskos, M. Churchfield, L. Cheung, A. Sharma, A. Almgren, S. Ananthan, M. J. Brazell, L. A. Martinez-Tossas, R. Thedin, J. Rood, P. Sakievich, G. Vijayakumar, W. Zhang, and M. Sprague, *Amr-wind: A performance-portable, high-fidelity flow solver for wind farm simulations,* Wind Energy **28** (2025), 10.1002/we.70010.

[49] J. Smagorinsky, *General circulation experiments with the primitive equations: I. the basic experiment,* Monthly Weather Review **91**, 99 (1963).

[50] M. Germano, U. Piomelli, P. Moin, and W. Cabot, *A dynamic subgrid-scale eddy viscosity model,* Physics of Fluids A **3**, 1760 (1991).

[51] C. Meneveau, T. S. Lund, and W. H. Cabot, *A Lagrangian dynamic subgrid-scale model of turbulence,* Journal of Fluid Mechanics **319**, 353–385 (1996).

[52] W. Rozema, H. J. Bae, P. Moin, and R. Verstappen, *Minimum-dissipation models for large-eddy simulation,* Physics of Fluids (2015), 10.1063/1.4928700.

[53] D. Allaerts, *Large-eddy Simulation of Wind Farms in Conventionally Neutral and Stable Atmospheric Boundary Layers*, Ph.D. thesis (2016).

[54] J. H. Ferziger and M. Perić, *Computational Methods for Fluid Dynamics*, 3rd ed. (Springer, Berlin, Heidelberg, 2002).

[55] A. S. Monin and A. M. Obukhov, *Basic laws of turbulent mixing in the surface layer of the atmosphere,* Trudy Geofizicheskogo Instituta, Akademii Nauk SSSR **24**, 163 (1954), in Russian.

[56] J. Fröhlich and D. von Terzi, *Hybrid LES/RANS methods for the simulation of turbulent flows,* J. Prog. Aerosp. Sci. **44**, 349 (2008).

[57] P. R. Spalart, *Detached-Eddy Simulation,* Annual Review of Fluid Mechanics **41**, 181 (2009).

[58] A. C. Fitch, J. B. Olson, J. K. Lundquist, J. Dudhia, A. K. Gupta, J. Michalakes, and I. Barstad, *Local and mesoscale impacts of wind farms as parameterized in a mesoscale nwp model,* Monthly Weather Review **140**, 3017 (2012).

[59] M. J. Lawson, J. Melvin, S. Ananthan, K. M. Gruchalla, J. S. Rood, and M. A. Sprague, *Blade-Resolved, Single-Turbine Simulations Under Atmospheric Flow*, Tech. Rep. (National Renewable Energy Laboratory (NREL), 2019).

[60] G. Vijayakumar and J. G. Brasseur, *Blade-resolved modeling with fluid-structure interaction,* in *Wind Energy Modeling and Simulation: Volume 1: Atmosphere and Plant*, IET Energy Engineering Series, edited by P. Veers (Institution of Engineering and Technology, 2019) pp. 23–64.

[61] R.-E. Keck, R. Mikkelsen, N. Troldborg, M. de Maré, and K. S. Hansen, *Synthetic atmospheric turbulence and wind shear in large eddy simulations of wind turbine wakes,* Wind Energy **17**, 1247 (2014), https://onlinelibrary.wiley.com/doi/pdf/10.1002/we.1631 .

[62] X. Wu, *Inflow Turbulence Generation Methods,* Annual Review of Fluid Mechanics **49**, 23 (2017).

Photo by Mehtab A. Khan,
Colorado, USA

3

A Systematic Simulation Procedure

for Linearly Stratified Conditions

*Part **I** of this thesis focused on the significance of wind-farm-induced gravity waves for wind-farm–atmosphere interactions and the need for their systematic investigation. LES was identified as a powerful means for studying wind-farm-induced atmospheric gravity waves. However, LES comes with the challenge of handling spurious reflections of these waves from domain boundaries. Typically, approaches that employ radiation boundary conditions and forcing zones are used to avoid these reflections. However, the simulation setup of these approaches relies heavily on ad hoc tuning of some of their parameters. This chapter aims to provide more systematic guidance on setting up realistic simulations of atmospheric gravity waves employing the widely used Rayleigh damping method. To this end, the LES studies of flow over a 2-D hill and through a wind farm canopy are presented. This study explores the optimum domain size and damping layer setup depending on the fundamental parameters that determine the flow characteristics.*

The chapter is presented as follows: Section 3.1 gives the context, goal, and scope of this chapter. Section 3.2 presents an overview of current approaches to avoid AGW reflection at domain boundaries and highlights why it is so challenging to obtain a good simulation setup for inflow-outflow type of simulations. Next, Section 3.3 describes the flow scenarios studied. In Section 3.4, the simulation methodology and the methods to analyze the LES data are explained. Section 3.5 presents the results for the hill and wind farm canopy scenario. In Section 3.6, the conclusions of this chapter are presented as recommendations on how to efficiently set up simulations involving internal gravity waves.

This chapter is published in Wind Energy Science, **Investigating the relationship between simulation parameters and flow variables in simulating atmospheric gravity waves for wind energy applications**, M. A. Khan, D. Allaerts, S. J. Watson, and M. J. Churchfield (2024) [1].

3.1. INTRODUCTION

The size of a modern wind farm, especially offshore, can extend several tens of kilometers horizontally, involving flow interactions on a regional scale with impacts well into the free atmosphere. The energy and momentum extraction caused by a large wind farm is significant enough to decelerate the flow in the atmospheric boundary layer (ABL) [2–4], which slowly recovers because of turbulent momentum transfer and the interplay of the large-scale driving pressure gradient and the Coriolis force. This is evident from the consolidated wake of a large wind farm, which extends far beyond the wind farm in the streamwise direction. Researchers frequently study the behavior of a wind farm within the ABL only and do not consider the free atmosphere above. However, a full understanding of large wind farm behavior requires an understanding of the farm's effect on the free atmosphere and vice versa.

The temperature stratification of both the ABL and the free atmosphere is strongly connected to the flow dynamics of large wind farms. For instance, the thickness of the ABL can significantly decrease during stable atmospheric conditions, which will affect the flow at turbine level in a variety of ways. In offshore environments in particular, the height of the capping inversion (the relatively thin strongly stable layer that often forms between the top of the ABL and the free atmosphere) can drop to a few hundred meters at night. In such conditions, wind farms can induce atmospheric gravity waves (AGWs), which include trapped gravity waves (TGWs) in the capping inversion and internal gravity waves (IGWs) in the free atmosphere aloft. wind-farm-induced AGWs were first hypothesized by Smith [4], who treated wind farms as semi-permeable obstacles that can deflect the flow upwards to displace the capping inversion, resulting in these buoyancy-driven waves.

Numerical flow simulation, particularly large-eddy simulation (LES), is a useful tool to study AGWs. Gravity waves induced by large wind farms were first investigated with LES by Allaerts and Meyers [5]. Since then, wind-farm-induced gravity waves have been studied using LES by Allaerts and Meyers [5, 6], Allaerts *et al.* [7], and Lanzilao and Meyers [8, 9], all of which used pseudo-spectral methods with a forcing fringe region to circumvent the horizontal periodicity that is inherent in the pseudo-spectral approach. Stipa *et al.* [10] and Maas [11] have also studied wind-farm-induced gravity wave effects using simulations with Finite Volume methods, where the former used periodic and the latter used inflow and outflow boundary conditions.

The goal of this study, of which this chapter is the first part, is to make the process more systematic by investigating possible relations between the simulation setup and the physical parameters driving the flow through wind farms under stable atmospheric conditions. We anticipate that appropriate simulation parameters like domain length and height, etc., are related to internal wave properties such as wavelength and direction. We therefore investigate the proper scaling of simulation parameters and their effectiveness in avoiding wave reflections for a range of physical parameters. Understanding the relation between the physical parameters, the internal wave properties, and the simulation setup, enables recommendations to be made on how to set up simulations involving internal atmospheric gravity waves.

As this is, to our knowledge, the first systematic LES study to investigate the relation between simulation setup and physical parameters, we start by only studying internal

gravity waves in the free atmosphere for reasons of simplicity. Investigating the free atmosphere separately is vital to handling the reflections, as IGWs propagate both horizontally and vertically and hence can reflect off all domain boundaries. To this end, we consider two linearly stratified flow scenarios: the flow over a bell-shaped 2D hill, and the flow through a wind farm canopy as a simpler surrogate for a wind farm consisting of discrete turbines. The former flow scenario can be solved analytically and is used mainly to validate the simulations and to understand the dependence of AGW properties on the governing flow parameters.

3.2. CURRENT PRACTICES TO AVOID SPURIOUS AGWS

Two main methods exist to mitigate spurious interactions of an AGW with the computational domain boundary: radiative boundary conditions and damping layers. Radiative boundary conditions often take the form

$$\frac{\partial \phi}{\partial t} + c_j \frac{\partial \phi}{\partial n_j} = 0 \tag{3.1}$$

where ϕ is the quantity being transported through a boundary over time t, n_j is the displacement in the direction j normal to the boundary, and c_j is the wave transport velocity in the normal direction. One way to imagine this boundary condition is that the transported quantity ϕ is set to be exactly the same value as that imparted by the wave as it propagates to the boundary, thus absorbing the wave. One major difficulty is accurately determining c_j. This is often only possible in idealized situations. The radiative boundary condition is capable of allowing wave energy out of the domain only if the waves are moving perfectly normal to the boundary [12]. However, internal gravity waves are typically moving at an angle relative to the horizontal plane.

A popular alternative to the radiative boundary condition is a damping layer. Damping layers, sometimes referred to as "sponge zones", attenuate waves as the wave moves through the zone. These zones are placed adjacent to domain boundaries and have a prescribed thickness. A downside to using such zones is that, because they have thickness, the domain size needs to be increased accordingly, which adds some extra computational cost. Typically, damping layers are either of the viscous type or of the relaxation type, with the latter also known as Rayleigh damping layers (RDLs). RDLs are more commonly used than viscous damping and are considered more effective than the latter. For example, a recent study by Lanzilao and Meyers [9] found that RDLs outperform radiative boundary conditions in minimizing AGW reflections in wind farm simulations. For this reason, we focus on the application of RDLs in this study.

In principle, the quantity of interest passing through an RDL, usually velocity but also sometimes temperature, is relaxed towards a prescribed reference value with a specified time scale as the wave travels through the RDL, reflects off the boundary, and travels back through the RDL once again. Rayleigh damping is introduced into the transport equations as a forcing term which, for the case that the quantity to be damped is a three-dimensional field $\phi(\mathbf{x})$, takes the form

$$f^{RDL}(\mathbf{x}) = -\frac{1}{\tau} f(\mathbf{x}) \cdot (\phi(\mathbf{x}) - \phi_{\text{ref}}(\mathbf{x})) \tag{3.2}$$

where $\phi_{\text{ref}}(\mathbf{x})$ is the reference value towards which the quantity of interest in a parcel of fluid is driven along a streamline. For example, where the velocity field is required to be damped then $\phi(\mathbf{x}) = u(\mathbf{x})$, and $\phi_{\text{ref}}(\mathbf{x}) = u_{\text{ref}}(\mathbf{x})$. In this case, $u_{\text{ref}}(\mathbf{x})$ could be defined as $[G_x, G_y, 0]$ where G is the geostrophic wind vector. Sometimes the situation is ageostrophic, and a reference horizontal velocity is not appropriate, in which case only the vertical (z) component of velocity is damped towards zero. The Rayleigh damping function, $f(\mathbf{x})$, is a critical part of an RDL that ensures that the wave gradually dissipates energy as it travels through the layer and that the attenuation does not cause waves to reflect from the interface between the non-damped and damped regions. The function $f(\mathbf{x})$ can be any shape like, a linear, exponential, polynomial, or cosine function. A cosine function is commonly used in the vertical, which, for the upper boundary, typically has the form [9]

$$f(z) = \left[1 - \cos\left(\frac{\pi}{s_{\text{ra}}} \frac{z - (L_{\text{z}} - L_{\text{d}})}{L_{\text{d}}}\right)\right] \tag{3.3}$$

where z is height above the ground, L_{z} is the height of the computational domain, L_{d} is the thickness of the damping layer, and s_{ra} is a constant which controls the gradient of the damping function in the vertical. This was tuned by [9] and the best results were obtained for a value of s_{ra}=2. Although this suggests some dependency of wave damping on the shape of the damping function, Perić [13] found that the form of the damping function had little impact while investigating different approaches to damping internal waves.

The time scale, τ, or damping coefficient, controls how fast the quantity is relaxed toward a reference value. In Lanzilao and Meyers [9], τ is scaled with the Brunt-Väisälä frequency (N) in pursuit of the optimal value for wind-farm simulations, suggesting an optimum value of $\xi = 1/(\tau N)$ of three, with s_{ra}=2, as mentioned above. By contrast, Allaerts [14], tuned the RDL damping coefficient and found an optimum value of $1/\tau = 0.0001\ \text{s}^{-1}$, translating into a typical value of $\xi = 0.017$, though it should be noted that this was for a value of s_{ra}=1; the same value of ξ was used in a number of later studies including [5–7].

The damping layer thickness is an important parameter as it determines the space available for the forcing to dissipate the incoming wave energy. Klemp and Lilly [15] suggested the thickness to be more than one vertical wavelength based on hydrostatic flow solutions of a single Fourier mode. More recent studies also follow this convention without any further investigation. [5, 6, 8, 9] use a 15 km thick RDL only at the top boundary as the vertical wavelengths in their simulations were always less than 15 km.

As mentioned above, many of the existing LES studies on wind-farm interactions with the ABL are performed with methods that are horizontally pseudo-spectral. Pseudo-spectral flow solvers have the advantage of nearly exponential error convergence with increasing spatial resolution, but they come with the limitation that all lateral domain boundaries must be periodic. This poses a challenge for wind-farm simulations because we wish to advect the turbulent ABL flow into the domain and allow that flow along with that produced by the wind turbine wakes to exit the domain. Periodic boundaries normally would cause the wake flow exiting the domain to re-enter at the inflow. The solution to this problem is the introduction of a forcing fringe region adjacent to the downstream boundary which forces the 'contaminated' inflow back toward the pre-

computed or concurrently computed pure turbulent ABL inflow solution [16]. However, it is important to remember that pseudo-spectral flow solvers with their periodic streamwise boundary conditions effectively have no streamwise boundaries. RDLs only have to be applied adjacent to the top boundary. Furthermore, the forcing fringe region used to force the downstream flow back toward the desired inflow state is a form of Rayleigh damping. This means that AGWs will not reflect off the streamwise boundaries in pseudo-spectral LES, rather they will simply exit the domain on one side and re-enter at the inflow. The forcing fringe region will have some effect on damping the streamwise progression of the AGWs or may trigger spurious gravity waves, requiring an additional treatment [8].

As opposed to pseudo-spectral simulations, simulations with inflow-outflow boundary conditions, which are more commonly used in engineering applications, do not have streamwise periodicity and hence do not need a forcing fringe region. Inflow is simply injected into the domain on the inflow boundary with a Dirichlet condition and the outflow boundary is often a Neumann or advection boundary condition that lets the waked flow exit the domain. There is no need for a fringe zone that forces the waked outflow back to the desired clean inflow. On the downside, this approach requires real lateral boundary conditions that gravity waves will either reflect off or spuriously interact with. Therefore, RDLs must be placed adjacent to these boundaries as well as adjacent to the top boundary. Very little guidance is given in the literature on how to effectively simulate gravity waves using inflow-outflow boundaries. Maas [11] used inflow-outflow boundary conditions for their large wind farm LES, but the approach is complicated when modelling AGWs. Any inconsistency between the inflow and the internal flow field, triggers non-physical waves at the inlet which propagate into the domain over time. Besides the generation of spurious waves due to these mismatches, avoiding gravity wave reflections from the domain boundaries is a significant challenge. Reflections are the spurious waves that are triggered by having a boundary that is not there in real but required in these simulations. As shown in Fig. 3.1, the gravity waves triggered by a small hill under linearly stratified conditions should move up and out of the numerical domain. But the reality of a finite domain with boundary conditions that do not exactly depict the actual physical conditions at the boundaries causes these waves to reflect. The non-dissipated wave energy accumulates at the boundaries and propagates back into the domain eventually making the solution non-physical.

The current approaches to setting up RDLs in wind farm simulations are rather ad hoc. Extensive fine-tuning of the damping parameters is required to set up a working simulation, which may be applicable only to a specific case [9, 14]. As a result, setting up reflection-free simulations is tedious, computationally expensive, and time-consuming. The aim of this chapter is to investigate how to make the process less ad hoc by investigating relationships between the simulation setup and the fundamental physical parameters driving wind farm flow under stable atmospheric conditions.

3.3. FLOW SCENARIOS

In this study, we consider two simple, two-dimensional flow scenarios that generate internal gravity waves: the flow over a bell-shaped hill, and the flow through a wind farm canopy. Our initial focus lies on the hill case, which is used in various meteorology and

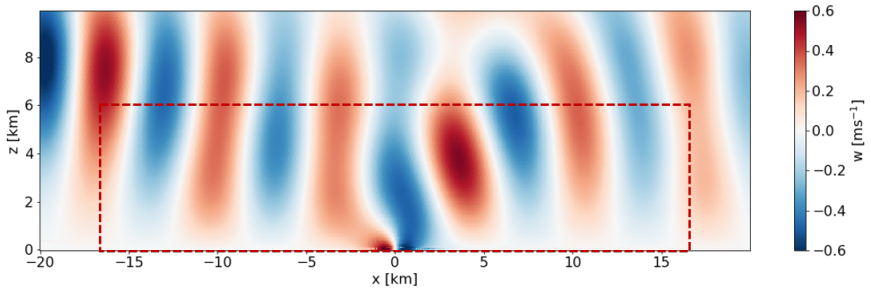

Figure 3.1: Vertical velocity contours of the flow over a small hill located at x = 0 km, produced by simulating a bell-shaped hill under linearly stratified laminar conditions in SOWFA. The region outside the red dotted box consists of Rayleigh damping layers at the inlet (left), top, and outlet (right).

earth sciences studies, such as [17] and [18]. The reasons to start with the hill case include the simplicity of the flow scenario, computational affordability, and the availability of a semi-analytical solution, which is useful for validation purposes. Moreover, the primary aim of this study is how best to handle atmospheric gravity waves in numerical simulations, and the wave source is thereby of less importance. Nevertheless, the simulated hill heights are similar to typical wind turbine rotor tip heights, and the half-width of the hill is of the same order as typical wind farm lengths. In the second flow case, we study the flow through wind farm canopies to extend the findings from the hill case to wind farm applications. Unlike the rigid hill, a wind farm canopy is a porous region in which the drag force of the wind turbines is applied homogeneously. The details of both flow scenarios are discussed in more detail in the following subsections.

3.3.1. SCENARIO 1: BELL-SHAPED HILL

The first flow scenario considers flow over a 2D bell-shaped hill. The height profile h of a bell-shaped hill – sometimes referred to as the Witch of Agnesi (WOA) profile – is defined in the horizontal direction x as

$$h(x) = \frac{H}{1 + (x/L)^2}. \tag{3.4}$$

This profile is governed by two parameters, i.e., the maximum hill height H and the half-width at half-height L.

To allow a direct comparison between an LES and a linear gravity wave potential flow solution, surface friction and the Coriolis force were excluded, and only a linearly stratified free atmosphere was considered with uniform inflow. Although the inflow was laminar, the LES model could still generate turbulence due to flow separation behind the hill.

A computationally inexpensive semi-analytical flow solution over the hill was used to understand the properties of the IGWs and validate the numerical solutions. We use the analytical solution along with the R-RMSE metric (discussed in Section 3.4.3) to quantify reflections in the simulations. The following subsection gives an overview of this semi-analytical solution and how it is used in this study.

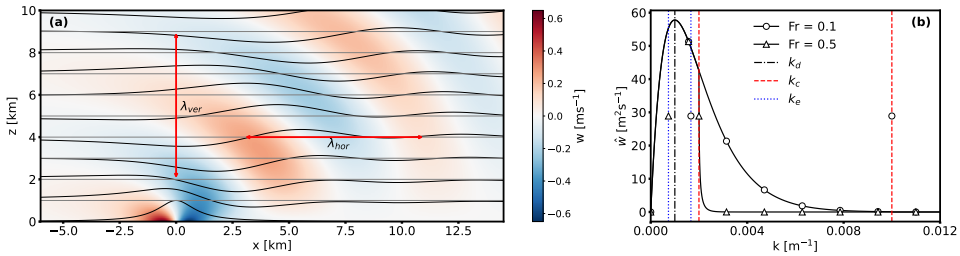

Figure 3.2: (a) Steady-state analytical solution of flow over a WOA hill centered at $x = 0km$. The color contours represent vertical velocity, and the streamlines from the displacement field show the wave propagation. (b) The streamwise wave spectrum for vertical velocity at a height, where critical, dominant, and effective wavenumbers are identified for $Fr = 0.1$ and 0.5. Figure created with LBoW [19].

3

SEMI-ANALYTICAL SOLUTION

Linear wave theory, particularly the Taylor-Goldstein equations, is commonly used to study atmospheric gravity waves. Allaerts [19] used these equations to develop a Python module called Linear Buoyancy Wave Package (LBoW) to solve linear buoyancy wave problems. In this research, we use a part of this code that computes a semi-analytical steady-state solution of the uniform, stratified flow over the WOA hill. The code solves the equations on a grid in frequency space using a Fast Fourier Transform (FFT). The solution is independent of the grid size in the vertical direction but not in the horizontal. A solution at any vertical level can be acquired without requiring a prior solution at lower and higher levels. The grid resolution in the horizontal direction dictates the solution accuracy. The FFT solution deviates from a theoretical Fourier transform of the bell-shaped hill for high horizontal wave numbers due to rounding errors. Mesh size in the range of 20 m to 100 m is recommended to compute the semi-analytical solution.

The steady-state, semi-analytical solution of uniform flow over the hill in a stably stratified free atmosphere with a uniformly increasing potential temperature with height is shown in Fig. 3.2(a) , where the upward flow deflection by the hill triggers only IGWs. The vertical velocity contour and streamlines of the displacement field clearly show the propagation of gravity waves in the vertical direction. The gravity waves transport energy mainly upward from their source, the hill or a wind farm, but some wave amplitude decays with height. At the same time, the waves are also blown downstream. The combined effect is a decrease in the amplitude of some parts of the wave with height and downstream distance. The properties of IGWs depend on the wind speed U, hill half-width at half-height L, hill maximum height H and Brunt-Väisälä frequency $N = \sqrt{(g/\theta)(\frac{d\theta}{dz})}$, where g is acceleration due to gravity and θ is the potential temperature at height z. Employing similarity theory, we normalize these variables to get two physical parameters, the Froude Number (Fr) and the Slope Parameter (S_h), where $Fr = U/NL$ and $S_h = H/L$. Thus, the wave properties depend mainly on the free-atmosphere Froude number and the Slope Parameter.

It is important to understand that the wave train seen in Fig. 3.2(a) is not monochromatic but is actually a wave spectrum, which is given by the following expression:

$$\hat{w}(k,z) = \pi HL\, iUk\, e^{-|k|L} e^{imz} \tag{3.5}$$

with

$$m(k) = \begin{cases} \mathrm{sgn}(k)\sqrt{k_c^2 - k^2} & \text{for } |k| < k_c\,, \\ i\sqrt{k^2 - k_c^2} & \text{for } |k| > k_c\,, \end{cases} \tag{3.6}$$

where k and $k_c = N/U$ are horizontal and critical wavenumbers, respectively. The *sgn* in Eq. 3.6 suggests using the actual value, positive or negative, acquired from the square root in the expression as Eq. 3.5 includes imaginary numbers. The spectrum for a specific height is shown in Fig. 3.2(b) together with the three important length scales corresponding to the dominant ($k_d = 1/L$), critical (k_c), and effective ($k_e = 1/\lambda_{hor}$) wavenumbers. Thus, there are three important wavelengths to consider:

1. The wavelength with the highest amplitude is the *dominant* wavelength, $\lambda_L = 2\pi L$, which depends on the hill width.

2. However, the dominant wavelength for the bell-shaped hill, is not necessarily the wavelength that is most visually apparent in contour plots. For example, the most apparent wavelength, which is termed the *effective* wavelength, is shown in Fig. 3.2(a) with a red horizontal arrow and labeled λ_{hor} .

3. Lastly, there is a *critical* wavelength (often we consider its reciprocal, the *critical* wavenumber). For wavelengths smaller (or wavenumbers larger) than the critical one, the waves cannot be supported by buoyancy so they dissipate and are called "evanescent" waves.

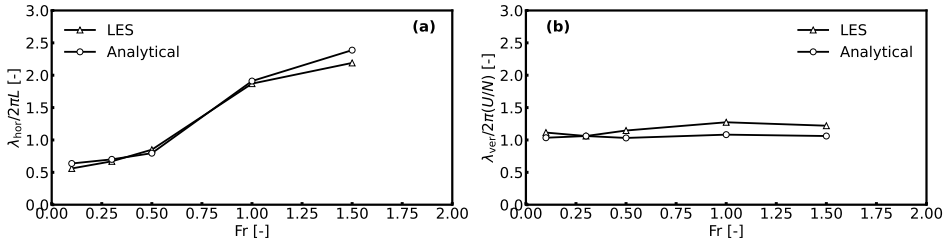

Figure 3.3: The variation of effective (a) horizontal and (b) vertical wavelengths with Fr.

Although the analytical solution tells us that wave amplitude depends more on the hill slope, particularly the height, the effective wavelengths and the inclination angles of the IGWs depend on Fr. The IGWs naturally tend to travel vertically, but the background flow forces them to bend. Since zero advection speed is impossible, these waves would always travel inclined. For Fr in the range of 0.1 to 1.5, the inclination angle to the streamwise direction, estimated from the vertical velocity field, is in the range $75-53°$, respectively. The effective horizontal wavelength, (λ_{hor}) is sensitive to the hill width for low Fr, but for $Fr > 0.5$, it depends more on the Scorer parameter (N/U), which is the reciprocal of the buoyancy length. This can be seen in Fig. 3.3(a), where the normalized

λ_{hor}, calculated from the semi-analytical solution and LES, is plotted against Fr. We measure λ_{hor} as twice the distance between the global maxima and minima determined from a vertical velocity plot at a constant height along the domain length. We see that as Fr is increased, λ_{hor} increases, but it is not a linear relation.

Although we visually identify with the effective wavelength of AGWs when we view figures like Figure 3.2(a), those AGWs are really a spectrum of waves. Based on the spectrum and wavenumbers shown in Figure 3.2(b), the situation can be classified into two different conditions:

1. When the critical wavenumber is greater than k_d or when $Fr < 0.5$, the dominant wavelength is greater than λ_{hor}. In this situation, λ_{hor} depends more on the hill half-width than the Scorer parameter, and the entire wave spectrum is preserved and the waves propagate.

2. On the other hand, when $Fr > 0.5$, the critical wave number is closer to k_d; thus, a part of the spectrum becomes evanescent, and wave numbers greater than k_c are dissipated. In this case, the dominant wavelength is less than λ_{hor}, which depends more on the Scorer parameter.

The effective vertical wavelength (λ_{ver}), shown as the red vertical arrow in Fig. 3.2(a), depends only on the Scorer parameter, which is proportional to the vertical wave number. This is evident from Fig. 3.3(b), where λ_{ver} normalized with the maximum vertical wavelength, $2\pi(U/N)$, is shown as a function of Fr. The constant $\lambda_{ver}/2\pi(U/N)$ for varying Fr indicates that λ_{ver} does not depend on L and is usually representative of the maximum vertical wavelength. λ_{ver} is measured as twice the distance between the global maxima and minima determined from a vertical velocity plot along the domain height at the x-location corresponding to H. The locations of global extrema are extracted from the vertical velocity on the physical coordinates such that grid stretching does not affect λ_{ver}. It is also important to note that the IGWs curve downstream of the hill; thus, λ_{ver} slightly varies at different streamwise locations for values of $Fr > 0.5$ as seen in Fig. 3.3(b). Therefore, the maximum vertical wavelength is better suited to scaling in the vertical direction, especially since it is almost equal to λ_{ver}.

Hence, it can be seen that the effective horizontal and vertical wavelengths can be greater than the dominant length scales, i.e., the hill width and height; thus, domains scaled with the hill width and height might be inappropriate for the accurate simulation of gravity waves.

This study focuses only on the Froude number as it concerns gravity wave properties that are critical to the simulation setup. The slope parameter is less critical for this research and the slope of the hill (S_h) is kept the same. With different hill shapes, the amplitude and wave spectrum would change, making comparisons between simulations with different hill shapes inconsistent. In addition, we only consider the steady-state solution.

3.3.2. SCENARIO 2: WIND FARM CANOPY

Wind farm flow interactions with the atmosphere involve a wide range of length scales. When focusing on wind-farm-induced IGWs, large length scales are important as the

expected IGW wavelengths are on the scale of the wind farm length which can be several kilometers. Since the intra-farm (turbine wake) interactions is not the focus of this study, wind farm canopies are a convenient way to model wind farms without the complexity of modelling individual wind turbines. The concept of a wind farm canopy was introduced by [20] through an analytical model to represent large wind farms in weather prediction models. In our work, we use a similar approach to simulate the cumulative drag force of a wind farm consisting of a number of wind turbines of a given type.

The standard coefficient of thrust associated with a wind turbine rotor is

$$C_t = \frac{\mathbf{T}}{\frac{1}{2}\rho \mathbf{U}^2 A_r} = \frac{\mathbf{T}}{\frac{1}{2}\rho \mathbf{U}^2 \pi \frac{D_r^2}{4}}, \tag{3.7}$$

where A_r is the rotor swept area, D_r is turbine rotor diameter, ρ is the density of air, T is dimensional rotor thrust force, and U is the free-stream velocity. Because we are distributing the force of the rotors in the wind farm over the volume occupied by the wind farm, it is better to define a thrust coefficient based on the area of the farm belonging to this rotor (i.e., the entire footprint area considering turbine spacing allocated to this wind turbine). This area is $A_f = (S_x D_r)(S_y D_r) = S_x S_y D_r^2$ where S_x and S_y are the turbine spacings in the two horizontal directions within the farm. This new thrust coefficient is

$$c_t = \frac{\mathbf{T}}{\frac{1}{2}\rho \mathbf{U}^2 S_x S_y D_r^2}. \tag{3.8}$$

The two thrust coefficients are related to each other through

$$c_t = \frac{\pi}{4 S_x S_y} C_t. \tag{3.9}$$

Defining dimensional thrust based on c_t, we have

$$\mathbf{T} = \frac{1}{2}\rho \mathbf{T}^2 S_x S_y D_r^2 c_t, \tag{3.10}$$

and normalizing dimensional thrust by volume of the farm occupied by a turbine, $V_f = S_x S_y D_r^2 (H_t - H_b)$, where H_t and H_b are the height of the top and bottom of the turbine rotor and also the height of the top and bottom of the wind-farm canopy, we have

$$f_{wf} = \frac{\mathbf{T}}{V_f} = \frac{1}{2}\frac{\rho \mathbf{U}^2 S_x S_y D_r^2}{S_x S_y D_r^2 (H_t - H_b)} c_t = \frac{1}{2}\frac{\rho \mathbf{U}^2}{(H_t - H_b)} c_t = \frac{1}{8}\frac{\rho \mathbf{U}^2 \pi}{S_x S_y (H_t - H_b)} C_t. \tag{3.11}$$

It is this thrust per unit volume that is applied to the momentum equations as a source term within the wind turbine canopy volume. The wind speed, U, is determined locally at each cell centers within the canopy.

3.4. METHODS

3.4.1. SIMULATION PARAMETERS AND SETUP

A set of non-dimensional parameters govern the flow over terrain and through wind farms under linearly stratified atmospheric conditions. These parameters can be determined by normalizing the flow equations or performing dimensional analysis of a

Table 3.1: Key variables in the simulation of atmospheric gravity waves under linearly stratified free atmospheric conditions with typical ranges in wind energy applications.

Variable	Variable Type	Range
Velocity (U)	Flow	1 ms^{-1}–25 ms^{-1}
Brunt-Väisälä frequency (N)	Flow	0.005 s^{-1}–0.02 s^{-1}
Half-Width of Hill or Canopy Length (L)	Shape	1 km–15 km
Hill or Canopy Height (H)	Shape	16 m–240 m
Domain Length (undamped) (X)	Simulation	0.5 km–200 km
Domain Height (undamped) (L_z)	Simulation	0.3 km–40 km
Damping thickness (L_d)	Damping characteristic	0.3 km–45 km
Damping coefficient ($1/\tau$)	Damping characteristic	0.001 s^{-1}–0.5 s^{-1}

Table 3.2: Non-dimensional parameters derived from the variables in Table 3.1 with typical ranges.

Non-dimensional parameter	Definition	Range
Fr	U/NL	0.1–0.5
S_h	H/L	0.016–0.4
$\tilde{X}$	X/λ_{hor}	0.5–6.0
$\tilde{L}_z$	L_z/λ_{ver}	0.3–2.0
$\tilde{L}_d$	L_d/λ_{ver}	0.5–2.0
ξ	$1/(\tau N)$	1–50

number of key variables. These variables are detailed in Table 3.1 along with their practical values in wind energy applications. From these variables, the set of non-dimensional parameters in Table 3.2 can be defined. The first two are physical parameters, namely the Froude number and slope parameter, whilst the remainder are simulation parameters.

Appropriate choice of grid structure, resolution, and time step are important in the simulation of gravity waves, particularly for very low values of Fr, because the flow interactions can trigger subgrid-scale wavelengths. Likewise, the frequencies of some waves in the spectrum could be shorter than the simulation time steps, leading to an unresolved fraction of the spectrum. However, the relevant value of Fr for wind farm applications is approximately between 0.1 and 0.5 for which a grid independence study was carried out. It was found that grid resolutions, roughly 10 m in all directions, used in wind farm LES to resolve the wind turbines and their wakes, is more than sufficient to resolve the wind-farm-induced AGWs.

LES of flow over the WOA hill and through the wind farm canopy is carried out with Simulator for Wind Farm Applications (SOWFA) [21]. Based on OpenFOAM, this code is mainly used for the LES of atmospheric flows over terrain and through wind farms, where a one-equation model is commonly used for sub-grid-scale turbulence modelling. SOWFA has actuator models for wind turbine aerodynamics that can be coupled with aero-servo-elastic tools. Moreover, it can use boundary inflow data from mesoscale weather data, and terrain can be included through non-conformal meshes. The model set-up solves the incompressible Navier-Stokes equations under non-hydrostatic conditions and with

the Boussinesq approximation for buoyancy. Equations for continuity, momentum, and potential temperature are those typically used in the LES of atmospheric flows. A more complete description is given in [22]. For simulations with the wind farm canopy, the drag force of the wind farm is added to the momentum equation as a body force. Rayleigh damping is applied as a body force in the forcing zones through the momentum equation, details of which are given in the following subsection.

Figure 3.4 shows the numerical setup for the hill and wind farm canopy cases. The flow is driven in and out of the domain by inflow-outflow boundary conditions. Periodic boundary conditions are used in the transverse direction only. Because SOWFA's inflow and outflow boundary conditions and lower and upper impenetrable boundaries set the velocity flux locally over each boundary face, there is no need for pressure boundary conditions (keeping in mind that the pressure solve in an incompressible code enforces continuity). To simplify the set-up, wind shear is neglected and a uniform inflow is imposed as the inlet boundary condition for wind speed and the zeroGradient boundary condition is implemented at the outlet. In addition, free-slip boundary conditions are imposed at the top and bottom of the domain. The temperature profile is linear in the vertical direction, giving a constant Brunt-Väisälä frequency with height. There is no heat flux at the ground. Also Coriolis forces are not considered. These conditions are intended to mimic those of a stable free atmosphere without the ABL and capping inversion.

A surface profile for the WOA hill is created using a Python script and the computational mesh conforms to the hill. A mesh with layered refinement is used with 20 $m \times 20$ $m \times 20$ m resolution in the non-damped domain, and 40 $m \times 20$ $m \times 40$ m in the top damping layer. The first mesh layer near the surface ends in the top damping layer to ensure any numerical noise for switching to a coarser mesh is damped. The domain for all cases is 100 m in the y direction, whereas the x and z extents are varied as a function of the effective horizontal and vertical wavelengths, respectively, as the domain length and height are critical simulation variables when simulating gravity waves. The exact domain length and height used for each simulation are reported while discussing the results. Both the hill and wind farm canopy are extended in the transverse direction to the sides of the domain, effectively creating an infinite ridge and a semi-infinite wind farm, respectively, as we are primarily interested in vertical and streamwise flow.

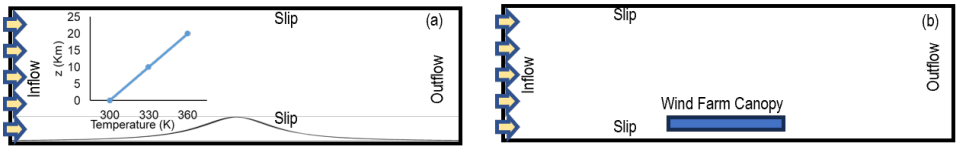

Figure 3.4: Lateral view of the simulation setup: (a) with a schematic WOA hill profile and (b) with a schematic wind farm canopy.

The guidelines to systematically model AGWs can be established based on the hill-scenario, however, the characteristics of the AGWs may vary for a porous wind farm canopy as opposed to a solid hill. Therefore, wind farm canopies are simulated to extend the findings from the hill-scenario to the wind farms. This approach reduces computa-

tional resources, which is desirable as hundreds of cases are run to evaluate the extent of wave reflections. The wind farm canopy model can be used with relatively coarse grids compared to conventional actuator models that resolve the wind turbines to a given extent. The numerical setup with the wind farm canopy is the same as that of the WOA hill, except that the hill is replaced with wind farm drag as a body force.

3.4.2. RAYLEIGH DAMPING

RDLs are implemented as zones adjacent to the reflective boundaries in the simulation domain and far from the region of interest, such as a wind farm. It is critical to note that RDLs are always implemented in the free atmosphere because it is the gravity waves in the free atmosphere that reflect from the boundaries. The primary role of an RDL is to dissipate the energy propagated through the zone by AGWs. In this study, only the vertical velocity is damped unless mentioned otherwise, as the prominent perturbation is the vertically deflected velocity by the hill or the wind farm canopy. If periodic streamwise boundary conditions are used, an RDL is implemented at the top boundary only with an RDL-like fringe region at the outlet where flow is recycled to the inlet. However, in a simulation setup with inflow-outflow boundary conditions, RDLs may be required at various boundaries. The RDL at the inlet will filter any incoming turbulence. Generally, damping incoming turbulence into the boundary layer is undesirable in wind farm simulations; however, in this study, for simplicity, we have neglected inflow turbulence. This should not impact the aim of the study which is to minimise gravity wave reflections efficiently.

3.4.3. QUANTIFYING REFLECTIONS

Reflectivity is quantified by the method proposed by Allaerts and Meyers [5], which is a modification of the procedure initially given by Taylor and Sarkar [23]. The reflection coefficient (Cr) is one of the two primary tools used here to analyze the simulation data, and its calculation can be summarised in the following two steps. First, the vertical velocity values on a vertical streamwise plane are converted to horizontal and vertical wave number space (K_s and M_s, respectively) through a 2D Fourier transform. The wave number coordinates centered at 0 are similar to the physical coordinates where K_s and M_s are on the horizontal and vertical axis, respectively. The upward and downward moving waves are separated based on the quadrants they fall into. The upward propagating waves are in the first and third quadrants, whereas the downward propagating are in the second and fourth quadrants on the K_s and M_s coordinates. Thus, only the Fourier coefficients in quadrants I (i.e., $K_s, M_s > 0$) and III (i.e., $K_s, M_s < 0$) are retained for upward waves, and those in the other two quadrants are set to zero. Likewise, quadrants II (i.e., $K_s < 0, M_s > 0$) and IV (i.e., $K_s > 0, M_s < 0$) are retained for the downward waves. The filtered coefficients are inverse-transformed to obtain the respective velocity fields, as shown in Fig. 3.5. The tilted phase fronts on these contours clearly show (a) the initial upward, and (b) the much weaker reflected downward propagating waves. Wave energy propagates normal to the phase fronts and is calculated from these decomposed vertical velocity fields. Finally, the reflection coefficient is estimated by taking the ratio of total downward to upward propagating energy. This Cr metric sometimes gives inconsistent values, especially for low Fr and L, possibly because the spectrum includes

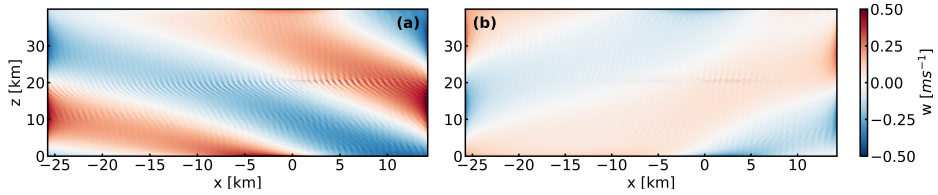

Figure 3.5: Decomposed vertical velocity fields for a WOA hill simulation showing: (a) upward and (b) downward propagating internal waves.

a large fraction of high-frequency waves. Therefore, visual inspection of the simulation fields, especially the vertical velocity, is critical to ensure the value predicted is realistic; improving or replacing this metric is future work.

In the case of the hill, the numerical solution can be compared to the semi-analytical solution using the Relative-Root Mean Square Error (R-RMSE) metric. The difference between the vertical velocity (w) fields from the numerical and analytical solutions are normalized with the maximum w from the analytical solution, to determine the R-RMSE over a vertical plane in the streamwise direction. The vertical velocity is always taken at time t when $t = 300/N$, which is equivalent to 2.083, 4.167, or 8.33 hrs for $N = 0.02,\ 0.01$ or 0.005 s^{-1}, respectively. As the R-RMSE metric depends on the number of points sampled, we only calculated this for the same section of the domain, around the hill or canopy. This has the drawback of not capturing reflections close to the boundaries. However, the R-RMSE can be better than Cr in capturing localized spurious wave sources, like numerical noise at the interface of the damping layers with the non-damped domain. Due to the strengths and weaknesses of the two metrics, we analyzed the results of both, and generally, it is found that R-RMSE metric detects the same patterns seen in Cr. Therefore, only results in Cr will be reported in the paper to be consistent with the literature. In all cases, unless otherwise mentioned, the vertical velocity values are taken from a vertical plane at the mid-point of the domain. For reflection-free simulations, we consider the criterion Cr and R-RMSE < 10% should be met.

3.4.4. SIMULATION SETS

Simulations were run initially to acquire a base case and then use it to explore reflection dependency on the non-dimensional parameters defined in Table 3.2. Various combinations of damping layers with different combinations of characteristics were simulated to investigate the most appropriate configuration with minimum reflections. The details on the configurations explored are given in the Appendix A. Besides exploring the configuration of the damping layers, three simulation sets are defined as detailed in Table 3.3. These three simulation sets were repeated for the wind farm canopy.

- The first set of simulations investigates the impact of damping characteristics on reflections and their optimal values for a range of Fr. Set 1(a) explores the extent of reflections when varying the damping coefficient for a range of Fr values, i.e., 0.1 to 1.5, where Fr was adjusted by changing U and L. In Set 1(b), the damping coefficient and thickness were changed when setting Fr= 0.1 and 0.5, where Fr was adjusted by changing either N and U, or U, N, and L, ensuring dynamically

Table 3.3: Simulation sets.

Set	Parameters Investigated		Variables Changed		N.O of Cases
	Physical	Simulation	Physical	Simulation	
1(a)	Fr [0.1, 0.3, 0.5, 1.0, 1.5]	ξ, $\tilde{L}_d$	U, L	$1/\tau$	25
1(b)	Fr [0.1, 0.5]	ξ, $\tilde{L}_d$	U, N, L	$1/\tau$, L_d	120
2	Fr [0.1, 0.5]	$\tilde{X}$	Fr	X	20
3	Fr [0.1, 0.5]	$\tilde{L}_z$	Fr	L_z	12

similar solutions.

- Set 2 explores the impact of the domain length on wave reflections. In this case, the domain length was varied for two values of Fr.
- Set 3 investigates the impact of domain height on wave reflections. In this case, for two values of Fr, the domain height was varied in proportion to the expected (λ_{ver}).

3.5. RESULTS

3.5.1. SCENARIO 1: BELL-SHAPED HILL

This section first considers the optimum damping configuration for the hill case as a baseline before moving on to the wind farm canopy set-up.

CONFIGURING THE DAMPING LAYERS

Correctly setting up the size and location of the damping layers is important for the accurate and effective simulation of AGWs. Therefore, we test various configurations of the damping layers that give minimum reflections and use this as a base case for further investigation of the sensitivity to the non-dimensional parameters. As mentioned earlier, we require that both Cr and R-RMSE are less than 10% for the simulation to qualify as what we define as "reflection-free." Following a brief investigation of various combinations of damping layers, it was found that RDLs at the inlet, outlet, and top boundaries give minimum reflections and thus all subsequent simulations use this configuration as the base case.

DYNAMIC SIMILARITY

We started the analysis by testing whether the non-dimensional parameters discussed in Section 3.4.1 are sufficient to ensure dynamic similarity, i.e. the non-dimensional solution remains the same if the non-dimensional parameters are the same irrespective of the values of the variables defining them. The simulations performed had a setup with a damping layer thickness and domain height 1.5 times the effective vertical wavelength and a domain length five times the expected effective horizontal wavelength. Figure 3.6 shows the dependency of wave reflections on the non-dimensional damping parameter, ξ for changing buoyancy and hill half-widths (U/N and L), and buoyancy and advection

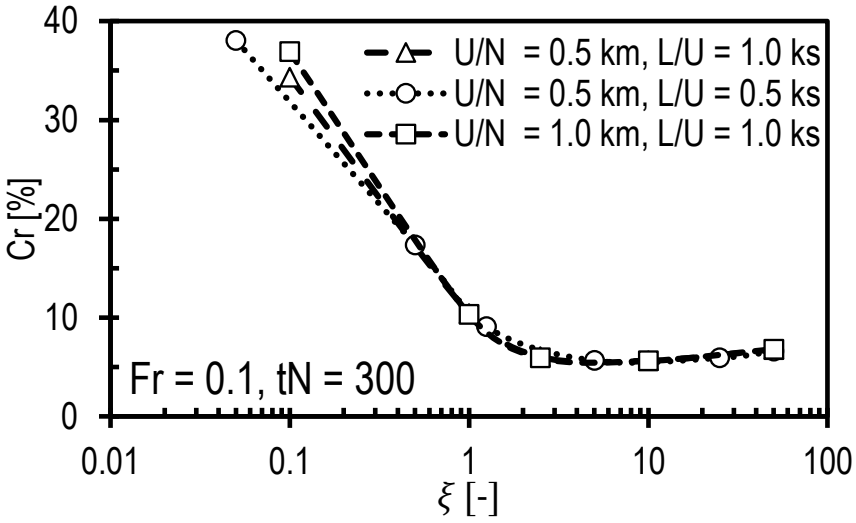

Figure 3.6: Reflection coefficient as a function of normalised damping coefficient ξ for varying length and time scales.

timescales ($1/N$ and L/U). In terms of minimising reflections, the plots indicate that a suitable range for ξ is between 1 to 10 when $Fr = 0.1$, and the buoyancy time scale is an appropriate scaling parameter for the damping coefficient. The plots further show that the results are independent of both the time and the length scales, because the solutions are dynamically similar. The buoyancy length was kept constant (i.e. $U/N = 0.5$ km) by changing the Brunt-Väisälä frequency and inflow velocity for a constant hill half-width (i.e. $L = 5$ km). Thus, the advection time scale was different for these two cases. Whereas, the buoyancy length was varied by adjusting the Brunt-Väisälä frequency and hill half-width to fix $Fr = 0.1$; the buoyancy time and physical length scales were varied. Thus, it is deduced that from the definition $Fr = U/NL$, L/U acts like N or free atmosphere's stability. This means that the stability of the free atmosphere is relative to the size of the disturbance source and the geostrophic wind. These three cases can be compared in different ways and it will establish dynamically similar solutions for all comparisons. Similar results are seen for $Fr = 0.5$, though these are not shown for clarity.

OPTIMAL DAMPING COEFFICIENT AS A FUNCTION OF FROUDE NUMBER

In general, very low damping coefficients lead to the highest reflections; however, very high damping coefficients, e.g. $\xi >> 10$, also enhance reflections as the IGWs reflect off the damping layer instead of the boundaries. These effects can be seen in Fig. 3.7. Strong reflections and energy accumulation can be seen visually in Fig. 3.7 (top) for $\xi = 0.1$, where they appear parallel to the inlet on the left and gradually contaminate the solution in the entire domain. Figure 3.7 (middle) shows vertical velocity contours when $\xi = 10$ that are least affected by reflections and energy accumulation at the inlet. Moreover, the gradual decay of IGWs with height inside the top RDL is evidence of suitable damping

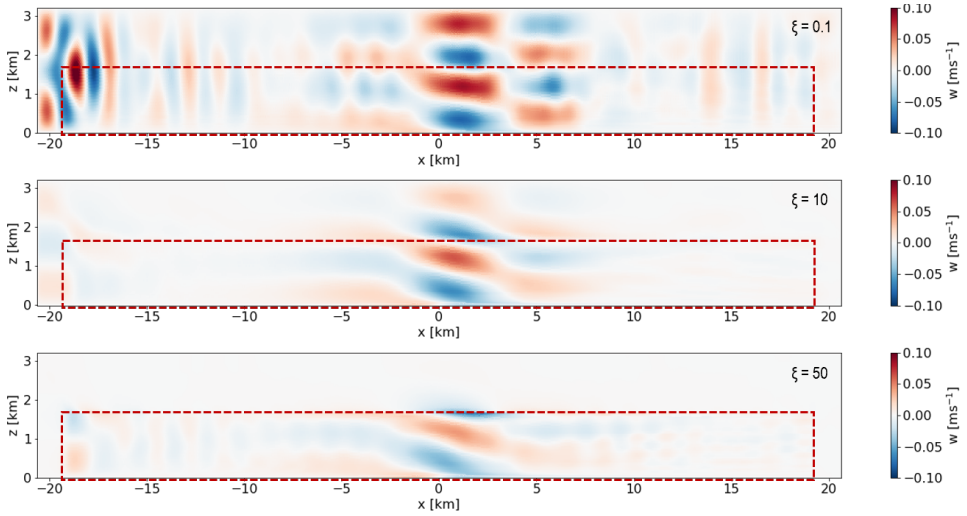

Figure 3.7: Contours of vertical velocity in a streamwise-oriented vertical plane at tN 300 for $Fr = 0.1$ with $\xi = 0.1$ (top), $\xi = 10$ (middle), and $\xi = 50$ (bottom). The red box shows the non-damped domain, and everything outside is the RDL.

characteristics. Whereas, Fig. 3.7 (bottom) shows vertical velocity contours when $\xi = 50$, where IGWs are abruptly attenuated right at the start of the top damping layer. Also accumulated waves appear at the end of inflow RDL as if it were a hard boundary.

It was shown in Section 3.5.1 that the optimal damping coefficient for $Fr = 0.1$ is around 10. However, Fig. 3.8 shows that for values of $Fr > 0.1$, the optimal damping coefficient is somewhat less with minimum reflections occurring for values of ξ between 2 and 10, although the sensitivity to ξ in this range is small. The adverse level of reflection for low and very high damping coefficients is also apparent from this plot. For $Fr = 0.1$ and 1.5, Cr cannot be made less than 10%, because the damping layer thickness is just one vertical wavelength which is insufficient for these very low and supercritical values of Fr, respectively. These simulations had damping layer thicknesses and domain heights equal to the effective vertical wavelength, and the domain length was twice the effective horizontal wavelength. Supercritical values of Fr ($Fr > 1$), a regime in which much of the wave content is evanescent, are less likely to occur for large wind farms, whereas low Fr values are very likely. For this reason, the following sections will restrict analysis to the expected upper and lower ranges of the Froude number for wind energy applications, i.e. $Fr = 0.1$ and 0.5.

IMPACT OF DAMPING LAYER THICKNESS ON REFLECTIONS

So far, we have considered the impact of ξ on the reflections while L_d is equal to or greater than the vertical wavelength. However, the impact of damping characteristics on reflections is coupled. A weak, thick damping layer may have the same impact as a strong, thin layer. Therefore, determining the coupled impact of the damping characteristics on reflections and the minimum damping thickness is desirable, as knowing the minimum effective damping layer thickness can help reduce the computational load.

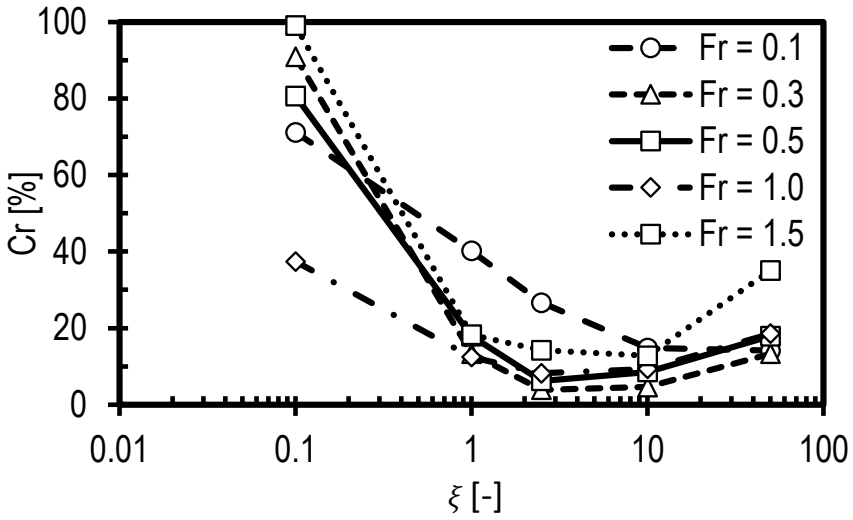

Figure 3.8: Reflection coefficient as a function of ξ for a range of Froude numbers.

The joint effect of different damping parameters is investigated for $Fr = 0.1$ and $Fr = 0.5$, where the damping thickness and coefficient are varied simultaneously. In general, thicker damping layers for all damping coefficient values should reduce reflections but thinner damping layers are desirable for low computational cost. Figure 3.9 shows that a damping layer set to the optimal damping coefficient and accommodating one effective vertical wavelength seems more effective than a thicker layer with a sub-optimal value of ξ. Figure 3.9(a) shows that Cr is minimum for all values of $\tilde{L}_d$ when ξ is 10. The non-monotonic nature of the plots in this figure indicate how optimizing the setup for a low value of Fr is more challenging. The exact reason for this non-monotonic behavior is hard to establish but it is most likely associated with the complicated wave properties for low values of Fr. For instance, wavelengths become shorter for low Fr. Thus, the resolved wave spectrum can vary significantly for even small changes in the domain size, which is linked with the amount of wave reflection. Furthermore, the waves are more aligned to the horizontal for a low value of Fr, complicating the interaction with the background advecting flow as the wave fronts are more directly aligned with the inlet wind flow than that of a higher Fr case. Moreover, the energy accumulation is higher for a low value of Fr as the wave speed is faster than the advection speed in turn causing more contamination of the solution. This also hints at inadequacy of the RDLs in terms of their ability to prevent energy accumulation at the inlet only delaying its propagation back into the domain.

Figure 3.9(b) shows monotonic reflection behavior for $Fr = 0.5$. It can be seen that a value of $\xi = 2.5$ provides an optimal solution when $\tilde{L}_d > 1.0$, and a value of $\xi = 10$ is best when $\tilde{L}_d < 1.0$. The damping layer thickness required when $Fr = 0.1$ is slightly bigger than that for $Fr = 0.5$ to limit the reflections to the same levels. This can be seen when comparing the optimal setups for $Fr = 0.1$ and $Fr = 0.5$, where Cr is limited to 5%

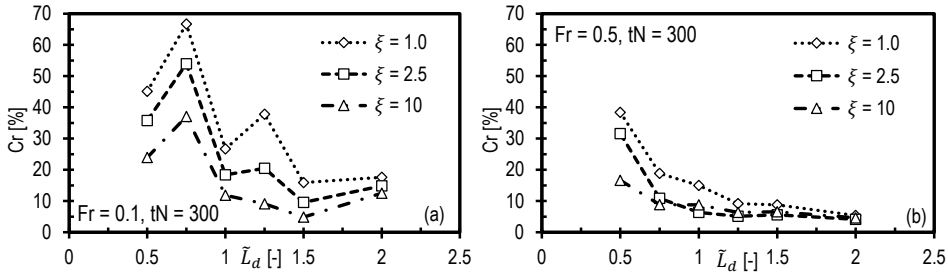

Figure 3.9: Reflection coefficient for the hill case as a function of normalised damping layer thickness for different values of the damping coefficient when (a) $Fr = 0.1$ and (b) $Fr = 0.5$.

whereby $\tilde{L}_d$ is 1.2 for $Fr = 0.5$ and $\tilde{L}_d$ is 1.5 for $Fr = 0.1$.

In summary, the damping layer thickness should be greater than one effective vertical wavelength to efficiently damp the IGWs. This aligns with the recommendation of [15] but is based on analyzing the entire wave spectrum instead of analyzing individual wave numbers, which was their approach.

DOMAIN LENGTH IMPACT ON REFLECTIONS

Intuitively, the location of the top boundary is more important than that of the other boundaries, as the gravity waves travel upwards, and reflections are mainly expected from the top boundary. However, the accumulation of energy at the inlet boundary, shown in Fig. 3.1 and Fig. 3.7, indicates the importance of appropriately positioning the inlet and outlet relative to the hill or wind farm (i.e. the zone of interest). One approach is to place boundaries far from the zone of interest to prevent spurious waves from affecting the flow around the zone of interest. This approach has two major flaws: it is costly in terms of computational resource for LES studies and simulations can run only for a limited time before the reflections reach the zone of interest. This constraint conflicts with the common practice in wind farm LES of simulating several domain flow-through times to obtain reliable statistics. Moreover, the contamination of the solution upstream of a wind farm may affect the inflow, and an unrealistic inflow to the wind farm would lead to an unreliable solution. Therefore, knowing the shortest possible domain length that ensures the least contaminated inflow approaching the zone of interest is important to produce accurate solutions and save computational resources and time. To this end, a set of simulations, denoted in Table 3.3 as Set 2, were performed for values of $Fr = 0.1$ and $Fr = 0.5$, where the domain length was varied between $0.5\lambda_{hor}$ and $4.0\lambda_{hor}$. Instead of simulating for several different values of the damping parameters, we used the results from Section 3.5.1 with $\xi = 10$ for $Fr = 0.1$ and $\xi = 2.5$ for $Fr = 0.5$. The value of $\tilde{L}_d$ was set to 1.5 for $Fr = 0.1$ and 1.2 for $Fr = 0.5$.

Figure 3.10(a) shows the impact of domain length on reflections. The reflection coefficient shows the same trend for $Fr = 0.1$ and $Fr = 0.5$. The domain length should be at least one effective horizontal wavelength, as Cr increases abruptly for shorter domains. We emphasize the discussion in Section 3.3.1 concerning the variation in effective horizontal wavelength with Fr. It was established that λ_{hor} depends on both L and U/N for $Fr < 0.5$ but predominantly on U/N for $Fr > 0.5$. In other words, the domain

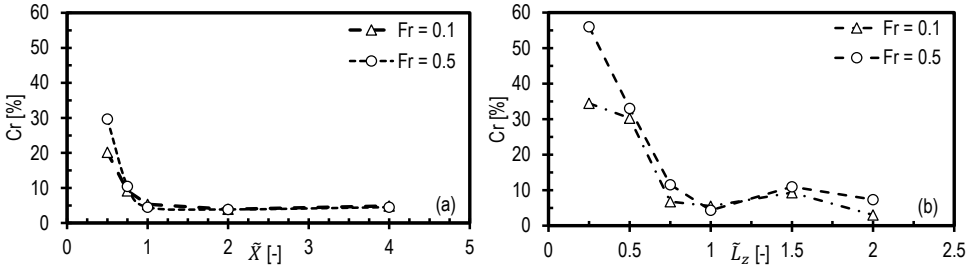

Figure 3.10: Reflection coefficient for the hill case as a function of: (a) domain length for $Fr = 0.1$ and $Fr = 0.5$; and (b) domain height for $Fr = 0.1$, $\tilde{L}_d = 1.5$ and $Fr = 0.5$, $\tilde{L}_d = 1.2$.

length should not be scaled with L. Instead, the expected effective horizontal wavelength should be calculated from linear theory, and this value should be used to set the domain length to accommodate at least one effective horizontal wavelength. It can be seen that domain lengths over λ_{hor} are unnecessary as Cr barely decreases for increasing domain length. The evolution of reflections in time is another critical aspect to highlight, as we observed increasing Cr values in time in all simulations. We run the simulations to a steady-state, which in general takes only a few flow-through times, and a domain length equal to λ_{hor} is sufficient for these short runs. For longer runs, like diurnal cycles, the wave energy accumulation at the inlet may eventually contaminate the solution, which is a topic for the future. It is also important to note that the simulated domains are symmetric about the hill top, i.e., the distance between the inlet and outlet is the same from the center. In wind farm simulations, there should be a minimum distance between the wind farm and the inlet to allow the flow to adjust to the pressure field created by the AGWs, avoiding non-physical blockage [9]. This minimum requirement will be the subject of a further study.

IMPACT OF DOMAIN HEIGHT ON REFLECTIONS

It is expected that the height of the domain should scale to the effective vertical wavelength. To investigate this, a set of simulations were designed (Set 3 in Table 3.3) by changing the height of the domain in proportion to the expected λ_{ver}. Six simulations were run with domain heights in the range of ($\tilde{L}_z = L_z/\lambda_{ver} = 0.25$ to 2.0) for values of $Fr = 0.1$ and 0.5. The domain length was set equal to λ_{hor} for all simulations, and the damping thickness was set to $1.5\lambda_{ver}$ for $Fr = 0.1$ and $1.2\lambda_{ver}$ for $Fr = 0.5$. Further, ξ was set to 10 for $Fr = 0.1$ and 2.5 for $Fr = 0.5$.

Figure 3.10(b) shows the reflection coefficient as a function of the non-damped domain height. A rapid reduction in the reflection coefficient is seen as the domain height is increased and approaches λ_{ver}. There is a slight increase in the reflection coefficient for $\tilde{L}_z$ 1.5 for both values of Fr, but further increasing the domain height beyond twice λ_{ver} has little effect. Our experience indicates that a higher domain height allows more waves to reach the inlet than a lower one. Since the waves are inclined, the wavefronts impinge on the top damping layer in the case of a lower domain before reaching the inlet. However, if the domain height is larger than one λ_{ver}, then, depending on Fr, the wavefronts farther from the source reach the inlet before impinging on the top damp-

Table 3.4: Wind farm canopy parameters. Note that the canopy only extends over the rotor diameter so the bottom of the canopy is at H_b and the top is at H_t.

Fr	S_h	c_t	S_x	S_y	L (km)	H_b (m)	H_t (m)	h_r (m)	D_r (m)
0.1	0.16	0.075	5	1.67	5	20	80	50	60
0.1	0.16	0.075	2.5	0.83	10	40	160	100	120
0.5	0.16	0.075	5	1.67	5	20	80	50	60
0.5	0.16	0.075	2.5	0.83	10	40	160	100	120

ing layer. Thus, the reflection pattern seen in Fig. 3.10(b) is not entirely monotonic. In any case, it is important to set the minimum height of the non-damped domain height to around one effective vertical wavelength. This recommendation may change when including a temperature profile which more closely reflects an ABL with an capping inversion in which case the inversion height might be critical in setting the non-damped domain height. This will be the subject of further work.

3.5.2. SCENARIO 2: WIND FARM CANOPY

The investigation of flow over the hill provided a baseline for simulating AGWs under linearly stratified free atmospheric conditions. This was then extended to the wind farm canopy (WFC). Simulation sets 2 and 3 from Table 3.3 are re-run, this time with the wind farm canopy. The setups are the same as that of the hill cases described in Section 3.5.1 and Section 3.5.1, except that the hill is replaced with a wind farm canopy where the canopy height and length correspond to the hill's half-width at half-height and maximum height, respectively. The parameters used to model the wind farm canopy are given in Table 3.4. Similarly to the hill case, the slope parameter is kept constant, i.e., $S_h = 0.16$, and two values of Fr, i.e. 0.1 and 0.5, are considered. The thickness of the wind farm layer, i.e., the rotor diameter, the hub height, and C_t are varied as c_t is kept constant, i.e. 0.075. As shown in Table 3.4, the WFC starts at $H_b = 20\ m$ and goes to $H_t = 80\ m$ vertically for $L = 5\ km$ such that hub height is $h_r = 50\ m$ and and the rotor diameter is $D_r = 60\ m$. For $L = 10\ km$, $H_b = 40\ m$ and $H_t = 160\ m$ with the wind farm layer being 120 m thick and hub height at 100 m. Therefore, the turbine thrust is stronger for the $L = 10\ km$ cases than the $L = 5\ km$ cases because of higher hub height and a bigger rotor.

IMPACT OF DAMPING LAYER THICKNESS

Figure 3.11 shows that the results for the canopy case are similar to those of the hill (Fig. 3.9) in terms of the sensitivity of the reflection coefficient of the damping layer thickness and the damping coefficient for the two Fr cases. The main difference is that the reduction in Cr with damping layer thickness when Fr=0.1 is monotonic for the canopy case and does not show the variation seen for the hill. The reasons for this are explored in Section 3.5.2.

Generally, thicker damping layers compensate for weaker damping coefficients. More importantly, for almost all values of ξ and $\tilde{L}_d < 1$, Cr exceeds the threshold selected in this study for an acceptable level of reflection. Figure 3.11(a) shows that the suit-

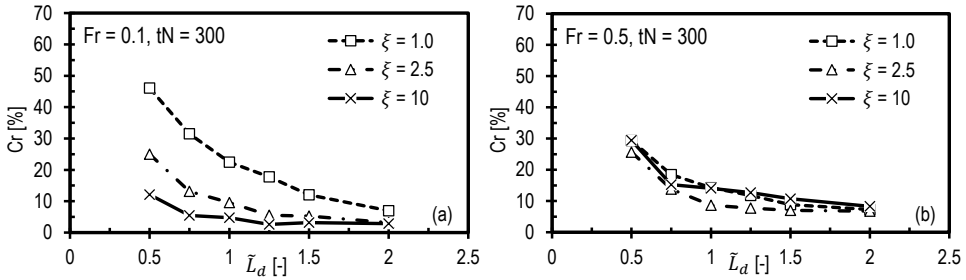

Figure 3.11: Reflection coefficient for the wind farm canopy case as a function of normalised damping layer thickness for different values of the damping coefficient when (a) $Fr = 0.1$ and (b) $Fr = 0.5$.

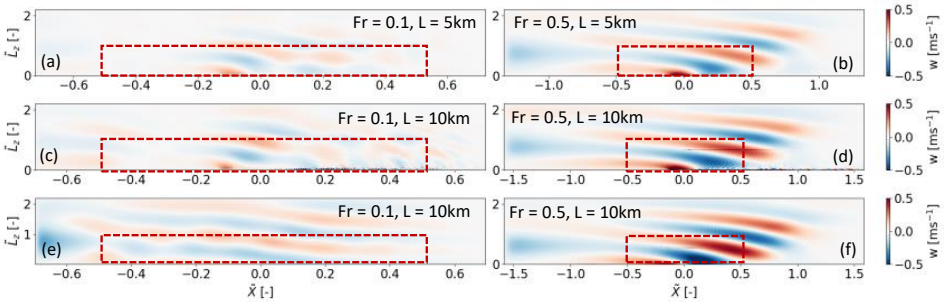

Figure 3.12: Plots (a-d) show vertical velocity of flow through and around the wind farm canopy with lengths $L = 5$ and 10 km for $Fr = 0.1$ and 0.5, and $\tilde{X} = 1.0$. For comparison, the plots (e-f) show the corresponding hill cases where $L = 10$ km for $Fr = 0.1$ and 0.5, and $\tilde{X} = 1.0$. The region inside the dashed red box is the non-damped domain.

able damping coefficient range for $Fr = 0.1$ is still 1.0 to 10, with 10 being optimal for all damping layer thicknesses. Likewise, Fig. 3.11(b) shows that $\xi = 2.5$ is the optimal damping coefficient for $Fr = 0.5$, for all damping layer thicknesses. Furthermore, values of $\xi = 1$ and 10 appear slightly less effective in damping reflections than a value of $\xi = 2.5$.

IMPACT OF DOMAIN SIZE

The domain length is normalized based on the horizontal wavelength predicted from the linear theory for a hill using the wind farm canopy height and length instead of the hill maximum height and half-width at half-height, respectively. We calculate the effective wavelengths from the simulations at $tN = 300$ to compare with the predicted wavelengths where the horizontal wavelength is calculated based on a horizontal slice at $\tilde{L}_z = 1.0$ through the flow fields shown in Fig. 3.12 and the vertical wavelength is similarly calculated based on a vertical slice at $X = 0$. In general, the calculated wavelengths match the predicted wavelengths.

It is interesting to notice that the wave shape for the canopy is significantly different from that of the hill for the same conditions and optimal simulation setup. The vertical velocity field for the two wind farm canopy lengths and one hill-half width (i.e. $L = 10km$) are shown in Fig. 3.12. For the WFC, there are two prominent wave trains

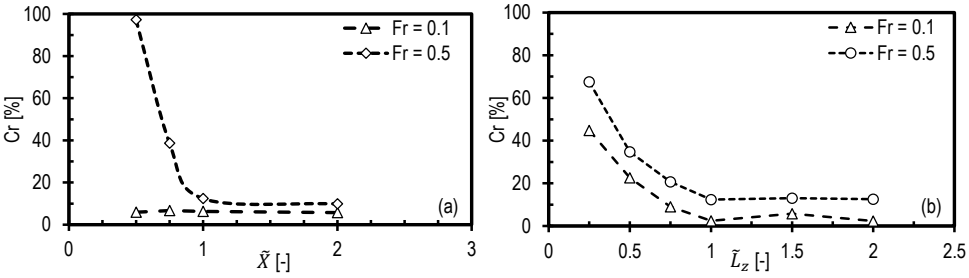

Figure 3.13: Reflection coefficient for the wind farm canopy case as a function of: (a) domain length for $Fr = 0.1$ and $Fr = 0.5$, and (b) domain height for $Fr = 0.1$, $\tilde{L}_d = 1.5$ and $Fr = 0.5$, $\tilde{L}_d = 1.2$.

for the $Fr = 0.1$ cases shown in Fig. 3.12 (a and c), one at the entrance and the second at the canopy exit. The most dominant is caused by upward flow deflection at the entrance due to the thrust force at the start of the canopy. The wave at the canopy exit results from the downward flow as the thrust force abruptly ends. These waves are out of phase and propagate at the same angle to the horizontal and their interaction leads to a distorted wave spectrum. Therefore, the effective wavelength from a canopy simulation differs from that predicted if the most dominant wave train is considered though the wavelength calculated using the global maxima at the canopy entrance and global minima at the canopy exit does provide a good match. This difference in wave shapes for the WFC and the hill case can be seen by comparing plots in Fig. 3.12 (a and c with e). When referring to the monotonic Cr plots in Fig. 3.11(a) and nearly constant values in Fig. 3.13(a) for $Fr = 0.1$ it seems that the dominant wave train triggered by canopy entrance is more critical in terms of simulation setup. For this case, the dominant wave train propagates out both upstream and downstream. The second smaller wave train at the exit propagates similarly, merging with the first to give the patterns seen in the plots Fig. 3.12 (a and c). For $Fr = 0.5$, we see only one wave train in plots in Fig. 3.12 (b and d) because the advection speeds in this case, 25 and 50 ms^{-1}, for the 10 km canopy and the 5 km canopy, respectively, are higher than the wave speed in this case. These advection speeds are higher than generally observed for a wind farm but are used here to fix the value of $Fr = 0.5$ for practical values of N when L is a constraint. As can be seen on plots Fig. 3.12 (b, d, and f), the wave shape and wavelengths are the same for the WFC and hill cases when $Fr = 0.5$, however, the amplitude of the vertical velocity is higher in the hill case.

Another important observation is the increased wave energy accumulation at the inlet in all cases compared with the hill simulations, suggesting that Dirichlet inflow boundary conditions are inappropriate when simulating AGWs. In contrast to the zero-gradient outflow boundary condition, which appears to advect the waves through the outlet, the inflow boundary condition is not influenced by any approaching waves (i.e., the prescribed boundary values remain as prescribed and are not perturbed by the gravity waves). Thus, the user-prescribed inflow velocity is not truly representative of a flow regime where AGWs are present. As a consequence, wave energy accumulates at the inlet, and the inlet-RDL can only delay its propagation back into the domain. Further work

concerning how to effectively contain or eliminate this energy accumulation at the inlet is required.

In terms of the main aim of this study, the waves are effectively damped, especially in the top and outlet RDLs, suggesting that the optimal setups from the hill case are also optimal for the wind farm canopy. Figure 3.13(a) shows that there is no impact of the domain length on Cr when $Fr = 0.1$. This is because the domain lengths were set as a function of λ_{hor} predicted from the linear theory, which is significantly greater than the wavelength of the dominant wave train at the entrance of canopy. When $Fr = 0.5$, similar behaviour is seen as for the hill case where Cr reduces with increasing domain length and is minimum when $\tilde{X} > 1.0$. However, Cr values remain more than 10% because of faster energy accumulation for higher advection speeds than observed wind speeds for a wind farm.

The impact of domain height on the reflections is also the same as that of the hill case. As shown in Fig. 3.13(b), Cr is minimised for domain heights greater than λ_{ver}. It is important to recall that vertical wavelength depends on U/N, which holds true for both canopy and hill cases. The value of Cr is higher when $Fr = 0.5$ because of high amplitudes due to a high advection speed, i.e. 25 ms^{-1}. Based on these observations, it is suggested to set the domain length and height in wind farm simulations to at least one predicted effective horizontal and vertical wavelength, respectively. However, the link between high inflow velocities, wave amplitudes, and wave trains will be investigated in chapter 5 by modeling wind farms with actuator models for a more accurate representation of the wind farm flow dynamics.

3.6. CONCLUSIONS

This study aims to provide guidelines for atmospheric flow simulations that include atmospheric gravity waves by relating the key physical and simulation parameters. The study is first carried out for a two-dimensional hill in stably stratified flow to compare the results to an analytical solution. The findings are then tested for flow through wind farms, approximated with a wind farm canopy model. Based on recent findings in the literature, only Rayleigh damping gravity wave treatment was investigated. Therefore, the findings apply to simulation setups with Rayleigh damping layers and inflow-outflow boundary conditions solved with Finite-Volume methods.

Simulation time is one of the most critical parameters in simulations, including gravity waves. In all cases, a longer simulation time would result in the accumulation of wave energy at the inlet boundary, and the reflections gradually become stronger. Thus, we conclude that the Rayleigh damping method attenuates the gravity waves to an extent that may not work for a long simulation, such as a diurnal simulation. Therefore, a robust technique is required to handle both the energy accumulation and reflections. In terms of time-step size and grid resolution, the typical values used in wind farm LES (i.e., $0.5 < t < 1.0$ and $5 < \Delta x, \Delta y, \Delta z < 20$) are more than sufficient to resolve the AGWs. Thus, the simulation setups used for the investigated Fr range are independent of the time-step size and grid resolution because the time periods and wavelengths of AGWs are several times bigger.

The results regarding the configuration of the damping layers show a trade-off between the ability to correctly resolve gravity waves and computational resources. With

periodic conditions in the lateral direction, the highest accuracy can be achieved with damping layers of a thickness exceeding the effective vertical wavelength at the inlet, top, and outlet. In case of limitations on the computational resources, a combination of damping layers of the same thickness at the inlet and top could still be reasonable.

Our test shows that for various Froude numbers, small damping coefficients would not be effective even for damping thickness 2 to 5 times greater than the effective vertical wavelength. Likewise, the reflections are higher for layers with excessively large damping coefficients and might distort the solution in regions of the non-damped domain close to the damping layer. The most suitable damping coefficients are values from 1 to 10 when the damping coefficient is normalized with Brunt-Väisälä frequency. The thickness of the damping layer should be at least one effective vertical wavelength, and thicknesses exceeding 1.5 times the effective vertical wavelength may be unnecessary. The wave direction is critical to understanding AGWs, but it should not affect the wave damping as it is applied to velocity components; usually, the vertical velocity is set to zero, and the other two are set to the geostrophic components.

The domain length should be scaled with the effective horizontal wavelength and not with the length of the hill or wind farm. The reflection coefficient as a function of domain length normalized by effective horizontal wavelength shows that large domains are more appropriate to avoid undesirable levels of reflections from the domain boundaries. For domain lengths exceeding one horizontal wavelength, the reflection of the upward propagating energy is less than 6% in the hill case. The reflection coefficient was slightly higher for the wind farm canopy cases due to the interaction of the wave trains at the canopy entrance and exit. Therefore, further investigation using such as an actuator disk approach to model the wind turbines is required to thoroughly test the optimal setups and understand the wave dynamics. For both flow scenarios, i.e., the hill case and the canopy case, increasing the domain length beyond λ_{hor} shows a small reduction in the reflection coefficient. A similar impact on the reflection coefficient is observed when varying the non-damped domain height, and setting it to at least one effective vertical wavelength is recommended. It is important to point out that the wave reflection coefficient in this study was calculated by taking the ratio of energy values. This can be misleading in some cases, as the reflected waves can be directed upwards, thus reducing the Cr value. Visual inspection of the vertical velocity fields is recommended to cross-check the Cr values.

These recommendations are based on linearly stratified atmospheric flows. Aspects like turbulence and a more realistic and complex temperature structure of the atmosphere are not considered in this study. Nevertheless, this work should help provide useful guidelines for setting up simulations that include atmospheric gravity waves in wind energy applications. We have tested these findings with another finite-volume code, TOSCA [10], and found consistent results with SOWFA.

In further work (Chapter 4)[24], we examine the effects of capping inversion (inversion Froude number and height), turbulence, and the Coriolis force. Extending this study, we validated these findings under conventionally neutral boundary layer conditions and found that combining Rayleigh and advection damping layers [9] more effectively limits energy accumulation at the inlet than the Rayleigh layer alone.

REFERENCES

[1] M. A. Khan, D. Allaerts, S. J. Watson, and M. J. Churchfield, *Investigating the relationship between simulation parameters and flow variables in simulating atmospheric gravity waves for wind energy applications,* Wind Energy Science **10**, 1167 (2025).

[2] S. Frandsen, *On the wind speed reduction in the center of large clusters of wind turbines,* Journal of Wind Engineering and Industrial Aerodynamics **39**, 251 (1992).

[3] M. Calaf, C. Meneveau, and J. Meyers, *Large eddy simulation study of fully developed wind-turbine array boundary layers,* Physics of Fluids **22**, 015110 (2010).

[4] R. B. Smith, *Gravity wave effects on wind farm efficiency,* Wind Energy **13**, 449 (2010).

[5] D. Allaerts and J. Meyers, *Boundary-layer development and gravity waves in conventionally neutral wind farms,* Journal of Fluid Mechanics **814**, 95 (2017).

[6] D. Allaerts and J. Meyers, *Gravity waves and wind-farm efficiency in neutral and stable conditions,* Boundary-Layer Meteorology **166**, 269 (2018).

[7] D. Allaerts, S. V. Broucke, N. Van Lipzig, and J. Meyers, *Annual impact of wind-farm gravity waves on the Belgian-Dutch offshore wind-farm cluster,* Journal of Physics: Conference Series **1037** (2018), 10.1088/1742-6596/1037/7/072006.

[8] L. Lanzilao and J. Meyers, *Set-point optimization in wind farms to mitigate effects of flow blockage induced by atmospheric gravity waves,* Wind Energy Science **6**, 247 (2021).

[9] L. Lanzilao and J. Meyers, *An improved fringe-region technique for the representation of gravity waves in large-eddy simulation with application to wind farms,* Boundary-Layer Meteorology **186**, 567 (2023).

[10] S. Stipa, A. Ajay, D. Allaerts, and J. Brinkerhoff, *TOSCA – an open-source, finite-volume, large-eddy simulation (LES) environment for wind farm flows,* Wind Energy Science **9**, 297 (2024).

[11] O. Maas, *From gigawatt to multi-gigawatt wind farms: wake effects, energy budgets and inertial gravity waves investigated by large-eddy simulations,* Wind Energy Science Discussions **2022**, 1 (2022).

[12] D. R. Durran, *Nonreflecting boundary conditions,* Springer, New York, NY , 395 (1999).

[13] R. Perić, *Minimizing undesired wave reflection at the domain boundaries in flow simulations with forcing zones,* Master's thesis, Technische Universität Hamburg (2019).

[14] D. Allaerts, *Large-eddy Simulation of Wind Farms in Conventionally Neutral and Stable Atmospheric Boundary Layers,* Ph.D. thesis (2016).

[15] J. Klemp and D. Lilly, *Numerical simulation of hydrostatic mountain waves,* Journal of the Atmospheric Sciences **35**, 78 (1978).

[16] M. Inoue, G. Matheou, and J. Teixeira, *LES of a spatially developing atmospheric boundary layer: Application of a fringe method for the stratocumulus to shallow cumulus cloud transition,* Monthly Weather Review **142**, 3418 (2014).

[17] S. B. Vosper and A. N. Ross, *Sampling errors in observed gravity wave momentum fluxes from vertical and tilted profiles,* Atmosphere **11** (2020), 10.3390/atmos11010057.

[18] W. H. Snyder, R. S. Thompson, R. E. Eskridge, R. E. Lawson, I. P. Castro, J. T. Lee, J. C. R. Hunt, and Y. Ogawa, *The structure of strongly stratified flow over hills: dividing-streamline concept,* Journal of Fluid Mechanics **152**, 249 (1985).

[19] D. Allaerts, *LBoW - linear buoyancy wave package,* (2022).

[20] C. Markfort, W. Zhang, and F. Porté-Agel, *Analytical model for mean flow and fluxes of momentum and energy in very large wind farms,* Boundary-Layer Meteorology **166** (2018), 10.1007/s10546-017-0294-6.

[21] M. Churchfield, S. Lee, and P. Moriarty, *Overview of the simulator for wind farm application (SOWFA),* National Renewable Energy Laboratory (2012).

[22] M. J. Churchfield, S. Lee, J. Michalakes, and P. J. Moriarty, *A numerical study of the effects of atmospheric and wake turbulence on wind turbine dynamics,* Journal of Turbulence **13**, 1 (2012).

[23] J. R. Taylor and S. Sarkar, *Internal gravity waves generated by a turbulent bottom [e]kman layer,* Journal of Fluid Mechanics **590**, 331 (2007).

[24] M. A. Khan, S. J. Watson, D. J. N. Allaerts, and M. Churchfield, *Recommendations on setup in simulating atmospheric gravity waves under conventionally neutral boundary layer conditions,* Journal of Physics: Conference Series **2767**, 092042 (2024).

Photo by Matthew J. Churchfield,
Bloomington, USA

4

THE SYSTEMATIC SIMULATION PROCEDURE

FOR CONVENTIONALLY NEUTRAL BOUNDARY LAYERS

Chapter 3 identified the length scales to set the sizes of the domain and damping layer and the time scale to configure the Rayleigh damping coefficient, but for linearly stratified temperature conditions. However, the real atmosphere has a more complicated temperature structure, and the recommendations from the previous chapter require validation for more realistic atmospheric conditions. This chapter aims to assess and extend the systematic modelling of internal gravity waves proposed in the preliminary investigation to the modelling of interfacial, internal, and trapped gravity waves. Thus, Large Eddy Simulations of flow through a wind farm are performed for conventionally neutral boundary layers (CNBL). Moreover, the commonly used Boussinesq approximation in wind farm LES is compared with the Anelastic approximation.

This chapter is presented as follows: Section 4.1 highlights the challenges in LES of wind farms in CNBLs and the need to include advection damping in addition to Rayleigh damping. Section 4.2 gives the basis for extending the systematic approach to CNBLs. It also describes the model setup and the set of simulations performed to extend and validate the preliminary findings. Section 4.3 presents the validation of the proposed systematic approach and the Boussinesq approximation for wind farm LES in CNBLs.

Parts of this chapter are published in Journal of Physics: Conference Series, **Recommendations on setup in simulating atmospheric gravity waves under conventionally neutral boundary layer conditions**, Mehtab A Khan, Simon J Watson, Dries J N Allaerts, and Matthew Churchfield (2024) [1].

4.1. INTRODUCTION

Numerical modelling is the most viable option for studying the impact of wind-farm-induced atmospheric gravity waves on array performance. Simulating the aerodynamics of wind farms, including AGWs, must include a finite domain. This is in contrast to the Earth's atmosphere, which is horizontally periodic and vertically extends to space. Confining the simulation domain misrepresents the AGW physics at the boundaries, which leads to spurious waves and reflections. For example, for the inflow-outflow boundary conditions that are used in this study, the wave energy accumulates at the inlet, especially for subcritical conditions. The reflections and accumulated wave energy at the inlet can contaminate the solution, compromising its accuracy.

As discussed in chapter 3, approaches used to minimize reflections are generally ad hoc, making them difficult to implement systematically. For instance, the commonly used Rayleigh damping layers (RDLs) require rigorous tuning to determine the optimal damping coefficient and thickness for the given flow conditions [2]. Applying radiation conditions (RCs) is computationally inexpensive and effective for boundaries that perfectly match wave propagation, i.e. the wave transport speed is known [3]. However, RCs are less effective for practical flow conditions in wind farm applications as AGWs propagate inclined to the horizontal. Moreover, the flow interaction with the wind farm triggers a wave spectrum instead of a single wave. Therefore, estimating the wave transport speed is complicated, particularly in finite volume codes [4]. Lanzilao and Meyers [5] compared the performance of RDLs with RCs for wind farm LES with SPWind, a pseudo-spectral code, and found that RDLs outperformed RCs for wind farm flow situations.

The spurious waves triggered by energy accumulation at the inlet can be excluded from wind farm simulations using periodic boundary conditions instead of inflow-outflow. However, mimicking inflow-outflow while using periodic boundary conditions is done with fringe layers. A fringe layer is an RDL that can prescribe transient reference velocities and eliminate recycling the wind farm wake [5]. The fringe layer mismatches the flow conditions inside the physical domain as it attempts to maintain the precursor or user-defined reference inflow velocity, thus becoming a source of spurious waves. These fringe-trigger waves are contained in the fringe layer by advection damping introduced by Lanzilao and Meyers [5]. In principle, in the advection damping layer, the horizontal advection of vertical velocity is eliminated by multiplying the convective term in the vertical momentum equation with a damping function, which is as follows.

$$d(x) = 1 - [F(\frac{x - x_s^d}{\delta_s^d}) - F(\frac{x - x_e^d}{\delta_e^d} + 1)] \tag{4.1}$$

where parameters with subscripts 's' and 'e' relate to function start and end. Thus, x_s^d and x_e^d are the starting and ending locations of the function. δ_s^d is the distance overlapping the fringe where the damping function gradually goes from maximum to zero while the fringe layer strength goes to zero from maximum. Likewise, δ_e^d is the region at the end where the damping function smoothly transits to the maximum. The damping function is zero in the buffer region between δ_s^d and δ_e^d. Lanzilao and Meyers [5] propose using at least eight grid points in the buffer zone for pseudo-spectral codes. The lengths of these zones are suggested in Lanzilao and Meyers [5] to be set as a fraction of the domain length. However, both suggestions appear ad hoc. In our current work, we

investigate whether advection damping is useful with inflow-outflow boundary conditions in restricting the spurious waves triggered due to energy accumulation at the inlet.

The previous chapter proposed a systematic approach to setting up wind farm simulations, including internal gravity waves (IGWs), by linking critical simulation parameters with flow parameters [4]. Conditions like the free atmosphere were idealized to connect IGW wavelengths, and the Brunt-Väisälä with domain and damping layer size and RDL coefficient, respectively. This chapter extends the proposed approach, referred to as the preliminary study here onwards, to CBNL conditions and investigates the systematic modeling of trapped gravity waves (TGWs), IGWs, and interfacial waves. We also investigate if the required length of the advection damping regions should relate to the TGW's horizontal wavelength instead of the domain length.

4.2. METHODOLOGY

LES of flow through wind farm canopies (WFCs) is carried out to test and refine the findings of the preliminary study for CNBL conditions. We recall from Chp. 3 that a WFC is a surrogate of a wind farm that uniformly distributes its total thrust force over a control volume covering its spatial extent. The wind farm thrust is the product of WFC volume and the wind turbine thrust per unit volume. The wind turbine thrust per unit volume, as given below, is based on a fixed wind farm thrust coefficient ($c_t = \frac{\pi C_t}{4 S_x S_y}$), where S_x and S_y are non-dimensional lateral and streamwise turbine distances, normalized to the rotor diameter.

$$\frac{F_D}{V} = \frac{1}{2}\rho U^2 \frac{\pi C_t}{4 S_x S_y} \frac{1}{H} \tag{4.2}$$

H is the WFC height analogous to the rotor diameter, and C_t is the turbine thrust coefficient. Chapter. 3 details WFC implementation.

Simulation runs performed in this chapter are categorized into four sets as shown in Table 4.1. The first set includes non-turbulent simulations, testing the proposed setups in the preliminary study by including the CNBL temperature profiles corresponding to $Fr_i = [0.3, 0.41, 0.51, 0.92]$ and Coriolis force. We also investigated the advection damping layer and the anticipated dependency of its length (L_a) on the TGW wavelengths. The second set tests the proposed setup by including ground roughness and inflow turbulence. The reported Fr_i cases are simulated by varying inversion heights; thus, integral scale eddy sizes would vary. Thus, the possibility of large eddy-induced IGWs is also highlighted. The third set investigates the impact of IGW reflections on the simulated wind farm power. Thus, a uniform actuator disk model was used for wind turbine modeling. The last set also simulates a wind farm of uniform ADs to compare the Boussinesq approximation with the anelastic approximation to account for compressibility effects on wind farm power predictions. We used Aspire for the last set of simulations, as TOSCA does not have the anelastic solvers yet. The model setup details are given in section 4.3.3.

Flow is simulated with the finite volume LES codes Simulator for Wind Farm Applications (SOWFA)[6] and Toolbox fOr Stratified Convective Atmospheres (TOSCA) [7].

Table 4.1: Set of simulations performed and key parameters investigated in each set.

Set	Fr	Fr_i	Physical parameters investigated	Simulation parameters investigated
1	[0.1, 0.5]	[0.3, 0.41, 0.51, 0.92]	λ, N_i, H_i, f	$\tilde{X}$, $\tilde{L}_z$, $\tilde{L}_d$, ξ, $\tilde{L}_a$
2	[0.1]	[0.41, 0.51]	H_i, Eddy size	With & without I-RDL
3	[0.15]	[1.3]	None	ξ
4	[0.15]	[1.3]	Density profile	None

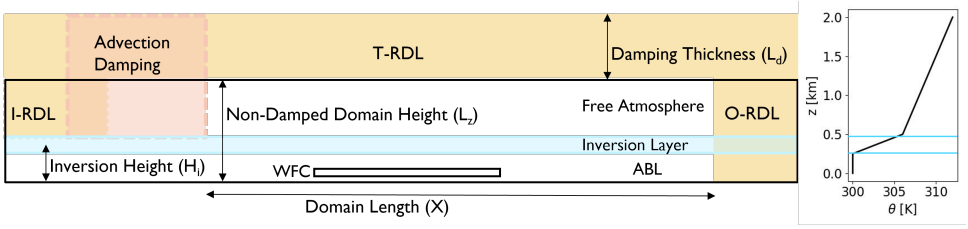

Figure 4.1: (Left) schematic diagram of the TOSCA model setup showing the configuration of advection damping and RDLs at the inlet, top, and outlet (I-RDL, T-RDL, and O-RDL), and (right) a CNBL potential temperature profile.

The potential temperature and incompressible Navier-Stokes equations are solved under non-hydrostatic conditions with the Boussinesq approximation for buoyancy. We use both codes, but present mainly the TOSCA results here. We use TOSCA for our actuator disc-resolved simulations in the following chapters. The TOSCA-simulation setup used in this chapter is shown in Fig. 4.1(left). For the non-turbulent simulations, a uniform velocity at the inlet and a pressure outlet are used in the streamwise direction. The rectangular domain is periodic laterally and is 100 m wide for the non-turbulent cases. Moreover, free slip conditions are used at the bottom and top boundaries. CNBL potential temperature profiles—an example shown in Fig. 4.1(right)—corresponding to H_i = [150 m, 500 m, 750 m, 1450 m] are initially simulated. The capping inversion thickness in all cases is 100 m, and $\Delta\theta$ = 6 K for the results reported in section 4.3. Then, the Coriolis force is included in the same setups to investigate its impact on the choice of RDL reference velocities. The boundary conditions for the turbulent cases are the same, except for ground roughness (with a no-slip boundary condition at the bottom of the domain), and turbulent inflow generated with precursor simulations is imposed at the inlet. The domain width is also increased to 2 km to allow turbulence build-up due to ground roughness. The non-damped domain length (X), unless mentioned, is 18 km for most simulations. The total domain length includes X, the advection damping layer length (10.5 to 15 km), and O-RDL thickness. L_d for all RDLs is 5.5 km; $1.5\lambda_{ver}$ as we simulated Fr = 0.1. L_z for each simulation was set to capture one IGW vertical wavelength above the capping inversion; $L_z = H_i + \lambda_{ver}$+50 m. The mesh resolution was 20 m×20 m×10 m and 10 m×10 m×10 m for the non-turbulent and turbulent runs, respectively.

4.3. RESULTS

An assessment of the proposed simulation procedure and the Boussinesq approximation is presented in this session. Section 4.3.1 shows the analysis done in refining the proposed setup in the previous chapter to more realistic wind farm simulations. The validity of the refined approach for wind farm power predictions with LES is analyzed in section 4.3.2. Finally, section 4.3.3 analyzes whether the Boussinesq approximation is valid for wind farm LES.

4.3.1. EXTENDING THE PROPOSED APPROACH TO CNBL SIMULATIONS

In chapter 3, we established links between the AGW properties, domain size, and damping layer characteristics to minimize reflections and prevent spurious waves. The results section recalls the proposed setups from the preliminary study in section 4.3.1. This section also compares the proposed setups from SOWFA and TOSCA to ensure consistency between the two finite volume codes. This is relevant because we switched from SOWFA to TOSCA for this study. The validity of the proposed setup for CNBL conditions and the requirement for advection damping to constrain the accumulating wave energy at the inlet are discussed in section 4.3.1. The impact of the Coriolis force on the choice of reference velocities in RDLs is also highlighted. Finally, in section 4.3.1, the validity of the refined setup with advection damping for inflow turbulence is addressed. The plots shown till section 4.3.1 are for the wind farm canopy except for those in Fig. 4.2(left), which are the hill cases.

PROPOSED SETUP WITH ONLY INTERNAL GRAVITY WAVES

The preliminary study simulates a bell-shaped 2D hill and WFCs for idealized linearly stratified conditions with SOWFA. Domain size and damping layer thickness are related to the effective wavelengths, which depend on Fr. The effective horizontal and vertical wavelengths are the representative length scales of the wave spectrum induced for a particular value of Fr. All the waves in the spectrum superimpose to form a wave that might differ from the wave corresponding to the dominant length scale, such as the wind farm canopy or hill length. Thus, scaling the domain size with the dominant length scales is inappropriate. The effective wavelengths can be estimated by the distance between the global maxima and minima on a vertical velocity plot along the horizontal and vertical. A plot from the preliminary study for flow over the 2D hill is shown in Fig. 4.2(left), which shows minimal reflections (characterized by Cr) for the Fr cases when the domain length is greater than the effective horizontal wavelength. Cr is the ratio of downwards to upward wave energies, which are the squares of vertical velocities on vertical planes decomposed into downwards and upwards propagating IGWs, respectively. By simulating the same hill, we tested this finding for two CNBL cases, $Fr_i = [0.92, 0.51]$. The CNBL plots are shifted left as λ_{hor} values are smaller by almost half of those estimated for the linearly stratified cases. More importantly, the large dip in Cr for domain lengths greater than the λ_{hor} is evident.

The preliminary study (i.e. Chapter 3) shows similar results, indicating that the domain height and damping layer thickness must exceed the effective vertical wavelength to minimize reflections. Moreover, RDLs, at least at the inlet and top, are suggested with inflow-outflow boundary conditions. The damping coefficient is related to the buoyancy

frequency N through the relationship $\xi = 1/\tau N$. Figure 4.2(right) shows that the reflections are minimum for a range of Fr when ξ is $1-10$. Figure 4.2(right) also compares SOWFA and TOSCA results using the simulation setup for $Fr = 0.1$ and a WFC. The Cr plots for the two codes, except for very low damping coefficients, show very similar results. These cases used X four times λ_{hor}, and L_z and L_d equal to λ_{ver}.

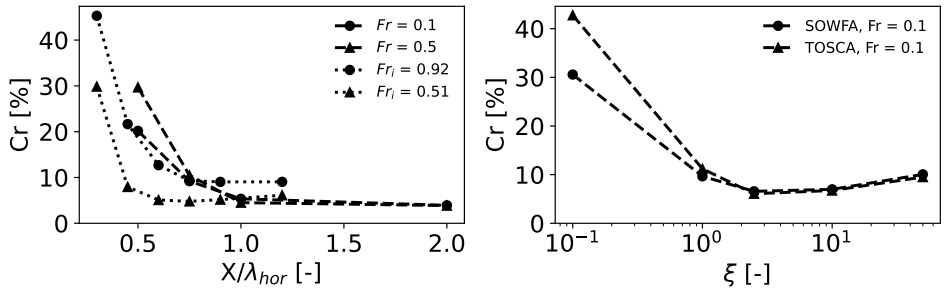

Figure 4.2: Reflection coefficient against (left) $\tilde{X}$ for linearly stratified [$Fr = 0.1, 0.5$] and CNBL [$Fr_{=}0.92, 0.51$] hill cases simulated with SOWFA, and (right) ξ for linearly stratified [$Fr = 0.1$] WFC cases simulated with both SOWFA and TOSCA.

THE IMPACT OF TRAPPED GRAVITY WAVES

Unlike the internal waves, the trapped waves are inside the capping inversion. The TGW properties are mainly dictated by Fr_i, such as increasing wave speed and amplitudes for decreasing Fr_i or vice versa. Based on Fr_i, there are three regimes. In the subcritical case ($Fr_i < 1$), the wave speed is greater than the advection speed, and thus, the TGWs can travel up and downstream. In the supercritical case ($Fr_i > 1$), the waves are slower than the advecting flow and can travel only downstream. Meanwhile, in the critical case ($Fr_i = 1$), the TGW speed is the same as the advecting flow. The buoyancy perturbation, proportional to capping inversion displacement, is the highest for critical conditions.

Subcritical conditions can be the most difficult to simulate as the TGWs traveling upstream can enhance the energy accumulation at the inlet. Therefore, we consider four subcritical cases to test and refine the proposed setup suggested in section 4.3.1. The value of Fr_i was adjusted by varying either H_i or the temperature difference across the capping inversion, which changes N_i. The results in both cases were the same, and only the H_i runs are discussed here. The proposed setup works fine to handle the WFC-induced IGWs, but the I-RDL cannot retain the accumulating energy as the upstream propagating TGWs bring more energy and at a faster rate than that brought by the IGWs. This can be seen from the instantaneous vertical velocity contours with just the I-RDL in Fig. 4.3(left column). We adopted the advection damping proposed by Lanzilao and Meyers [5] and tested it for all Fr_i runs. As shown on the vertical velocity plots in Fig. 4.3(middle and right column), the advection damping is effective, with and without the I-RDL, in containing both the accumulated energy at the inlet and the TGWs. Although advection damping alone seems sufficient, runs exceeding a few flow transits through the domain might become contaminated if the I-RDL is not combined with ad-

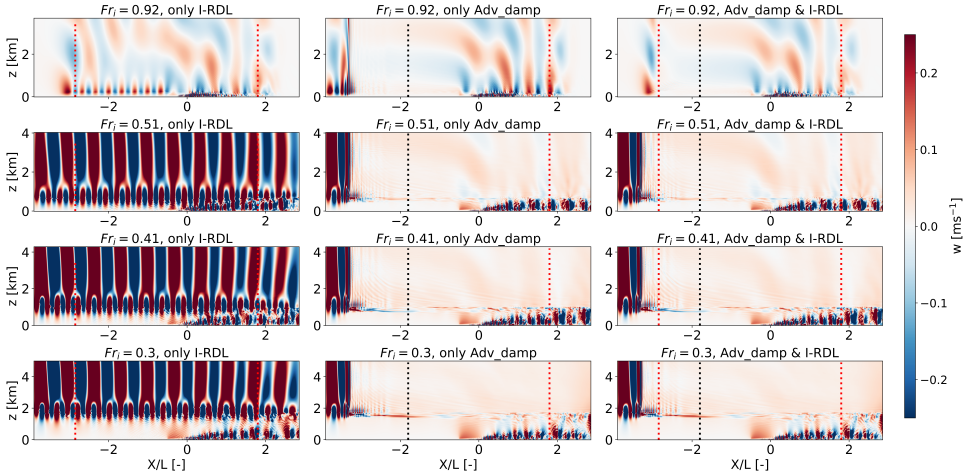

Figure 4.3: Instantaneous vertical velocity at $tN = 200$ through a WFC extending from -0.5 to 0.5. (Left): only I-RDL, (middle): only advection damping, and (right): both I-RDL and advection damping at the inlet. The region left of the dotted black line is the advection damping layer, and the regions between the red dotted line and the closest parallel boundary are RDLs.

vection damping. We can also see the TGWs amplifying towards the inlet, especially with decreasing Fr_i. This is because the TGW wavelength and amplitude increase with increasingly sub-critical conditions. The TGW horizontal wavelengths were estimated to be around $4-5$ km for $Fr_i = 0.41$ and 0.3, and $1.5-3$ km for the other two values of Fr_i. We observed that advection damping buffer zones matching the TGW horizontal wavelengths work better.

Figure 4.4(left) shows the reflection coefficient for the simulated Fr_i cases estimated from the temporally averaged vertical velocity fields smoothed towards the damping zones to eliminate the damping layer-induced noise. In most cases in Fig. 4.4(left), Cr is the same with only advection damping and when combined with the I-RDL. More importantly, it is less than 10% for all cases, which, in our experience, is a fairly reflection-free simulation. It is important to note that the Cr metric is very sensitive to wave direction and noise. For instance, the WFC-induced eddies seem to trigger AGWs, seen even on the temporally averaged vertical velocity contour in Fig. 4.4(right). These eddy-induced IGWs propagate randomly as their source is random but still form impact the velocity field assessed to calculate Cr. This is also the reason for the relatively high Cr values for the ($Fr_i = 0.92$) cases, where the capping inversion is close to the WFC and eddy-induced AGWs are prominent. On the other hand, the higher Cr for the least sub-critical case $Fr_i = 0.3$ might be the footprint of strong TGWs affecting the flow along the capping inversion in the free atmosphere aloft. Simulating large domains may reduce the reflection, but a proper investigation of the impact of reflections on the blockage effect and wake recovery is essential. Such an investigation is less meaningful with the WFC model; thus, we will address it with actuator discs modeling of wind farms in section 4.3.2.

The effect of the Coriolis force on the choice of reference velocities was also investi-

gated. To this end, we simulated the $Fr_i = 0.41$ case for a few latitudes. We noticed that the Coriolis force has minimal to no impact on the damping setup. The Coriolis force might deflect the flow around the WFC just as it does around a wind farm [8]. However, this deflection may not be felt in the RDLs at least a wavelength away from the WFC.

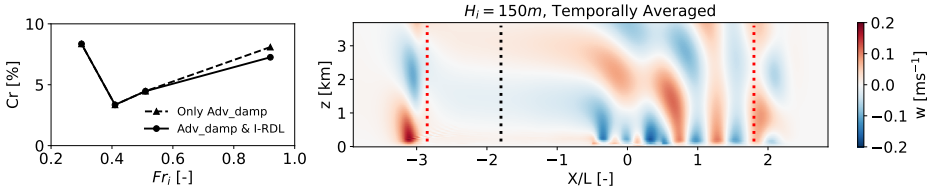

Figure 4.4: (Left) Reflection coefficient computed from temporally averaged vertical velocity fields for the tested Fr_i and (right), vertical velocity for $Fr_i = 0.92$ on a vertical plane temporally averaged over two flow-through times. The averaging period for all cases is 10 s.

4

THE IMPACT OF TURBULENCE

Finally, we investigate the impact of inflow turbulence on the optimized setup. The four Fr_i cases are tested by including Coriolis force for latitude 41.3°, ground roughness length of 0.01 m, and feeding inflow turbulence from precursor simulations. The spin-up time for the precursor simulations was 20 ks, and the inflow data were stored for 20 ks beyond spin-up. The eddy size along the streamwise direction is several times H_i, and should change for varying boundary layer height [9]. Therefore, the incoming turbulence also induces IGWs, which appear as noise or turbulence in the free atmosphere.

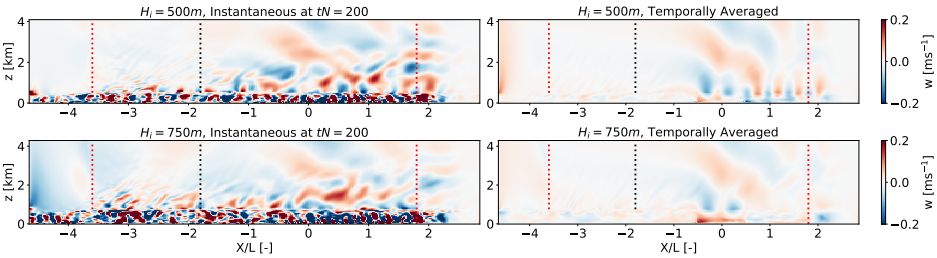

Figure 4.5: (Left) Instantaneous, (right) temporally averaged vertical velocity contours from the turbulent simulations for Fr 0.1, and $Fr_i = 0.51$ and 0.41. The WFC extends from −0.5 to 0.5, and the region left of the dotted black line is the advection damping layer. The regions between the red dotted line and the closest parallel boundary are RDLs.

Figure 4.5 (left) shows the instantaneous vertical velocity contours at $tN = 200$ ($N = 0.01$) for Fr 0.1 and Fr_i 0.51, 0.41 in the first and second row, respectively. The relatively high-frequency waves atop the capping inversion are the eddy-induced IGWs, which are not seen in the I-RDL. Moreover, the accumulating energy at the inlet is also contained towards the end of I-RDL, which overlaps the first advection damping zone. These waves would propagate into the domain parallel to the inlet if advection damping were not there.

The WFC-induced IGWs can be seen on all plots but are more prominent on the temporally averaged vertical velocity contours in Fig. 4.5 (right). The averaging period was 5 s over 20 ks of data. The clear AGW signature on the temporally averaged velocity shows that the AGWs are steady as the flow conditions, i.e., Fr, S_h, Fr_i, and H_i were fixed. The WFC-induced IGWs have a greater amplitude for high Fr_i cases, as the capping inversion is closer to the WFC top. The amplitudes, however, diminish by an order of magnitude resembling the eddy-induced IGWs for the low Fr_i cases. Unlike the plots in the left column, only some traces of the eddy-induced IGWs are seen. Thus, it is evident that the most eddy-induced IGWs are averaged out just like their source, turbulence. We show Fr_i 0.51 and 0.41 cases as H_i 500 m and 750 m are more realistic CNBLs. Simulating H_i 150 m and 1450 m was done to get initial insight into the AGWs for stable and unstable surface conditions, respectively.

Cr, estimated from the temporally averaged vertical velocities, is 9.8% and 12% for Fr_i 0.51 and 0.41, respectively. The eddy-induced IGWs, both from the WFC and inflow turbulence, are still visible in the free atmosphere that affect the value of Cr. The proposed approach in the preliminary study with advection damping is promising for setting up wind farm simulations, including wind-farm-induced AGWs. The possibility of eddy-induced IGWs and their interaction with wind-farm-induced IGWs requires further investigation, preferably by relating the eddy size to the eddy-induced IGWs.

4.3.2. VALIDATING THE REFINED APPROACH FOR WIND FARM SIMULATIONS

It is established in section 2.1.4 how flow variations in the free atmosphere are coupled to the inversion displacement and, in turn, to the flow variations in ABL. Since AGWs predominantly occur in the free atmosphere, improper boundary treatment can lead to their reflection from the domain boundaries. In case of improper treatment, the reflected waves affect the flow in the free atmosphere and might affect the displacement of the capping inversion. Therefore, it is vital to identify the possible impact of the reflections from the top boundary on the inversion displacement and wind farm power output. These impacts are analyzed based on the solution of precursor-driven flow through a uniform-ADM resolved wind farm. To this end, the reflections from the top boundary are controlled by setting T-RDL strength. As shown on the temporally averaged vertical velocity plots in Fig. 4.6, the AGWs reflect mainly from the top boundary when the damping strength (i.e., ξ) is the weakest; the waves are not damped enough through the T-RDL. The waves are damped significantly, and the AGW amplitude decreases towards the top boundary for ξ in the $1.0-10.0$ range. But, increasing ξ beyond 10 turns the T-RDL almost into a wall as the AGWs reflect off it, as seen in Fig. 4.6 for $\xi = 50$. The same can also be seen on the plots for the downward waves where there is a phase shift in the T-RDL when $\xi = 0.1$ as the waves reflect from the top boundary and inside the non-damped layer when $\xi = 50$ as the waves reflect off the T-RDL itself. For $\xi = 1.0–10.0$, the wave fronts show no phase shift. Note that the strength of downward waves is roughly the same for all values of ξ, as the reflected wave energy is in range of 8 to 11.5% of the upward wave energy. See Section 3.4.3 for more details about extracting the upward and downward waves from the vertical velocity.

The particle paths shown in Fig. 4.7 give insight into the impact of reflections on the inversion displacement. For $\xi = 1.0$ to 10, the inversion displacement is almost the same

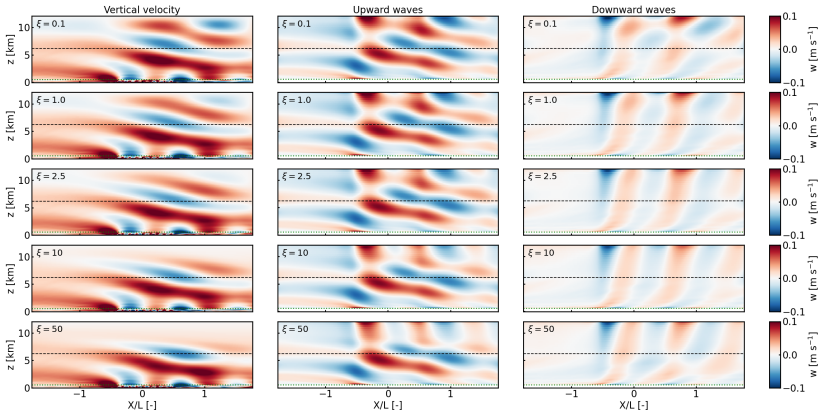

Figure 4.6: Contours of temporally averaged vertical velocity, upwards, and downwards propagating waves in a streamwise-oriented vertical plane for varying Rayleigh damping strength (ξ) of the T-RDL. The flow conditions are defined by $Fr = 0.15$, $Fr_i = 1.3$, $\tilde{H}_i = 0.087$, and $S_h = 0.0255$. The green and black dashed lines show the capping inversion mid-height and start of T-RDL, respectively.

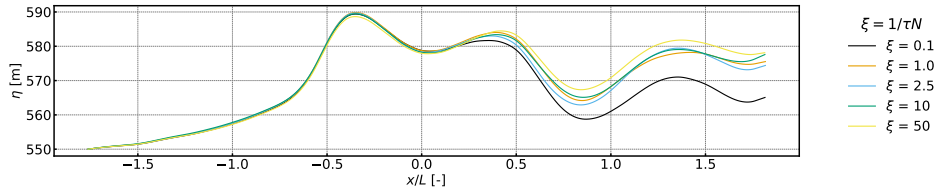

Figure 4.7: capping inversion displacement, extracted by tracing particle paths at $z = 550m$, for varying ξ.

as the reflection coefficient is small and varies little, i.e., $Cr = 8-9\%$. In contrast, the inversion displacement is most different for $\xi = 0.1$, especially towards the end of the wind farm and downstream. This is because the waves reflecting off the top boundary depend on the inclination angle, and for the simulated conditions, they refract downwards more, downstream of the wind farm. The waves reflecting off the T-RDL are evident from the inversion displacement for $\xi = 50$, as it looks different across the domain length. This means the waves are reflected from the T-RDL across the length of the domain, and the reflected waves perturb the capping inversion differently.

The impact of reflections from the T-RDL on the wind turbine and farm output is quite small and correlates with the capping inversion displacement. As shown in Fig. 4.8(b), the temporal and row-averaged plots of the wind farm turbine outputs are the same except for reduced power predicted towards the end of the wind farm for $\xi = 0.1$. The power outputs look slightly different for $\xi = 50$, where the power is higher for the first row of turbines and lower for all other rows except the fifth compared with the results for the other values of ξ. This analysis shows little to no impact of AGW-reflections on the predicted wind farm power when the simulation setup follows the refined procedure discussed in

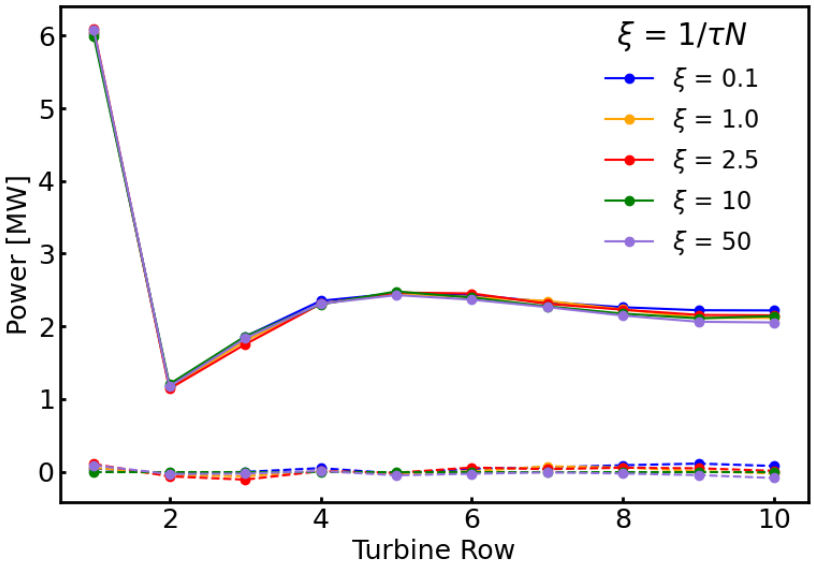

Figure 4.8: Temporal and row-averaged power as a function of ξ. The solid lines show actual power, whereas the dashed lines show the difference between the actual power predicted by each case and that of the least contaminated by reflections (i.e. $\xi = 10$).

section 4.3.1.

4.3.3. VALIDATING THE BOUSSINESQ APPROXIMATION

As mentioned several times so far, the Boussinesq approximation is almost always used in wind farm CFD to include buoyancy effects. This approximation is valid for investigations confined to wind-farm–ABL interactions, as the vertical perturbations are much smaller than the density scale height. However, investigation of wind-farm–atmosphere interactions, including the AGW, requires taller domains that might reach up to tens of kilometers. From a meteorologist's perspective, density is not constant at such heights; thus, the Boussinesq approximation is invalid. In fact, the argument based on the simulation domain height for wind farm flows is invalid itself, as the real basis for the validity of the Boussinesq approximation is the size of a vertical perturbation. Wind-farm-induced vertical perturbations are only as large as a hundred meters, which is two orders of magnitude less than the density scale height, 10 km. Nonetheless, the argument based on the domain height is addressed here by comparing the solution of wind farm flow with the Boussinesq approximation against that of the Anelastics approximation. The governing equations and assumptions of both approximations have already been introduced in section 2.4.1 of chapter 2.

It is noted here that Aspire, instead of TOSCA, is used for these comparisons to exploit the availability of both anelastic and Boussinesq implementations in Aspire. Therefore, the model setup for this comparison is different from that used in TOSCA, which is described in section 4.3.1. The Aspire-model setup, used only for the simulations discussed

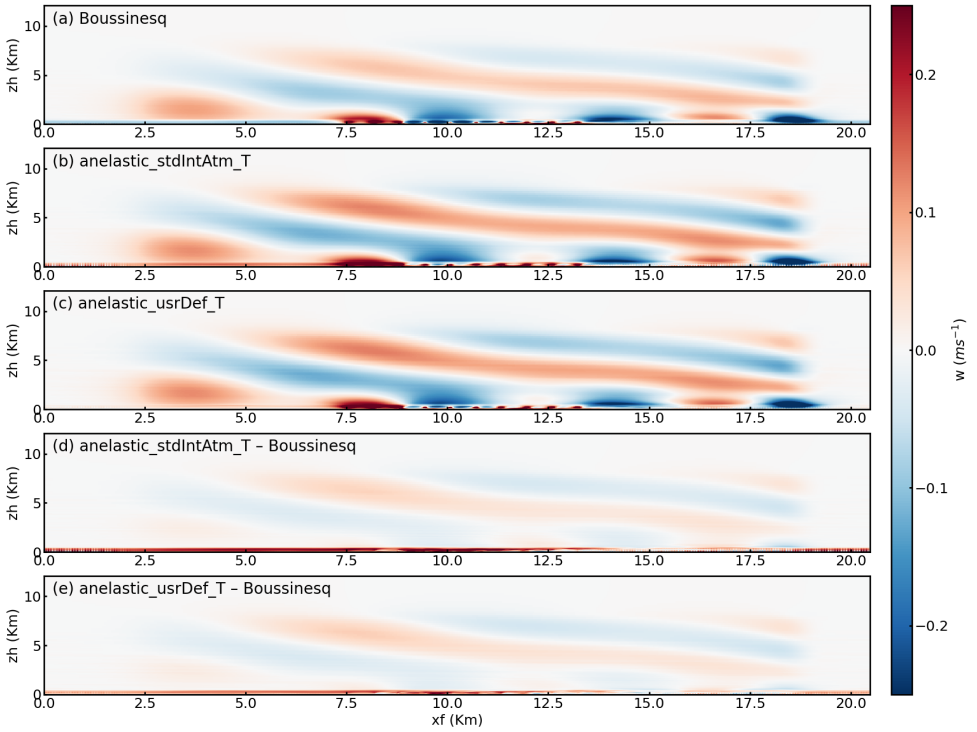

Figure 4.9: Contours of temporally averaged vertical velocity in a streamwise-oriented vertical plane for (a): Boussinesq, (b): anelastic with standard atmospheric surface temperature, (c): anelastic with user-defined surface temperature, (d): difference of plot b and a, and (e): difference of plot c and a.

in this section, has the same domain size and grid resolution as that of the TOSCA setup. However, the concurrent-precursor data were imposed on the successor (i.e. wind farm simulation) at all horizontal boundaries. Thus, periodic boundary conditions were used in the horizontal directions, with a typical rough wall at the bottom and a slip condition at the top. The flow conditions in the precursors were defined to be the same as those of the TOSCA configurations described in section 4.3.2; $Fr = 0.15$, $Fr_i = 1.3$, $\tilde{H}_i = 0.087$, and $S_h = 0.0255$. However, the Coriolis force was excluded as it would change the wind direction over time. The flow was driven through the precursor and successor simulations with a constant pressure gradient or the geostrophic wind set to 12 ms^{-1}, which is consistent with that of the TOSCA setup. Unlike the TOSCA setup, the successor data is nudged at the horizontal and top boundaries to match the transient precursor data. Nudging zones adjacent to the boundaries are similar to Rayleigh damping layers, as they force the successor solution towards that of the precursor. However, advection damping is not available in Aspire, so spurious waves are expected at the interface of the nudging zone at the inlet and the physical domain.

As described in chapter 2-section 2.4.1, the anelastic solvers assume a vertically varying base density instead of a constant density assumed by the Boussinesq solvers. As-

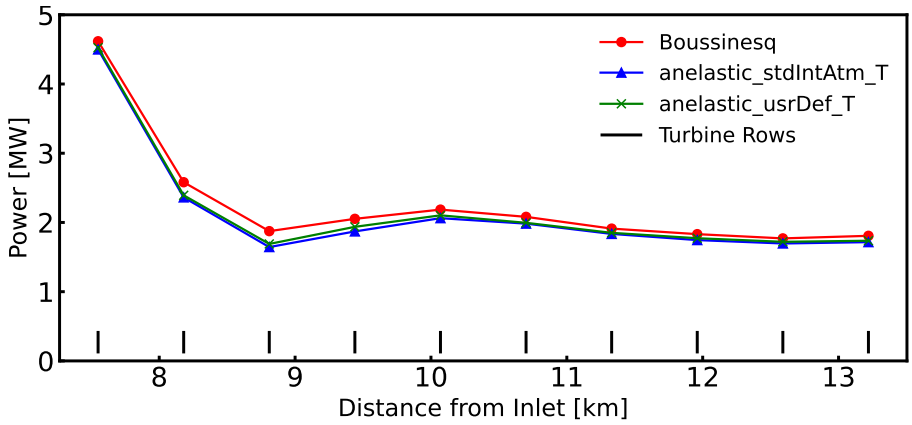

Figure 4.10: Temporal and row-averaged power for the two anelastic and the Boussinesq models.

pire has several options to define the base density profile, two of which were considered for this analysis. These approaches are mainly based on whether the surface temperature and pressure are defined by the user (i.e. anelatic_usrDef_T) or are based on the standard international atmosphere (i.e. anelatic_stdIntAtm_T). The former acquires the base density profile from the defined temperature and pressure profiles at hydrostatic balance. Whereas the latter computes it based on the temperature and pressure profiles taken from the standard international atmosphere. The user-defined surface temperature and pressure were set to 288.15 K and 101325.0 Pa, respectively, to match that of the standard international atmosphere for latitude 41.5°. This way, the two anelastic models are fairly similar.

Figure 4.9 shows the temporally averaged vertical velocity fields for the Boussinesq and anelastic solutions, and the difference between each anelastic and the Boussinesq solutions. It can be clearly seen that the wavelengths and direction of the AGWs are the same in all cases, but the amplitudes are slightly higher in the anelastic fields. This difference in the amplitudes is negligible for the interfacial waves at the capping inversion and more pronounced for the IGWs, particularly at higher altitudes. This indicates that the IGWs amplify as the density decreases vertically, but this would not affect the wind farm performance as IGWs propagate away from it. Otherwise, the differences at lower altitudes, around the wind farm, are insignificant. The nudging zones at the left, top, and right boundaries are obvious as the vertical velocity in these zones is zero, given the geostrophic wind set in the precursor. More importantly, spurious waves at the interface of the left-nudging zone and the physical domain are prominent when compared to the plots in Fig. 4.6. These spurious internal waves are propagating upwards, but significantly far from the wind farm. Thus, their impact on the wind farm flow is assumed to be minimal, although they would affect the inflow to the wind farm.

The wind farm power predictions from the Boussinesq and anelastic solutions are shown in Fig. 4.10. These temporal and row-averaged power plots show slightly higher values for the Boussinesq model. The anelastic models are almost perfectly matched. Note that the TOSCA and Aspire values are not wholly comparable due to the differences

in the model setups already mentioned above. Still, the power output trend from the Aspire simulations is similar to that of Fig. 4.8. The increased power in the fifth row after significant wake-related losses in the entrance region and towards the exit region of the wind farm is consistent. The only major difference is that the second row shows higher values than in the Aspire solutions. The main reason for this is unclear, although it is speculated that this could be due to differences in how the ADM imposes the turbine forces onto the flow and differences in turbulence intensity.

4.4. CONCLUSIONS AND RECOMMENDATIONS

This chapter extends the links between atmospheric gravity wave properties and critical simulation parameters to simulate wind-farm-induced AGWs under CNBL conditions. Rayleigh damping layers effectively damp IGWs at the top and outlet boundaries, and advection damping layers seem to constrain the reflections and energy accumulation at the inlet. However, the configuration of these numerical approaches to handle spurious waves in wind farm simulations is ad hoc. This study gives systematic, quantifiable recommendations on implementing RDLs and advection-damping layers in simulations with inflow-outflow boundary conditions solved with finite volume LES codes. Moreover, the Boussinesq approximation is compared to the anelastic approximation showing negligible difference in the region of interest when determining wind farm performance.

We identified the key physical and simulation parameters in simulating wind-farm-induced AGWs by dimensional analysis informed by preliminary results. We noticed that the AGW wavelength, amplitude, and direction vary with varying Fr, Fr_i, and $\tilde{H}_i$. The preliminary study linked the IGW properties to simulation parameters based on simulating 2D hills and a WFC for idealized linearly stratified conditions. We extended and tested the proposed links to CNBL conditions by simulating WFCs and ADs, including Coriolis force, ground roughness, and inflow turbulence.

The proposed setups in chapter 3 are valid for CNBL cases with one main modification. The inlet-RDL cannot contain energy accumulating at the inlet, triggering spurious waves. Thus, advection damping is tested with and without an inlet-RDL to retain the accumulating wave energy at the inlet. We suggest using advection damping at the inlet and RDLs at the inlet and top for runs that persist for a few flow transits through the domain. If computational resources are sufficient, an RDL at the outlet would further reduce the reflections. The buffer zone of the advection-damping layer should be greater than the TGW horizontal wavelengths. These wavelengths can be estimated from vertical velocity plots along the domain length at the vertical start of the capping inversion. We noticed the TGW amplitudes increase for decreasing Fr_i, amplifying over simulation time as they are not damped. The Rayleigh damping layers are only a function of one damping coefficient, normally set to dampen the IGWs. An implementation allowing piece-wise damping coefficients in the vertical direction may dampen the TGWs in the capping inversion if a damping coefficient scaled with the inversion buoyancy frequency is used.

The Coriolis force has little to no impact on the setup, as far as reference velocity components matching the geostrophic velocity components are used in the RDLs. The inflow turbulence has larger eddies with smaller Fr_i due to increasing H_i, and these

eddies seem to displace the capping inversion and induce IGWs of amplitudes similar to the WFC-induced IGWs. However, further investigation is required to fully understand the causes and characteristics of these eddy-induced IGWs.

The impact of AGW reflections on wind farm flow and power output is negligible if the reflection coefficient is < 10%, which can be achieved by adopting a systematic approach. This approach is to compute Fr, Fr_i, and $\tilde{H}_i$, and estimate the effective horizontal and vertical wavelengths accordingly. The linear theory of the AGWs, or a reduced order model like MSC, can be used to estimate these wavelengths. The domain length should be greater than the effective horizontal wavelength, and the non-damped domain height should include the capping inversion and at least one effective vertical wavelength. The RDL thickness should be greater than the effective vertical wavelength, and the buffer zone of the advection damping layer should accommodate at least one TGW horizontal wavelength. The RDL damping coefficient should be between 1 and 10 on a scale normalized by N. A similar range might work for damping TGWs in the capping inversion, but the damping coefficient should relate to the buoyancy frequency in the capping inversion.

Although negligible, the Boussinesq solver in Aspire predicts a slightly higher wind farm power output compared to that of the two anelastic solvers. The wavelengths and inclination angles of the AGWs are exactly the same in the Boussinesq and anelastic cases. Only the amplitudes of internal gravity waves are marginally higher in the solutions with the anelastic solvers, but mainly at altitudes far away from the capping inversion. Overall, the Boussinesq approximation gives the same solution as that of the anelastic solvers, and hence is appropriate for wind farm LES with large AGW-resolving domain heights.

REFERENCES

[1] M. A. Khan, S. J. Watson, D. J. N. Allaerts, and M. Churchfield, *Recommendations on setup in simulating atmospheric gravity waves under conventionally neutral boundary layer conditions,* Journal of Physics: Conference Series **2767**, 092042 (2024).

[2] D. Allaerts, *Large-eddy Simulation of Wind Farms in Conventionally Neutral and Stable Atmospheric Boundary Layers,* Ph.D. thesis (2016).

[3] D. R. Durran, *Nonreflecting Boundary Conditions* (2010) pp. 453–495.

[4] M. A. Khan, D. Allaerts, S. J. Watson, and M. J. Churchfield, *Investigating the relationship between simulation parameters and flow variables in simulating atmospheric gravity waves for wind energy applications,* Wind Energy Science **10**, 1167 (2025).

[5] L. Lanzilao and J. Meyers, *An improved fringe-region technique for the representation of gravity waves in large-eddy simulation with application to wind farms,* Boundary-Layer Meteorology **186**, 567 (2023).

[6] M. Churchfield, S. Lee, and P. Moriarty, *Overview of the simulator for wind farm application (SOWFA),* National Renewable Energy Laboratory (2012).

[7] S. Stipa, A. Ajay, D. Allaerts, and J. Brinkerhoff, *TOSCA – an open-source, finite-volume, large-eddy simulation (LES) environment for wind farm flows,* Wind Energy Science **9**, 297 (2024).

[8] S. N. Gadde and R. J. Stevens, *Effect of coriolis force on a wind farm wake,* Journal of Physics: Conference Series **1256**, 012026 (2019).

[9] J. S. Brooke, R. Thedin, A. Sharma, E. Branlard, G. Vijayakumar, and A. S. Michael, *Effect of the integral length scales of turbulent inflows on wind turbine loads,* Renewable Energy **217**, 119 (2023).

Photo by Sebastiano Stipa,
Delft, Netherlands

5

IMPACT ON WIND FARM PERFORMANCE

Part II of this dissertation focused on establishing and validating a systematic procedure to simulate wind-farm-induced atmospheric gravity waves. However, the atmospheric gravity wave phenomenon and its characteristics are still a new topic for the wind energy community. Moreover, the link between AGW characteristics and wind farm performance is yet to be fully explored. Therefore, the aim of this chapter is to apply a systematic approach to investigate the AGW phenomenon, its characteristics, and its relationship to the performance of an isolated offshore wind farm under CNBL conditions.

This chapter is presented as follows: Section 5.1 gives a background on how configurations used to simulate the neutral atmospheric boundary layer can limit the understanding of wind-farm–atmosphere interaction. It also highlights the limited insight the wind energy community has into the AGW phenomenon and its characteristics. Section 5.2 describes numerical models, simulation configurations, and the metric to analyze AGW characteristics used in this study. Section 5.3.1 compares three approaches in simulating neutral ABL conditions. Section 5.3.2 and Section 5.3.3 show the dependence of AGW characteristics and wind farm performance on non-dimensional parameters, respectively. In Section 5.4, we present our conclusions concerning the most realistic simulation configuration for wind-farm–atmosphere interactions and provide insight on it when a wind farm is operating in a CNBL.

This chapter is currently under review for publication in Wind Energy Science, **Dependence of wind-farm-induced Gravity Waves and Wind-Farm Performance on Non-Dimensional Atmospheric Parameters and Simulation Configuration**, M. A. Khan, M. J. Churchfield, and S. J. Watson (2025) [1].

5.1. INTRODUCTION

Numerical flow simulations are often used to investigate the interaction of wind farms with the atmosphere. Thermal stratification within the atmospheric boundary layer (ABL), which significantly affects the strength and structure of ABL turbulence, is often a focus of numerical studies. For example, many studies look to correlate wind turbine wake recovery with ABL stratification. The community often focuses solely on the thermal stratification *within* the ABL; however, it has become clear that the stratification *above* the ABL is also significant. A conventionally neutral boundary layer (CNBL), for instance, consists of a neutrally-stratified ABL capped by a strongly stable inversion layer and a weakly stable free atmosphere aloft. A wind farm operating in a CNBL can trigger atmospheric gravity waves (AGWs) in the layers above the ABL that contribute to the wind farm blockage effect [2]. For numerical models to accurately capture AGW effects, thermal and buoyancy effects must be well modeled, and the simulation domain has to be properly configured. This study seeks to investigate AGW effects on wind farms while providing guidance on proper simulation design and configuration.

Researchers conduct simulations of offshore wind farms within the neutral ABL at varying levels of complexity depending on the research question. For example, if the focus is on turbulent wake effects, then simulating a truly neutral boundary layer (TNBL) with neutral stability throughout the entire vertical extent of the computational domain, or by neglecting buoyancy altogether, may be sufficient. To provide the next level of realism and complexity, one may include a capping inversion (a roughly 100 m thick layer of very stable stratification) followed by only a few hundred meters of the more weakly stably stratified free atmosphere above [3, 4]. With this additional realism, the capping inversion acts as a flexible lid on the top of the ABL that can move vertically in response to a strong perturbation from below, such as a large wind farm or terrain. The most realistic simulation configuration, though, is to simulate a CNBL that is capable of fully resolving AGWs by including a capping inversion followed by many kilometers of the weakly stably stratified free atmosphere above. Such a simulation configuration allows the study of wind farm behavior as a function of both ABL stratification and AGW characteristics, a subject that is rapidly gaining attention [5]. Finally, a recent simplified approach is to neglect any stratified layers and to place a stress-free, rigid, impermeable boundary condition at the expected height of the capping inversion, instead of well above it. Using such a boundary condition at the top of the computational domain is commonplace, but to use it as an inflexible capping inversion is uncommon [6]. Although this simplified simulation configuration has similarities with the other configurations, it will contain inaccuracies in the velocity and pressure fields because the ABL height cannot adjust to obstacles such as wind turbines[7].

Properly defining the height of the top boundary of the simulation domain is always critical. Suppose one performs a wind farm flow simulation and uses an impermeable top boundary condition; not allowing enough distance between the top of the ABL and the top boundary will unrealistically constrain the flow within the ABL, leading to errors. The top boundary should be placed high enough that the boundary layer can freely expand in the vertical direction while its flow advects through the wind farm, as shown by Stevens *et al.* [8], for example. If one wants to capture AGW effects, the simulation domain should be tall enough to accommodate at least one AGW wavelength, usually ex-

tending a few kilometers above the capping inversion, as shown by Khan *et al.* [2, 9]. The impact of using a domain height shorter than one AGW vertical wavelength is unclear. In addition to the location of simulation boundaries, the ability of those boundaries to properly handle AGW reflections is important. If an AGW reflects off simulation boundaries, it can seriously contaminate the solution. Khan *et al.* [9] explains the criterion that if 90% or more of the upward-propagating wave energy is absorbed or let out of the domain, the solution will be sufficiently reflection-free. The impact of AGW reflections on predicted wind farm power output has not been thoroughly explored.

If the wind farm is large enough and contains tall enough turbines relative to the ABL height, AGWs are inevitable under CNBL conditions. To simulate this situation, the CNBL configuration with a many-kilometers-tall domain is the most realistic amongst those discussed above, especially for offshore sites [5, 9]. The literature focuses on the impacts of AGWs on wind farm performance, with limited insight into the AGW phenomenon itself [5, 6, 10]. For instance, the literature consistently shows that AGWs cause a feedback effect on the flow in the ABL. Lanzilao and Meyers [5], Stipa *et al.* [6], Smith [11], Allaerts and Meyers [12], Stipa *et al.* [13] argue that AGWs are responsible for the adverse pressure gradients upstream of the wind farm that create a blockage effect and favorable pressure gradients over and downstream of it. Smith [11] describes the capping inversion displacement caused by the deceleration of the flow within the wind farm as the trigger of the AGWs. Stipa *et al.* [6] describes how the capping inversion displacement couples AGW flow perturbations in the free atmosphere to perturbations within the ABL.

A good description of how AGWs then affect the capping inversion displacement, which trigger those waves in the first place, is lacking. Moreover, different types of wind-farm-induced AGW are mentioned in the literature without clearly distinguishing them. For example, the work of Khan *et al.* [2, 9] is related to "internal" AGWs, whereas Lanzilao and Meyers [5], Stipa *et al.* [6], Smith [11], Allaerts and Meyers [12] speak of "interfacial" AGWs as most critical for wind farm performance. "Trapped" AGWs in the capping inversion and even AGWs within the ABL are mentioned [2, 5, 14]. There is a need to describe the AGW phenomena clearly, distinguish all the kinds of AGWs, and identify how each kind influences wind farm performance and simulation set-up.

Past studies of AGW impacts on wind farms focused on either dimensional or non-dimensional quantities. Allaerts and Meyers [15] and Lanzilao and Meyers [5] focused on dimensional quantities of interest, including ABL depth and thermal stratification strength of the capping inversion and free atmosphere. In contrast, Smith [11] focuses on non-dimensional quantities. Similarly, Khan *et al.* [2, 9] examined various non-dimensional quantities used to establish an optimal large-eddy simulation (LES) setup for capturing realistic AGW behavior. In this work, we adopt this non-dimensional approach to investigate AGWs and their impact on wind farm performance in a CNBL. We have two objectives, that relate to realistic and accurate modeling and understanding of wind-farm–atmosphere interactions under offshore CNBL conditions:

- We characterize the effects of modeling choices on the simulation of wind-farm–atmosphere interactions, by comparing four configurations: a) the TNBL, b) the CNBL with a tall domain height, c) a CNBL with a neutrally stratified free atmosphere, and d) replacing the flexible capping inversion with an impermeable, rigid

top boundary.

- We study the dependence of AGWs and wind farm performance on various non-dimensional parameters defined by Khan *et al.* [2] and given in Chp. 1.

The remainder of this chapter is organized as follows: Section 5.2 summarizes the non-dimensional metrics used to analyze AGW characteristics and wind farm aerodynamics. The models and simulation configurations are also explained in this section. We compare the different approaches in simulating neutral ABL conditions in Section 5.3.1. Section 5.3.2 and Section 5.3.3 show the dependence of AGW characteristics and wind farm performance on the non-dimensional parameters, respectively. We conclude with Section 5.4.

5.2. METHODS

5.2.1. SIMULATION CONFIGURATION BASED ON NON-DIMENSIONAL PARAMETERS

We simulate a wind farm consisting of a regular 10×5 array of wind turbines with a spacing of five rotor diameters in the streamwise and three rotor diameters in the lateral direction. We use the Toolbox fOr Stratified Convective Atmospheres (TOSCA) [13], an LES code specifically developed to simulate atmospheric flows through wind farms. TOSCA can simulate turbines as actuator lines or actuator discs with controllers for blade pitch, nacelle yaw, and generator speed. This study uses the uniform actuator disc model with a thrust coefficient, with normalizing velocity taken at the disc, C_t' of 1.3. The actuator discs have the same diameter and hub heights as those of the NREL-5MW wind turbine, 126 m and 90 m, respectively. TOSCA solves the filtered incompressible Navier-Stokes equations under non-hydrostatic conditions using the Boussinesq approximation for buoyancy. The code solves equations for continuity, momentum, and potential temperature. An advection damping layer and Rayleigh damping layers (RDLs) are applied as body forces in the respective forcing zones through the momentum equation, details of which are given in Khan *et al.* [2] and Lanzilao and Meyers [16]. We denote the inlet, top, and outlet boundary RDLs as I-RDL, T-RDL, and O-RDL, respectively. Subgrid-scale turbulence is modeled using the dynamic Smagorinsky model with Lagrangian averaging [17]. Further details are given by Stipa *et al.* [13].

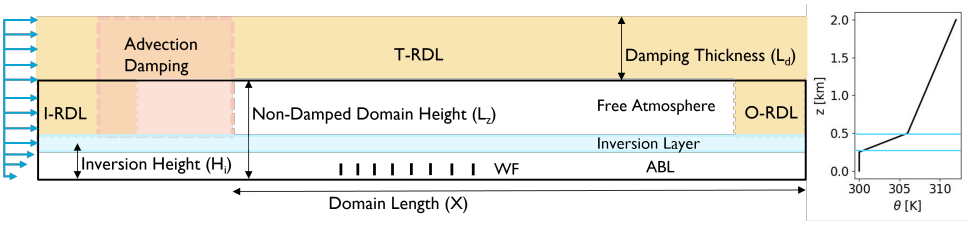

Figure 5.1: Lateral view of the simulation domain that resolves ABL, the capping inversion, and the free atmosphere around a wind farm. Rayleigh damping layers are at the inlet, top, and outlet boundaries, and an advection damping layer is applied, overlapping the inlet Rayleigh damping layer, all in the free atmosphere. A CNBL potential temperature profile is shown on the right for completeness.

Figure 5.1 shows the simulation domain for the wind farm. Turbulent inflow conditions, including wind shear and veer, generated with an offline precursor simulation are

driven into the domain using an inflow Dirichlet boundary condition. Flow exits the domain using an outflow Neumann boundary condition. A typical wall shear stress lower boundary condition is used. It uses Monin-Obukhov similarity to relate the computed flow within the domain to the wall shear stress; Monin-Obukhov similarity is applied locally. An aerodynamic roughness height of 0.0001 m is used to mimic offshore conditions. Periodic boundary conditions are used in the transverse direction only. The upper boundary is set to a free-slip condition for wind speed. The temperature in the ABL is constant with height, then strongly and linearly increasing in the capping inversion, and finally linearly but more weakly increasing in the free atmosphere. This gives a buoyancy and Brunt-Väisälä frequencies constant with height in both layers. There is no heat flux at the ground, which maintains a neutral ABL throughout the simulation. We impose Coriolis forces corresponding to 41° north latitude.

The precursor simulations have the same configuration except that the inflow-outflow boundary conditions are replaced with periodic boundary conditions. The precursor spin-up time is 25 ks, and inflow data are saved for two flow-through times of the successor domain beyond the spin-up. A driving horizontal pressure-gradient controller maintains hub height velocity at 11.5 ms^{-1} with the direction aligned to the horizontal axis. The computed pressure-gradient is also saved and used later by the successor simulation. Moreover, geostrophic damping, details given in Stipa *et al.* [13], is used in the precursor to damp inertial oscillations in the free atmosphere.

A graded mesh in the y- and z-directions is used with 20 m ×15 m ×10 m resolution in the wind turbine rotor layer. From the rotor tips, the mesh stretches horizontally to a resolution of 20 m at the lateral boundaries. The mesh is graded vertically; it reduces from uniformly 10 m in the ABL to 5 m in the capping inversion to effectively resolve the trapped waves. The mesh resolution above the capping inversion is uniformly 10 m up to 1 km and stretches above the capping inversion to 200 m resolution at the start of the top of the Rayleigh damping layer. The stretching ratios are 0.9 and 1.1, respectively. Following the recommendations by Khan *et al.* [2], the domain size, advection, and Rayleigh damping layer thicknesses are set greater than one effective horizontal and vertical internal gravity wavelength for the respective directions. The domain size, including the damping layers for all cases, unless mentioned otherwise, is 35 km in the x-direction, 6 km in the y-direction, and 12 km in the z-direction.

The behavior of atmospheric gravity waves can be characterized using non-dimensional flow parameters. Likewise, the configuration of simulations that capture atmospheric gravity waves can also be defined using non-dimensional parameters. The non-dimensional parameters central to this work, as identified by Khan *et al.* [2], are given in Table 1.2. We recall the physical non-dimensional numbers, the Froude numbers for the free atmosphere and capping inversion (Fr and Fr_i), and the vertical aspect ratios of the ABL and the wind farm ($\tilde{H}_i$ and $\tilde{S}_h$), that characterize the physics of the flow, whereas the remaining five characterize the simulation configuration.

5.2.2. METRIC FOR WAVE CHARACTERISTICS AND CR

AGW inclination angles and wavelengths are estimated using a metric that advances an approach proposed by Allaerts *et al.* [18] to calculate the inclination of internal waves induced by a hill. The approach of Allaerts *et al.* [18] can be applied to the displace-

ment, pressure, and vertical velocity fields; we apply it to only the vertical velocity. A time-averaged vertical velocity plane above the ABL is analyzed to consider only the interfacial and internal waves. The apparent wavelengths of the AGWs can be measured by identifying the local maxima and minima in the vertical velocity field, as shown in Fig. 5.2 (left) [9]. Because wind farms induce two internal wave trains, the upstream one is chosen because it is usually undistorted, especially upstream of the wind farm. Meanwhile, the second wave train superimposes onto the first one, leading to complicated wave characteristics that are difficult to characterize. The maxima/minima finding algorithm identifies even local maxima and minima, so the results are filtered to include only the primary maxima and minima of the first wave train as shown in Fig. 5.2 (right). While filtering, the first peak, a maximum, is always the one where the wind farm starts and right at the top of the capping inversion, that is, (-3000, 550) m for the case shown in Fig. 5.2. The minima and maxima locations of the wave field sweep upward and downstream of the first maximum following a roughly parabolic path [18, 19]. Thus, a parabola is fit to these locations, starting at the first maximum, always passing through the next minimum, and best fitting the remaining minima and maxima. One AGW metric we wish to obtain is wave field inclination angle. Because the curved parabola has a range of tangent angles, we choose the tangent at the third minimum/maximum from the one at (-3000, 550) m to estimate the representative inclination angle of the first wave train, as shown in Fig. 5.2 (right). This peak is a maximum corresponding to a vertical location of $z = H_i + 3L_s/4$, where $L_s = 2\pi U/N$ is the buoyancy length. This differs from the observation of Queney [19] and Allaerts *et al.* [18] that the third AGW maximum above the surface occurs at $z = 5L_s/8$ for their simple ridge flow cases.

The apparent wavelength of internal waves in the direction of energy propagation is calculated using the metric suggested by Khan *et al.* [9]. Here, a wavelength is twice the distance between consecutive maxima and minima of vertical velocity along the parabolic fit line. We measure the distance between the consecutive extrema located along the tangent at the third maximum in the $z = 1/2L_s$ to $H_i + Ls$ range. This eliminates the possibility of capturing extrema affected by the interfacial waves close to the capping inversion and the propagating internal waves damped by the damping layer beyond one vertical wavelength, which is $z \geq H_i + L_s$. The horizontal and vertical wavelengths can be estimated by calculating the streamwise and vertical components of the actual apparent wavelength (i.e. we split the wavelength distance vector into its x- and y-components).

The wavelength of the resultant interfacial wave is calculated using the same metric, but by plotting vertical velocity in the streamwise direction stretching over the length of the wind farm at the top of the capping inversion. The reason for confining the streamwise length in measuring the interfacial wavelength is twofold. First, for low Fr, the two interfacial waves may not or partly superimpose onto each other, modulating the interfacial wave field over the wind farm, and second, the waves downstream of the wind farm are imprints of internal waves for supercritical conditions and a merged form of the imprints and the trapped lee waves for subcritical and critical conditions. Thus, measuring interfacial wavelength over the wind farm length would give a better idea of their involvement in the aerodynamics of the wind farm that induces them.

The amplitude of internal waves is estimated by tracing the path of a Lagrangian particle being carried in the computed velocity field. The path of a particle at $z = H_i + 3L_s/4$

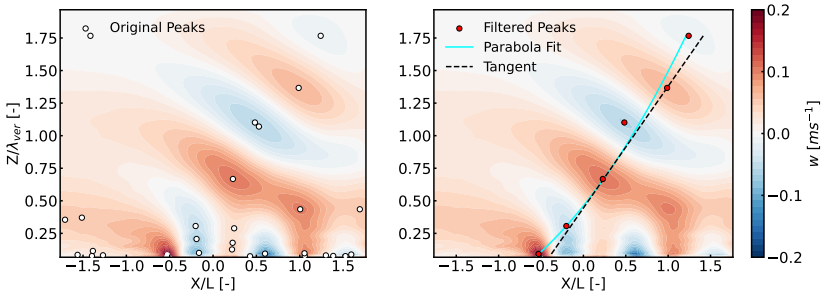

Figure 5.2: Time averaged vertical velocity field above the ABL extending up to the top boundary, including the T-RDL beyond $z/\lambda_{ver} = 1.0$, where the initially identified peaks are shown with white and filtered peaks with red markers.

is traced from the inlet to the outlet. The amplitude is the maximum vertical distance between two consecutive peaks and troughs on the traced particle path. The same strategy is used to estimate the vertical displacement of the capping inversion or the amplitude of the interfacial wave as a function of x. An air parcel is traced along the top of the capping inversion. Thus, local and maximum inversion layer displacements are extracted, which are useful in determining the capping inversion's response to perturbations from individual wind turbine rows and the entire wind farm, respectively.

Accurate simulations must be free of spurious AGW reflections off domain boundaries. AGW boundary reflection is quantified using the reflection coefficient (Cr), which is estimated with the method used in Khan *et al.* [9] proposed by Allaerts and Meyers [14]. The Cr metric is a modification of the procedure initially given by Taylor and Sarkar [20]. For reflection-free simulations, the criterion $Cr < 10\%$ proposed by Khan *et al.* [9] is followed, which was discussed in Section 4.3.2.

5.2.3. SIMULATION SUITE

The simulation suite given in Table 5.1 is categorized into two sets, each answering one or two of the research questions outlined in Section 5.1. The first set compares simulation configurations, truly neutral, rigid lid, and CNBL, used in modeling wind farms under neutral surface conditions. It is established that the CNBL configuration fully resolving AGWs, proposed by Khan *et al.* [2] and adopted for this research, is a more realistic representation of wind-farm–atmosphere interaction. The second simulation set explores the dependence of AGW characteristics and wind farm performance on non-dimensional parameters so that a baseline for wind-farm–atmosphere interaction in CNBLs can be proposed. The following breakdown gives the approach taken for each simulation set to achieve the aims highlighted above.

- Set 1 focuses on the impact of the vertical temperature profile and the vertical extent of the model domain on the simulated power output of an offshore wind farm. We run four simulation sets:
  - (a) Truly neutral ABL and free atmosphere, which contains no gradients of

potential temperature, so no buoyancy effects. This uses a domain height of $L_z = 12$ km and contains a wind farm. In this simulation, the turbulent inflow from a 500 m tall precursor domain, without a wind farm, is fed into the tall successor domain. The ABL in the successor simulation can vertically expand without restriction as it flows through the domain.

  - (b) Rigid Lid, where only a neutral ABL and no capping inversion and free atmosphere above is simulated, and the domain height is set to $L_z = 500$ m, and 750 m in two separate simulations.
  - (c) CNBL, with a capping inversion of 100 m thickness at a mid-point height of $H_i = 500$ m, and a less stable layer above in the free atmosphere where the domain height is set such that the simulations only partly resolve AGWs; that is, $L_z = 750$ m and 1 km. A further CNBL reference case with the same capping inversion set-up is run, but $L_z = 12$ km to fully resolve AGWs and avoid reflections; and, for conditions defined by $Fr = 0.15$, $Fr_i = 1.3$, $\tilde{H}_i = 0.084$, and $S_h = 0.0255$.
  - (d) NFA-ABL, where the setup is the same as the reference CNBL case, but the free atmosphere is neutrally stratified.

- Set 2 explores two aspects, the dependence of AGW characteristics and wind farm performance on the physical non-dimensional parameters. In this regard, several simulations are run for each physical non-dimensional parameter by varying only one at a time and keeping the rest constant. Further details are given in Table 5.1, Set 2(a-d).

Table 5.1: Details of the simulation sets.

Set	Description	Values of physical non-dimensional parameters				Variables Changed	
		Fr	Fr_i	$\tilde{H}_i$	S_h	Physical	Simulation
1 (a)	Truly neutral ABL	-	-	-	0.0255	-	L_z [12 km]
1 (b)	Rigid Lid	-	-	-	0.0255	-	L_z [0.5, 0.75 km]
1 (c)	CNBLs	0.15	1.3	0.084	0.0255	-	L_z [0.5, 0.75, 1, 12 km]
1 (d)	NFA-ABL	-	1.3	0.084	0.0255	-	L_z [12 km]
2 (a)	Varying Fr	[0.075–0.25]	1.3	0.084	0.0255	N	-
2 (b)	Varying Fr_i	0.15	[0.25–1.5]	0.084	0.0255	$\Delta\theta$	-
2 (c)	Varying $\tilde{H}_i$	0.15	1.3	[0.043–0.26]	0.0255	$H_i, \Delta\theta$	-
2 (d)	Varying S_h	0.15	1.3	0.084	[0.0255–0.048]	H	-

5.3. RESULTS

This section analyzes two major aspects of modeling the interaction of wind farms with the atmosphere. First, three common approaches to configuring wind farm simulations for neutral ABL conditions are compared to distinguish the most realistic one. As will be shown later in this section, accurate wind farm performance predictions require simulation configurations that include a significant part of the stratified free atmosphere above the capping inversion, thus fully resolving AGWs. Second, the dependence of AGW characteristics and wind farm performance on the physical non-dimensional parameters is

analyzed to better understand the underlying phenomena of wind farm interaction with the atmosphere.

5.3.1. COMPARISON OF WIND FARM SIMULATION CONFIGURATIONS

Three commonly used wind farm flow simulation configurations, truly neutral, rigid-lid, and CNBL, are compared in this section. The aim in this regard is to identify any shortcomings associated with each configuration in accurately mimicking the wind-farm–atmosphere interaction. The analysis to compare these configurations is done on the simulations detailed in Table 5.1, Set 1 (a-d). CNBL conditions are defined by $Fr = 0.15$, $Fr_i = 1.3$, $\tilde{H}_i = 0.084$, and $S_h = 0.025$, which are irrelevant for the other two configurations.

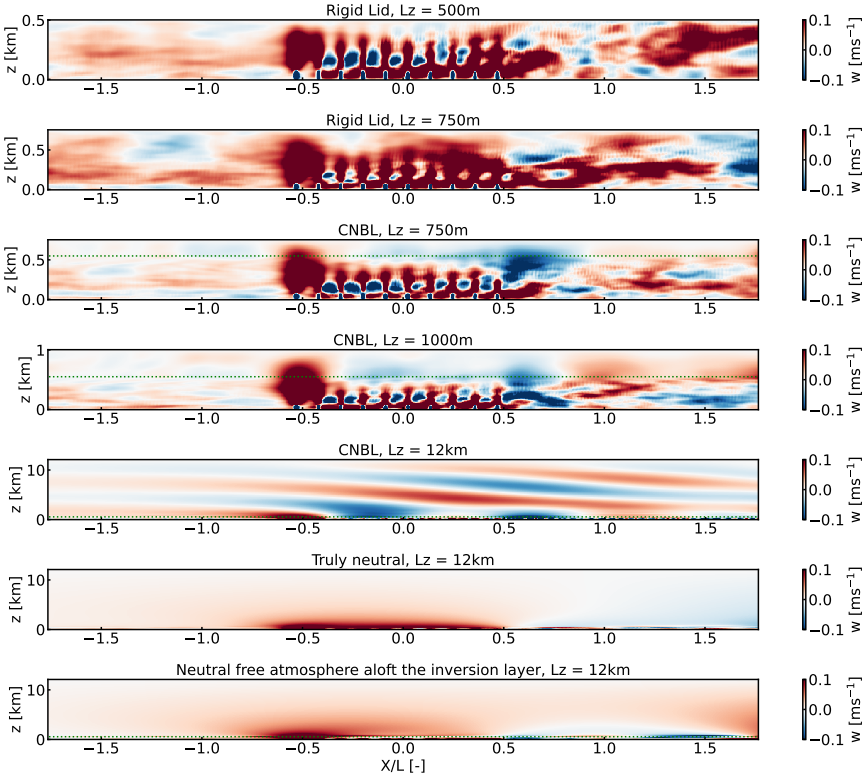

Figure 5.3: Temporally averaged vertical velocity through and around the wind farm with lengths $L = 5.67$ km from simulation configurations characterizing rigid lids, CNBLs, truly neutral, and the idealized configuration with both the ABL and free atmosphere being neutral. The horizontal dotted line shows the capping inversion mid-height where implemented.

TRULY NEUTRAL AND RIGID LID CONFIGURATIONS

Truly neutral configurations are helpful when the interaction of the wind farm with only a neutral ABL is of interest. This approach is somewhat of an academic curiosity and

might not occur realistically, as it assumes that the atmosphere, even beyond the turbulent ABL, is neutral. It can be of use to study turbines with heights much smaller than the ABL. However, modern wind turbines in large wind farms can interact with the atmosphere above the ABL [10]. Still, many LES studies have used the TNBL configuration, where a pressure gradient or constant geostrophic wind drives the boundary layer. [21, 22]

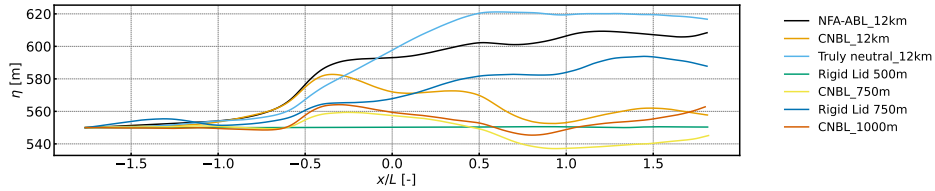

Figure 5.4: Particle vertical displacement, η, versus horizontal distance along the domain at capping inversion mid-height $L_z = 500$ m, thus representing the displacement of an air parcel perturbed by the wind farm and analogous to capping inversion displacement for the cases simulating one. The wind farm stretches from $x/L = -0.5$ to 0.47.

For a TNBL simulation, a constant potential temperature in a domain a few times taller than the intended ABL height is simulated. The ABL can freely expand vertically until an equilibrium with the non-turbulent free atmosphere is achieved. Therefore, the truly neutral simulation configuration detailed in Table 5.1, Set 1 (a) has an ABL height of $H_i = 500$ m at the inflow boundary, and the domain height is $L_z = 12$ km. The domain height matches that of the reference case (i.e. CNBL configuration fully resolving AGWs), but the simulation does not use a top RDL because there is no buoyancy to trigger AGWs in the truly neutral case. As shown on the vertical velocity plots in Fig. 5.3, the ABL displaces vertically in reaction to horizontal flow deceleration through the wind farm without being constrained by the rigid top boundary. This is also confirmed in Fig. 5.4, as the particle path traced through the domain starting at an initial ABL height of 500 m at the inflow initially rises and then asymptotes at a height far lower than the domain height. Moreover, this particle path shows the highest vertical expansion among the cases investigated, as there is no capping inversion to cap the vertical displacement of the ABL.

Like truly neutral cases, the rigid-lid configurations have a constant potential temperature, but the domain height is defined at the inversion layer or ABL height. In a physical sense, the top boundary acts like an immovable capping inversion that constrains the vertical displacement of the flow in reaction to the horizontal flow deceleration caused by the wind farm. This constraint on vertical velocity suggests that, to enforce continuity, the flow cannot decelerate as it naturally would. The closer the top boundary is placed to the top of the turbines, the greater this effect on the wind farm. The fact that the top boundary placement decreased horizontal flow deceleration through the wind farm can be witnessed on the vertical velocity contours for the rigid lid simulations shown in Fig. 5.3, where the domain heights are 500 m and 750 m. The particle paths for the rigid lid cases shown in Fig. 5.4 are concrete evidence of an immovable top boundary; vertical flow is completely suppressed when $L_z = 500$ m compared to the truly

neutral case. This "channel" effect is small for the rigid-lid $L_z = 750$ m case but is very pronounced compared to the truly neutral and the reference cases that use much taller domains.

PARTIAL-TO-FULLY RESOLVED CNBL CONFIGURATIONS

The discussion in Section 5.3.1 clearly shows the importance of simulating domains tall enough to exclude channel effects caused by too low a top boundary. However, temperature conditions beyond a few hundred meters above the sea surface are not always neutral; instead, a stable capping inversion and free atmosphere aloft are frequent. Thus, the discussion naturally leads to whether or not an inversion layer and the free atmosphere should be included in wind farm simulations. Moreover, to what extent should the free atmosphere be resolved to capture all phenomena relevant to wind-farm–atmosphere interaction? These questions can be answered by comparing CNBL configurations that partially resolve AGWs with a configuration that fully resolves them; these configurations are detailed in Table 5.1, Set 1 (c). Only inlet Rayleigh and advection damping layers are implemented for CNBL-750 m and CNBL-1000 m setups, as there is barely any free atmosphere resolved for the internal waves to form.

Besides properly resolving AGWs, avoiding the effect of the top boundary to constrain the capping inversion displacement is critical. The evidence of unresolved, partially, and fully resolved AGWs can be seen on the temporally averaged vertical velocity contours for three CNBL cases, $L_z = 750$ m, 1000 m, and 12 km, shown in Fig. 5.3. No AGWs are seen for the case with $L_z = 750$ m, traces of interfacial waves are seen when $L_z = 1000$ m, and all AGWs are resolved when $L_z = 12$ km. Since AGWs perturb the capping inversion, improperly resolved AGWs will show unrealistic impacts on the flow in the ABL. In less tall computational domains, improperly resolved AGWs and the channel effect both contribute to unrealistic flows in the ABL. This can be appreciated from the particle paths for CNBL cases shown in Fig. 5.4. A particle traced at the top of the capping inversion shows suppressed vertical movement for the cases with less tall domains compared to the tallest one. Placing the top boundary close to the capping inversion accelerates the flow in the free atmosphere and suppresses the realistic displacement of the capping inversion.

Fully resolving AGWs requires a computational domain much taller (i.e. $L_z = 2L_s$) than one sufficient to eliminate the constraining channel effect of the top boundary. This is obvious when the particle path for the case of fully resolved AGWs is compared to the truly neutral case. The particle path for the case of fully resolving AGWs characterizes the perturbations from the wind farm and the AGWs. The ABL does not expand progressively, and flow acceleration effects from the top boundary are absent. The global maxima and minima on this path are evidence of two disturbance sources, each inducing a wave train in the free atmosphere. The fact that the path is wavy downstream of the wind farm shows the resultant interfacial wave, which is the result of superimposed internal waves in that region and the interfacial waves advected downstream for this supercritical case. Therefore, the configuration fully resolving AGWs is most realistic and accurate in mimicking wind-farm–atmosphere interaction for shallow ABL conditions (i.e. CNBLs).

CAPPING INVERSION BETWEEN NEUTRAL FREE ATMOSPHERE AND ABL

The discussion on CNBL configurations in Section 5.3.1 asks whether modeling a stratified free atmosphere is essential. This curiosity is settled by simulating a configuration similar to the case that fully resolves the AGWs, with the key difference that the free atmosphere potential temperature profile is neutral, details of which are given in Table 5.1, Set 1 (d). The only stable layer is the capping inversion. Figure 5.3 shows that there are no internal waves, but trapped lee waves at the capping inversion are present. We use no damping layers in this simulation setup. The significance of including the free atmosphere's stability can be appreciated from the particle path traced for this scenario. The path is similar to that of the case that fully resolves AGWs up to the second row of the wind farm; beyond that, the capping inversion slowly moves upwards and approaches that of the truly neutral case far downstream. This rising tendency of the capping inversion in response to the wind farm perturbation is because the buoyancy of the free atmosphere is absent to mask it. In the physical sense, the free atmosphere's buoyancy acts like a spring's stiffness; the buoyancy of the free atmosphere restores the displaced capping inversion. Without buoyancy, the restoring force that suppresses capping inversion vertical displacement is missing. The impact of flow entrainment at the end of the wind farm on the capping inversion is almost unnoticeable. Moreover, the wavy path downstream of the wind farm is the signature of trapped lee waves only because there are no internal waves.

COMPARISON OF WIND FARM POWER FOR THE CONFIGURATIONS

Figure 5.5 compares wind farm power output for the configurations described earlier. The solid lines show the averaged power output of the wind turbines, where we average both in time and along spanwise turbine rows. The dashed lines show the difference between averaged power output for each configuration and that of the case that fully resolves AGWs (the CNBL-12 km case) assuming it is the most realistic. Several conclusions can be drawn from these power plots and their comparisons. First, the power output follows the same trend along the wind farm length, regardless of the configuration used. A few notable aspects of this trend include the greatest power decrease for the turbines in the second row, increasing power output until the fifth row, and slightly decreasing towards the last row. The highest drop for the second turbine is because of the velocity deficit caused by the first turbine, and little to no turbulent flow entrainment from above. The increasing power output after the second row suggests better wake mixing and recovery from the sides and above the wakes. The flow has fully developed by the fifth row and mixing has reached equilibrium. The truly neutral simulation gives the best perspective of the power for turbines beyond the fifth row, as it excludes flow "channeling" effects caused either erroneously by too low a top boundary or realistically by inversion layer displacement effects.

Comparing the configurations, we observe that the rigid-lid cases appear to have the most overestimated wind farm power output, inferred in the above discussions as the consequence of the channel effect caused by too low a top boundary. It is further inferred that the power curves for the rigid-lid cases would approach that of the truly neutral case if one keeps increasing the domain height. Surprisingly, the power profile predicted by the CNBL cases, partially resolving the AGWs, is almost the same as that of the rigid-lid

case with $L_z = 750$ m. This shows that including a capping inversion without sufficiently resolving the free atmosphere has the channeling effect almost completely dominating the stratification effects. The power plot for the case where the free atmosphere was kept neutral above the capping inversion of the same strength as that of the CNBL cases is interesting: this plot roughly matches the reference tall CNBL case until the fourth row. Beyond the fourth row, the simulated power is less than the reference case, signifying the absence of favorable pressure gradients in that region caused by internal waves and the capping inversion constraining the vertical flow mixing in the ABL when compared to the truly neutral case. This mismatch shows the importance of modeling a stable free atmosphere.

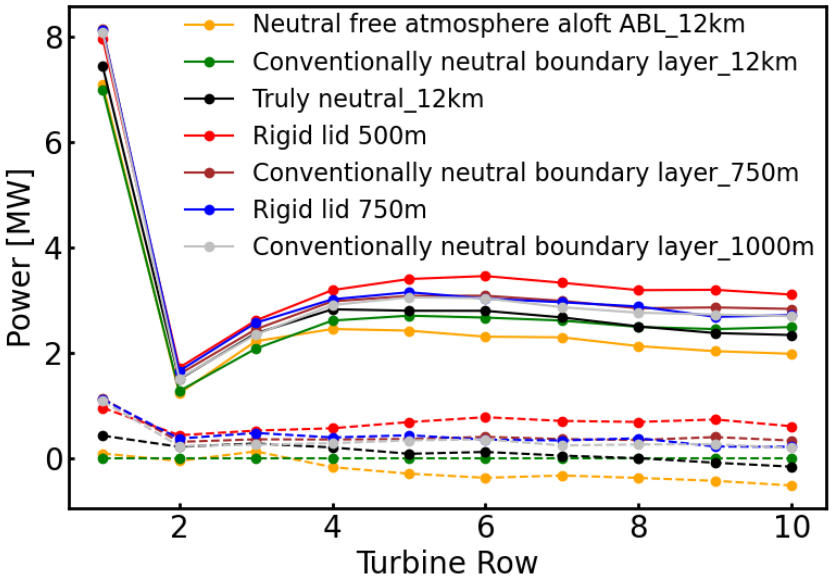

Figure 5.5: Temporal and row-averaged power as a function of domain height for truly neutral, Rigid lid, CNBL, and NFA-ABL configurations to mimic neutral surface conditions. The solid lines show actual power, whereas the dashed lines show the difference between the actual power predicted by each configuration and that of the reference case.

The dashed lines show that all configurations, except the one with a neutral free atmosphere, underestimate the global blockage effect and overestimate wind farm power output compared to the reference case that fully resolves AGWs. The higher power produced by the first row turbines in all cases compared to the reference case is evidence of the underestimated global blockage effect. Interestingly, the simulated power of the reference case approaches that of the truly neutral case towards the far end of the wind farm.

5.3.2. NON-DIMENSIONAL PARAMETER DEPENDENCE OF CAPPING INVERSION LAYER SHAPE AND AGW CHARACTERISTICS

With optimal T-RDL strength established, we now address the dependence of the AGW characteristics on the physical non-dimensional parameters listed in Table 1.2. The following subsections discuss capping inversion shape and interfacial and internal wave characteristics as a function of the physical non-dimensional parameters. The capping inversion shape at steady state shows how the flow in the ABL, capping inversion, and free atmosphere are coupled Stipa *et al.* [6]. We estimate the capping inversion shape from temporally averaged streamwise and vertical velocity fields, and examine AGW characteristics using the vertical velocity field only. The methods used to measure these representative features should always be used with a thorough visual analysis of flow fields. Note that the domain width was set to 18 km for the case $\tilde{H}_i = 0.042$. The initially used 6 km wide domain was too narrow for simulating the capping inversion at a height of only 250 m. The AGWs are strong in shallow boundary layers and high wind veer recycled the AGWs from the lateral boundaries into the wind farm, effecting its power output.

CAPPING INVERSION DISPLACEMENT DEPENDENCE ON PHYSICAL NON-DIMENSIONAL PARAMETERS

AGW characteristics are strongly related to the displacement of the capping inversion, which can be depicted by its shape at steady state. For instance, the positive and negative displacements of the capping inversion at the start and the end of the wind farm are a result of the two main flow disturbances that trigger gravity waves, the bulk upflow and downflow at the upstream and downstream wind farm edges, respectively. Moreover, the wavy capping inversion shape downstream of the wind farm shows the resultant interfacial waves. Each positive and negative vertical displacement of the capping inversion is inherently linked to diverging and converging flows underneath in the ABL. The size and strength of these convergent and divergent ABL flow zones are related to AGW characteristics. With a convergence comes a horizontal flow acceleration; with a divergence comes a deceleration.

After initial temporal transients, the capping inversion settles into an equilibrium shape that depends on the flow conditions and wind farm size, which we describe with the physical non-dimensional parameters. The capping inversion height varying in streamwise direction as a function of the physical non-dimensional numbers, is shown in Fig. 5.6. In analyzing these graphs, the focus is on the shape of the capping inversion at various streamwise locations to relate it to the global blockage effect and favorable and unfavorable pressure distributions through and downstream of the wind farm. As described in Section 5.3.1, the capping inversion shape is computed by tracing a particle path along the capping inversion top. As seen in Fig. 5.6, the general capping inversion shape has global maxima, always at around the wind farm start, linked to the horizontal flow deceleration caused by the wind farm. Conversely, global minima are usually at the end of the wind farm, thus linked to the acceleration of the horizontal flow in the exit and wake regions of the wind farm. In some cases, wave interference leads to complex capping inversion shapes. The maximum capping inversion displacement is also measured from its shape by differencing the highest and lowest vertical positions on the particle path.

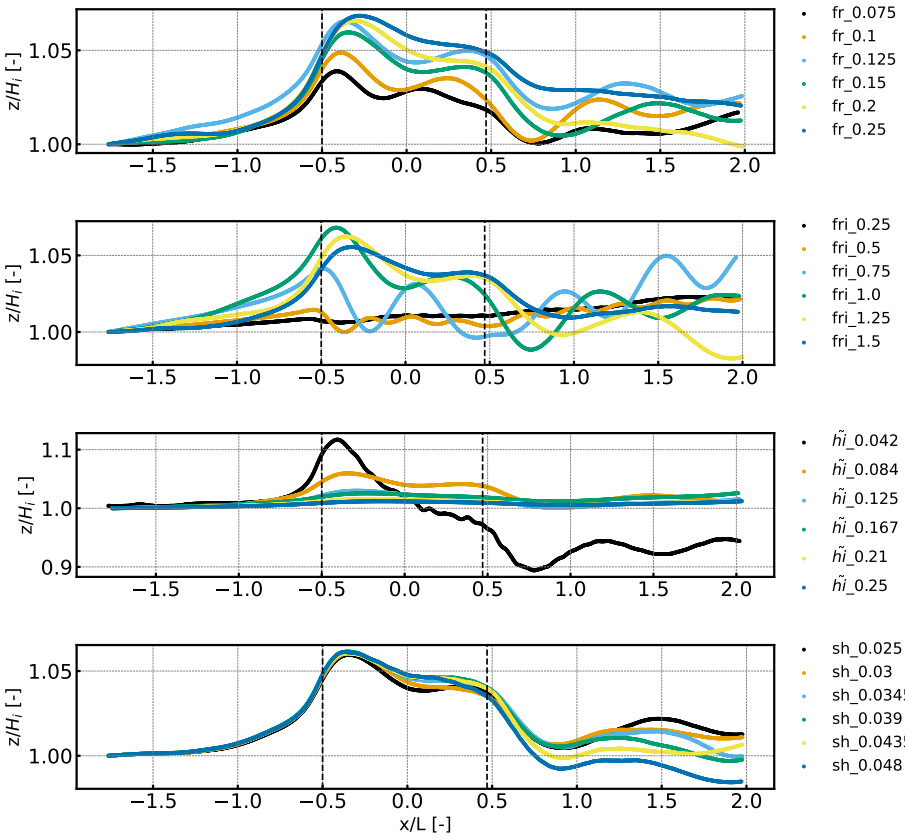

Figure 5.6: Capping inversion displacement along the streamwise direction as a function of Fr, Fr_i, $\tilde{H}_i$, and S_h. Unlike the rest, data points $Fr_i = 0.25$ and 0.5, given for completeness, are created from simulations with laminar inflows.

The variations in interfacial wavelengths for varying values of the non-dimensional parameters can also be appreciated from these capping inversion shapes.

The maximum capping inversion displacement normalized by turbine diameter (CI_{disp}/D) as a function of Fr, Fr_i, $\tilde{H}_i$, and S_h is shown Fig. 5.7. CI_{disp}/D increases abruptly for increasing Fr until 0.0125, increases only slightly for larger Fr. The physical meaning of increasing maximum displacement can be inferred as reduced atmospheric stability or milder response by buoyancy. A disturbance can displace the capping inversion slightly more than it could for a more stable-free atmosphere. The trend is not monotonic around $Fr = 0.15$, though, which is likely caused by the complex interference of the two internal wave trains. CI_{disp}/D is maximum for $Fr_i = 1.0$, as positive capping inversion displacement is the highest for critical conditions. Note that only one value of $Fr_i < 1.0$ is practical because values of $Fr_i < 0.75$ require impractical capping inversion strengths when H_i is kept constant. The estimated capping inversion displacements

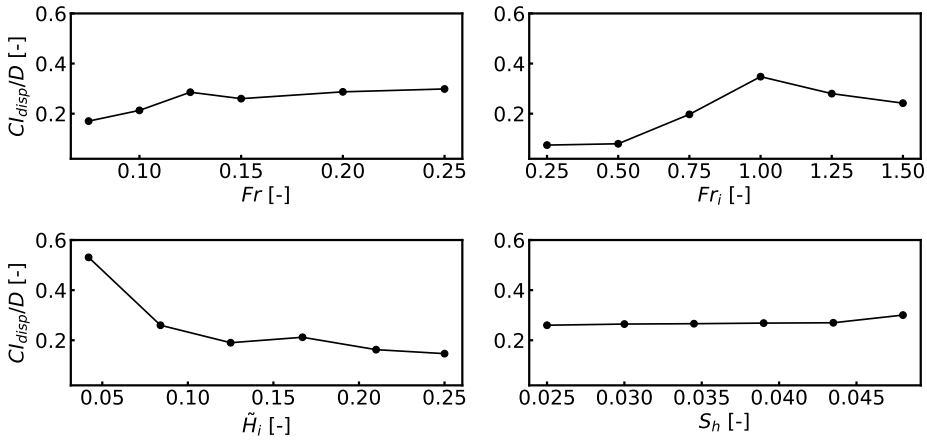

Figure 5.7: Maximum inversion layer displacement as a function of Fr, Fr_i, $\tilde{H}_i$, and S_h.

5

from the two simulations with impractical capping inversion strengths (i.e., $Fr_i = 0.25$ and 0.5) confirm capping inversion displacement smaller than that of the $Fr_i = 1.0$ case. In a physical sense, Fr_i approaching 0 would mimic a rigid lid that would barely move due to the disturbance from a wind farm. On the other hand, the decreasing CI_{disp}/D for values of $Fr_i > 1.0$ is because of background flow washing away buoyancy effects, thus weakly perturbing the capping inversion.

The maximum capping inversion displacement as a function of the ABL-aspect ratio shows an intuitive behavior. The maximum capping inversion displacement decreases for increasing $\tilde{H}_i$ values because the capping inversion is further from the wind farm. Thus, the global minimum of capping inversion displacement in the wind farm wake region is barely noticed for values of $\tilde{H}_i > 0.17$. The maximum capping inversion displacement is mildly sensitive to S_h as placing the wind turbines closer to the capping inversion perturbs it slightly more than the rotors at standard hub heights, i.e. $90-150$ m, but still negligible when normalized with the rotor diameter. Note that this observation is in the context of the wind farm layout and turbine size simulated in this study. We infer that a wind farm of higher power density and one with bigger turbines might be stronger momentum sinks, causing bigger capping inversion displacements.

NON-DIMENSIONAL PARAMETER DEPENDENCE OF INTERFACIAL WAVES

In Section 5.3.2, we indicate that the properties of AGWs depend on the physical non-dimensional parameters. This section analyzes the dependence of interfacial wave characteristics on these parameters.

Interfacial waves are bound to the capping inversion, and their wavelengths are correlated to the sizes of converging and diverging zones in the ABL. Thus, the average interfacial wavelengths can be calculated along the inversion layer top by using the following expression.

$$\lambda_{ifgw} = \frac{2\sqrt{(x_e - x_s)^2 + (y_e - y_s)^2}}{n_{peaks}}, \tag{5.1}$$

where (x_s, y_s) and (x_e, y_e) are the coordinates of the first and last peaks along the capping inversion that extends from the wind farm entrance to exit, respectively, and n_{peaks} is the total number of peaks (i.e. maxima and minima). Since it is calculated in the streamwise direction, it is the average horizontal wavelength. We calculate the interfacial wavelength over the length of the wind farm, as it is more suitable for this study.

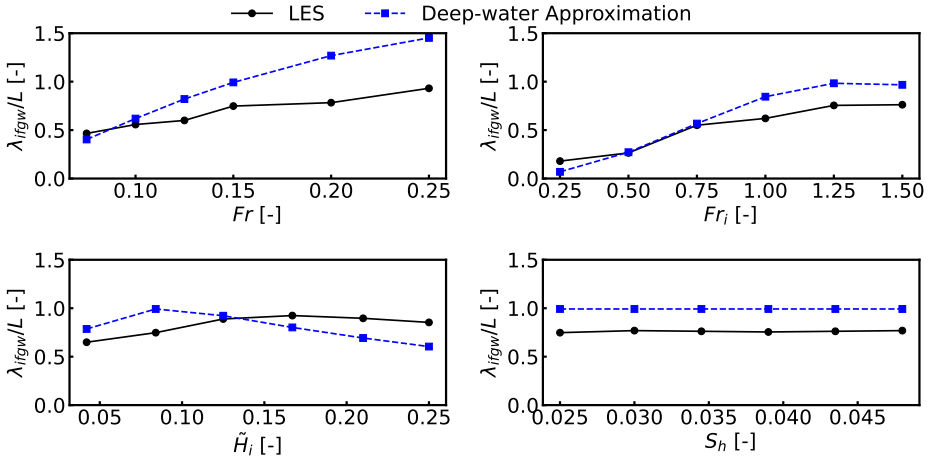

Figure 5.8: Interfacial wavelengths normalized with wind farm length as a function of Fr, Fr_i, $\tilde{H}_i$, and S_h. A comparison of wavelengths calculated from LES data with those estimated with the deep-water approximation, where the ABL depth is considered large enough and therefore insignificant.

The interfacial wavelengths normalized with wind farm length (λ_{ifgw}/L) as a function of Fr, Fr_i, $\tilde{H}_i$, and S_h are shown in Fig. 5.8. The interfacial wavelengths based on the deep-water approximation are also calculated, referred hereafter as theoretical wavelengths, and presented for comparison. This approximation excludes the impact of ABL depth on the interfacial wavelengths and is valid when $kH_i \gg 1$, where k is the horizontal wavenumber given by Sachsperger *et al.* [23] as

$$k = \frac{g'}{2U^2} + \frac{N^2}{2g'}. \tag{5.2}$$

The theoretical wavelengths calculated from the deep-water equations is then $\lambda_{ifgw} = 2\pi/k$, which depends on the reference potential temperature and the temperature jump across the capping inversion, and the stability in the free atmosphere. Clearly, the theoretical λ_{ifgw} is independent of the boundary layer height, thus applicable to deep boundary layers only.

As can be visually seen in Fig. 5.9, the calculated λ_{ifgw} increases for increasing Fr; the interfacial waves become skewed, which means the height of the darkest-colored

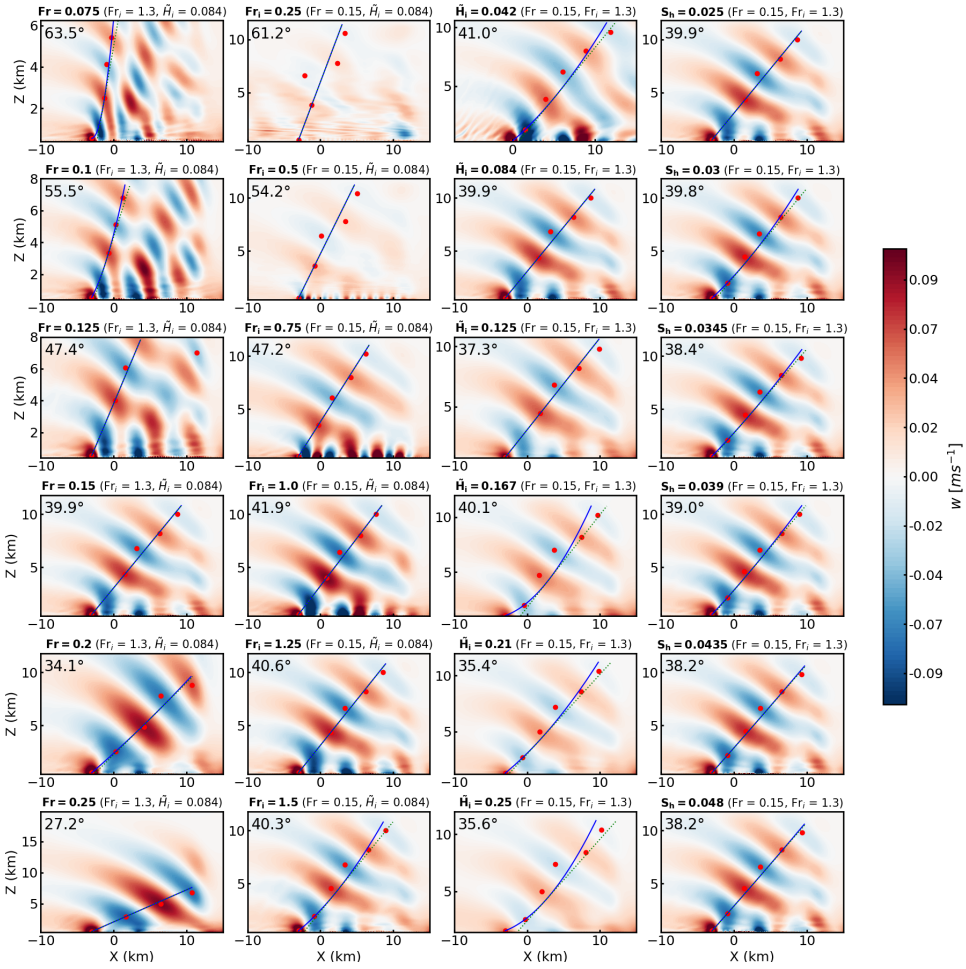

Figure 5.9: Temporally averaged vertical velocity plots, inclination angles with the horizontal axis, and peaks at maximum and minimum vertical velocities fitted with a parabolic curve. The vertical planes in a column are for the varying value of Fr, Fr_i, $\tilde{H}_i$, or S_h, while the other parameters were kept constant. Note that plots for $Fr_i = 0.25$ and 0.5 are taken from simulations driven by uniform inflows, given for completeness.

regions at the bottom of the contours, which is representative of the interfacial waves, shrinks. Even the propagating internal waves are strongly constrained from propagating vertically, so the wave field appears tilted more downstream. The calculated interfacial wavelengths are observed to be half the wind farm length for the lowest Fr and gradually increase to about full wind farm length for the highest Fr. Thus, the sizes of zones of favorable and unfavorable pressure gradient in the ABL vary between $0.25L$ and $0.5L$ for increasing Fr. The calculated λ_{ifgw} for Fr also shows an increasing trend but is distinct from that of the calculated one. The calculated values agree with the calculated only for low values of Fr. This could be because kH_i for constant H_i = 500 m is significantly

greater than unity for only low values of Fr.

Both calculated and theoretical λ_{ifgw} increase roughly linearly with Fr_i until an asymptote at 0.75 L for the calculated and at L for the theoretical is reached when Fr_i = 1.25. There is good agreement between calculated and theoretical for sub-critical conditions, but a discrepancy arises beyond critical conditions ($Fr_i \geq 1.0$). The matching values of λ_{ifgw} are mainly because it varies in response to only varying $\Delta\theta$ in setting Fr_i while holding H_i and N fixed at 500 m and 0.01 s^{-1}, respectively. We recall from Section 5.3.2 that the capping inversion becomes more sensitive for sub-critical values of Fr_i and interfacial waves are smaller than for super-critical values. For instance, the two laminar inflow cases mentioned in Section 5.3.2 (i.e. Fr_i = 0.25 and 0.5) showed that λ_{ifgw} approaches the streamwise turbine distancing as if each turbine row is triggering an interfacial wave. Whereas, for super-critical conditions, the capping inversion perturbs on length scales increasing between half to three-quarters of the wind farm length. This means that the sizes of zones of favorable and unfavorable pressure gradient in the ABL vary between row-distancing and 0.4L for increasing Fr_i.

Unlike the theoretical λ_{ifgw}, the calculated values show an increasing trend against $\tilde{H}_i$ until they reach a maximum of about λ_{ifgw}/L = 1.0 for $\tilde{H}_i$ = 0.17. The interfacial wavelengths become slightly shorter for further increasing $\tilde{H}_i$. This shows that the wind farm is seen as a single disturbance beyond a certain ABL-aspect ratio, and the capping inversion receives a weaker and spread-out disturbance. The theoretical λ_{ifgw} shows the increasing trend only until $\tilde{H}_i$ = 0.084, beyond which it shows a linearly decreasing trend with an almost perfect match between theoretical and calculated for $\tilde{H}_i$ = 0.0125. These observations indicate that the deep-water approximation follows these simulations only for deep ABLs. The sizes of zones of favorable and unfavorable pressure gradient in the ABL vary between 0.25L and 0.4L for increasing $\tilde{H}_i$. As expected, S_h has a negligible impact on the interfacial wavelengths; both theoretical and calculated λ_{ifgw} are independent of it. The λ_{ifgw} is the same as that of Fr = 0.15.

Generally, the amplitude of interfacial waves varies in the narrow range of 0.19D – 0.3D, where D is rotor diameter, against the physical non-dimensional parameters, except for $\tilde{H}_i$, where the range is 0.2D – 0.6D, which is shown in Fig. 5.7. For low values of $\tilde{H}_i$, the capping inversion displacement is higher, and strong waves are present, as the two are directly proportional [10]. Amplitudes of interfacial waves are analogous to capping inversion displacements, which are already reported in Section 5.3.2. Moreover, the inclination angles of interfacial waves with respect the lateral axis are dependent only on Fr_i and have already been investigated by Lanzilao and Meyers [5].

NON-DIMENSIONAL PARAMETER DEPENDENCE OF INTERNAL WAVES

The propagating internal waves are relatively weaker in strength than the interfacial waves, and their properties depend mainly on Fr and Fr_i. A major challenge in measuring their properties is that there are two internal wave trains superimposing on each other, one from the front of the farm and one from the rear. Especially for high Fr, the superimposition is evident as the inclination angle is expected to be higher. Therefore, we focus on the first wave train, as we did in Section 5.2.2, as it is less distorted.

Figure 5.10 shows wave field inclination angle, as defined in Section 5.2.2, extracted from average vertical velocity fields as a function of the four physical non-dimensional

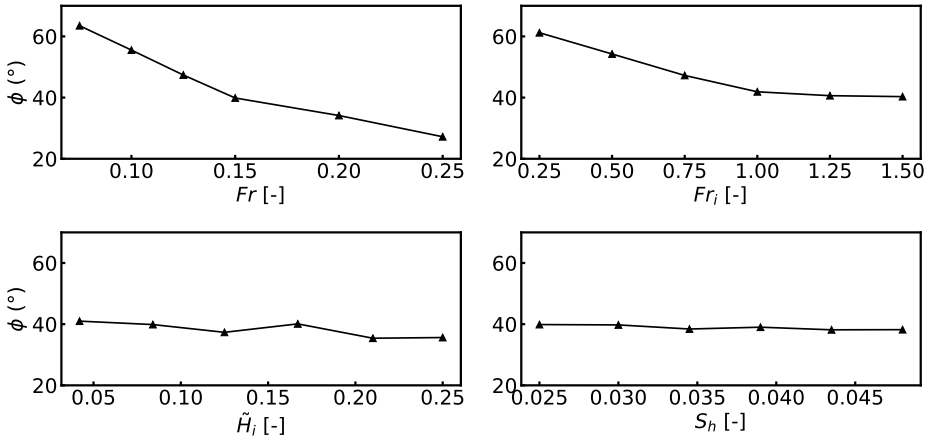

Figure 5.10: Inclination angle of internal waves as a function of Fr, Fr_i, $\tilde{H}_i$, and S_h.

5

parameters. The inclination angle shows a decreasing trend against increasing Fr starting at around 63°, for $Fr = 0.075$, and approaching around 27° for $Fr = 0.25$. The reduced slope for $Fr \geq 0.15$ of the line connecting the data points means that the two internal wave trains are more distinct; for higher values of Fr, the first wave train stretches across the length of the domain, see in Fig. 5.9. The inclination angle has the same decreasing trend with increasing Fr_i, decreasing from 61° to 40°. This 40° value is roughly the same as for $Fr = 0.15$, and in the varying Fr_i cases, Fr is held at 0.15. The inclination angle of the internal waves seems almost independent of $\tilde{H}_i$ and S_h. There is a variation for the former, but in a narrow range of $41 - 35$°, probably caused by varying capping inversion displacement against $\tilde{H}_i$.

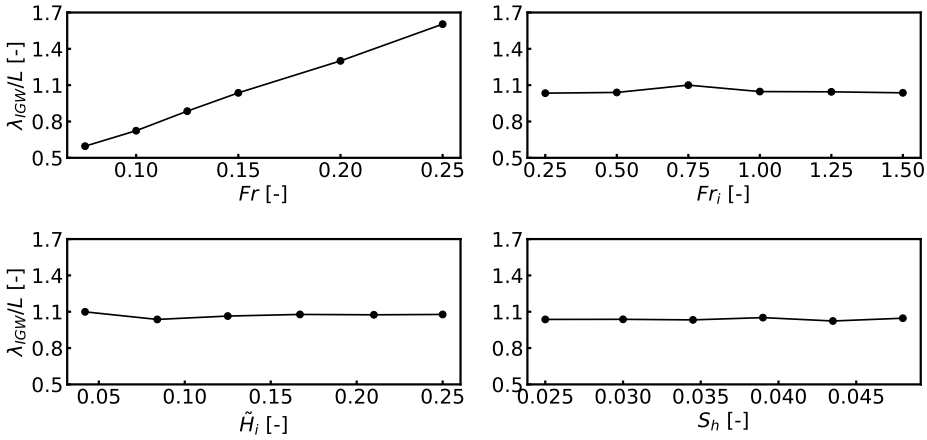

Figure 5.11: Actual wavelength of internal gravity waves as a function of Fr, Fr_i, $\tilde{H}_i$, and S_h.

The apparent wavelength, measured along the fit parabola, of the first wave train is dependent on its inclination angle. In measuring this wavelength, it is assumed that the interference of the two wave trains is minimal for values of $Fr \leq 0.15$. We also recall that the measured wavelength with the method proposed in Section 5.2.2 allows us to estimate horizontal and vertical components of the actual wavelength. Thus, the effective horizontal wavelength could be $\lambda_a = 2\lambda_a \cos\phi$, equivalent to the sum of horizontal wavelengths of the two dominant wave trains. The apparent wavelength of the first wave train, normalized with L and as a function of the physical non-dimensional parameters, is given in Fig. 5.11. Generally, this wavelength increases linearly and is smaller than the wind farm length for values of $Fr \leq 0.15$. This linear increase is mainly due to increasing buoyancy length (i.e. L_s), which is directly proportional to Fr. Note that the first wave train is dilated and merged with the second for $Fr > 0.15$ by the increasing background speed, and only one wave train is obvious in the solution, as shown in Fig. 5.9.

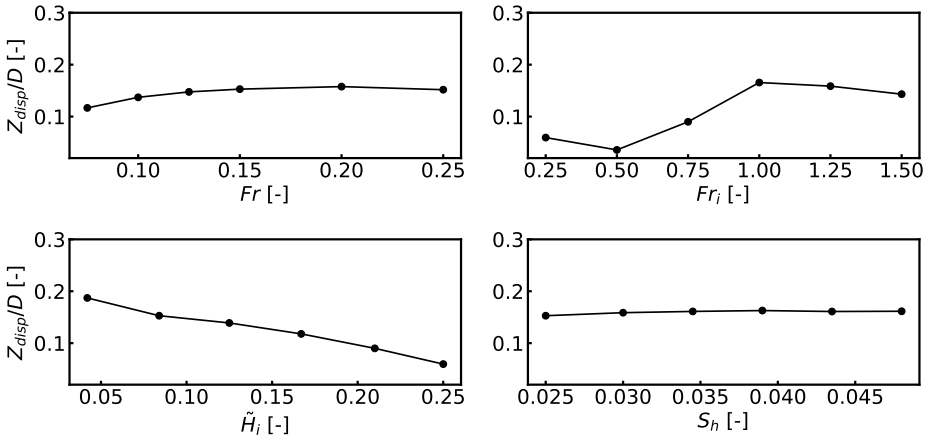

Figure 5.12: The amplitudes of internal waves calculated as the amplitude of streamline displacement at a height $H_i + 3/4L_s$ as a function of Fr, Fr_i, $\tilde{H}_i$, and S_h.

As stated at the start of this section, the internal wave properties are mainly affected by Fr. This is obvious when the apparent wavelength plots for the remaining physical non-dimensional parameters are analyzed, where $Fr = 0.15$ while varying each. Thus, λ_{igw}/L varies in the narrow range of $0.9L - 1.1L$ for the simulated values of Fr_i, $\tilde{H}_i$, and S_h. The values reported for $Fr_i = 0.25$ and 0.5 are inaccurate, as negligible internal waves were observed for these idealized cases, as can be seen in Fig. 5.9. Small variations about the average value (i.e. $1.0L$), which is roughly the value for $Fr = 0.15$, for varying Fr_i, $\tilde{H}_i$, and S_h are the impacts of the interference of the two wave trains that depend on the inclination angles. For instance, the λ_{igw}/L plot against Fr_i resembles the decreasing inclination angle trend against Fr_i shown in Fig. 5.10. In the case of $\tilde{H}_i$, the wavelength increases with increasing $\tilde{H}_i$, where for the shallowest boundary layer simulated, the wavelength is slightly smaller than that for $Fr = 0.15$. For low $\tilde{H}_i$, the capping inversion feels both disturbance sources more isolated, but beyond $\tilde{H}_i = 0.17$, the wind farm is an entity, as the growing internal boundary layer rather than the two disturbance

sources perturb the capping inversion. Thus, the wavelength resembles a dilated single disturbance. There is barely any change in the wavelength against S_h, as all simulated S_h values yield a wavelength as wide as $1.0L$, a virtue of the constant $Fr = 0.15$.

The amplitudes of internal waves, which are measured as the amplitude of streamline displacement, as a function of the physical non-dimensional parameters, are shown in Fig. 5.12. The amplitudes are measured by tracing a particle at $z = H_i + 3/4L_s$. There is little variation in the amplitudes as a function of Fr, except for a small increase from $0.11D$ to $0.14D$ between $Fr = 0.075$ and 0.125. The amplitude increases as a function of Fr_i only until $0.17D$, suggesting that the capping inversion becomes less rigid until the amplitude depends only on Fr. There is an almost linearly decreasing amplitude trend against $\tilde{H}_i$, going from $0.19D$ for $\tilde{H}_i = 0.025$ to $0.08D$ for $\tilde{H}_i = 0.25$. The reason for weaker internal waves for increasing $\tilde{H}_i$ was discussed in Section 5.3.2. The amplitudes only slightly increase over $0.17D$ against S_h, which is the value of amplitude for $Fr = 0.15$.

5.3.3. NON-DIMENSIONAL PARAMETERS DEPENDENCE OF WIND FARM AERODYNAMICS

Here, we analyze and discuss the dependence of wind farm performance on the physical non-dimensional parameters that define CNBL flow conditions. The capping inversion displacement couples the flow in the ABL with the capping inversion and the free atmosphere aloft. In this section, the simulated wind turbine power as a function of distance downstream is investigated and related to the capping inversion displacement. It is hypothesized that the local capping inversion displacement affects the power output of the wind turbines below, mainly as an additional effect to the prevailing induction effect for the first row and wake effects for the remaining rows. Thus, an element of the global blockage effect is a consequence of the capping inversion displacement upstream to the first row of the wind turbines as a result of the wind farm's solidity and energy extraction from the atmosphere. Moreover, the internal and interfacial waves, the latter only under sub-critical conditions, may contribute to the global blockage effect, as they can propagate upstream. This is strictly in the case that upstream propagation of these waves affects the capping inversion displacement, which is difficult to measure in an isolated manner. However, it is obvious that the first interfacial wave strongly contributes to the blockage effect. Often, it is stretched downstream, which affects the localized power output of the first few turbine rows. For values of $Fr > 0.15$, internal waves tilt downstream significantly and may superimpose onto the interfacial waves, affecting localized capping inversion displacement and impacting the localized power output. The enhanced wind farm wake recovery is mainly associated with the dropping of the capping inversion at the end of the wind farm. Under supercritical conditions, internal waves leave an imprint in the velocity field of the wake of the wind farm. Trapped lee waves dominate this imprint for $Fr_i \leq 1$. Adverse and favorable pressure gradients are correlated with the gradient of the capping inversion displacement, which varies in the streamwise direction. The dominant pressure variations are due to the capping inversion displacement caused by upward flow deflection at the entrance of a wind farm and downward deflection in its wake. The intensity of the pressure gradients is most sensitive to the ABL depth. For high values of ABL-aspect ratio, these gradients are relatively small. In

the following subsections, all of these preliminary claims will be supported by simulated turbine power outputs.

WIND FARM POWER OUTPUT

Here, we discuss how the global blockage effect and pressure variations relate to each non-dimensional parameter via the capping inversion displacement height at steady state. Generally, the localized capping inversion displacement has a negative correlation with the row-averaged power output. This means that a higher capping inversion corresponds to decreased power of the row underneath it and vice versa. Temporal and row-averaged power output are analyzed to uncover general trends in wind farm performance in the maximum wake loss scenario (i.e., when wind is straight down the rows). Figure 5.13 (a) shows the temporal and row-averaged wind turbine power output as a function of Fr and streamwise distance. Wind farm blockage decreases as Fr is increased. However, a narrow variation of 0.2 MW is observed for the power output of the 1st row over the simulated values of Fr. It is astonishing how the power output of the second row is completely independent of Fr as the wake effects dominate. Beyond the second row, the row-wise power output varies about a trend characteristic of aligned wind farm aerodynamics, with a maximum at the fifth or sixth row. Although subtle, variations are bound to the localized capping layer displacement aloft as discussed in Section 5.3.2. Generally, row-wise power output decreases beyond the fifth row until a slight increase is observed for the last two rows. The power output of individual rows beyond the second decreases slightly with increasing Fr except for $Fr = 0.075$ due to its unique capping inversion shape, which is shown in Fig. 5.6.

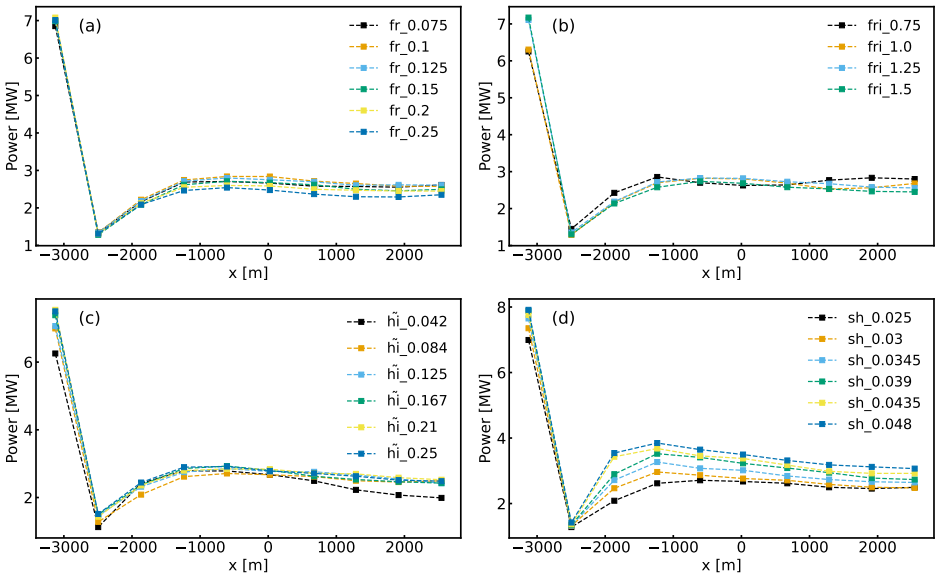

Figure 5.13: Temporal and row-averaged wind turbine power output as a function of (a) Fr, (b) Fr_i, (c) $\tilde{H}_i$, and (d) S_h.

Figure 5.13 (b) shows the row-wise power output for a few values of Fr_i. The wind farm blockage effect reduces with increasing Fr_i, where the strongest blockage is observed for the subcritical case (i.e. $Fr_i = 0.75$), but is almost the same as the critical case. The simulated power of the second row is the same for values of $Fr_i \geq 1.0$ but higher for $Fr_i = 0.75$ because the capping inversion displacement is negative in contrast to positive in the remaining cases. The fourth row produces the highest power for $Fr_i = 0.75$ among the waked rows because of the localized favorable pressure, as the capping inversion in the vicinity is at its lowest point. The highest power output among the waked rows is from the fifth-row turbines for the critical and supercritical cases. The simulated power shows a gradual decrease past the fifth row for values of $Fr_i \geq 1.0$ until the seventh row, beyond which it increases slightly. The fact that power oscillates with distance downstream for $Fr_i = 0.75$ is evidence of power's negative correlation to the localized capping inversion displacement. This also confirms that gravity waves can cause several zones of converging and diverging flow through the wind farm.

The simulated row-wise power profile is the most sensitive to the ABL-aspect ratio, as shown in Fig. 5.13 (c). For $\tilde{H}_i \leq 0.167$, the power profile follows the trend as that of $Fr = 0.15$ and $Fr_i = 1.3$ because these are the constant values simulated while varying $\tilde{H}_i$. However, the power profile for the shallowest ABL ($\tilde{H}_i = 0.042$) is most affected by localized capping inversion displacement, which can be revisited in Fig. 5.7. The wind farm blockage is highest for $\tilde{H}_i = 0.042$ and reduces as $\tilde{H}_i$ increases until it becomes almost independent for $\tilde{H}_i \geq 0.21$ because the deflected flow at the wind farm entrance barely perturbs the capping inversion. The simulated power of the individual turbines increases with increasing $\tilde{H}_i$ as inflow turbulence intensity increases, as the ABL gets deeper [24]. The simulated power output profiles for $\tilde{H}_i \geq 0.167$ are almost the same, as the capping inversion hardly affects the flow build-up through the wind farm. Thus, the flow around the wind farm becomes similar to that of a truly neutral boundary layer with the same ABL height. We can infer that the internal boundary layer has sufficient space to grow vertically, and pressure variations caused by stratification effects or gravity waves become smaller with increasing $\tilde{H}_i$. For shallow ABLs, the pressure perturbations caused by the stratification effects dominate the internal boundary layer growth and hence the power output profile. Thus, the capping inversion's height determines which phenomenon dominates and, in turn, the wind farm flow aerodynamics. When it is low, the stratification effects are increasingly critical to wind farm performance; otherwise, these effects are secondary when compared to wake losses. Thus, inflow characteristics and wake effects still remain primary to wind farm performance.

The vertical wind farm aspect ratio impacts the row-wise power profile mainly in the first half of the wind farm, as shown in Fig. 5.13 (d). Again, fixed values of non-dimensional parameters simulated include $Fr = 0.15$, $Fr_i = 1.3$, and $\tilde{H}_i = 0.084$. Thus, the power profiles follow the trend for $Fr = 0.15$ and $Fr_i = 1.3$, except that the highest power-producing row among the waked turbines shifts from the fifth row to the fourth as S_h increases. Higher velocities for increasing S_h are a clear factor in improved wind turbine and farm powers. However, stratification effects, though small, are still relevant as increasing S_h means putting the turbines closer to the capping inversion, which is similar to stronger perturbations and a different response for varying S_h.

Altogether, it is obvious that $\tilde{H}_i$ is the most critical physical non-dimensional pa-

rameter in terms of wind farm performance. Therefore, for low $\tilde{H}_i$, Fr and Fr_i can alter the capping inversion shape characteristic of the underlying $\tilde{H}_i$, thus affecting the row-wise power output. S_h can affect the power output mainly because of placing the wind turbines at higher or lower wind speeds, which has little to do with gravity waves or blockage. While simulating CNBLs, $\tilde{H}_i$ becomes more critical for shallow ABLs and will be of even greater importance for stable surface conditions with shallower ABLs than in CNBLs.

5.4. CONCLUSIONS

This study provides a systematic investigation of wind-farm–atmosphere interactions under neutral surface conditions using LES. Among the tested simulation configurations, CNBL simulation configurations that fully resolve AGWs are likely the most realistic for capturing stratification effects and differ significantly from TNBL cases. The CNBL configurations that only partially resolve AGWs predicted similar power outputs to rigid-lid cases, which are less practical. We showed that capping inversion displacement plays a central role in coupling the fluctuations in the ABL with those in the free atmosphere (i.e. AGWs). Interfacial and internal waves were identified as the main AGW types shaping the capping inversion, such that interfacial wavelength and the formation of converging and diverging zones in the ABL are correlated. The trapped waves confined within the capping inversion were transient and negligible. Overall, AGW behavior depends strongly on the ABL aspect ratio ($\tilde{H}_i$) and the Froude numbers of the free atmosphere (Fr) and the capping inversion (Fr_i). The interfacial wavelength reduces for decreasing Fr_i and approaches a quarter of the wind farm length for $Fr_i = 0.25$, whereas the amplitudes grow stronger for shallower inversions. Internal wave characteristics depend mainly on Fr.

Wind farm performance was most sensitive to the ABL aspect ratio: shallow inversions increased wind farm blockage and reduced wind farm efficiency, while deeper layers facilitated wake recovery and improved power output. Increasing Fr, Fr_i, and the wind farm aspect ratio (S_h) reduced blockage, enhancing efficiency. Localized spatial variations in power arose from the converging and diverging zones in the ABL associated with the wavy capping inversion. As a result, the total wind farm efficiency—which accounts for both wake losses and stratification effects—remained nearly constant with respect to Fr and Fr_i, but improved with increasing $\tilde{H}_i$ and S_h. These findings suggest that increased wind farm blockage always happens when there is stratification, primarily affecting the front row of turbines. Although weaker than the blockage effect, stratification-induced flow variations can cause downstream turbines to gain or lose power, but these effects were often dominated by stronger wakes.

This work clarifies the role of AGWs, which exist only in the stably stratified atmosphere, in wind-farm–atmosphere interactions and establishes the importance of selecting appropriate LES configurations. Beyond providing a coherent description of wind-farm-induced AGWs, it also gives guidelines for expected AGW characteristics such that one can configure reflection-free domains in CFD simulations. Although this study spans a wide range of CNBL conditions, it remains largely confined to canonical CNBL setups. We use a simple actuator disc model that is sufficient for generating gross wake effects and for estimating relative power levels. Therefore, we present relative trends in wind

farm performance, as opposed to absolute changes, as a function of changes in stratification. Future extensions could explore canonical stable and unstable ABLs, realistic atmospheric conditions, and more advanced actuator models. The results also point to the need for further study of clustered wind farms, particularly under shallow boundary layers where AGWs (i.e. stratification) have clear impacts.

REFERENCES

[1] M. A. Khan, M. J. Churchfield, and S. J. Watson, *Dependence of wind-farm-induced gravity waves and wind-farm performance on non-dimensional atmospheric parameters and simulation configuration,* Wind Energy Science Discussions **2025**, 1 (2025).

[2] M. A. Khan, S. J. Watson, D. J. N. Allaerts, and M. Churchfield, *Recommendations on setup in simulating atmospheric gravity waves under conventionally neutral boundary layer conditions,* Journal of Physics: Conference Series **2767**, 092042 (2024).

[3] M. Churchfield, S. Lee, and P. Moriarty, *Overview of the simulator for wind farm application (SOWFA),* National Renewable Energy Laboratory (2012).

[4] C. L. Archer, S. Mirzaeisefat, and S. Lee, *Quantifying the sensitivity of wind farm performance to array layout options using large-eddy simulation,* Geophysical Research Letters **40**, 4963 (2013), https://agupubs.onlinelibrary.wiley.com/doi/pdf/10.1002/grl.50911 .

[5] L. Lanzilao and J. Meyers, *A parametric large-eddy simulation study of wind-farm blockage and gravity waves in conventionally neutral boundary layers,* Journal of Fluid Mechanics **979**, A54 (2024).

[6] S. Stipa, M. Ahmed Khan, D. Allaerts, and J. Brinkerhoff, *A large-eddy simulation (LES) model for wind-farm-induced atmospheric gravity wave effects inside conventionally neutral boundary layers,* Wind Energy Science **9**, 1647 (2024).

[7] R. Smith, *The wind farm pressure field,* Wind Energy Science Discussions **2023**, 1 (2023).

[8] R. J. A. M. Stevens, J. Graham, and C. Meneveau, *A concurrent precursor inflow method for large eddy simulations and applications to finite length wind farms,* Renewable Energy **68**, 46 (2014).

[9] M. A. Khan, D. Allaerts, S. J. Watson, and M. J. Churchfield, *Investigating the relationship between simulation parameters and flow variables in simulating atmospheric gravity waves for wind energy applications,* Wind Energy Science **10**, 1167 (2025).

[10] D. Allaerts, S. V. Broucke, N. Van Lipzig, and J. Meyers, *Annual impact of wind-farm gravity waves on the Belgian-Dutch offshore wind-farm cluster,* Journal of Physics: Conference Series **1037** (2018), 10.1088/1742-6596/1037/7/072006.

[11] R. B. Smith, *Gravity wave effects on wind farm efficiency,* Wind Energy **13**, 449 (2010).

[12] D. Allaerts and J. Meyers, *Large eddy simulation of a large wind-turbine array in a conventionally neutral atmospheric boundary layer,* Physics of Fluids **27**, 065108 (2015).

[13] S. Stipa, A. Ajay, D. Allaerts, and J. Brinkerhoff, *TOSCA – an open-source, finite-volume, large-eddy simulation (LES) environment for wind farm flows,* Wind Energy Science **9**, 297 (2024).

[14] D. Allaerts and J. Meyers, *Boundary-layer development and gravity waves in conventionally neutral wind farms,* Journal of Fluid Mechanics **814**, 95 (2017).

[15] D. Allaerts and J. Meyers, *Gravity waves and wind-farm efficiency in neutral and stable conditions,* Boundary-Layer Meteorology **166**, 269 (2018).

[16] L. Lanzilao and J. Meyers, *An improved fringe-region technique for the representation of gravity waves in large-eddy simulation with application to wind farms,* Boundary-Layer Meteorology **186**, 567 (2023).

[17] C. Meneveau, T. S. Lund, and W. H. Cabot, *A Lagrangian dynamic subgrid-scale model of turbulence,* Journal of Fluid Mechanics **319**, 353–385 (1996).

[18] D. Allaerts, M. Khan, and M. Churchfield, *Froude number dependency of atmospheric gravity waves: Apparent horizontal wavelength and wave field inclination,* Submitted to Journal of Fluid Mechanics (2025).

[19] P. Queney, *The problem of air flow over mountains: A summary of theoretical studies,* Bulletin of the American Meteorological Society **29**, 16 (1948).

[20] J. R. Taylor and S. Sarkar, *Internal gravity waves generated by a turbulent bottom [e]kman layer,* Journal of Fluid Mechanics **590**, 331 (2007).

[21] Y.-T. Wu and F. Porté-Agel, *Modeling turbine wakes and power losses within a wind farm using LES: An application to the horns rev offshore wind farm,* Renewable Energy **75**, 945 (2015).

[22] A. Stieren and R. J. A. M. Stevens, *Impact of wind farm wakes on flow structures in and around downstream wind farms,* Flow **2**, E21 (2022).

[23] J. Sachsperger, S. Serafin, and V. Grubišić, *Lee waves on the boundary-layer inversion and their dependence on free-atmospheric stability,* Frontiers in Earth Science **3** (2015), 10.3389/feart.2015.00070.

[24] J. S. Brooke, R. Thedin, A. Sharma, E. Branlard, G. Vijayakumar, and A. S. Michael, *Effect of the integral length scales of turbulent inflows on wind turbine loads,* Renewable Energy **217**, 119 (2023).

Photo from D. von Terzi and M. Jonkhof,
"How to manage innovations and tech-
nologies to lower wind cost of energy",
EAWE PhD Seminar, Stuttgart, Sep. 25, 2015

6

Impact on Clustered Wind Farms

In Chapter 5, we investigated AGWs, including their characteristics, and their relation to the performance of an isolated offshore wind farm under CNBL conditions. Since offshore wind farms are increasingly placed in the vicinity of existing farms, it is vital to study the impact of AGWs on such clusters. Therefore, the aim of this chapter is to apply a systematic approach to investigate the characteristics of AGWs in and around two neighboring offshore wind farms under CNBL conditions and the impact on performance.

This chapter is structured as follows. Section 6.1 motivates the need to investigate AGWs in clustered wind farm scenarios. Section 6.2 describes the computational setup and the set of simulations performed with varying atmospheric CNBL conditions. Section 6.3 describes the AGW characteristics and performance of each wind farm as a function of the non-dimensional parameters. The development of the internal boundary layer and wind-farm wake is also presented. Section 6.4 provides insights on clustered-wind-farm–atmosphere interactions under varying CNBL conditions as a function of the physical non-dimensional parameters.

6.1. INTRODUCTION

An increase in offshore wind farm clusters is evident in the pursuit of net zero goals set by many countries, but the efficient performance of these clusters requires a thorough understanding of their interactions with the atmosphere. Multi-Gigawatt wind farm clusters are expected in the North Sea, Celtic Sea, and the coasts of the United States and China [1]. Some European countries have ambitious 2030 targets set for offshore wind: Denmark, the Netherlands, Germany, and the United Kingdom aim at 9, 21, 26, and 50 GW, respectively. This booming trend of building offshore wind-farm clusters brings challenges; one of the main ones is the understanding of wind-farm cluster interactions with the atmosphere. From an aerodynamic perspective, a change in the available wind resource of a farm downstream of another is an obvious risk. In addition, several atmospheric aspects become increasingly significant, given the large size of a cluster. For instance, the Coriolis effect, the thermal state of the atmosphere and synoptic-scale pressure gradients can all affect wind-farm cluster interactions with the atmosphere. Evidence of such effects can be discerned in Satellite Aperture Radar (SAR) images, where wind-farm cluster wakes can be visualized extending to several tens of kilometers. Moreover, the cluster wakes tend to skew and deflect due to the Coriolis effect at several wind-farm-cluster lengths downstream. This is indicated in the SAR image of wind farms in the North Sea shown in Fig. 6.1. In this figure, the roughness of the sea surface is shown. It is related to the wind speed and, therefore, visualizes the reduced wind speed areas resulting from cluster wakes. Inter-wind farm wake interactions are also measured using dual-doppler radar, like in the AWAKEN onshore field measurement campaign, where the wake of one of the three wind farms considered extends up to 30 km downstream for stable boundary layer conditions [2]. Moreover, both spanwise and vertical momentum transfer are found to be key mechanisms in wind-farm wake development and recovery.

Several numerical investigations, discussed in more detail below, of both real and hypothetical wind-farm clusters confirm the observations mentioned above. Non-CFD frameworks or engineering models are yet to include the full extent of thermal effects, Coriolis forcing, and accurate wake superposition techniques to capture wind-farm wakes [1]. At this point, CFD frameworks are more suitable than reduced-order models for investigating inter-farm interactions, as they include thermal and Coriolis effects and naturally capture wake characteristics. Nevertheless, some researchers have employed engineering models, often with comparison either against CFD predictions, SCADA data, or LIDAR measurements, to estimate infer-farm wake and blockage losses [3–7]. The Weather Research and Forecast (WRF) model is a commonly used mesoscale model to investigate wind-farm clusters using a relatively simple parameterization, see van der Laan *et al.* [6], Berge *et al.* [7], Mayol *et al.* [8], Ali *et al.* [9], Cañadillas *et al.* [10], for example. Solving flow on a coarse grid and using such a simple parameterization make mesoscale WRF simulations of wind-farm clusters computationally more viable than microscale CFD frameworks. Moreover, flow driven by mesoscale weather data naturally includes atmospheric thermal effects, Coriolis forcing, and flow heterogeneity due to varying pressure gradients. However, significant inaccuracy arises in the predicted losses and performance of wind farms due to the crude parameterizations used, such as the Fitch model or its modifications [1]. WRF-LES, besides being computationally costly,

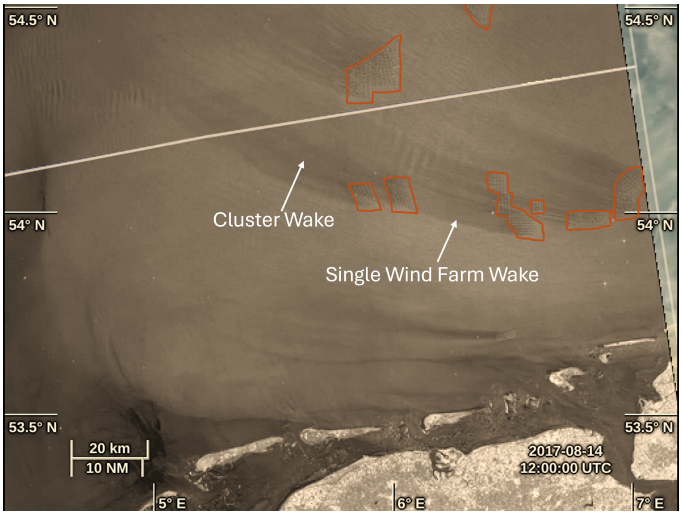

Figure 6.1: A processed SAR image of the North Sea close to the coast of Germany, showing sea surface roughness that indicates wind farm wakes. The wind farm layouts are highlighted with maroon boxes. Image from the OVL portal https://ovl.oceandatalab.com/ that contains modified Copernicus Sentinel data.

has the challenge of losing information at the interface of the meso-to-microscale grid, often called *terra incognita* in the literature. Baas *et al.* [11] simulated the power output of six hypothetical wind farms with GRASP (GPU-Resident Atmospheric Simulation Platform), which is another mesoscale-LES framework, using a year of ERA5 weather data as boundary conditions. They found that the global blockage effect, which is associated with AGWs, can generally cause 2 % to 3 % yearly losses, which can increase up to 10 % for stably stratified conditions. Note that their analysis is specific to simulated wind conditions, turbine types, and layouts. More importantly, they assessed that the gravity wave impacts were masked by the large variety of synoptic forcings and boundary layer conditions taken from the year-long data period.

CFD studies in microscale frameworks have focused on inter-farm wave effects and cluster-wake characteristics, primarily in truly neutral boundary layers. For instance, van der Laan *et al.* [6] proposed a modified RANS closure and an actuator farm model to study wind-farm clusters. Whereas Stipa *et al.* [12] proposed their version of the actuator farm model for LES solvers. Both studies showed great potential for actuator farm models in reducing computational cost and, therefore, are suitable for wind-farm cluster modeling. Stieren and Stevens [13] simulated two neighboring wind farms of aligned and staggered layouts in an LES framework and found that the infer-farm wake can affect the power output of all turbines in the downstream wind farm. Only Maas and Raasch [14] simulated wind-farm clusters with realistic thermal stratification up to a few kilometers, including the free atmosphere. They simulated a stable, two conventionally neutral, and two convective boundary layer simulations. The boundary layer heights and potential temperature profiles were based on realistic atmospheric conditions for the German Bight wind-farm clusters, and the flow was driven with geostrophic wind. Atmospheric

gravity waves were claimed to be observed in the SBL simulation, but no related results are reported. The domain heights used, 3.6 km for the SBL and the CBL with $H_i = 1.4$ km, and only 2 km for the remaining cases, including a Rayleigh damping layer, were likely lower than required to fully resolve atmospheric gravity waves. Therefore, their investigations are similar to those performed assuming a rigid-lid approximation, as addressed in chapter 5. Clearly, Maas and Raasch [14]'s study was not focused on fully-resolved AGWs and their impacts on the wind-farm clusters. Thus, wind-farm cluster-induced AGWs and the stratification impacts (i.e. inversion-layer displacement while fully resolving AGWs) on wind-farm clusters are yet to be investigated.

To fill this knowledge gap, the present study aims to investigate the impact of stratification on clustered wind farms for several CNBL conditions. Following the main approach of this thesis, CNBL conditions are defined by varying the free-atmospheric and capping- inversion Froude numbers (Fr and Fr_i, respectively) and the ABL-aspect ratio ($\tilde{H}_i$). An LES framework is used to simulate two wind farms placed horizontally apart at a distance where the interfacial waves triggered by each one are expected to constructively superimpose. This scenario is likely to enhance the blockage effect of the second wind farm. Moreover, the wind farms are aligned in the streamwise direction. Therefore, wind farm orientation is set in a scenario where the second wind farm is likely to incur maximum losses.

6.2. METHODS

6.2.1. COMPUTATIONAL SETUP

We simulate two wind farms aligned in the streamwise direction that are 4.3 km ($34D$) apart. Each wind farm consists of a regular 10×5 array of turbines with a spacing of five rotor diameters in the streamwise and three rotor diameters in the spanwise direction. The wind turbines are modeled with a uniform actuator disc model with a disc-based thrust coefficient (C_t') of 1.3, and have the same rotor diameter and hub height as the NREL 5-MW reference turbine. Simulations are performed using the Toolbox fOr Stratified Convective Atmospheres (TOSCA) [15], which solves the filtered incompressible Navier-Stokes equations under non-hydrostatic conditions using the Boussinesq approximation for buoyancy. Equations for continuity, momentum, and potential temperature transport are given in Stipa *et al.* [15]. Advection damping and Rayleigh damping are applied as body forces in the respective forcing zones through the momentum equation, details of which are given in Khan *et al.* [16] and Khan *et al.* [17]. Subgrid-scale turbulence is modeled using the dynamic Smagorinsky model with scale-independent Lagrangian averaging [18].

Figure 6.2 shows the domains with boundary conditions for simulating the two wind farms and one in isolation for comparison, indicated by the orange box. The dimensions of the simulated domains for both cases are given in Table 6.1. It is important to note that, laterally, an 18 km wide domain is used for the clustered wind farms to avoid interfacial waves from recycling through the periodic lateral boundaries and, hence, artificially contaminating the inflow for the second wind farm. In contrast, a 6 km wide domain was used to model the flow around the first wind farm in isolation, except for the case $\tilde{H}_i = 0.044$ where the domain size is the same as for the clustered cases (i.e. 18 km wide). Moreover, the induction zone of the clustered wind farms (i.e. L_{ind}) is 3 km

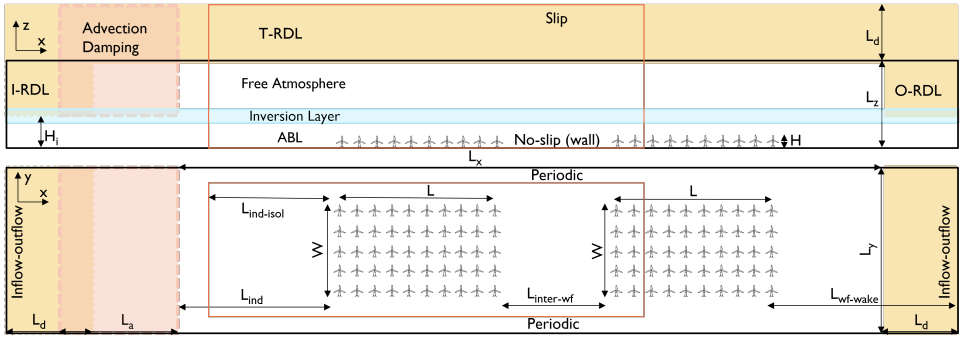

Figure 6.2: Schematic diagram (not to scale) of the TOSCA-model setup showing the configuration of advection damping and Rayleigh damping layers at the inlet, top, and outlet, which are denoted by I-RDL, T-RDL, and O-RDL, respectively. The orange box shows the domain size, excluding damping layers, to simulate the first wind farm alone.

longer than that of the isolated wind farm (i.e. $L_{ind-isol}$). This was precautionary, as it was unclear whether the interaction of AGWs in clustered wind farms would lead to wider AGWs, requiring a longer induction zone than for the isolated case.

Offline precursor-generated turbulent inflow conditions are driven through the domain by an inflow Dirichlet boundary condition. Thus, an inflow function maps the inflow data—velocity and potential temperature—onto the inflow boundary upstream of the wind farms. The outflow boundary of the wind farm simulations has zero-gradient Neumann conditions for all three variables. A typical wall shear-stress lower boundary condition relates the computed flow within the domain to the wall shear-stress using Monin-Obukhov similarity, which is applied locally. An aerodynamic roughness height of 0.0001 m is used to mimic offshore conditions. Periodic boundary conditions are used in the transverse direction only, and the upper boundary is set to a free-slip condition for wind speed, and fixed-gradient for potential temperature. The Coriolis force corresponds to a northern latitude of 41°. The precursor simulations have the same computational setup except for the inflow-outflow boundary conditions, which are replaced with periodic boundary conditions to spin up turbulence. The precursor spin-up time is 2.2×10^4 s, and inflow data are saved for two flow-through times of the successor domain after the spin-up. Constant potential temperature is initialized in the precursor domains for truly neutral boundary layers. CNBL potential temperature profiles based on the Rampanelli-Zardi model [19] are initialized for the canonical CNBL precursors. An adiabatic ground condition in all precursors allows for a neutral ABL throughout the precursor simulations. A pressure controller maintains the hub height velocity at a fixed value, chosen as 11.5 ms^{-1} for the simulations reported here, and the flow direction is aligned to the horizontal axis. Moreover, geostrophic damping is used in the precursor to attenuate inertial gravity waves in the free atmosphere Stipa *et al.* [15]. The precursor domains are only 6 km wide in the spanwise direction. Thus, the saved inflow planes are laterally repeated three times to fit the successor inflow boundary. The inflow planes are shifted in the spanwise direction by 1 ms^{-1} to eliminate the possibility of streaks at the junction of the repeated planes.

Table 6.1: Dimensions of the simulation domains for the clustered wind farms and the first wind farm alone.

Variable	Two wind farms	1^{st} wind farm only
Name (Symbol)	Value (km)	Value (km)
Capping inversion heights (H_i)	0.25, 0.5, 0.75	0.25, 0.5, 0.75
Wind farm length (L)	5.67	5.67
Wind farm width (W)	1.512	1.512
Rotor tip height (H)	0.153	0.153
Domain length (L_x)	30	17
Domain width (L_y)	18	6
Domain height (L_z)	6.2	6.2
Top-Rayleigh damping layer thickness (L_d)	5.8	5.8
Inlet-Rayleigh damping layer thickness (L_d)	5	5
Outlet-Rayleigh damping layer thickness (L_d)	5	5
Advection damping layer thickness (L_a)	6	6
Length of wind farm induction zone (L_{ind})	10	7
Inter-wind farm distance ($L_{inter-wf}$)	4.3	-
Length of wind farm wake zone ($L_{wf-wake}$)	9.6	12.33

In view of computational affordability, the successor mesh is graded in a specific way. In the x-direction, the mesh is equidistant with a spacing of 20 m for 15 diameters downstream of the second wind farm. Thereafter, the spacing expands to a maximum cell size of 200 m for the cell adjacent to the outlet boundary. In the spanwise direction, the mesh is uniform with a spacing of 15 m in the wind farm region, outside of which it is set to 20 m for 3 km on each side, and then it expands to 200 m at the spanwise boundary. The mesh size is 10 m in the ABL in the vertical direction and contracts to 5 m in the capping inversion. The mesh is again 10 m for the first kilometer above the capping inversion, beyond which it increases to 200 m at the start of the T-RDL, from where it remains uniform. In all cases, the expansion and compression ratios are 1.1 and 0.9, respectively. The domain size, advection, and Rayleigh damping layer thicknesses follow the recommendations of Khan *et al.* [17].

6.2.2. SIMULATION SUITE

In this study, we intend to capture inter-farm flow interactions for several CNBL conditions, which are defined by Fr, Fr_i, and $\tilde{H}_i$. These non-dimensional parameters are already defined in Tab. 1.2. Simulating wind farms in CNBL conditions includes the effects of the capping inversion and the free atmosphere on the inter-farm flow. Distinguishing these effects requires a comparison with TNBL conditions. Therefore, two sets of simulations are performed in this study: first, the impact of the three non-dimensional parameters—varying CNBL conditions—on the inter-farm flow is investigated by varying one at a time. These simulations are detailed in Table 6.2 set 1(a-c). The second simulation set, given in Table 6.2 set 2, is for TNBL conditions, where we run a simulation for each of the ABL heights simulated in the CNBL cases.

Simulations in set 1(a) are performed for $Fr = 0.1, 0.15$, and 0.2, while $Fr_i = 1.3$ and $\tilde{H}_i = 0.084$ for each case. A subcritical, critical, and supercritical case are simulated for

set 1(b) by setting Fr_i to 0.75, 1.0, and 1.33, respectively; in all of these cases $Fr = 0.15$ and $\tilde{H}_i = 0.084$. In set 1(c), $\tilde{H}_i$ is varied by setting its values to 0.042, 0.084, and 0.125, while $Fr = 0.15$ and $Fr_i = 1.3$. Lastly, the set 2 details three TNBL cases that were simulated to match each CNBL case with a different $\tilde{H}_i$. In fact, the ABL expands vertically in the TNBL simulations. Only at the inflow boundary can the ABL height be matched to that of the CNBL cases. Therefore, we run TNBL precursors with an ABL height as tall as the desired ABL depth (i.e. 250 m, 500 m, and 750 m), and populate the free atmosphere of the wind farm simulation with the velocity averaged from the top ten precursor cells over the duration of the wind farm simulation. This way, the ambient turbulence characteristics for both CNBLs and TNBLs are expected to be roughly the same, enabling a fair comparison. The equivalent ABL height ratio, $\tilde{H}_{TNBL}$, is the ABL height at inlet of the TNBL simulation to wind farm length.

Table 6.2: Simulation sets for the clustered wind farms.

Set	Parameters Investigated	Variables Changed
	Name [Simulated values]	Name [Simulated values] (Units)
1(a)	Fr [0.1, 0.15, 0.2], Fri [1.3], $\tilde{H}_i$ [0.084]	N [0.021, 0.014, 0.011] (s^{-1})
1(b)	Fr_i [0.75, 1.0, 1.3], Fr [0.15], $\tilde{H}_i$ [0.084]	$\Delta\theta$ [15.66, 8.8, 5] (K)
1(c)	$\tilde{H}_i$ [0.042, 0.084, 0.125], Fr [0.15], Fr_i [1.3]	H_i [250, 500, 750] (m), $\Delta\theta$ [10, 5, 3.33] (K)
2	$\tilde{H}_{TNBL}$ [0.042, 0.084, 0.125]	TNBL height at inflow [250, 500, 750] (m)

6.3. RESULTS

In this section, we present a qualitative analysis of interfacial and internal gravity waves induced by two neighboring wind farms in comparison to the isolated wind farm scenario. TNBL solutions are also reported to emphasize the effects of CNBLs on the flow around clustered wind farms. In the latter part, we quantify the impact of CNBLs on the turbine-level power output of wind farms in a cluster. We also highlight trends in wind-farm efficiencies (i.e. total, non-local, and wake efficiencies) as a function of the non-dimensional parameters. Total wind-farm efficiency refers to the overall aerodynamic performance of a wind farm, which is the product of non-local and wake efficiency that account for losses due to the blockage effect and wakes, respectively.

6.3.1. AGW CHARACTERISTICS OF CLUSTERED WIND FARMS

In Chapter 5, interfacial and internal gravity waves were identified as having a significant effect on wind farm performance based on investigations of an isolated wind farm. The interfacial waves created converging and diverging zones in the ABL, and the internal waves were refracted downstream, impinging on the capping inversion downstream of the wind farm, affecting its displacement. Therefore, it is expected that two neighboring wind farms having the same characteristics as those of the isolated farm might trigger similar AGWs, but their interactions might lead to significant differences in wave characteristics. It is important to recall that the wave interaction is specific to the inter-farm distance used which corresponds to $34D$ or $0.76L$, for which we expect the interfacial waves to constructively superimpose in most of the simulated CNBL conditions. Most of

the simulated cases are supercritical, where the interfacial wavelength is expected to be roughly the inter-farm distance we chose. In the following discussions, we present the interfacial and internal wave fields, which are mostly visible from their vertical velocity. The differences in wave characteristics due to the superimposition of waves induced by each wind farm are given by subtracting the vertical velocity field around the isolated wind farm from those in the vicinity of the first and second wind farms.

INTERFACIAL WAVE CHARACTERISTICS

Figure 6.3 depicts the temporally-averaged vertical velocity component in a horizontal plane at the capping inversion top for the CNBL cases (i.e. Fr, Fr_i, and $\tilde{H}_i$). The horizontal plane for the TNBL simulations is at 300 m, 550 m, and 800 m, from a simulation each for the ABL heights simulated in the CNBL cases. Interfacial waves are prominent in all CNBL fields, and trapped lee waves that extend to the spanwise boundaries downstream of the wind farms can be observed for the subcritical ($Fr_i = 0.75$) and critical ($Fr_i = 1.0$) cases. The remaining CNBL simulations are for supercritical conditions, which do not support trapped lee waves, thus the waves extending to the lateral boundaries in the shallowest boundary layer case ($\tilde{H}_i = 0.044$) are strong interfacial waves. Interfacial wave characteristics mainly depend on Fr_i and $\tilde{H}_i$. This can easily be seen in these plots as wavelengths are the same for most CNBL cases, which simulated conditions defined by $Fr_i = 1.3$ and $\tilde{H}_i = 0.084$. However, a broader red patch is visible between the first and second wind farms, indicating the constructive superimposition of the second wave train at the end of the first wind farm and the first wave train at the start of the second wind farm. The interfacial wavelengths around both wind farms are roughly the same as those measured in the isolated wind farm simulations for the same conditions (indicated with white arrows). However, the subcritical, critical, and the shallowest boundary-layer cases have slightly different wavelengths around the second wind farm pertaining to the first wind farm's waves advected downstream. A phase shift is also evident, on the left side and downstream of the first wind farm, between the trapped lee waves of the first wind farm and those of the second wind farm for the subcritical case. Another observation is the enhanced amplitudes and clockwise turning of interfacial waves for decreasing Fr_i and $\tilde{H}_i$. However, amplitudes become more benign with decreasing value of Fr, with negligible turning of the waves. However, waves turn significantly in the cluster wake region for $Fr_i \leq 1.0$ and $\tilde{H}_i = 0.04$. Thus, resulting in interfacial waves recycling into the domain but in the cluster wake region. The TNBL cases show rising flow over both wind farms and an asymmetric flow entrainment in the spanwise direction in the wind farm wakes that is more pronounced downstream of the second wind farm. This asymmetric flow is due to the Coriolis effect, which causes the flow to turn as a function of the streamwise direction.

The interfacial waves are expected to advect with the flow for most of these simulations, except for the subcritical case. Thus, the difference in the interfacial wave fields of the first and the isolated wind farm should be close to zero. Fig. 6.4 shows the difference in vertical velocity between the two farm cluster and the single isolated wind farm case in the region around the first wind farm and at the inflow region of the second farm. The plots in Fig. 6.4 confirm that interfacial wave characteristics around the first wind farm are almost identical to those of the isolated wind farm. The differences are

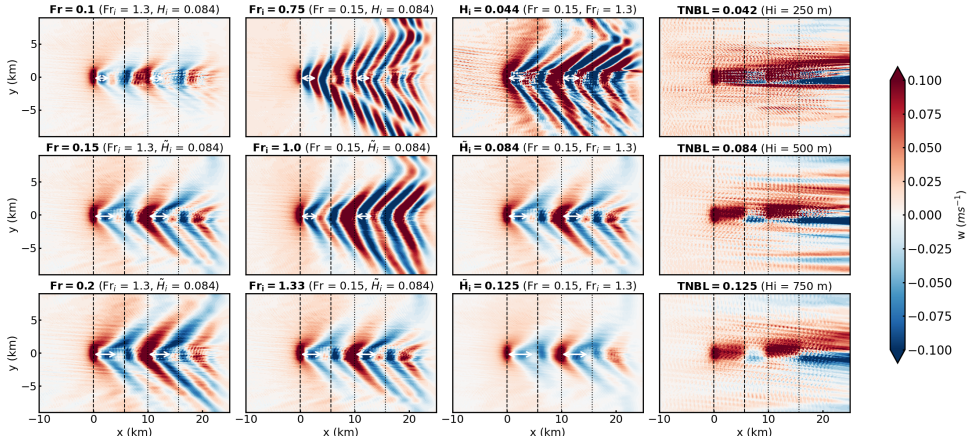

Figure 6.3: Temporally averaged vertical velocity on a horizontal plane at the top of the capping inversion layer for the CNBLs and at the same height for TNBLs. The white arrows are to the scale representation of average interfacial wavelengths measured for the isolated wind farm. The black dashed and dotted lines represent the start and end of the first and the second wind farm, respectively.

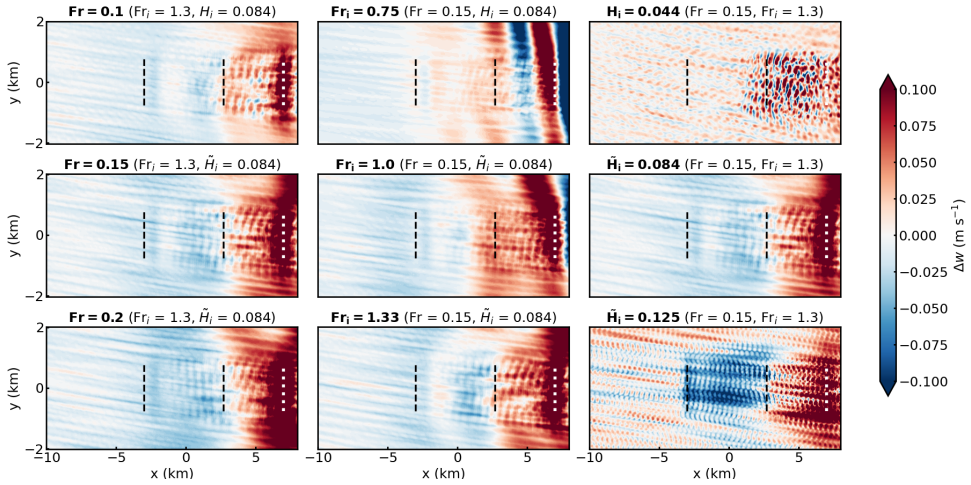

Figure 6.4: The difference between the temporally averaged vertical velocities measured at the capping inversion top around the first wind farm and the isolated wind farm. The black dashed lines represent the start and end of the first wind farm, and the dotted white line shows the start of the second wind farm.

relatively higher downstream of the wind farm, particularly for the subcritical and critical cases. In these cases, the interfacial waves induced by the second wind farm, whose starting location is shown with a white dotted line, seem to propagate upstream and affect the wave field in the exit and wake regions of the first wind farm. The interfacial waves recycled from the lateral boundaries for simulating the isolated wind farm in a relatively narrow domain may also affect these difference-fields downstream of the first wind farm. We note that these difference-fields do not show the actual characteristics of

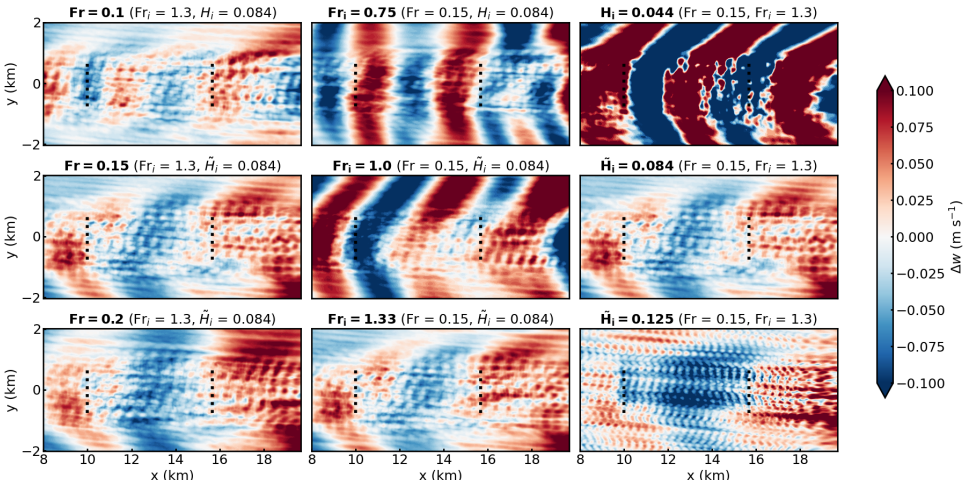

Figure 6.5: The difference between the temporally averaged vertical velocities measured at the capping inversion top around the second wind farm and the isolated wind farm. The black dotted lines represent the start and end of the second wind farm.

6

the waves; rather, the differences indicate whether the waves induced by the two wind farms interact.

Table 6.3: Comparison of measured interfacial wavelengths over each wind farm with those measured over the isolated wind farm.

Case	$\lambda_{\text{ifgw\_isol}}$ (m)	First wind farm		Second wind farm	
		λ_{ifgw} (m)	$\Delta\lambda_{\text{ifgw}}$ (%)	λ_{ifgw} (m)	$\Delta\lambda_{\text{ifgw}}$ (%)
$Fr = 0.10$	3160.0	3120.0	-1.27	3920.0	+24.05
$Fr = 0.15$	4240.0	4400.0	+3.77	4920.0	+16.04
$Fr = 0.20$	4440.0	5120.0	+15.32	5720.0	+28.83
$Fr_i = 0.75$	3120.0	3120.0	0.00	2560.0	-17.95
$Fr_i = 1.00$	3520.0	3280.0	-6.82	5040.0	+43.18
$Fr_i = 1.33$	4280.0	4400.0	+2.80	4920.0	+14.95
$\tilde{H}_i = 0.04$	3680.0	3040.0	-17.4	2980.0	-19.02
$\tilde{H}_i = 0.08$	4240.0	4400.0	+3.77	4920.0	+16.04
$\tilde{H}_i = 0.13$	5040.0	4600.0	-8.73	5760.0	+14.29

Figure 6.5 shows the difference in the interfacial wave fields between the second and the isolated wind farm. Note that in this case, the flow field simulated in the orange box shown in Fig. 6.2 for the single isolated farm case is subtracted from the two farm cluster wind field such that the turbine positions align with those of the second wind farm. The differences are obvious in all cases, with the most prominent for the subcritical, critical, and shallowest boundary layer cases. The interfacial waves of the first wind farm are advected into the second one for the supercritical cases, and the modified waves are different from those of the isolated wind farm. For the subcritical and critical cases, the

waves propagate into the second wind farm before they are advected by the background flow. Since interfacial wavelengths become shorter with decreasing Fr_i, the superimposition of the interfacial waves induced by the second wind farm and those propagated into it from the first one causes a wave field that differs significantly from that of the isolated wind farm. The shallowest boundary layer case is supercritical, but the capping inversion is very close to the wind turbines, leading to strong interfacial waves. More importantly, these interfacial waves prevail downstream of the wind farm, thus interaction with those of the second wind farm forms stronger waves than observed for deeper boundary layers. In all cases, the interfacial waves are bent into a V-shape, whereas the subcritical case shows 'blunter' waves; straight phase lines, which indicate waves faster than the background speed. Table 6.3 gives a brief quantitative comparison of the interfacial wavelengths measured above each wind farm with those measured above the isolated one.

INTERNAL WAVE CHARACTERISTICS

We learned in chapter 5 that internal wave characteristics are mostly dependent on Fr, and Fr_i and $\tilde{H}_i$ affect their amplitudes. Similar behavior is observed for the internal waves induced by the two wind farms. Figure 6.6 illustrates this by showing the temporally averaged vertical velocity on a vertical plane starting at the inversion top. The wavelengths, amplitudes, and angle of inclination increase with increasing Fr. Two phase shifts are seen for $Fr = 0.1$: the first is between the second internal wave train of the first wind farm and the first internal wave train of the second wind farm; and the second is roughly at the end of the second wind farm. These phase shifts indicate the internal waves propagate both upstream and downstream and superimpose on each other. The phase shifts disappear for the higher values of Fr, as the inclination angles increase and upstream propagation is contained, which dilates the internal waves in the streamwise direction. While varying Fr_i, Fr and $\tilde{H}_i$ are set to 0.15 and 0.084, respectively. Thus, the wavelengths and inclination angles are the same, but the amplitudes decrease with decreasing Fr_i. This is because the wave spectrum becomes increasingly evanescent for decreasing Fr_i, which leads to trapped lee waves that can be seen along the capping inversion for the subcritical and critical cases. This also means that only a portion of the wave spectrum is propagating, resulting in lower amplitude waves for lower Fr_i. Similarly, Fr is fixed to 0.15 and Fr_i to 1.3 when varying $\tilde{H}_i$ only. Varying only the boundary height in this manner mainly affects the internal wave amplitudes. Weaker internal waves are obvious when increasing $\tilde{H}_i$, as the capping inversion is further from the flow deflected by the wind farm. The wavelengths and direction of the internal waves are the same as those of the isolated scenario. The arrows indicate the wavelengths and inclination measured in the direction of the apparent first wave train of the isolated wind farm. In most cases, except for $Fr = 0.1$ and $Fr_i \leq 1.0$, the wavelengths and orientations resemble those induced by both wind farms. As already indicated in section 6.3.1, the TNBL cases should show vertically expanding flow over both wind farms, entraining flow in the wind farm wakes. The flow entrainment is particularly strong for the TBNL with the shallowest inflow boundary layer (i.e. TNBL = 0.044).

Figure 6.7 shows the difference between the internal wave field around the first wind farm and that of the isolated wind farm. In addition to the observations discussed in

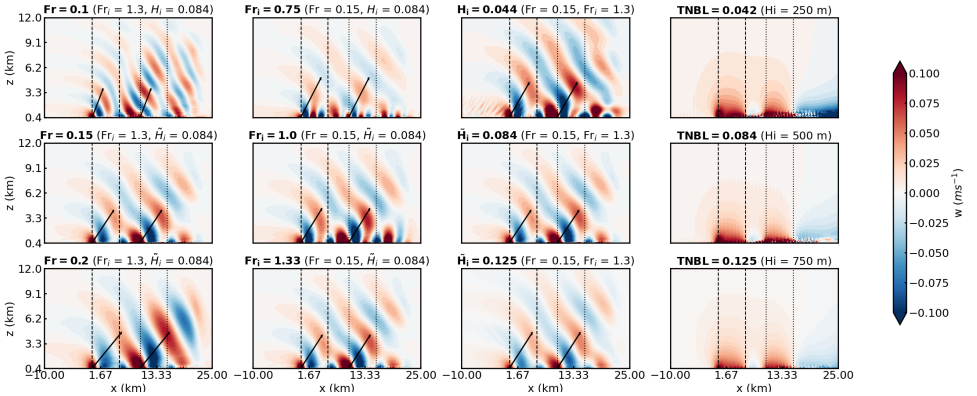

Figure 6.6: Temporally averaged vertical velocity on a vertical plane through the middle column of the wind farms for the CNBLs and TNBLs. The arrows are drawn to the scale of the wavelengths and orientation of the first internal wave train measured from the isolated wind farm simulations. The black dashed and dotted lines represent the start and end of the first and the second wind farm, respectively.

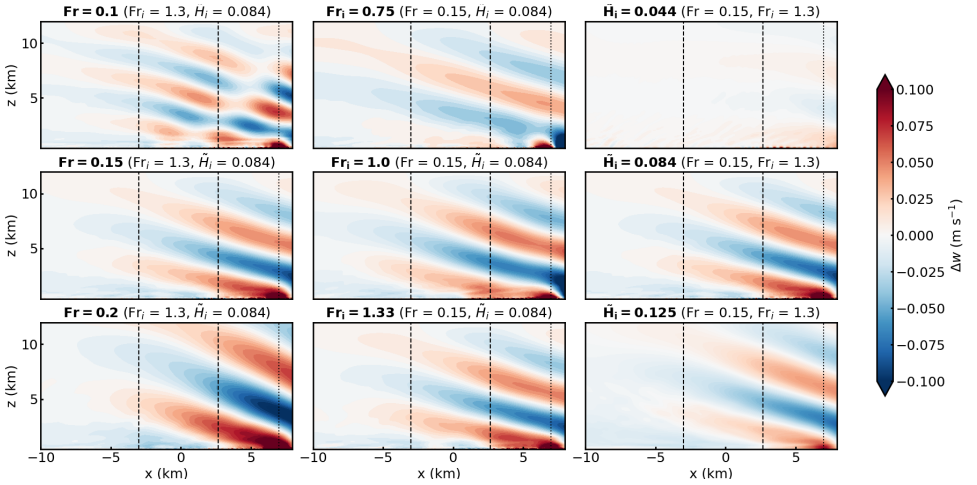

Figure 6.7: The difference of temporally averaged vertical velocities measured on a vertical plane around the first and the isolated wind farms. The black dashed lines represent the overlapping start and end of the first and the isolated wind farm, and the dotted black line shows the start of the second wind farm.

the previous paragraph, we notice differences mainly in the wake region of the first wind farm and further from the capping inversion. Almost no differences are seen along the capping inversion over the first wind farm, which reconfirms that the interfacial waves are the same as those of the isolated case. These waves seen on the plots are internal waves induced by the second wind farm that propagate upstream into the regions over the first wind farm. The wave trains emerging at the start of the second wind farm and propagating upstream are evident on all the plots.

The internal wave fields around the second wind farm are significantly different from

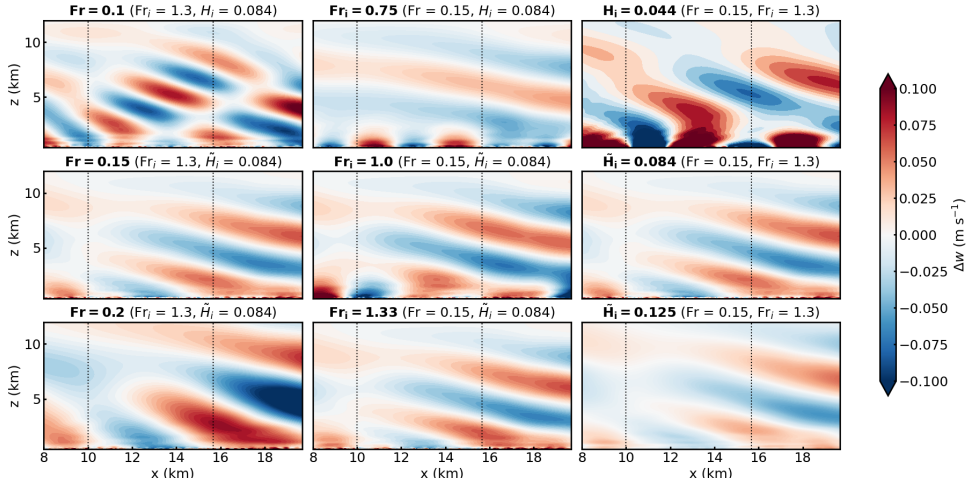

Figure 6.8: The difference of temporally averaged vertical velocities measured on a vertical plane around the first and the isolated wind farm. The black dotted lines represent the overlapping start and end of the second and the isolated wind farm.

those of the isolated one. This is because the internal waves induced by the first wind farm propagate downstream into the second. Moreover, trapped lee waves that propagate into the second wind farm, for the subcritical and critical cases, are clearly visible. The shallowest boundary layer case shows strong interfacial waves advected into the second wind farm, causing pronounced differences with the wave fields of the isolated wind farm.

6.3.2. FLOW AROUND CLUSTERED WIND FARMS IN CNBLS

Simulating wind farms in CNBLs with AGWs results in pressure fields which show both wind farm blockage effect and flow speed-ups through and downstream of a wind farm. These effects can vary for clustered wind farms due to varying wind farm interactions with the CNBL. Analysing hub-height velocity magnitude in comparison to the same in the free stream is a simple way to assess the impact of CNBLs, including AGWs, on the flow around clustered wind farms. Figure 6.9 shows such fields for both the CNBL and TNBL simulations. The horizontal velocity magnitude of the free stream is considered to be that at 10 km upstream of the first row of wind turbines of the first wind farm. A common observation is the reduced velocity at the start of both wind farms, which indicates enhanced wind farm blockage compared to the respective TNBL fields. The subcritical, critical, and the shallowest boundary layer cases show a clear signature of interfacial and trapped lee waves through both wind farms. This is the evidence that there are converging and diverging zones in the ABL that correlate to the interfacial wave/lengths. Atmospheric conditions are supercritical for the remaining cases, and traces of mildly converging and diverging zones can be seen on these plots.

The ABL-aspect ratio (ratio of ABL height to wind farm length, $\tilde{H}_i$) was identified in the previous chapter as the most critical parameter in terms of the performance of a wind farm in a CNBL. From the results in Figure 6.9, it can be seen that this parameter is

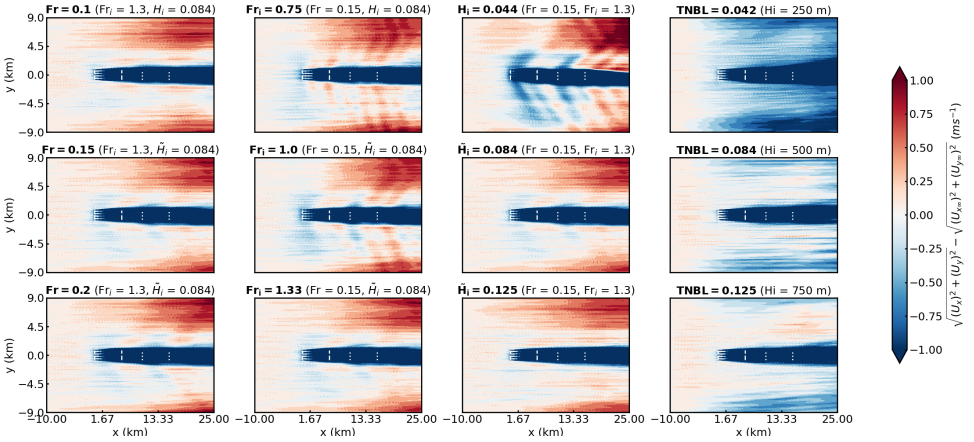

Figure 6.9: The difference between the temporally averaged horizontal velocity magnitude measured on a hub-height plane and that of the free stream. The dashed and dotted lines represent the starts and ends of the first and second wind farms.

even more important for clustered wind farms. The horizontal velocity fields show how with increasing $\tilde{H}_i$ the CNBL results approach those of a TNBL with the same $\tilde{H}_{TNBL}$; the flow field at hub height when $\tilde{H}_i = 0.0125$ appears similar to that of $\tilde{H}_{TNBL} = 0.125$. However, as $\tilde{H}_i$ is reduced, the CNBL shows clear gravity waves at the hub height. More importantly, the mean flow around the wind farms is distinct from that in a TNBL, and the wind-farm cluster wake becomes skewed instead of expanding, as is the case for the TNBL cases. The skewing of the cluster wake for low ABL-aspect ratios is attributed to spanwise transfer of momentum due to the low capping inversion confining vertical entrainment [20]. However, it is not obvious if the wind-farm cluster wake is turning anticlockwise for the lowest $\tilde{H}_i$ case, as only the first ~10 km of the flow downstream of the cluster is resolved. For low capping inversions, Lanzilao and Meyers [20] have noticed the wind farm wake deflecting anticlockwise in the Northern hemisphere at downstream distances greater than a few wind farm lengths.

Figure 6.10 shows velocity magnitude on a vertical streamwise plane through the middle column of the wind farms. The internal boundary layer growth is shown as locations over the wind farms where velocity magnitude reaches 95 % of the free stream velocity sampled at a height 5 m above the rotor tip. In all CNBL cases the IBL gradually expands vertically as function of streamwise distance, and suddenly rises at the start of the second wind farm. Since H_i is 500 m in most cases, IBL hits the capping inversion at the start of second wind farm and appears wavy similarly to the capping inversion itself. As expected, the IBL growth is completely confined in the shallowest boundary layer. This reiterates how low capping inversions restrict vertical mixing of flow. Moreover, the IBL seems to drop in height in the cluster wake region, something worth further investigation. The IBL growth for $\tilde{H}_i = 0.0125$ appears almost the same as that of $\tilde{H}_{TBNL} = 0.0125$. This confirms that IBL growth is mostly dependent on $\tilde{H}_i$.

In the following sections, we will quantitatively investigate stratification impacts on the performance of both wind farms in comparison to TNBLs and the same wind farm

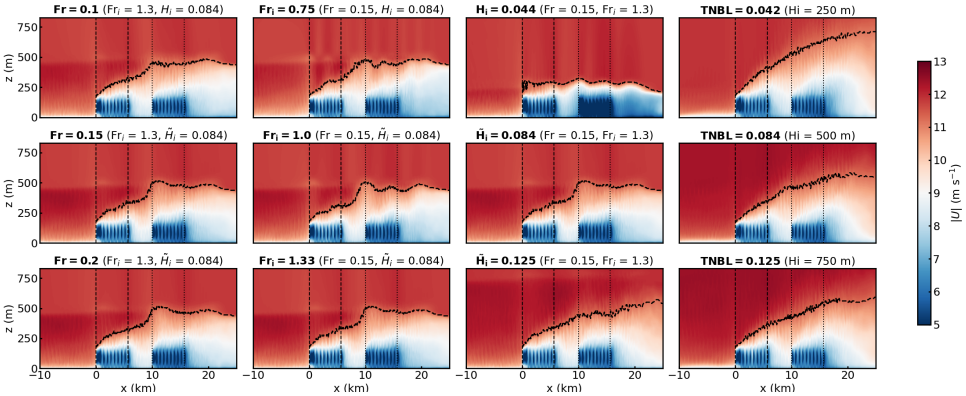

Figure 6.10: Temporally averaged velocity magnitude on a vertical streamwise plane through the middle column of wind farms. The internal boundary layer growth as a function of streamwise and vertical distance is shown by the dashed black line. The vertical dashed and dotted lines represent the starts and ends of the first and second wind farms.

operating in isolation but in the same CNBL conditions. The stratification impacts refer to the capping inversion displacement—thickening and thinning of the boundary layer—under the effect of AGWs. We refrain from attributing these impacts to one or the other, as capping inversion displacement is tightly coupled to AGWs and perturbations in the ABL.

6.3.3. IMPACT ON PERFORMANCE OF CLUSTERED WIND FARMS

CNBL IN COMPARISON TO TNBL

As highlighted in Section 6.1, intra-farm wake effects have been investigated with LES for mainly truly neutral boundary layers or by neglecting the stable layers aloft the ABL. These assumptions exclude both direct and indirect effects of stratification above the ABL on the flow inside it. The direct effects refer to confining ABL growth, thus channeling flow in the horizontal direction, and inducing AGWs. In contrast, indirect effects include the inflow characteristics, such as turbulence intensity, shear, and veer profiles. Therefore, intra-farm interactions might differ substantially from those found in studies that resolve only the ABL or ignore stratification in the layers above.

A wind farm wake will always affect a closely spaced downstream wind farm, but the intensity of the velocity deficit in the wind farm wake is different in CBNLs than TNBLs. This can be seen in Fig. 6.11, where the wind turbine power output averaged in time and per row is shown for the two wind farms as a function of Fr, Fr_i, and $\tilde{H}_i$. TNBL cases are included to distinguish stratification impacts on both wind farms. Irrespective of the simulated atmospheric conditions, the second wind farm is severely affected by the wake of the first wind farm (i.e. 24.4 to 50.5 % power losses compared to the first one in the CNBL and 20 to 21.5 % in the TNBL simulations). Another significant impact of stratification, the enhancement of farm blockage, can be discerned by comparing the CNBL cases to the corresponding TNBL cases. This means the first rows of both wind farms in CNBLs produce less than those of the TNBL simulation. Another common stratifi-

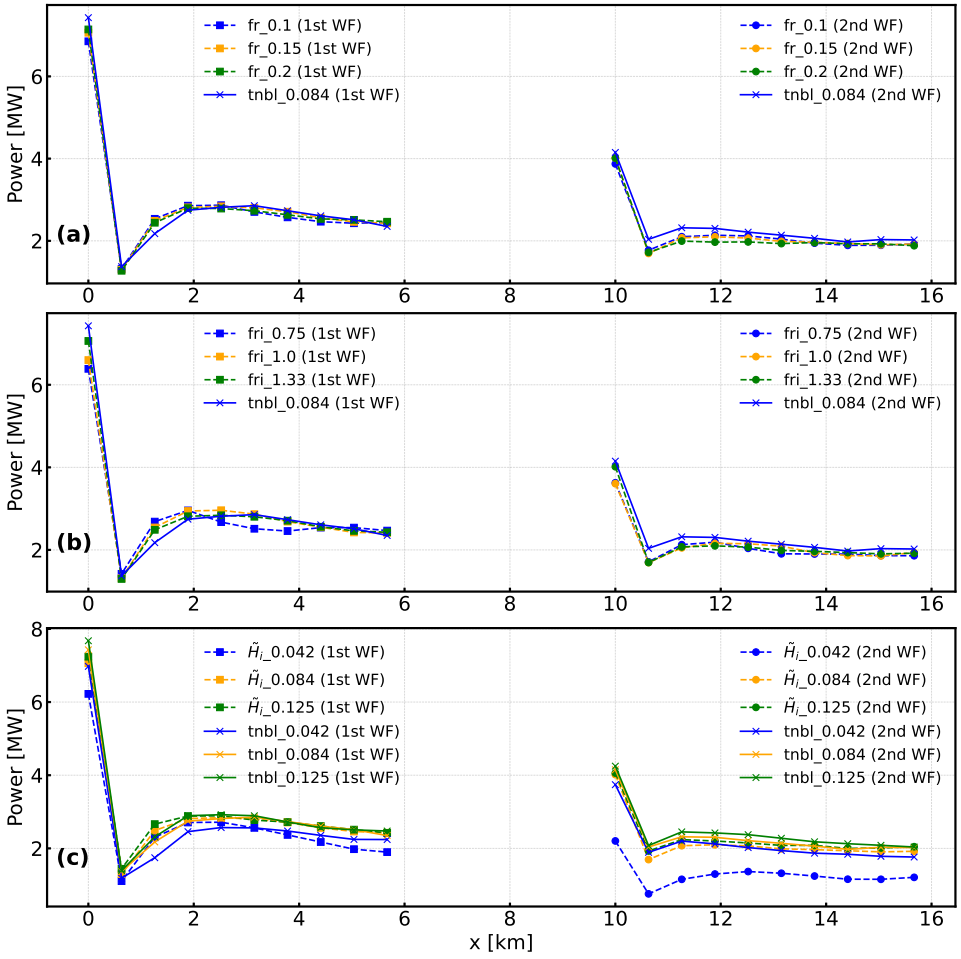

Figure 6.11: Temporal and row-averaged wind turbine power output as a function of (a) Fr, (b) Fr_i, and (c) $\tilde{H}_i$. Each CNBL power profile is compared to a TNBL simulation with the same inflow boundary layer height, which is 500 m for the Fr and Fr_i cases, and 250 m, 500 m, and 750 m for the $\tilde{H}_i$ cases.

cation impact is the increase in power output of the wind turbines towards the end of the entrance region, i.e. the third or fourth row, and in the wind farm exit region, i.e. the ninth to tenth row, compared to those in the developing region,i.e. the fifth to eighth row. These variations, less pronounced for the second wind farm, are due to the thinning ABL in vicinity of the rows gaining power and the thickening at the start of the developing region. The thinning and thickening of the ABL can also be depicted from the wavy IBLs shown in Fig. 6.10.

Figure 6.11 (a) shows the simulated power of both wind farms as a function of Fr compared with the TNBL simulation with ABL height at the domain inlet matching the capping inversion height, 500 m, used in the CNBL simulations. Capping inversion

Froude number and ABL aspect ratio were fixed to 1.3 and 0.084, respectively. The wind farm blockage of both wind farms reduces with increasing Fr, which was also observed in Chapter 5 for the isolated wind farm operating in the same conditions. However, there is little difference between the power outputs of the first row turbines of the second wind farm as a function of Fr. The turbines in the third, fourth, and tenth rows of all Fr simulations produce more than those of the TNBL case. Whereas, the sixth to eighth rows for all Fr cases produce a lower power than those in the TNBL simulation. This trend does not prevail for the second wind farm, as all Fr cases predict a lower power output compared to that of the TNBL simulation. The reason might be that the capping inversion is confining the vertical flow entrainment in the CNBLs, leading to a greater velocity deficit for the second wind farm than for the TNBL case.

We observed in Section 6.3.2 that Fr_i affects the wavelengths of the interfacial waves, which are shorter than half the wind farm length for subcritical conditions. Furthermore, trapped lee waves perturb the capping inversion with amplitudes strong enough to cause fluctuations down to the hub-height in subcritical and critical conditions. These observations are confirmed by the simulated turbine power outputs as a function of Fr_i shown in Fig. 6.11 (b). The trends seen in the power output plots are due to varying Fr_i, as the free atmospheric Froude number Fr and the ABL aspect ratio were kept constant at 0.15 and 0.084, respectively. The wind farm blockage effect of the first wind farm decreases with increasing Fr_i, whereas, for the second wind farm, it remains the same for the subcritical and critical cases. As expected, the wind turbine outputs of both wind farms are spatially varying for the subcritical case due to converging and diverging zones in the ABL. These zones are correlated to the wavelength of the interfacial waves as established in Chapter 5. The corresponding TNBL simulation predicts a lower power output for the first wind farm until the fifth and the last row compared to that of the critical and supercritical cases. The wind turbine outputs of all rows of the second wind farm are higher in the TNBL simulation compared to all the Fr_i cases.

Figure 6.11 (c) shows the predicted power outputs for varying ABL aspect ratio for $Fr = 0.15$ and $Fr_i = 1.3$. Each simulated $\tilde{H}_i$ has a corresponding TNBL case with the same ABL height at the domain inlet. The wind farm blockage effect of both wind farms decreases for increasing $\tilde{H}_i$. Interestingly, the predicted power of waked turbines in the first wind farm for the deepest boundary layer resembles its TNBL counterpart, except that the third row produces more in the CNBL simulation. This confirms one of the main conclusions of the previous chapter that the stratification effects on the ABL flow diminish as the ABL aspect ratio increases. However, the power output of the second wind farm is still higher in the TNBL simulation with the deepest ABL compared to the CNBL with the same ABL aspect ratio. The most prominent difference between a CNBL and its comparable TNBL is the case with the smallest $\tilde{H}_i$ or shallowest ABL. In this case, the power output is less than the TNBL case for rows beyond the sixth for the first wind farm. This could either be the low capping inversion preventing sufficient vertical flow entrainment to the wind farm exit region or a strong interfacial wave of the downstream wind farm pushing the capping inversion upwards. The former reason seems more likely as the second wind farm in the shallowest CNBL case is significantly affected by the inter-farm wake with a much reduced power output for all turbines compared to all the other cases. This suggests that insufficient vertical flow mixing results in stronger wakes in low

CNBLs. This hypothesis is evident as the first row of the second wind farm produces only slightly more than the last row of the first wind farm. In other words, the first wind farm's wake has barely recovered to wind speeds similar to its exit region. In fact, the blockage effect of the second wind farm and the strong interfacial waves advected from the upstream wind farm also contribute to lower speeds in its induction zone. These effects were shown in Fig. 6.5 and 6.9, and discussed in section 6.3.2.

The cumulative power outputs of both wind farms operating in CNBLs in comparison to those operating in TNBLs are summarized in the Table 6.4. Both wind farms, particularly the second one, produce less power in the CNBL case compared to a TNBL. The first wind farm produces 0.5 to 3 % less power, whereas for the second, this increases to 6 to 9 % less power. As described above, the shallowest boundary layer case is an exception; the second wind farm incurs 39 % extra losses than the same wind farm operating in the TNBL with a domain of the same ABL height.

Table 6.4: Comparison of clustered CNBL wind farm power output with that of the TNBL wind farm.

Case	1st WF Power (MW)		2nd WF Power (MW)		ΔP (MW) & (%)			
	CNBL	TNBL	CNBL	TNBL	1st WF		2nd WF	
$Fr = 0.10$	29.04	29.59	21.69	23.25	-0.55	(1.86)	-1.56	(6.71)
$Fr = 0.15$	29.46	29.59	21.66	23.25	-0.13	(0.44)	-1.58	(6.79)
$Fr = 0.20$	29.31	29.59	21.30	23.25	-0.28	(0.95)	-1.95	(8.39)
$Fr_i = 0.75$	28.64	29.59	21.12	23.25	-0.95	(3.21)	-2.13	(9.16)
$Fr_i = 1.00$	29.30	29.59	21.33	23.25	-0.30	(1.01)	-1.92	(8.26)
$Fr_i = 1.33$	29.46	29.59	21.66	23.25	-0.13	(0.44)	-1.58	(6.79)
$\tilde{H}_i = 0.04$	26.04	26.81	12.87	21.17	-0.77	(2.87)	-8.31	(39.24)
$\tilde{H}_i = 0.08$	29.46	29.59	21.66	23.25	-0.13	(0.44)	-1.58	(6.79)
$\tilde{H}_i = 0.13$	30.16	30.36	22.80	24.28	-0.20	(0.66)	-1.48	(6.10)

COMPARISON OF CLUSTERED AND ISOLATED WIND FARMS

In the previous section, we distinguished the stratification impacts on both wind farms compared to the same wind farms operating in TNBL conditions. Here, we compare the simulated power outputs of both wind farms with that of the wind farm operating in isolation but in the same CNBL conditions. This comparison should determine the impact each wind farm has on the other while operating in a CNBL. We will discuss observations other than those already made while comparing power predictions from CNBL simulations with those of TNBLs.

Figure 6.12 shows the wind turbine power output averaged in time and per row for the two wind farms in a clustered configuration and an isolated one of the same turbines and layout operating under the same conditions. We discuss the comparison wind farm-wise instead of basing it on the non-dimensional numbers: first and second wind farms versus the isolated wind farm in that order. The wind farm blockage effect of the first wind farm is the same as that of the isolated one.The second row in all cases has the same time-averaged power output when compared to that of the isolated wind farm. For the remaining waked turbines, the first wind farm has higher power outputs until the fifth row. For rows farther downstream, the same or slightly less power is achieved than for the

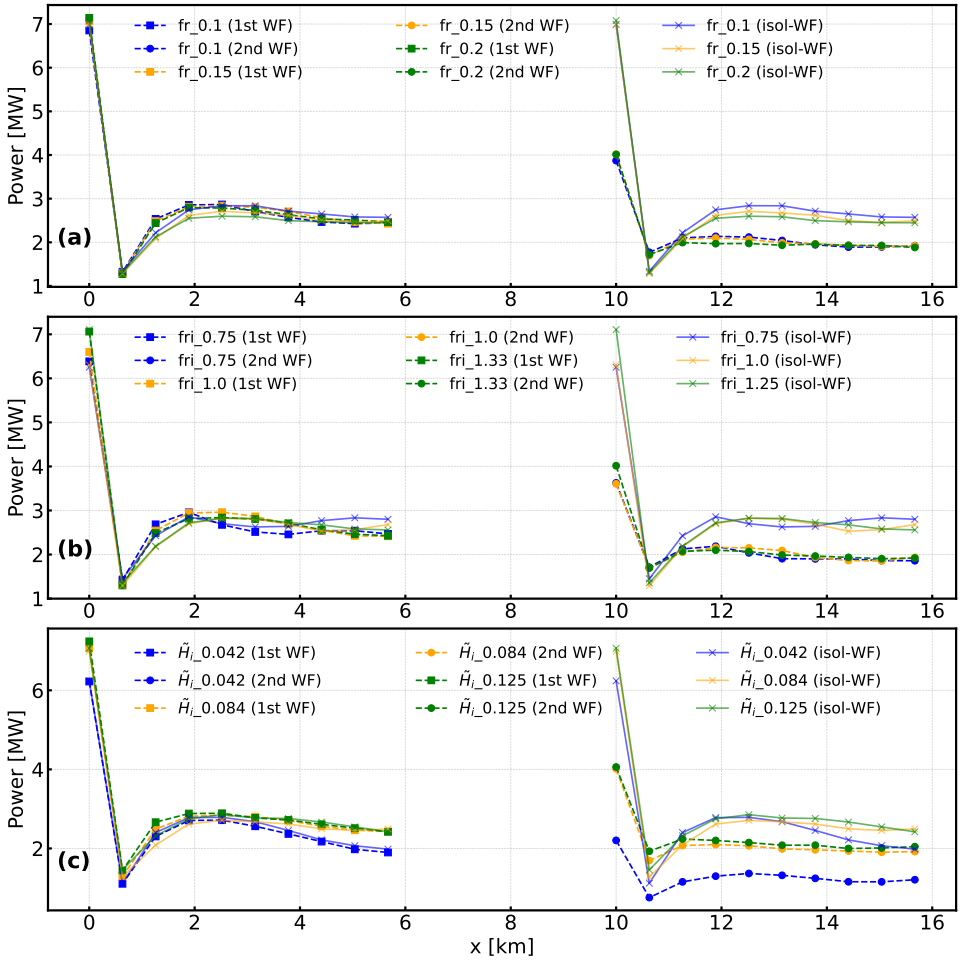

Figure 6.12: Temporal and row-averaged wind turbine power output as a function of (a) Fr, (b) Fr_i, and (c) $\tilde{H}_i$; each compared to that of the isolated wind farm.

isolated case. These differences in the power output compared to the isolated wind farm indicate that upstream wind farms can be affected in clustered wind farms. However, we do not fully understand why the first wind farm is producing more and there is no clear trend in the gains and losses as a function of the non-dimensional parameters. Thus, a detailed investigation is required establish the underlying phenomenon, if any.

The comparison of the second wind farm's power output to that of the isolated one is clearly biased due to different inflows. Obviously, the wake and AGWs induced by the first wind farm affect the inflow to the second. Therefore, this comparison shows the losses incurred by the second wind farm due to wakes and stratification impacts. In all cases, except $\tilde{H}_i = 0.042$, the second wind farm is losing roughly 25% of what it could produce in isolation for operation in the same CNBL conditions. Other observations in-

clude the second row producing more, the third one producing almost the same, and less pronounced variations due to wavy capping inversion or AGW activity. The last observation suggests that stronger wakes dominate the impact of converging and diverging zones in the ABL due to the capping inversion displacement.

Table 6.5: Comparison of clustered wind farm power output with that of the isolated wind farm.

Case	Isolated wind farm	First wind farm		Second wind farm	
	P (MW)	P (MW)	ΔP (MW) & (%)	P (MW)	ΔP (MW) & (%)
$Fr = 0.10$	29.49	29.04	-0.44 (1.49)	21.69	-7.79 (26.42)
$Fr = 0.15$	28.43	29.46	1.04 (3.66)	21.66	-6.76 (23.78)
$Fr = 0.20$	28.11	29.31	1.20 (4.26)	21.30	-6.81 (24.22)
$Fr_i = 0.75$	29.35	28.64	-0.71 (2.42)	21.12	-8.24 (28.09)
$Fr_i = 1.00$	28.55	29.30	0.74 (2.58)	21.33	-7.22 (25.28)
$Fr_i = 1.33$	29.55	29.46	-0.09 (0.30)	21.66	-7.89 (26.70)
$\tilde{H}_i = 0.04$	26.73	26.04	-0.69 (2.58)	12.87	-13.86 (51.85)
$\tilde{H}_i = 0.08$	28.43	29.46	1.04 (3.66)	21.66	-6.76 (23.78)
$\tilde{H}_i = 0.13$	29.61	30.16	0.54 (1.82)	22.80	-6.81 (23.00)

The cumulative power output of the two wind farms, the isolated one, and the difference of each wind farm's power from that of the isolated one are given in Table 6.5. Interestingly, the first wind farm seems to benefit in some cases with the highest gain, roughly 4 %, when the Froude number of the free atmosphere is high. On the contrary, the second wind farm is always losing power, with the highest loss (i.e. 52 %) for the shallowest boundary layer case, and in the range of 24 to 28 % for the remaining cases.

TRENDS IN FARM EFFICIENCIES OF CLUSTERS

The non-local, wake, and total efficiencies are convenient metrics to assess wind farm performance as a function of Fr, Fr_i, and $\tilde{H}_i$. These three efficiencies were defined by Allaerts and Meyers [21] to emphasize the wind farm blockage effect in contrast to the wake losses. The non-local efficiency is defined as the power output of the first row turbines in comparison to one operating in isolation or in the free stream. Lanzilao and Meyers [22] used the power output of an isolated wind turbine operating in a TNBL to determine non-local efficiency, but that requires extra simulations. A simpler approach is to use the rotor-averaged velocity from the TNBL simulation in the free stream to estimate the available aerodynamic power. In this analysis, we compute aerodynamic power in the free stream by rotor-averaging velocity from the TNBL with the deepest inflow boundary layer (i.e. $TNBL\_0.125$). Thus, the non-local efficiency of the first row turbines in this TNBL simulation is 1.0, and that of the shallower TNBLs is smaller as the ambient flow has lower rotor-averaged wind speeds. Note that the same aerodynamic power in the free stream (i.e. P_∞) is used to estimate the non-local efficiency of the second wind farm. The non-local efficiencies of the second wind farm also account for inter-farm wake losses and any gains or losses due to the stratification effects. The wake efficiency compares the total power of waked turbines of the same wind farm (i.e. P_w) with the total power of the same number of turbines (i.e. N_w) operating in the first row of the same wind farm, thus excluding only the inter-farm wake effects. The total wind farm

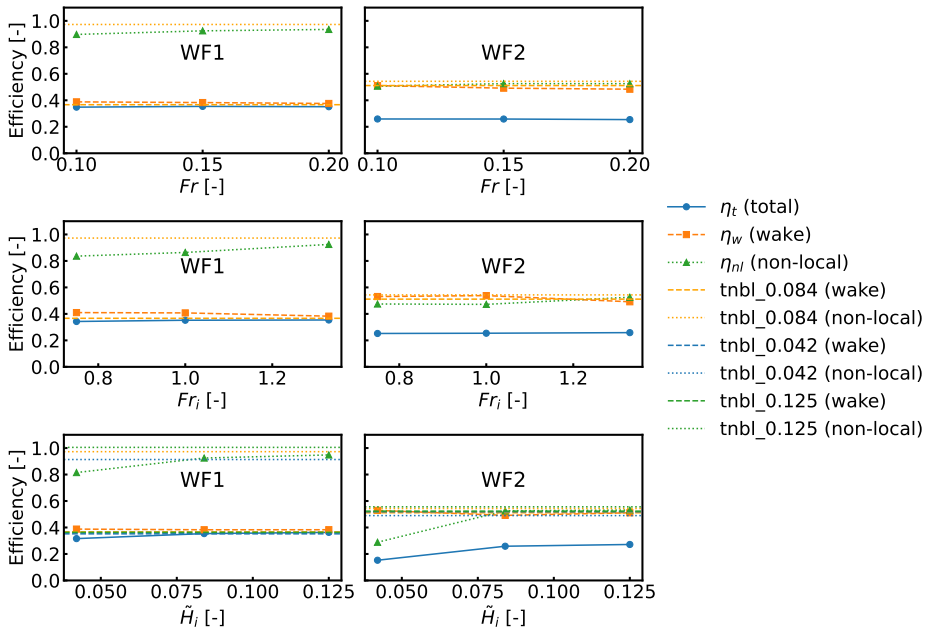

Figure 6.13: Non-local, wake, and total efficiencies of the two neighboring wind farms as a function of Fr, Fr_i, and $\tilde{H}_i$. The dotted and dashed lines without markers show the non-local and wake efficiencies of the TNBL cases.

efficiency is the product of non-local and wake efficiencies. The expressions for all three are given below, where η_{nl}, η_w, and η_t are the non-local, wake, and total efficiencies, respectively.

$$\eta_{nl} = \frac{P_1}{P_\infty}, \quad \eta_w = \frac{P_w}{N_w \cdot P_1}, \quad \eta_t = \eta_{nl} \cdot \eta_w$$

Figure 6.13 shows efficiencies of the first and second wind farm as a function of Fr, Fr_i, and $\tilde{H}_i$ along with the equivalent efficiencies from the relevant TNBL simulation. The non-local efficiency increases linearly with a gentle slope for both wind farms with increasing values of Fr, Fr_i, and $\tilde{H}_i$, except that it is constant for the second wind farm for the subcritical and critical cases. Also, for $\tilde{H}_i = 0.04$, the non-local efficiencies of the first and second wind farms drop by 10 % and 15 %, respectively compared to $\tilde{H}_i = 0.08$. In contrast, the change in non-local efficiencies between $\tilde{H}_i = 0.08$ and 0.125 is 5 % for the first and 2 % for the second wind farm. The trends in the wake and total efficiencies are less pronounced when viscous effects dominate stratification effects. However, an increasing trend is noticed in the total wind farm efficiency as a function of $\tilde{H}_i$ mainly due to the same trend in the non-local efficiency. In terms of comparing the efficiencies of the two wind farms, the non-local efficiency drops by 35 % to 50 % for the second wind farm. The intra-farm wake efficiency of the second wind farm is slightly higher than that of the first wind farm.

6.4. CONCLUSIONS

This study used LES to investigate clustered wind farm performance under varying CNBL conditions, focusing on the role of stratification effects— thickening and thinning of the atmospheric boundary layer under the effect of fully resolved atmospheric gravity waves. By varying the free-atmosphere and capping-inversion Froude numbers and the ABL aspect ratio, we assessed how interfacial and internal waves interact with neighboring wind farms. Compared with isolated wind farms, the clustered configuration showed that wave fields around the second farm differ significantly, with interfacial and internal waves always advecting into it. The strongest wave field interactions were observed under subcritical, critical, and shallow boundary layer conditions, even around the upstream wind farm.

Stratification strongly influenced hub-height flow and, in turn, turbine power output under subcritical, critical, and shallow boundary layer conditions. Shallow boundary layers enhanced wind farm blockage effect but diminished wake recovery, leading to large performance losses, while deeper layers reduced these effects and CNBL predictions resembled those of TNBLs. The first wind farm often produced slightly more power than its isolated counterpart. This requires detailed investigation to establish any underlying phenomena. The highest gain was 4.3 % compared to an isolated wind farm under CNBL conditions with mildest free atmospheric stability (i.e. $Fr = 0.2$). In contrast, the second farm consistently underperformed relative to both the isolated case and the TNBL cases. On average 25 % less power than that of the isolated wind farm is predicted, which reduces to 52 % for the shallowest boundary layer case. In comparison to the second wind farm operating in a TNBL, it incurred a mean loss of around 7 % and as high as 39 % for the shallowest boundary layer. The drastic losses by the second farm for the shallowest boundary layer indicate how vertical mixing is confined and wake recovery relies on, rather slow, spanwise mixing. The skewing of the cluster wake in the shallowest boundary layer case confirms spanwise mixing of the flow.

Overall, performance trends were governed by the ABL aspect ratio, with higher values reducing blockage effect and improving non-local efficiency for both farms. While increasing Fr, Fr_i, and $\tilde{H}_i$ was generally associated with improved performance, the strongest gains occurred between the shallowest aspect ratio cases. These findings show that TNBL simulations always overpredict power in clustered wind farms and underestimate the blockage effect. In other words, excluding stratification effects leads to inaccurate power predictions in LES of wind farms. Therefore, LES configurations capturing AGWs are essential for realistic assessments of wind farm performance in multi-farm layouts, particularly for shallow boundary layers where stratification impacts are most severe.

We note that these conclusions are based on canonical CNBL and TNBL simulations of two neighboring wind farms of regular layouts with a fixed inter-farm distance. Moreover, a uniform actuator disc is used to model the wind turbine's effects on the flow. Therefore, there is a need to extend this study for stable and unstable boundary layers, ideally based on realistic atmospheric conditions. Also, varying the inter-farm distance is suggested as that can change the stratification impacts on individual wind farms in a cluster. Moreover, using an actuator line model may improve the wind turbine level power predictions.

REFERENCES

[1] P. Ouro, M. Ghobrial, K. Ali, and T. Stallard, *Numerical modelling of offshore wind-farm cluster wakes,* Renewable and Sustainable Energy Reviews **215**, 115526 (2025).

[2] A. Abraham, N. Hamilton, N. Bodini, B. Hirth, J. Schroeder, S. Letizia, R. Krishnamurthy, R. Newsom, and P. Moriarty, *Land-based wind plant wake characterization using dual-doppler radar measurements at AWAKEN,* Journal of Physics: Conference Series **2767**, 092037 (2024).

[3] N. Nygaard and S. Hansen, *Wake effects between two neighbouring wind farms,* in *Journal of Physics: Conference Series*, Vol. 753 (IOP Publishing, 2016) p. 032020.

[4] N. Nygaard, S. Steen, L. Poulsen, and J. Pedersen, *Modelling cluster wakes and wind farm blockage,* in *Journal of Physics: Conference Series*, Vol. 1618 (IOP Publishing, 2020) p. 062072.

[5] J. Fischereit, K. Schaldemose Hansen, X. Larsén, M. van der Laan, P.-E. Réthoré, and J. Murcia Leon, *Comparing and validating intra-farm and farm-to-farm wakes across different mesoscale and high-resolution wake models,* Wind Energy Science **7**, 1069 (2022).

[6] M. van der Laan, O. García-Santiago, M. Kelly, A. Meyer Forsting, C. Dubreuil-Boisclair, K. Seim, M. Imberger, A. Peña, N. Sørensen, and P.-E. Réthoré, *A new RANS-based wind farm parameterization and inflow model for wind farm cluster modeling,* Wind Energy Science **8**, 819 (2023).

[7] K. Berge, G. Centurelli, M. Dörenkämper, J. Bange, and A. Platis, *Evaluation of engineering models for large-scale cluster wakes with the help of in situ airborne measurements,* Wind Energy **27**, 1040 (2024).

[8] M. Mayol, A. Saulo, and A. Otero, *Farm to farm wake interaction in WRF: impact on power production,* in *Journal of Physics: Conference Series*, Vol. 1934 (IOP Publishing, 2021) p. 012017.

[9] K. Ali, D. Schultz, A. Revell, T. Stallard, and P. Ouro, *Assessment of five wind-farm parameterizations in the weather research and forecasting model: A case study of wind farms in the north sea,* Monthly Weather Review **151**, 2333 (2023).

[10] B. Cañadillas, R. Foreman, G. Steinfeld, and N. Robinson, *Cumulative interactions between the global blockage and wake effects as observed by an engineering model and large-eddy simulations,* Energies **16**, 3040 (2023).

[11] P. Baas, R. Verzijlbergh, P. van Dorp, and H. Jonker, *Investigating energy production and wake losses of multi-gigawatt offshore wind farms with atmospheric large-eddy simulation,* Wind Energy Science **8**, 787 (2023).

[12] S. Stipa, A. Ajay, and J. Brinkerhoff, *The actuator farm model for large eddy simulation (LES) of wind-farm-induced atmospheric gravity waves and farm–farm interaction,* Wind Energy Science **9**, 2301 (2024).

[13] A. Stieren and R. J. A. M. Stevens, *Impact of wind farm wakes on flow structures in and around downstream wind farms,* Flow **2**, E21 (2022).

[14] O. Maas and S. Raasch, *Wake properties and power output of very large wind farms for different meteorological conditions and turbine spacings: A large-eddy simulation case study for the German bight,* Wind Energy Science **7**, 715 (2022).

[15] S. Stipa, A. Ajay, D. Allaerts, and J. Brinkerhoff, *TOSCA – an open-source, finite-volume, large-eddy simulation (LES) environment for wind farm flows,* Wind Energy Science **9**, 297 (2024).

[16] M. A. Khan, D. Allaerts, S. J. Watson, and M. J. Churchfield, *Investigating the relationship between simulation parameters and flow variables in simulating atmospheric gravity waves for wind energy applications,* Wind Energy Science **10**, 1167 (2025).

[17] M. A. Khan, S. J. Watson, D. J. N. Allaerts, and M. Churchfield, *Recommendations on setup in simulating atmospheric gravity waves under conventionally neutral boundary layer conditions,* Journal of Physics: Conference Series **2767**, 092042 (2024).

[18] C. Meneveau, T. S. Lund, and W. H. Cabot, *A Lagrangian dynamic subgrid-scale model of turbulence,* Journal of Fluid Mechanics **319**, 353–385 (1996).

[19] G. Rampanelli and D. Zardi, *A method to determine the capping inversion of the convective boundary layer,* Journal of Applied Meteorology - J APPL METEOROL **43**, 925 (2004).

[20] L. Lanzilao and J. Meyers, *Wind-farm wake recovery mechanisms in conventionally neutral boundary layers,* Journal of Fluid Mechanics **1015**, A5 (2025).

[21] D. Allaerts and J. Meyers, *Boundary-layer development and gravity waves in conventionally neutral wind farms,* Journal of Fluid Mechanics **814**, 95 (2017).

[22] L. Lanzilao and J. Meyers, *A parametric large-eddy simulation study of wind-farm blockage and gravity waves in conventionally neutral boundary layers,* Journal of Fluid Mechanics **979**, A54 (2024).

Photo by Jeppe de Boer,
Flevoland, Netherlands

7

CONCLUSIONS

To conclude this thesis, the final chapter describes the main findings and limitations of this study, and provides recommendations for future research. The conclusions are presented as answers to the key questions portrayed in the introduction chapter, which are reiterated below.

- *How can atmospheric gravity waves be systematically modeled within frameworks for high-fidelity flow simulations of wind farms?*
- *How can the proposed systematic method be extended to practical wind farm flow conditions?*
- *How can the systematic method be applied to investigate atmospheric gravity waves induced by an isolated wind farm and their impacts on wind farm performance?*
- *How can the systematic method be applied to investigate atmospheric gravity waves induced by a wind-farm cluster and their impacts on cluster performance?*

7.1. MAIN FINDINGS

Regional-scale wind farms trigger atmospheric gravity waves in the stable capping inversion and the free atmosphere aloft of the turbulent atmospheric boundary layer. Several recent large eddy simulations-based studies have investigated wind-farm-induced atmospheric gravity waves and showed that they contribute to the wind farm blockage effect and intra-farm wake recovery. More importantly, these investigations highlighted how ad hoc tuning of the simulation setup is laborious when trying to avoid spurious waves and their reflections from the domain boundaries. Since AGW knowledge is new to the wind energy community, the relevant literature is fragmented in describing these phenomena. Moreover, AGW characteristics need further investigation with regard to linking them to both isolated and cluster wind farms. Therefore, the aim of this thesis was to systematically investigate wind-farm-induced atmospheric gravity waves using large eddy simulations to gain the required understanding of the regional-scale wind farm aerodynamics. This aim was pursued in two main parts: firstly, a systematic method was proposed to overcome the ad hoc Rayleigh damping layer parameter tuning and domain sizing required in setting up wind farm simulations that include AGWs, and secondly, the systematic method was applied to advance the understanding of AGWs and their impacts on the performance of both isolated and clustered wind farms. This research is concluded by providing guidelines on how to set up reflection-free wind farm LES and by reporting findings on how AGWs impact regional-scale wind farm performance.

7.1.1. HOW CAN SPURIOUS AGWS BE MITIGATED IN WIND FARM SIMULATIONS?

Setting up wind farm simulations is a procedure that involves using Rayleigh and advection damping layers to dampen gravity waves and handle those traveling towards the inflow boundary from reflecting back into the domain. The following are the steps in a proposed best practice procedure when using inflow-outflow boundary conditions to simulate a wind farm.

1. Calculate the Froude numbers of the free atmosphere and the capping inversion, and the vertical aspect ratios of the atmospheric boundary layer and the wind farm.

2. Find the wavelengths of the internal and interfacial waves for the values of the above non-dimensional parameters. The wavelengths can be taken from this study or calculated using linear theory or reduced-order models like the linear buoyancy wave package and the multi-scale coupled model.

3. Define the domain length that accommodates an effective horizontal wavelength of the internal waves, and the domain height should accommodate a vertical internal wave. In the case of using periodic boundary conditions at lateral boundaries, they should be far enough from the wind farm to avoid recirculation of interfacial waves back into the wind farm zone. This also prevent hydrodynamic effects of simulating wind farms in narrow domains.

4. Place Rayleigh damping layers adjacent to all inflow-outflow and the top boundaries, and the thickness of these layers should be greater than the vertical wave-

length of the internal waves.

5. Pick a Rayleigh damping coefficient, normalized with the Brunt-Väisälä frequency, close to 10 for values of $Fr < 0.15$ and close to 1 for higher values.

6. The reference velocity of the Rayleigh damping layers should be set to the geostrophic wind components, which can be taken from the precursor simulations.

7. Place an advection-damping layer overlapping the inlet-Rayleigh-damping layer to contain the energy accumulating at the inlet boundary. The buffer length of the advection damping, the length where its forcing is maximum (i.e. unity), should be greater than the interfacial wavelength, whereas a kilometer-long region on either side of it should smoothly transition the forcing between minimum and maximum.

8. Ensure that all damping layers are applied only in the free atmosphere, particularly at the inflow, so that free-stream turbulence in the ABL is unaffected. In other words, on the inflow boundary, the damping layer should not extend all the way to the ground, it should attenuate just above the top of the boundary layer.

Note that a fringe layer overlapping the advection damping layer is required instead of the inlet- and outlet-Rayleigh damping layers if periodic boundary conditions are used in the streamwise direction; the remaining procedure remains the same.

7.1.2. HOW ARE AGW CHARACTERISTICS IMPORTANT TO WIND FARMS?

We investigated AGWs and their characteristics for varying CNBL conditions with the aim of relating the turbine level output to AGW properties. It is important to recognize that AGW phenomena can be interpreted in different ways, but such interpretations are useful only in describing the phenomena and less important from a wind farm performance perspective. Therefore, we highlight the most obvious correlations observed between AGW characteristics and the flow in the ABL, mainly at the hub height.

- Interfacial waves are the most important manifestation of AGWs with respect to wind farm flows, as their wavelengths and amplitudes are directly proportional to the capping inversion displacement, and hence to the size and strength of converging and diverging zones in the ABL. The interfacial wavelength is close to the wind farm length for supercritical conditions, thus there is a diverging zone causing deceleration through the entrance region and a converging zone in the wind farm exit region. The interfacial wavelength gets shorter than the wind farm length for conditions critical through subcritical, which leads to zones of diverging and converging flow with the same corresponding wavelength in the ABL that are much stronger than seen for supercritical conditions. ABL-aspect ratios ≤ 0.05 (i.e. boundary layer depths resembling stable conditions in the ABL) give rise to strong zones of diverging and converging flow even for supercritical conditions, as the capping inversion is very close to the top of the wind turbine rotors.

- The interfacial wave characteristics are more important for wind farm clusters as the resultant wave over each wind farm is determined by the interaction of those

triggered by individual wind farms. Such interaction is highly dependent on the inter-farm distance, which defines whether the waves interfere constructively or destructively. The flow in the ABL then relates to the resultant wavelength, especially for the downstream wind farm.

- The impact of internal waves on the flow in the ABL is difficult to assess, as they are propagating and carry energy away from the capping inversion. However, for $Fr \geq 0.2$, they propagate primarily in the horizontal, such that the two wave trains triggered at the start and end of the wind farm merge into one. This, together with their tendency to curve downstream of their source, suggests that they might refract back onto the capping inversion and affect its shape, and hence the flow in the ABL. However, we refrain from drawing firm conclusions regarding their impact on the ABL.

- Transient trapped waves confined in the capping inversion probably do not affect the flow in the ABL. Further, investigation is required to confirm any affects these waves may have on the flow in the ABL.

7.1.3. HOW DOES STRATIFICATION AFFECT WIND FARM PERFORMANCE?

When talking about stratification effects, we have considered variations in the power output of wind farms due to a stable capping inversion with a more weakly stratified free atmosphere above, such that the AGWs are triggered. We emphasize that simulations partially resolving or excluding AGWs predict drastically different behavior. Such simulations general employ a set-up with a rigid lid boundary condition at the top of the ABL, giving rise to what is essentially an immovable capping inversion. It is critical to note that stratification effects are secondary to wind farm performance in comparison to wake losses. Moreover, in deep boundary layers, wake effects completely dominate stratification effects when velocity deficits are higher, like behind the upstream wind turbines and in the inter-farm wake region. However, stratification effects become more important for shallow boundary layers, particularly when capping inversions are strong. For these conditions, stratification affects the inflow, and both the intra- and inter-farm wake recovery. Here, we highlight the key conclusions related to stratification effects on wind farm performance and the related trends as a function of the non-dimensional parameters.

- The capping inversion acts like a flexible lid that caps turbulence from the ABL preventing its growth into the free atmosphere. More importantly, it acts as an interface between the free atmosphere and the ABL supporting waves triggered in stably stratified layers by an object such as a wind farm. These waves can affect the flow in the ABL and affect wind farm performance.

- Wind farm blockage is always enhanced by stratification effects where a deeper boundary layer forms in the induction and entrance region of a wind farm due to the flow being deflected upwards at the start of the wind farm. The degree to which this flow is deflected and the magnitude of the pressure wave which results due to the resulting capping inversion displacement depends on the stratification in the capping inversion and aloft.

- The stratified conditions can be represented by the Froude numbers of the free atmosphere (Fr) and the capping inversion (Fr_i), and the aspect-ratio of the atmospheric boundary layer ($\tilde{H}_i$). We observe a slight decrease in the blockage effect with increasing values of Fr and Fr_i, whereas a much stronger decrease is observed with increasing $\tilde{H}_i$. Which means that stratification effects are most sensitive to $\tilde{H}_i$ or ABL-depth.

- Stratification effects cause enhanced or diminished power outputs for waked wind turbines. It can be seen insupercritical conditions ($Fr_i > 1.0$) that turbines around $L/2$ downstream of the start of the wind farm and in the exit region show enhanced power output compared to the case where stratification effects are absent. In below or around critical conditions ($Fr_i \leq 1.0$), multiple modulations of turbine power output can be seen downstream of the wind farm entrance.

- Stratification effects are particularly strong for low ABL-aspect ratios or shallow boundary layers. For instance, wind turbine outputs are more sensitive to the capping inversion shape compared to a deeper boundary layer with the same Fr and Fr_i. Besides stratification effects, wake recovery is slow due to confined vertical flow entrainment by the low capping inversion, and the wind farm and cluster wakes are skewed (i.e. wakes narrow instead of expanding horizontally).

- When considering a cluster of two wind farms, stratification effects are shown to benefit or detriment an upstream wind farm in CNBL conditions, compared to the same operating in isolation. However, both wind farms, particularly the downstream wind farm, lose more power than they would operating in a truly neutral ABL. This is mainly due to flow mixing being constrained by an capping inversion. Interestingly, the wake efficiency of the downstream wind farm is better than that of the upstream one. This again highlights that fluctuations in row-wise power outputs due to stratification effects are less pronounced for the downstream wind farm due to higher velocity deficits through it.

7.2. RESEARCH LIMITATIONS

This study made several assumptions and choices, mainly for the sake of simplicity, in defining its scope. We simulated canonical atmospheres: the thermal structure of the CNBLs was approximated with constant potential temperature gradients in the capping inversion and the free atmosphere. Moreover, the simulated capping inversions are horizontally uniform with initially a constant thickness of 100 m, both of which might vary in reality. Only unidirectional wind was simulated, which in reality changes over time. We did simulate shallow and deep CNBLs that would resemble stable and convective boundary layers, respectively, but the effect of surface layer thermal stability was not studied.

The present study focused on the simulation domain, damping layer sizes, and damping coefficient. Other important parameters were taken from the literature. For instance, the size of the Gaussian kernel that project the wind turbine thrust onto the grid was taken from TOSCA recommendations. Likewise, the grid size, Smagorinsky constant, numerical schemes, and pressure and geostrophic controller settings were all taken from

the literature. Although the proposed method to simulate atmospheric gravity waves might not be sensitive to these choices, this study did not investigate these assumptions.

7.3. RECOMMENDATIONS

7.3.1. EXTENDING THE METHOD

The non-dimensional approach taken in this study can be extended by including other important variables, like turbulence intensity, boundary layer stability, wind direction, Coriolis effect, and wind farm power density. Such an extended set of non-dimensional parameters can be used to assess the ambient flows in order to systematically categorize inflow characteristics. The same can be applied to a more complete and realistic investigation of wind farm aerodynamics. Besides making this method more holistic, there is a need to simulate real atmospheric conditions for a real wind farm to validate the stratification effects on wind farm performance.

7.3.2. MEASURING WIND-FARM-INDUCED ATMOSPHERIC GRAVITY WAVES

As mentioned previously, an experimental campaign to capture wind farm-induced AGWs is needed. Such a campaign would require measuring potential temperature and vertical velocity at heights up to a few kilometers above an offshore wind farm. Moreover, the wind farm should be significantly far from the coast and any orographic features to ensure there are no obvious sources of naturally occurring gravity waves. Amplitudes of wind-farm-induced atmospheric gravity waves are relatively small compared with naturally occurring ones, making them difficult to detect. Moreover, measuring them or their signature in the flow fields is a challenge, as many atmospheric phenomena are tightly coupled where disentangling one from another is hard. However, SAR images have shown atmospheric gravity waves around wind farm clusters in the North Sea, and lidar and radar measurements have shown naturally occurring atmospheric gravity waves. This gives hope that wind farm-induced atmospheric gravity waves could be detected using such instruments.

7.3.3. DEVELOPING A NON-REFLECTIVE INFLOW BOUNDARY CONDITION

The proposed method in this thesis uses existing methods to dampen AGWs that are based on forcing zones. Damping layers have an additional computational cost, which can be mitigated if a boundary condition, at least at inflow boundaries, is developed to mitigate spurious waves. The main challenge is for the boundary condition to detect a wave spectrum coming towards it. If the speeds of the wave modes approaching a boundary are known a priori, there is a potential to modify the boundary condition by blending the inflow with the information of the spectrum approaching it. A suggestion in this regard is to monitor flow fields at various locations far from the boundary and determine changes to the fields among the monitored locations. The rate of these changes could be used to predict how the field would appear at the boundary and adjust the boundary condition accordingly. Such a boundary condition can at least assist a Rayleigh damping layer to limit the accumulation of wave energy at the inflow for a simulation time spanning a diurnal cycle and without requiring an additional damping layer.

A

CONFIGURATION OF RAYLEIGH DAMPING LAYERS

The reflection of waves from the top boundary is expected as the typically used boundary conditions to model an arbitrary location in the atmosphere are mostly fully reflective. Since gravity waves travel vertically, one would anticipate reflections from the top boundary if forcing zones are not used there. Intriguingly, with inflow/outflow boundary conditions, the damping layers are needed at other boundaries, too. For instance, the reflected waves from the top are directed towards the outlet, and weak reflections may also appear there. Likewise, the wave energy distributes throughout the domain and accumulates over time if not damped at the boundaries. This is evident as reflections from the inlet propagate into the domain after one to two flow-through times. Thus, damping the waves at various boundaries is necessary for realistic simulations. Sometimes, the solution for a setup without an appropriate damping layer configuration will diverge due to numerical instability caused by excessive flow velocity from complex reflected wave interactions.

In this context, deciding the configuration of damping layers becomes important when setting up simulations involving gravity waves. We explored the configuration of damping layers to come up with a base case. The test cases and normalised errors are shown in Fig. A.1.

At this point, it is important to highlight that the minimum amount of reflections is a user choice. Since the reflections intensify over simulation time, it may be the case that a user will opt for a configuration based on the availability of computational resources and the simulation time of their interest. Thus, a simulation without any forcing zones is the first possibility. The domain height is critical when there is no damping. This can be established by comparing cases 1, 2, and 3, where the domain height (L_z) is 1, 2, and 3 times the effective vertical wavelength, respectively. Reflections increase rapidly when increasing the domain height, from 22% to 33% and 120% in cases 1 to 3, respectively. However, none of these cases fall below the criterion for an acceptable amount of reflection. Thus, we opt to use Rayleigh damping, and it is evident that only having a

A

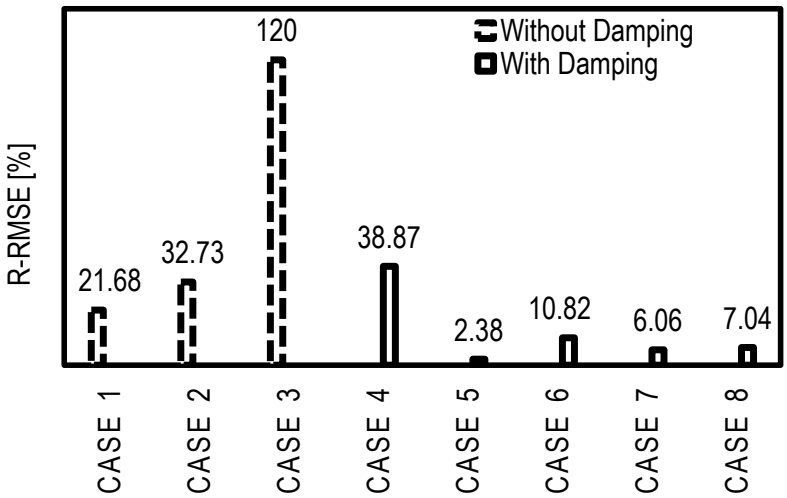

Figure A.1: Comparison of R-RMSE for various damping configurations designed to acquire the most suitable arrangement for the base case.

top Rayleigh-damped layer (case 4) is insufficient to reduce reflections to an acceptable level. The R-RMSE for this case is 39%, and the solution for the hill case is contaminated by reflections from the inlet such that the actual gravity waves disappear entirely. This suggests that it is better not to have a damping layer rather than only having a damping layer at the top and instead have a setup with a domain height just over one effective vertical wavelength. This would be viable only when a maximum value of R-RMSE or Cr of about 20% is an acceptable criterion for a given problem.

The most suitable setup is to have damping layers at the inlet, outlet, and top with the same damping characteristics. This is Case 5 in Fig. A.1, where R-RMSE is only 2.38%. If the damping layer thickness is reduced by half whilst having damping on all three sides (Case 6), the R-RMSE increases to 10%. A combination of damping layers at the top and outlet (Case 7) appears better than Case 6 as R-RMSE here is 6%. Damping at the top and inlet (Case 8), is slightly more reflective (R-RMSE 7%) than in Case 7. There can be other possible configurations, but this analysis gives enough insight to decide on a suitable configuration for a sufficiently accurate base case. Altogether, the configuration of damping layers is a trade-off between computational resources and the desired accuracy of the solution that depends on the user's choice regarding the acceptable degree of reflection.

B

IMPLICATIONS OF STRATIFICATION EFFECTS

In this section, we speculate on the implications of stratification effects. Most of the analysis in this study has focused on row-averaged power predictions and some on wind farm performance. It is beneficial to extend the analysis to Annual Energy Production (AEP) estimates, as an assessment of wind farm planning and design to harness and/or mitigate stratification effects follows naturally. Moreover, future wind farms might be built with turbines bigger than the 5MW turbine considered in this thesis. Thus, it is desirable to speculate on the expected stratification impacts on wind farms of large wind turbines.

Table B.1 shows AEP estimates from LES data for an isolated wind farm and a cluster of two wind farms. AEP is estimated for a scenario that assumes 40 % capacity factor, typical for offshore wind farms, and that the simulated CNBL condition existed 15 % over the year. The occurrence of 15 % CNBL conditions over a year is motivated by [1], who analyzed both numerical and measured data for a site in the Baltic Sea and determined 15 %, 23 %, and 66 % of the filtered conditions as CNBL, SBL, and CBL, respectively. The percentage AEP difference is estimated by differencing AEP_CNBL and AEP_TNBL; thus, the quantified impacts are based on AEP predictions from TNBL simulations. As already discussed in Chapters 5 and 6, stratification negatively impacts both isolated and clustered wind farms, which is highlighted again in the Table B.1 by percentage AEP differences for each wind farm. In fact, each CNBL condition simulated does not occur for 15 % of the time over a year in reality. Therefore, a more realistic yet simple approach to estimate AEP is to average the simulated CNBL conditions. This means the unique CNBL conditions simulated occur equally over the 15 % of yearly CNBL time. Although we simulated 21 unique CNBL conditions for the isolated wind farm, we considered only 10 in estimating the average AEP, as each of these has a comparable TNBL simulation. We require additional TNBL simulations to include all the CNBL conditions simulated, which is computationally infeasible. For clustered wind farms, we have 7 unique simulations to estimate the average AEP, as three of the total 9 cases shown are the same. The AEP of

the isolated wind farm averaged over the 10 CNBL conditions is 3.1 % less than that of the AEP of the same wind farm for TNBL conditions. For the upstream wind farm in the clustered scenario, the average AEP over the 7 simulations is 1.2 % less than that of TNBL conditions. Whereas the downstream wind farm produces 7.6 % less energy under CNBL conditions than the TNBL conditions. Overall, the average AEP of the two wind farms is 5.4 % less due to stratification effects.

Case	Isolated (AEP [MWh])			Clustered (AEP [MWh])					
	CNBL	TNBL	Diff [%]	Upstream Wind Farm			Downstream Wind Farm		
				CNBL	TNBL	Diff [%]	CNBL	TNBL	Diff [%]
Fr_0.075	7.550×10^4	7.794×10^4	-3.15	–	–	–	–	–	–
Fr_0.1	7.749×10^4	7.794×10^4	-0.58	7.632×10^4	7.776×10^4	-1.86	5.700×10^4	6.110×10^4	-6.71
Fr_0.125	7.695×10^4	7.794×10^4	-1.26	–	–	–	–	–	–
Fr_0.15	7.470×10^4	7.794×10^4	-4.14	7.742×10^4	7.776×10^4	-0.44	5.692×10^4	6.110×10^4	-6.84
Fr_0.2	7.387×10^4	7.794×10^4	-5.23	7.703×10^4	7.776×10^4	-0.95	5.598×10^4	6.110×10^4	-8.39
Fr_0.25	7.149×10^4	7.794×10^4	-8.28	–	–	–	–	–	–
Fri_0.25	3.881×10^4	–	–	–	–	–	–	–	–
Fri_0.5	3.379×10^4	–	–	–	–	–	–	–	–
Fri_0.75	7.714×10^4	7.794×10^4	-1.02	7.527×10^4	7.776×10^4	-3.21	5.550×10^4	6.110×10^4	-9.17
Fri_1.0	7.504×10^4	7.794×10^4	-3.71	7.700×10^4	7.776×10^4	-0.98	5.606×10^4	6.110×10^4	-8.26
Fri_1.25	7.767×10^4	7.794×10^4	-0.35	7.742×10^4	7.776×10^4	-0.44	5.692×10^4	6.110×10^4	-6.84
Fri_1.50	7.525×10^4	7.794×10^4	-3.46	–	–	–	–	–	–
$\tilde{H}_i$_0.042	6.730×10^4	–	–	6.843×10^4	7.046×10^4	-2.87	3.382×10^4	5.563×10^4	-39.23
$\tilde{H}_i$_0.084	7.470×10^4	7.794×10^4	-4.14	7.742×10^4	7.776×10^4	-0.44	5.692×10^4	6.110×10^4	-6.84
$\tilde{H}_i$_0.125	7.782×10^4	–	–	7.926×10^4	7.979×10^4	-0.66	5.992×10^4	6.381×10^4	-6.10
$\tilde{H}_i$_0.167	7.860×10^4	–	–	–	–	–	–	–	–
$\tilde{H}_i$_0.21	7.973×10^4	–	–	–	–	–	–	–	–
$\tilde{H}_i$_0.25	7.987×10^4	–	–	–	–	–	–	–	–
Sh_0.026	7.470×10^4	7.794×10^4	-4.14	–	–	–	–	–	–
Sh_0.03	7.886×10^4	–	–	–	–	–	–	–	–
Sh_0.0345	8.392×10^4	–	–	–	–	–	–	–	–
Sh_0.039	8.887×10^4	–	–	–	–	–	–	–	–
Sh_0.0435	9.215×10^4	–	–	–	–	–	–	–	–
Sh_0.048	9.605×10^4	–	–	–	–	–	–	–	–

Table B.1: Estimated annual energy production for isolated and clustered wind farm cases. AEP values shown are estimated considering 40% capacity factor and assuming 15% CNBL conditions over a year. The percentage differences for each wind farm are based on the TNBL estimates using Diff = (AEP_CNBL – AEP_TNBL)/AEP_TNBL × 100.

Stratification clearly negatively impacts wind farm performance, and these impacts are either direct or indirect. The former refers to how a given stratification condition affects the ambient flow and wake recovery. The latter refers to the blockage effect and power gains through the wind farm due to gravity waves. The blockage effect is the main stratification effect, which always has a negative impact and is linked with the strength of the flow deflected upward. The intensity of upward deflected flow and, therefore, the capping inversion displacement may be reduced by increasing lateral distancing. More spanwise space around the wind turbines would reduce the upward deflected flow.

Since both direct and indirect impacts are strictly related to prevailing stratification conditions, it is vital for wind farm planning and design to measure temperature besides wind speed and direction at the site. The typical 10-minute sampling time is sufficient, as the potential temperature conditions might vary on a timescale slower than 10 minutes. Once the frequency of the stratification conditions is known, the wind farm layout can be optimized with the most occurring stratification conditions in view. For instance, if shallow boundary layers and subcritical conditions are common, both wind turbine and inter-farm distances need to be greater than what could be fine for non-stratified conditions and deeper boundary layers. In clustered wind farms, the inter-farm distancing can be decided based on the interfacial wavelengths. The blockage effect of the downstream wind farm can be minimized by placing it at a distance where its wave destructively interacts with that of the advecting one from the upstream wind farm. The downstream wind farms in clusters need to be placed much further apart if shallow boundary layers are frequent at a site, to allow enough space for wake recovery. However, skewing of the wind farm wake can be beneficial for wind farms further downstream in a cluster, as they can be built out of the concentrating cluster wake region.

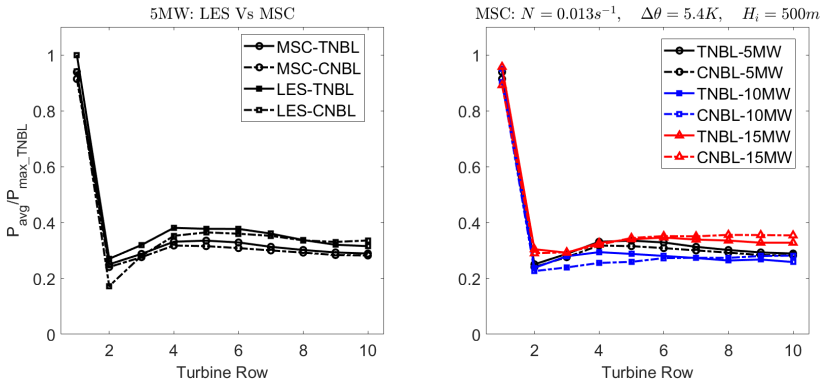

Figure B.1: Row averaged power as a function of (left): TNBL and CNBL flow conditions for a 5MW turbine, predicted by LES and MSC simulations, and (right): turbine size, predicted by MSC simulations only. The simulated CNBL flow conditions are defined by $N = 0.013s^{-1}$, $\Delta\theta = 5.4K$, and $H_i = 500m$.

In this thesis, we simulated wind farms of 5 MW wind turbines only. Stratification effects on wind farms of bigger wind turbines is an obvious concern, as the turbine size of wind farms installed lately is larger than 5 MW and those in the future wind farms might be larger too. To this end we simulated there isolated wind farms, one each containing

5 MW, 10 MW, and 15 MW turbines. Due to the lack of computational resources, these simulations are conducted with Multi-Scale Coupled model. As described in Chapter 2, MSC is an engineering model that includes stratification effects in modeling wind farms.

Figure B.1 shows row-averaged power predicted by LES and MSC simulations. The plot on the left is for a wind farm of 5 MW turbines, that shows how MSC reasonably captures blockage effect and power variation trends through the wind farm. Although, the exact power predictions by MSC are smaller than those predicted by LES, except for the second row, where MSC overpredicts the power output. The row averaged power outputs of wind farms of the three turbine sizes are shown on the right plot. Similar trends are obvious in power loses due to blockage effect and power variations through the wind farm for each wind farm of a specific turbine size. The powers predicted for CNBL simulations are smaller for the first row compared to the respective TNBL simulations. Moreover, the turbines in the entrance produce less in the CNBL simulations but slightly more in the exit region. These row-wise power variations are typical stratification effects. However, a clear trend in the variation of stratification effects for varying turbine size is not clear. Which means, we cannot conclude based on these predictions whether stratification effects become milder or stronger with changing turbine size. Note that the simulated CNBL and TBNL conditions were the same, and turbine distancing was set to 5D and 3D in streamwise and spanwise directions, respectively.

REFERENCES

[1] G. P. N. Diaz, M. L. Mayol, M. Rowen, B. Schliffke, S. Freitas, and S. Erbsloeh, *Impact of coastal gradients on wind farm energy yield assessment: model comparison,* Journal of Physics: Conference Series **3016**, 012039 (2025), article number: 012039.

REFERENCES

[1] M. A. Khan, D. Allaerts, S. J. Watson, and M. J. Churchfield, *Investigating the relationship between simulation parameters and flow variables in simulating atmospheric gravity waves for wind energy applications,* Wind Energy Science **10**, 1167 (2025).

[2] G. (2024), *Global wind report*, Tech. Rep. (GWEC, 2024).

[3] I. (2024), *Integrating Solar and Wind*, Tech. Rep. (IEA, Paris, 2024).

[4] G. (2016), *Global Wind Report: Annual Market Update 2015*, Tech. Rep. (GWEC, 2016).

[5] G. (2025), *Global wind report*, Tech. Rep. (GWEC, 2025).

[6] S. E. Haupt, B. E. Kosovie, J. A. Lee, and P. A. Jiménez, *Mesoscale modeling of the atmosphere,* in *Wind Energy Modeling and Simulation - Volume 1: Atmosphere and Plant*, Chap. Chapter 3, pp. 65–115, https://digital-library.theiet.org/doi/pdf/10.1049/PBPO125F$_c h3$.

[7] R. J. Stevens and C. Meneveau, *Flow structure and turbulence in wind farms,* Annual Review of Fluid Mechanics **49**, 311 (2017).

[8] F. Porté-Agel, M. Bastankhah, and S. Shamsoddin, *Wind-turbine and wind-farm flows: A review,* Boundary-Layer Meteorology **174**, 1 (2020).

[9] D. Mehta, A. H. van Zuijlen, B. Koren, J. G. Holierhoek, and H. Bijl, *Large eddy simulation of wind farm aerodynamics: A review,* Journal of Wind Engineering and Industrial Aerodynamics **133**, 1 (2014).

[10] D. Allaerts and J. Meyers, *Boundary-layer development and gravity waves in conventionally neutral wind farms,* Journal of Fluid Mechanics **814**, 95 (2017).

[11] S. Stipa, M. Ahmed Khan, D. Allaerts, and J. Brinkerhoff, *A large-eddy simulation (LES) model for wind-farm-induced atmospheric gravity wave effects inside conventionally neutral boundary layers,* Wind Energy Science **9**, 1647 (2024).

[12] L. Lanzilao and J. Meyers, *A parametric large-eddy simulation study of wind-farm blockage and gravity waves in conventionally neutral boundary layers,* Journal of Fluid Mechanics **979**, A54 (2024).

[13] R. B. Smith, *Gravity wave effects on wind farm efficiency,* Wind Energy **13**, 449 (2010).

[14] D. Allaerts, S. V. Broucke, N. Van Lipzig, and J. Meyers, *Annual impact of wind-farm gravity waves on the Belgian-Dutch offshore wind-farm cluster,* Journal of Physics: Conference Series **1037** (2018), 10.1088/1742-6596/1037/7/072006.

[15] L. Lanzilao and J. Meyers, *Set-point optimization in wind farms to mitigate effects of flow blockage induced by atmospheric gravity waves,* Wind Energy Science **6**, 247 (2021).

[16] K. L. Wu and F. Porté-Agel, *Flow adjustment inside and around large finite-size wind farms,* Energies **10**, 4 (2017).

[17] D. Allaerts and J. Meyers, *Gravity waves and wind-farm efficiency in neutral and stable conditions,* Boundary-Layer Meteorology **166**, 269 (2018).

[18] L. Lanzilao and J. Meyers, *An improved fringe-region technique for the representation of gravity waves in large-eddy simulation with application to wind farms,* Boundary-Layer Meteorology **186**, 567 (2023).

[19] S. Stipa, A. Ajay, D. Allaerts, and J. Brinkerhoff, *TOSCA – an open-source, finite-volume, large-eddy simulation (LES) environment for wind farm flows,* Wind Energy Science **9**, 297 (2024).

[20] D. Allaerts, *Large-eddy Simulation of Wind Farms in Conventionally Neutral and Stable Atmospheric Boundary Layers*, Ph.D. thesis (2016).

[21] D. Allaerts and J. Meyers, *Large eddy simulation of a large wind-turbine array in a conventionally neutral atmospheric boundary layer,* Physics of Fluids **27**, 065108 (2015).

[22] M. A. Khan, S. J. Watson, D. J. N. Allaerts, and M. Churchfield, *Recommendations on setup in simulating atmospheric gravity waves under conventionally neutral boundary layer conditions,* Journal of Physics: Conference Series **2767**, 092042 (2024).

[23] A. Stieren and R. J. A. M. Stevens, *Impact of wind farm wakes on flow structures in and around downstream wind farms,* Flow **2**, E21 (2022).

[24] A. Abraham, N. Hamilton, N. Bodini, B. Hirth, J. Schroeder, S. Letizia, R. Krishnamurthy, R. Newsom, and P. Moriarty, *Land-based wind plant wake characterization using dual-doppler radar measurements at AWAKEN,* Journal of Physics: Conference Series **2767**, 092037 (2024).

[25] P. Ouro, M. Ghobrial, K. Ali, and T. Stallard, *Numerical modelling of offshore wind-farm cluster wakes,* Renewable and Sustainable Energy Reviews **215**, 115526 (2025).

[26] G. P. N. Diaz, M. L. Mayol, M. Rowen, B. Schliffke, S. Freitas, and S. Erbsloeh, *Impact of coastal gradients on wind farm energy yield assessment: model comparison,* Journal of Physics: Conference Series **3016**, 012039 (2025), article number: 012039.

[27] M. A. Khan, M. J. Churchfield, and S. J. Watson, *Dependence of wind-farm-induced gravity waves and wind-farm performance on non-dimensional atmospheric parameters and simulation configuration,* Wind Energy Science Discussions **2025**, 1 (2025).

[28] R. B. Stull, *An Introduction to Boundary Layer Meteorology*, Atmospheric and Oceanographic Sciences Library, Vol. 13 (Springer Netherlands, Dordrecht, 1988).

[29] S. J. Ollier and S. J. Watson, *Modelling the impact of trapped lee waves on offshore wind farm power output,* Wind Energy Science **8**, 1179 (2023).

[30] J. Sachsperger, S. Serafin, and V. Grubišić, *Lee waves on the boundary-layer inversion and their dependence on free-atmospheric stability,* Frontiers in Earth Science **3** (2015), 10.3389/feart.2015.00070.

[31] R. J. Barthelmie, S. C. Pryor, S. T. Frandsen, K. S. Hansen, J. G. Schepers, K. Rados, W. Schlez, A. Neubert, L. E. Jensen, and S. Neckelmann, *Quantifying the impact of wind turbine wakes on power output at offshore wind farms,* Journal of Atmospheric and Oceanic Technology **27**, 1302 (2010).

[32] L. P. Chamorro and F. Porté-Agel, *Turbulent flow inside and above a wind farm: A wind-tunnel study,* Energies **4**, 1916 (2011).

[33] C. L. Archer, S. Mirzaeisefat, and S. Lee, *Quantifying the sensitivity of wind farm performance to array layout options using large-eddy simulation,* Geophysical Research Letters **40**, 4963 (2013), https://agupubs.onlinelibrary.wiley.com/doi/pdf/10.1002/grl.50911 .

[34] N. Hamilton, M. Melius, and R. B. Cal, *Wind turbine boundary layer arrays for cartesian and staggered configurations – part i: Flow field and power measurements,* Wind Energy **17**, 939 (2014).

[35] M. Calaf, C. Meneveau, and J. Meyers, *Large eddy simulation study of fully developed wind-turbine array boundary layers,* Physics of Fluids **22**, 015110 (2010).

[36] M. Abkar and F. Porté-Agel, *The effect of free-atmosphere stratification on boundary-layer flow and power output from very large wind farms,* Energies **6**, 2338 (2013).

[37] S. Frandsen, *On the wind speed reduction in the center of large clusters of wind turbines,* Journal of Wind Engineering and Industrial Aerodynamics **39**, 251 (1992).

[38] M. Calaf, M. B. Parlange, and C. Meneveau, *Large eddy simulation study of scalar transport in fully developed wind-turbine array boundary layers,* Physics of Fluids **23**, 126603 (2011), https://pubs.aip.org/aip/pof/article-pdf/doi/10.1063/1.3663376/13704482/126603_1_online.pdf .

[39] D. Yang, C. Meneveau, and L. Shen, *Large-eddy simulation of offshore wind farm,* Physics of Fluids **26** (2014), 10.1063/1.4863096.

[40] M. Gaumond, P.-E. Réthoré, S. Ott, A. Peña, A. Bechmann, and K. S. Hansen, *Evaluation of the wind direction uncertainty and its impact on wake modeling at the horns rev offshore wind farm,* Wind Energy **17**, 1169 (2014), https://onlinelibrary.wiley.com/doi/pdf/10.1002/we.1625 .

[41] J. Bleeg, M. Purcell, R. Ruisi, and E. Traiger, *Wind farm blockage and the consequences of neglecting its impact on energy production,* Energies **11** (2018), 10.3390/en11061609.

[42] C. Rodaway, K. Gunn, S. Williams, A. Sebastiani, E. Simon, M. Courtney, G. R. Thorsen, E. Clausen, M. Turrini, D. Wouters, Y. Liu, J. Gottschall, M. Dörenkämper, E. Patschke, L.-Y. Hun, and N. Adams, *Owa globe: Measuring and modelling the global blockage effect to achieve industry consensus,* in *WindEurope Technology Workshop 2024: Resource Assessment & Analysis of Operating Wind Farms* (Dublin, Ireland, 2024) poster.

[43] A. S. Wise, R. S. Arthur, A. Abraham, S. Wharton, R. Krishnamurthy, R. Newsom, B. Hirth, J. Schroeder, P. Moriarty, and F. K. Chow, *Large-eddy simulation of an atmospheric bore and associated gravity wave effects on wind farm performance in the southern great plains,* Wind Energy Science Discussions **2024**, 1 (2024).

[44] L. P. Chamorro and F. Porté-Agel, *Experimental study on the wake meandering within a scale model wind farm subject to a wind-tunnel flow simulating an atmospheric boundary layer,* Boundary-Layer Meteorology **166**, 449 (2017).

[45] M. B. Christiansen and C. B. Hasager, *Wake effects of large offshore wind farms identified from satellite SAR,* Remote Sensing of Environment **98**, 251 (2005).

[46] M. Abkar and F. Porté-Agel, *Influence of atmospheric stability on wind-turbine wakes: A large-eddy simulation study,* Physics of Fluids **27**, 035104 (2015).

[47] S. Xie and C. L. Archer, *A numerical study of wind-turbine wakes for three atmospheric stability conditions,* Boundary-Layer Meteorology **165**, 87 (2017).

[48] Z. Wang, J. Jacob, F. Marlow, and P. Sagaut, *Lattice boltzmann method-based large eddy simulation of the influence of atmospheric stability on wind farm wake,* Physics of Fluids **37**, 065131 (2025).

[49] A. C. Fitch, J. K. Lundquist, and J. B. Olson, *Mesoscale influences of wind farms throughout a diurnal cycle,* Monthly Weather Review **141**, 2173 (2013).

[50] V. Sharma, M. B. Parlange, and M. Calaf, *Perturbations to the spatial and temporal characteristics of the diurnally-varying atmospheric boundary layer due to an extensive wind farm,* Boundary-Layer Meteorology **162**, 255 (2017).

[51] S. Stipa, A. Ajay, and J. Brinkerhoff, *The actuator farm model for large eddy simulation (LES) of wind-farm-induced atmospheric gravity waves and farm–farm interaction,* Wind Energy Science **9**, 2301 (2024).

[52] O. Maas, *From gigawatt to multi-gigawatt wind farms: wake effects, energy budgets and inertial gravity waves investigated by large-eddy simulations,* Wind Energy Science Discussions **2022**, 1 (2022).

[53] M. Souaiby and F. Porte-Agel, *Atmospheric stability effect on wind farm flow and performance,* Physics of Fluids **37**, 095152 (2025).

[54] S. Stipa, A. Ajay, D. Allaerts, and J. Brinkerhoff, *The multi-scale coupled model: a new framework capturing wind farm-atmosphere interaction and global blockage effects,* Wind Energy Science Discussions **2023**, 1 (2023).

[55] N. G. Mortensen and E. L. Petersen, *WAsP – The Wind Atlas Analysis and Application Program: User's Guide*, Risø DTU, Technical University of Denmark, Roskilde, Denmark (2008).

[56] J. Annoni, P. Fleming, A. Scholbrock, J. Roadman, S. Dana, C. Adcock, F. Porte-Agel, S. Raach, F. Haizmann, and D. Schlipf, *Analysis of control-oriented wake modeling tools using lidar field results,* Wind Energy Science **3**, 819 (2018).

[57] M. J. Churchfield, S. Lee, J. Michalakes, and P. J. Moriarty, *A numerical study of the effects of atmospheric and wake turbulence on wind turbine dynamics,* Journal of Turbulence **13**, 1 (2012).

[58] J. Schalkwijk, H. J. J. Jonker, A. P. Siebesma, and E. van Meijgaard, *Weather forecasting using gpu-based large-eddy simulations,* Bulletin of the American Meteorological Society **96**, 715 (2015).

[59] B. Maronga, M. Gryschka, R. Heinze, F. Hoffmann, F. Kanani-Sühring, M. Keck, K. Ketelsen, M. O. Letzel, M. Sühring, and S. Raasch, *The parallelized large-eddy simulation model (palm) version 4.0 for atmospheric and oceanic flows: model formulation, recent developments, and future perspectives,* Geoscientific Model Development **8**, 1539 (2015).

[60] N. N. Sørensen, *General Purpose Flow Solver Applied to Flow Over Hills*, Doctoral thesis, Risø National Laboratory for Sustainable Energy, Wind Energy Division, Aeroelastic Design (1995).

[61] M. B. Kuhn, M. T. Henry de Frahan, P. Mohan, G. Deskos, M. Churchfield, L. Cheung, A. Sharma, A. Almgren, S. Ananthan, M. J. Brazell, L. A. Martinez-Tossas, R. Thedin, J. Rood, P. Sakievich, G. Vijayakumar, W. Zhang, and M. Sprague, *Amrwind: A performance-portable, high-fidelity flow solver for wind farm simulations,* Wind Energy **28** (2025), 10.1002/we.70010.

[62] J. Smagorinsky, *General circulation experiments with the primitive equations: I. the basic experiment,* Monthly Weather Review **91**, 99 (1963).

[63] M. Germano, U. Piomelli, P. Moin, and W. Cabot, *A dynamic subgrid-scale eddy viscosity model,* Physics of Fluids A **3**, 1760 (1991).

[64] C. Meneveau, T. S. Lund, and W. H. Cabot, *A Lagrangian dynamic subgrid-scale model of turbulence,* Journal of Fluid Mechanics **319**, 353–385 (1996).

[65] W. Rozema, H. J. Bae, P. Moin, and R. Verstappen, *Minimum-dissipation models for large-eddy simulation,* Physics of Fluids (2015), 10.1063/1.4928700.

[66] J. H. Ferziger and M. Perić, *Computational Methods for Fluid Dynamics*, 3rd ed. (Springer, Berlin, Heidelberg, 2002).

[67] A. S. Monin and A. M. Obukhov, *Basic laws of turbulent mixing in the surface layer of the atmosphere,* Trudy Geofizicheskogo Instituta, Akademii Nauk SSSR **24**, 163 (1954), in Russian.

[68] J. Fröhlich and D. von Terzi, *Hybrid LES/RANS methods for the simulation of turbulent flows,* J. Prog. Aerosp. Sci. **44**, 349 (2008).

[69] P. R. Spalart, *Detached-Eddy Simulation,* Annual Review of Fluid Mechanics **41**, 181 (2009).

[70] A. C. Fitch, J. B. Olson, J. K. Lundquist, J. Dudhia, A. K. Gupta, J. Michalakes, and I. Barstad, *Local and mesoscale impacts of wind farms as parameterized in a mesoscale nwp model,* Monthly Weather Review **140**, 3017 (2012).

[71] M. J. Lawson, J. Melvin, S. Ananthan, K. M. Gruchalla, J. S. Rood, and M. A. Sprague, *Blade-Resolved, Single-Turbine Simulations Under Atmospheric Flow*, Tech. Rep. (National Renewable Energy Laboratory (NREL), 2019).

[72] G. Vijayakumar and J. G. Brasseur, *Blade-resolved modeling with fluid-structure interaction,* in *Wind Energy Modeling and Simulation: Volume 1: Atmosphere and Plant*, IET Energy Engineering Series, edited by P. Veers (Institution of Engineering and Technology, 2019) pp. 23–64.

[73] R.-E. Keck, R. Mikkelsen, N. Troldborg, M. de Maré, and K. S. Hansen, *Synthetic atmospheric turbulence and wind shear in large eddy simulations of wind turbine wakes,* Wind Energy **17**, 1247 (2014), https://onlinelibrary.wiley.com/doi/pdf/10.1002/we.1631 .

[74] X. Wu, *Inflow Turbulence Generation Methods,* Annual Review of Fluid Mechanics **49**, 23 (2017).

[75] D. R. Durran, *Nonreflecting boundary conditions,* Springer, New York, NY , 395 (1999).

[76] R. Perić, *Minimizing undesired wave reflection at the domain boundaries in flow simulations with forcing zones*, Master's thesis, Technische Universität Hamburg (2019).

[77] J. Klemp and D. Lilly, *Numerical simulation of hydrostatic mountain waves,* Journal of the Atmospheric Sciences **35**, 78 (1978).

[78] M. Inoue, G. Matheou, and J. Teixeira, *LES of a spatially developing atmospheric boundary layer: Application of a fringe method for the stratocumulus to shallow cumulus cloud transition,* Monthly Weather Review **142**, 3418 (2014).

[79] S. B. Vosper and A. N. Ross, *Sampling errors in observed gravity wave momentum fluxes from vertical and tilted profiles,* Atmosphere **11** (2020), 10.3390/atmos11010057.

[80] W. H. Snyder, R. S. Thompson, R. E. Eskridge, R. E. Lawson, I. P. Castro, J. T. Lee, J. C. R. Hunt, and Y. Ogawa, *The structure of strongly stratified flow over hills: dividing-streamline concept,* Journal of Fluid Mechanics **152**, 249 (1985).

[81] D. Allaerts, *LBoW - linear buoyancy wave package,* (2022).

[82] C. Markfort, W. Zhang, and F. Porté-Agel, *Analytical model for mean flow and fluxes of momentum and energy in very large wind farms,* Boundary-Layer Meteorology **166** (2018), 10.1007/s10546-017-0294-6.

[83] M. Churchfield, S. Lee, and P. Moriarty, *Overview of the simulator for wind farm application (SOWFA),* National Renewable Energy Laboratory (2012).

[84] J. R. Taylor and S. Sarkar, *Internal gravity waves generated by a turbulent bottom [e]kman layer,* Journal of Fluid Mechanics **590**, 331 (2007).

[85] D. R. Durran, *Nonreflecting Boundary Conditions* (2010) pp. 453–495.

[86] S. N. Gadde and R. J. Stevens, *Effect of coriolis force on a wind farm wake,* Journal of Physics: Conference Series **1256**, 012026 (2019).

[87] J. S. Brooke, R. Thedin, A. Sharma, E. Branlard, G. Vijayakumar, and A. S. Michael, *Effect of the integral length scales of turbulent inflows on wind turbine loads,* Renewable Energy **217**, 119 (2023).

[88] R. Smith, *The wind farm pressure field,* Wind Energy Science Discussions **2023**, 1 (2023).

[89] R. J. A. M. Stevens, J. Graham, and C. Meneveau, *A concurrent precursor inflow method for large eddy simulations and applications to finite length wind farms,* Renewable Energy **68**, 46 (2014).

[90] D. Allaerts, M. Khan, and M. Churchfield, *Froude number dependency of atmospheric gravity waves: Apparent horizontal wavelength and wave field inclination,* Submitted to Journal of Fluid Mechanics (2025).

[91] P. Queney, *The problem of air flow over mountains: A summary of theoretical studies,* Bulletin of the American Meteorological Society **29**, 16 (1948).

[92] Y.-T. Wu and F. Porté-Agel, *Modeling turbine wakes and power losses within a wind farm using LES: An application to the horns rev offshore wind farm,* Renewable Energy **75**, 945 (2015).

[93] N. Nygaard and S. Hansen, *Wake effects between two neighbouring wind farms,* in *Journal of Physics: Conference Series*, Vol. 753 (IOP Publishing, 2016) p. 032020.

[94] N. Nygaard, S. Steen, L. Poulsen, and J. Pedersen, *Modelling cluster wakes and wind farm blockage,* in *Journal of Physics: Conference Series*, Vol. 1618 (IOP Publishing, 2020) p. 062072.

[95] J. Fischereit, K. Schaldemose Hansen, X. Larsén, M. van der Laan, P.-E. Réthoré, and J. Murcia Leon, *Comparing and validating intra-farm and farm-to-farm wakes across different mesoscale and high-resolution wake models,* Wind Energy Science **7**, 1069 (2022).

[96] M. van der Laan, O. García-Santiago, M. Kelly, A. Meyer Forsting, C. Dubreuil-Boisclair, K. Seim, M. Imberger, A. Peña, N. Sørensen, and P.-E. Réthoré, *A new RANS-based wind farm parameterization and inflow model for wind farm cluster modeling,* Wind Energy Science **8**, 819 (2023).

[97] K. Berge, G. Centurelli, M. Dörenkämper, J. Bange, and A. Platis, *Evaluation of engineering models for large-scale cluster wakes with the help of in situ airborne measurements,* Wind Energy **27**, 1040 (2024).

[98] M. Mayol, A. Saulo, and A. Otero, *Farm to farm wake interaction in WRF: impact on power production,* in *Journal of Physics: Conference Series*, Vol. 1934 (IOP Publishing, 2021) p. 012017.

[99] K. Ali, D. Schultz, A. Revell, T. Stallard, and P. Ouro, *Assessment of five wind-farm parameterizations in the weather research and forecasting model: A case study of wind farms in the north sea,* Monthly Weather Review **151**, 2333 (2023).

[100] B. Cañadillas, R. Foreman, G. Steinfeld, and N. Robinson, *Cumulative interactions between the global blockage and wake effects as observed by an engineering model and large-eddy simulations,* Energies **16**, 3040 (2023).

[101] P. Baas, R. Verzijlbergh, P. van Dorp, and H. Jonker, *Investigating energy production and wake losses of multi-gigawatt offshore wind farms with atmospheric large-eddy simulation,* Wind Energy Science **8**, 787 (2023).

[102] O. Maas and S. Raasch, *Wake properties and power output of very large wind farms for different meteorological conditions and turbine spacings: A large-eddy simulation case study for the German bight,* Wind Energy Science **7**, 715 (2022).

[103] G. Rampanelli and D. Zardi, *A method to determine the capping inversion of the convective boundary layer,* Journal of Applied Meteorology - J APPL METEOROL **43**, 925 (2004).

[104] L. Lanzilao and J. Meyers, *Wind-farm wake recovery mechanisms in conventionally neutral boundary layers,* Journal of Fluid Mechanics **1015**, A5 (2025).

ACKNOWLEDGEMENTS

This PhD is the greatest intellectual challenge I have taken on so far, one that pushes me to keep striving for more. However, it did not happen overnight. I have long been passionate about rocket propulsion; yet after completing my undergraduate degree in Aerospace Engineering, my options for pursuing a master's and building a career in the space industry were rather limited. Since rocketry is predominantly linked to defense, a military career would have been the natural path, but it did not align with my interests. Moreover, entering a private space company abroad, would have required citizenship. Gradually, I came to realize that space propulsion was out of reach. Consequently, through a master's focused on wind energy, I redirected my interests toward fluid mechanics and its application to wind farm aerodynamics with the intention of pursuing a PhD in wind energy. This journey commenced with a computational fluid dynamics (CFD) study I conducted for my master's thesis investigating inter-farm wake effects and proposed a wind farm re-powering strategy to maximize yield of a re-powered wind farm. Fortunately, the very first PhD position I applied for aligned with my interest in wind farm aerodynamics but little did I know, however, that I would soon find myself working on atmospheric gravity waves. My late supervisor, Dries Allaerts, and I often joked that I had skipped the chapters on waves in high school, only for my PhD to revolve around a particular class of them. The track I had planned seemed reachable, and I hope that my work in wind farm aerodynamics makes a substantial scientific contribution.

As I reflect on my journey, I recall several esteemed people under whom I had the privilege of working in the field. Firstly, I would like to thank the committee members for reading my thesis and giving feedback. Their valuable feedback expanded my thought process and the scope of my work. Secondly, I would like to express my utmost gratitude to **Simon** and **Dries** who granted me the opportunity to pursue a PhD in the field. Looking back on the time when I was readying my application to the graduate school, I can recall a cautious warning by a friend doing his PhD at the institute regarding the fierce competition at TU Delft. He encouraged me to hope for the best but prepare for the worst. I was in disbelief when I was accepted. I still do not know what convinced Simon and Dries to hire me, but I regard it as an opportunity they gave me to pursue the path I had envisaged. I am deeply grateful for their support and guidance. **Simon** continues to give more opportunities as I advance toward a postdoctoral researcher position for which I am truly indebted to him, especially as Dries was unable to continue with supervision.

Dries, I am deeply saddened by your untimely demise; however, your formative guidance and holistic supervision contributed immensely to conceptualizing my PhD and shaping my journey. Besides technical help, you guided me in availing opportunities that were useful for networking and career development. For instance, you initiated collaborations with researchers at National Renewable Energy Laboratory and Indiana University on my behalf, which resulted in my research stay at these institutions. I re-

member your persuading me and helping me with the application for a sponsorship to attend a colloquium at National Center for Atmospheric Research, USA, which I was able to avail. It was delightful to know Dries on a personal level, which was key to our bonding and helped make my journey smoother. I vividly remember him being in the hospital for a chemo session while we were discussing my first paper. This meeting led to Dries and me exploring the dating culture in the Netherlands and Belgium and his dating tips for me. In summary, I will need a separate chapter to express what a pleasure it has been to know him and his wonderful family, **Fran, Emil, Nora, and Suzan**. Our time together has been one of the highlights of my PhD journey and wish to extend my sincere appreciation to him and **Fran**.

Matt, you have been inspiring me in so many ways, and I cannot find words to acknowledge your support, guidance, and supervision. I do not know what motivated you to first take the trouble of bringing me to NREL and then to agreeing to supervise me. I would surmise that it was your respect and affection for your friend Dries and your tireless commitment to advancing research. It is truly admirable how selflessly you chose to take on the additional stress and workload to assist me. I was often stunned that you would wake up 4 am to meet me online, ensuring that I was not stalled with my work. This was after going through the trouble of arranging all the administration at NREL's end to get me there, and you were kind enough to help me with the logistics. I was extremely impressed when you gave me your bike to commute to work in Indiana, then invited me to your place to meet your family, and involved me in your routine life there. Those two months are by far some of the best in my PhD. I would also like to thank **Jill**, for treating me like family when I was there and for gifting the book to help me improve my writing.

Dominic it has been a pleasure to have you in my supervisory team and previous progress meetings. I veritably respect the time you took out of your heavy workload. This thesis has taken its current shape thanks to your thorough and valuable feedback, that too in a very short time so that I could finish my PhD on time. I appreciate your understanding of the circumstances I faced while writing this thesis.

Seba, what a pleasure it has been to get to know you. I am thankful to you for lending an ear to my complex thoughts about gravity waves, complaints about life abroad, and of course, for all the TOSCA and MSC-related help. It still remains a challenge to discuss science via whatsApp. I am moved by your generosity and humbleness. **Asif**, it would have been impossible to survive the weather and bachelor's life in Delft if it were not for you allowing me to rant and complain, that too in Burushaski. Your companionship made me feel closer to home. I greatly enjoyed your Biryani and us playing tennis, cricket, and volleyball together. **Anand**, many thanks for understanding, at times, even my incorrect views and questioning them to help me see the flaws. I would love to add that I am certain that there is no restaurant in Europe that makes a better palak paneer than yours. **Likhitha**, our friendship came at a particularly demanding time but one that has been invaluable. The are many fond memories we share: the walks in Delft, ice cream treats, brunches, homemade meals and more. Yet, the common theme has been your willingness to lend an ear to anything I say and your tolerance of my roasting you. How nice of you to introduce me to **Arsheep**; a man whom well-informed political views and thoughts on society I particularly enjoyed coupled with the delicious meals he cooked. **Ali** I am impressed by your openness to views and understanding of others. I

know you will be instrumental in realizing my dream of the Hunza state; this is, of course, a joke! **Marie**, your hospitality is admirable and I consider myself lucky to have enjoyed it. **Emanuel**, your overwhelming support during our time together in Colorado will always be remembered. I had not expected you to modify your plans to assist me during my trouble with the US visa process. You have my profound respect for all your help, and I would like to say thanks to you for adding pumpkin to my lamb recipe. **Ivan**, your brief stay in Delft was enough for us to connect on a deeper level, and I am delighted to call you a friend; you are a genuine, hardworking, and humble person, and I appreciate you for that.

David, Dawood! I have sincerely enjoyed your smart and funny presence through this journey and hope it continues. "Inshallah Biryani" still remains a shared dream! **Illaria**, I was inspired by your networking skills; thank you for the leads on several things. **Hrishi and Deepti**, you guys made me feel at home in Bloomington. Thank you for all the help during my stay there. **Rishi**, Sir Jee! I admire your steadfastness to your values and your ability to always wear a smiling face. **Evert**, I must thank you for all the conversations and discussions on both scientific and general topics. Much respect for devoting your precious time to translate the summary of my thesis into Dutch. **Marcus**, **Jonas**, **David**, it has been such an awesome experience to know you; the hike-and-camp trip you organized in the US will always be one of my favorite moments. **Matteo**, though our interactions have been brief, I will remember you as a kind person and my deepest appreciation for the assistance you offered when I needed it the most. **Kiran**, thank you for all the tennis sessions you organized and for tolerating my sometimes annoying playing technique. **Guanqun, Adhyanth, Zhao, Jingna** the hotpot dinners and movie nights with you have stood out as delightful memories during my Delft life. **Isabelle**, it has been enjoyable discussing difficult and controversial topics like religion with an intelligent person like yourself.

Over the last four years, I have been in four different offices and feel blessed to have had the company of some amazing and talented office mates. **Erik, Ali, Guanqun, Shyam, Rention, and Mathis** at Aerospace, **Robin, Faegheh, Tim, Alexandra, and Sachin** at the Controls group, **Regis, Ulrike, and Aliza** at NREL, and **Hrishi, Jovanka, and Quan** at Indiana University. Thank you all for tolerating me. **Regis**, I am extremely grateful to you for helping me with SOWFA right from the beginning of my PhD. **Gareth and Ben**, thank you so very much for making my visit to NREL and Indiana University possible. I would also like to thank **Robin and Mikko** for their sincere help with Aspire and **Remco** for arranging the license for me to use this incredibly helpful code. **Jan-Willem**, it was very kind of you to allow me to share the office with your group. **Kelsey, Pramod, Bas, and Jasper**, I really enjoyed supervising your master's thesis. Thank you for contributing to my understanding of gravity waves. Thanks a lot **Mishal** for all the help with proofreading and rephrasing my broken English.

As I reflect on my takeaways from this journey, I find several ideas, expressions, views, discussions, and moments shared with colleagues that I deeply cherish. I pay my deepest respects to my exceptionally talented colleagues in Aerospace: **Dachuan, Udhaya, Simone, Malte, Tercio, Mihir, Ricardo, Michiel, Jelle, Deepali, Mark, Fedrico, Sumit, Raja, Wim, Dani, Shantanu, Niels, Hugo, Claudia, Felipe, Brian, Uwe, Abhratej, Jenna, Carlos, Andrea, Oriol, Haoyuan, Cristina, George, Julia, Sen, Livia, Yanan, Am-**

bar, Jiaxin, Kaj, Falvio, Abhyuday, Fernanda, Clem, Nirav, Isaac, Dylan, Augustin, Helena, Anastasia, Hafiz, Nikhita, Mirko, Kherlen, Yannick, Jatinder, Martino, Hendrick, Olivier, Usman, Xin, Chairs, Rushikesh, Carlos Morales Ruvalcaba, and Federico Di Verniere. I also want to express my gratitude to **Axelle, Donatella, Frits, Wei, and Delphine** for your concern and support in the absence of Dries. A big thank you to **Sylvia** for all the help with the considerable amount of administration work she undertook during my PhD, especially while I was unavailable due to my move.

Last but not least, with heartfelt gratitude, I thank my family - my parents, siblings, aunts, and uncles – for their love, patience, and endless support and encouragement. I often reflect on my academic path and realize that their collective vision and unwavering support in providing excellent educational opportunities to the younger members of the family enabled this journey for me. Only you can truly understand what this journey took and what it means to me and our family.

CURRICULUM VITÆ

Mehtab Ahmed KHAN

06-10-1993	Born in Khyber Hunza, Pakistan.

EDUCATION

1998–2012	Aga Khan Diamond Jubilee School, Khyber Hunza Aga Khan Higher Secondary School, Gilgit (2007–2010) Aga Khan Higher Secondary School, Karachi (2010–2012)
2013–2017	Bachelor of Science in Aerospace Engineering Institute of Space Technology, Islamabad
2018–2021	Master of Science in Energy Systems Engineering National University of Science and Technology, Islamabad
2021–2025	PhD. Candidate Technical University Delft, Netherlands *Thesis:* Regional Scale Wind Farm Aerodynamics The Role of Atmospheric Gravity Waves *Promotors:* Prof. dr. S.J. Watson AND Prof. dr. D.A. Von Terzi

List of Publications

Publications included in this Thesis

4. **Khan, Mehtab A.** and Watson, Simon J. and Churchfield, Matthew, *The performance of neighboring wind farms for varying inter-farm distances and atmospheric stratification*, Journal of Physics: Conference Series (Torque 2026).

3. **Khan, M. A.** and Churchfield, M. J. and Watson, S. J., *Dependence of Wind-Farm-Induced Gravity Waves and Wind-Farm Performance on Non-Dimensional Atmospheric Parameters and Simulation Configuration*, Wind Energy Science Discussions **2025**, 1–34 (2025).

2. **Khan, M. A.**and Allaerts, D. and Watson, S. J. and Churchfield, M. J., *Investigating the relationship between simulation parameters and flow variables in simulating atmospheric gravity waves for wind energy applications*, Wind Energy Science **10**, 1167–1185 (2025).

1. **Khan, Mehtab A.** and Watson, Simon J. and Allaerts, Dries J. N. and Churchfield, Matthew, *Recommendations on setup in simulating atmospheric gravity waves under conventionally neutral boundary layer conditions*, Journal of Physics: Conference Series **2767**, 092042 (2024).

Other Contributions

3. Sivanandan, H. and Churchfield, M. J. and Kravitz, B. and Quon, E. and **Khan, M.**, *Impact of compressibility approximations on atmospheric gravity wave characteristics*, Journal of Fluid Mechanics, **Submitted** (2026).

2. Allaerts, D.A. and **Khan, M.** and Churchfield, M. J., *Froude number dependency of atmospheric gravity waves: Apparent horizontal wavelength and wave field inclination*, Journal of Fluid Mechanics, **Under Review** (2025).

1. Stipa, S. and **Khan, Mehtab A.** and Allaerts, D. and Brinkerhoff, J., *A large-eddy simulation (LES) model for wind-farm-induced atmospheric gravity wave effects inside conventionally neutral boundary layers*, Wind Energy Science **9**, 1647–1668 (2024).